UNIVERSITÀ DEGLI STUDI DI MILANO

Ph.D. course in Industrial Chemistry

XXXVIII cycle

New GO- and RGO-based MORALs and Carbene-Functionalized Gold Nanoparticles for Heterogeneously Catalyzed Reductions

Tutor: Prof. Cristina Della Pina

Co-tutor: Dr. Mario Pagliaro

Ph.D. course coordinator: Prof. Laura Prati

Ph.D. Thesis of Matteo Formenti

R13687

ORCID: 0000-0003-0580-0499

A.Y. 2024-2025

Summary

List of Abbreviations

$_{a}$Ti-OH	acidic titania surface hydroxyl groups
AuNPs	gold nanoparticles
Au_{per}	fraction of perimetral gold atoms
Au_{surf}	fraction of surface gold atoms
B.E.	binding energy
$_{b}$Ti-OH	basic titania surface hydroxyl groups
DFT	density functional theory
DMF	N,N-dimethylformamide
DMSO	dimethyl sulfoxide
FT-IR	Fourier-transform infrared
FWHM	full-width half maximum
GO	graphene oxide
iso-TT	triimidazo[1,2-*a*:1',2'-*c*:1",5"-*e*][1,3,5]triazine
iso-TTBnHAuCl$_4$	10-benzyltriimidazo[1,2-*a*:1',2'-*c*:1",5"-*e*][1,3,5]triazin-10-ium tetrachloroaurate
iso-TTBnHBr	10-benzyltriimidazo[1,2-*a*:1',2'-*c*:1",5"-*e*][1,3,5]triazin-10-ium bromide
iso-TTEtHI	10-ethyltriimidazo[1,2-*a*:1',2'-*c*:1",5"-*e*][1,3,5]triazin-10-ium iodide
iso-TTEtHPF$_6$	10-ethyltriimidazo[1,2-*a*:1',2'-*c*:1",5"-*e*][1,3,5]triazin-10-ium hexafluorophospate
MSI	metal-support interface
$_{MSI}$Ti-OH	titania surface hydroxyl groups at the metal-support interface
NHC	N-heterocyclic carbene
NMR	nuclear magnetic resonance
RGO	reduced graphene oxide
SAO	strong adsorbed oxygen
THF	tetrahydrofuran
THT	tetrahydrothiophene
TT	triimidazo[1,2-*a*:1',2'-*c*:1",2"-*e*][1,3,5]triazine
XPS	X-ray photoelectron spectroscopy

Aim of this Work

This work aims to develop and study new materials for catalytic uses, with a specific focus on reducing aromatic nitrocompounds.

The work focuses on two main classes of materials. The first one is MORALs, an acronym for Metal-ORganic ALloys, a class of materials composed of organic molecules embedded in metal particles. In previous studies, this class of materials has been reported to exhibit improved catalytic properties compared to the single metal or organic molecule that constitutes it. In this work, the chosen organic molecule is graphene oxide, combined with two different metals, palladium and nickel. The resulting materials can also be further modified by reducing graphene oxide to reduced graphene oxide. All materials were analyzed using various analytical techniques and evaluated for their ability to reduce nitrobenzene.

This work focuses on two main classes of materials that have recently attracted growing interest in the field of heterogeneous catalysis. The first class comprises the so-called MORALs, an acronym for Metal-ORganic ALloys. These hybrid systems consist of organic molecules embedded within metallic particles. Previous studies have shown that MORALs can display catalytic properties superior to those of either the pure metal or the isolated organic molecule, suggesting the emergence of synergistic effects arising from their intimate combination. Graphene oxide (GO) was selected as the organic component due to its high specific area and ability to interact strongly with metal species. GO was combined with two different metals, palladium and nickel, chosen for their well-established catalytic roles in reduction reactions. The resulting MORALs were further diversified by subjecting graphene oxide to chemical reduction, yielding reduced graphene oxide (RGO) and enabling a direct comparison between the two different modifications. All synthesized materials were thoroughly characterized using a variety of analytical techniques aimed at elucidating their structural and chemical composition. Their catalytic performance was then evaluated in the reduction of nitrobenzene, a model reaction of both academic and industrial relevance.

The second class of materials investigated consists of N-heterocyclic carbene (NHC)-functionalized gold nanoparticles. Gold nanoparticles (AuNPs) are widely recognized for their unique optical, electronic, and catalytic properties, which have enabled applications ranging from sensing and biomedicine to fine-chemical synthesis. However, the performance and stability of AuNPs are strongly influenced by the nature of the ligands that cap their surface. In recent years, NHCs have emerged as a powerful alternative to traditional thiol-based ligands, offering stronger metal-ligand bonds, enhanced robustness under reaction conditions, and the possibility of fine-tuning the electronic environment of the metal surface. Two iso-TT derivative were selected as the NHC precursors. This choice was motivated by the

opportunity to explore the applicability of a novel ligand scaffold and to assess how its structural features influence the stabilization and reactivity of gold nanoparticles. The synthesis of the NHC-functionalized AuNPs was followed by a comprehensive characterization aimed at elucidating the properties of both the organic ligand and the resulting hybrid nanomaterials. Particular attention was dedicated to understanding the interaction between the NHC and the gold surface. To evaluate their practical relevance, the supported gold nanoparticles were tested in the reduction of nitrobenzene. This reaction served as a benchmark to assess the robustness, activity, and potential advantages of the different functionalized materials.

Functionalization with N-heterocyclic carbenes has also been explored as a strategy to modify catalytic materials for the study of the hydrogen spillover phenomenon, a process in which activated hydrogen atoms migrate from a metal surface onto an adjacent support. Understanding and controlling spillover is of considerable interest, as it can influence reaction pathways, extend the effective catalytic surface, and enhance the performance of supported metal catalysts in hydrogenation reactions. In collaboration with Professor Bert Chandler and his research group, NHC ligands were employed to functionalize Au/rutile catalysts. This system provides an ideal platform for investigating spillover, as gold nanoparticles can activate hydrogen under specific conditions, while rutile offers well-defined surface sites capable of participating in hydrogen migration. By introducing NHCs , the study aimed to probe how ligand functionalization affects the hydrogen activation step. A comprehensive set of measurements was carried out using *in situ* FT-IR spectroscopy, enabling real-time monitoring of surface species. Kinetic analyses, including Arrhenius plots and reaction order determination, were performed to highlight differences between the unfunctionalized and NHC-functionalized catalysts. These experiments provided insight into how the presence of the organic ligand modifies the mechanism of hydrogen transfer across the metal–oxide interface. Finally, the materials were evaluated in the reduction of p-nitrophenol. Comparing the catalytic behavior of the functionalized and unfunctionalized systems allowed for a deeper understanding of the role of NHCs in modulating hydrogen mobility and reactivity.

I. INTRODUCTION

Catalysis

The term catalysis, from the Greek *katàlysis,* meaning "dissolution", accurately describes how a catalyst works by breaking bonds that hinder reactions. Catalysts participate in reactions without being consumed, changing the mechanism: uncatalyzed reactions often have fewer steps, while catalyzed ones have multiple. Using a catalyst significantly reduces activation energy, replacing high-energy steps with less energy-intensive ones, resulting in faster reactions under the same conditions. The main goal of catalysis isn't just speeding up reactions but also aligning conditions with ambient temperature and pressure to lower costs, ensure high productivity, meet market demands, and increase profits.

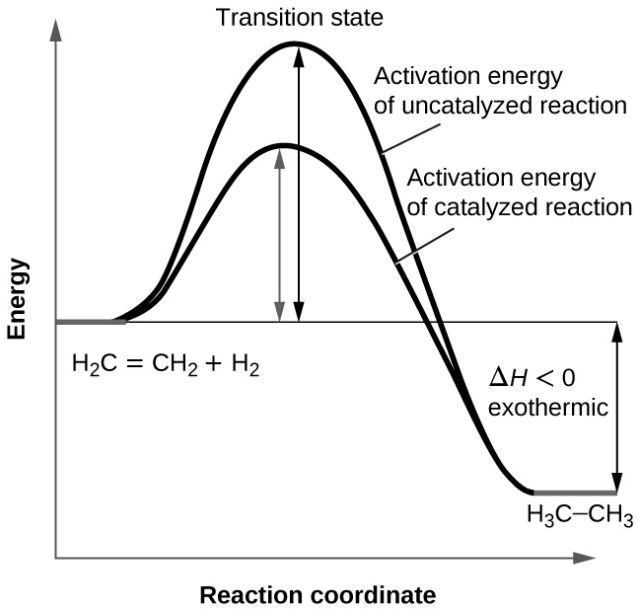

Figure I.1. Diagram illustrating the relative energy during uncatalyzed and catalyzed hydrogenation of ethylene.

The catalyst does not change the reaction's dynamic equilibrium but affects only the formation energy of the activated complex, seen as the peak in the reaction potential energy graph (**Figure I.1**). A thermodynamically unfavorable reaction stays so even with a catalyst, which influences the reaction kinetically by enabling the formation of activated complexes with lower activation energies. Consider the generic equilibrium reaction:

$$aA+bB \leftrightarrows cC+dD$$

Generally, the catalyst reacts with one of the reactants to form an intermediate, which then reacts with other reactants to produce the final products. The reaction mechanism can be roughly outlined as a fast pre-equilibrium stage (*Equation I.1* and *Equation I.2*) between a reactant and the catalyst, followed by a slower stage (*Equation I.3* and *Equation I.4*) which leads to the formation of the products and the regeneration of the catalyst.

$$aA + cat \leftrightarrows [A - cat] \qquad \textit{Equation I.1}$$

$$K = [[A - cat]]/([A]^a\,[cat]) \qquad \textit{Equation I.2}$$

$$[A - cat] + bB \rightarrow \ cC + dD \qquad \textit{Equation I.3}$$

$$r = \frac{d[C]}{dt} = \frac{d[D]}{dt} = k[A - cat][B]^b = kK[A]^a[B]^b[cat] \qquad \textit{Equation I.4}$$

The kinetic equation obtained in the previous example is a greatly simplified version compared to the majority of real cases, which do not fully meet the assumptions that were considered valid: in fact, the mechanism of a catalytic reaction can be significantly more complex than the same reaction carried out in the absence of a catalyst, consequently increasing the difficulty of mathematic interpretation of the chemical phenomenon underway.

Catalysts are traditionally classified into two categories, defined as homogeneous and heterogeneous, based on whether the phases of the reactants and the catalyst are the same or not. Both categories offer significant advantages and disadvantages, depending on the type of reaction being performed.

Heterogeneous catalysis

Heterogeneous catalysis is a key industrial process for sustainable and profitable chemical production. Solid catalysts can be dispersed in gases or liquids or anchored to inert supports, making separation and recycling easy. Reactions occur at the interface between fluid and solid phases, so high surface area maximizes efficiency. Reactants must adsorb onto the catalyst surface before reactions can proceed, a spontaneous process under suitable conditions.

Depending on the nature of the energies binding the reactant molecules to the catalytic surface, adsorption is categorized as physisorption or chemisorption:

- Physical adsorption, or physisorption, occurs above a fluid's critical temperature. Below this temperature, the fluid condenses onto the solid surface; adsorption occurs but with insufficient interaction energies for significant bonding. These interactions are usually Van der Waals forces.
- Chemical adsorption, or *chemisorption*, is characterized by the formation of a chemical bond, so that the adsorbed molecules achieve maximum coordination with the substrate. Chemisorption

requires a high activation energy, and the bonds form at specific characteristic zones called active sites.[1]

The rate of a catalytic reaction depends on the concentration of reactants adsorbed onto the surface: the higher the concentration, the greater the reaction rate. Consequently, many catalysts are dispersed onto highly porous inert supports, so that a small amount of catalyst can cover a vast surface area while avoiding aggregation.

The steps of a heterogeneous catalytic reaction are multiple:

1. The reactant must diffuse from the bulk of the fluid phase to the surface of the catalyst. This process is known as external diffusion.
2. Through internal diffusion, once the catalytic surface is reached, the reactant diffuses into its pores.
3. Adsorption, which is assumed to consist of a rapid equilibrium between adsorbed and free molecules near the solid phase.
4. Once adsorbed, the molecules are not completely immobilized; instead, they retain a certain degree of mobility along the catalytic surface. Depending on the nature of the reaction, the transformation from reactants to products occurs with different kinetics.
5. Once the reaction occurs, the product no longer has the same affinity for the catalyst as before and thus desorbs.
6. The products back-diffuse from the pores to the solid-liquid interface, driven by the concentration gradient that causes mass flux.
7. From the solid-liquid interface, the products further back-diffuse into the fluid phase.

Heterogeneous catalysis is therefore the result of mass transport phenomena and chemical reactions. The kinetic equations describing these phenomena depend on the configuration, location, and density of active sites, the surface reaction kinetics between active sites and the solute, and the thermodynamic equilibria between the fluid phase and the solid phase to which the catalyst is anchored. Several models have been developed to describe this series of phenomena mathematically, but the most commonly used one is the Langmuir-Hinshelwood mechanism.

Langmuir-Hinshelwood Mechanism

Many catalysts owe their action to co-adsorption, that is, the adsorption of two or more reactive species. In the Langmuir–Hinshelwood mechanism, the reaction proceeds through encounters between

molecules adsorbed on the surface; it follows naturally that the rate law is second order with respect to the degree of surface coverage. For the general reaction:

$$A + B \rightarrow P \qquad \textit{Equation I.5}$$

The rate law will be of the form:

$$r = k\theta_A\theta_B \qquad \textit{Equation I.6}$$

Where k is the kinetic constant of the process, and θ_A, $\theta_B$are respectively the degrees of surface coverage by molecules of type A and molecules of type B. The degree of surface coverage is defined as:

$$\theta = \frac{\text{number of occupied adsorption sites}}{\text{total number of adsorption sites}} \qquad \textit{Equation I.7}$$

Equivalent to the equation:

$$\theta = \frac{\text{volume of adsorbate}}{\text{volume of adsorbate corresponding to a monolayer}} \qquad \textit{Equation I.8}$$

Surface coverage depends on fluid pressure; how theta varies with pressure at fixed temperature can be modeled by an adsorption isotherm. Common ones include Langmuir, BET, Temkin, and Freundlich isotherms. Each relies on different assumptions and fits data variably; the best model depends on experimental results.

By introducing the appropriate adsorption isotherms for the degrees of coverage θ_A and θ_B into the kinetic equation of the Langmuir-Hinshelwood model, the reaction rate is obtained as a function of the partial pressures of the reactants, namely:

$$r = \frac{kK_AK_Bp_Ap_B}{(1 + K_Ap_A + K_Bp_B)^2} \qquad \textit{Equation I.9}$$

where $K_A$and $K_B$are respectively the thermodynamic adsorption constants of molecules of type A and B on the surface, and p_A, $p_B$are the partial pressures of A and B. Since both the kinetic constant k and the thermodynamic constants K_A, $K_B$are functions of temperature, the thermal dependence of the rate can differ significantly from that predicted by the Arrhenius equation.

MORALs

The term *Metal-Organic Alloys* (MORALs)[2] was coined in 2009 to describe a novel class of materials consisting of a metal doped with organic molecules. These materials were initially developed by David Avnir in 2002[3] and first applied as catalysts in 2005.[4]

The doping of metals with organic molecules is performed for several reasons:

- Hybrid materials composed of native metals and organic molecules remain largely unexplored;
- A significant portion of the periodic table is made up of metals, and their wide availability could enable the development of this new class of materials;
- Synergistic effects between the metal and the organic molecule may enhance specific physicochemical properties of both components, including their chemical reactivity;
- Metals are applied in different fields, and any modifications of their properties are potentially interesting.

The potential applications of these materials gave rise to a new and compelling concept in catalysis: the encapsulation of an organic molecule, polymer, or biomolecule within a catalytic metal can yield hybrid materials capable of performing at different catalytic stages. Subsequently, this new class of catalysts has demonstrated promising yields across a broad spectrum of chemical reactions.

The synthetic approach for this class of composite materials is conceptually straightforward: the metal cation of interest is reduced in the presence of the organic molecule intended for encapsulation; as the metal precipitates, it incorporates the dopant. It is crucial to employ a reducing agent that is chemically inert toward the organic molecule and whose byproducts can be readily removed from the final material.

Alternative synthetic pathways also exist, such as the heterogeneous reduction of the metal cation using a metal located lower in the electrochemical series, or electrochemical reduction of metal cations to entrap molecules or small polymers. However, these methods may encounter some issues if the dopant is not water-soluble. In such cases, different strategies can be adopted:

- The use of a reducing agent with a solution containing both the metal precursor and the doping molecules,[3] such as in the case of Ag reduction in the presence of Congo-red with NaH_2PO_2
- Using a metal with a lower reduction potential, such as in the case of the reduction of copper in the presence of Congo-red using zinc;[5-6]
- Electrochemical reduction of metal cations can be used for easily reducible metals, e.g., in the synthesis of thionine@Cu or thionine@Ag;[7]

- Dissolving the dopant in water by means of a surfactant, thereby forming a fine dispersion, as in the case of silver reduction in the presence of the water-insoluble Sudan-III;[3]
- Using an alternative solvent, such as DMF, that can solubilize both the metal salt and the organic dopant and furthermore act as a reducing agent if an equimolar quantity of water is added;[8]
- The employment of a zero-valent metal precursor, such as $Fe(CO)_5$, to avoid a strong reducing environment that can be too harsh for the organic dopant;[9]
- The use of amalgams, since mercury is a suitable solvent for metals.[10]

The resulting materials are named based on the two components divided by an @, so to be dopant@metal (e.g., Sudan-III@Cu, Nafion@Pd).

In the synthesis, different parameters can be changed. As discussed above, the choice of metal-dopant combination yields a myriad of possibilities. Also, the doping range can be varied to try optimizing the properties of the final materials; anyway, it is usually relatively low, consisting the materials of organic molecules embedded into metals and having metal atoms a mass usually much higher than the components of organic molecules. They are often employed as a powder for catalytic applications, but they have also been applied as pressed coins, nanometric supported particles, and thin films.

To give an idea of the catalytic potential of these materials, in 2007, Shter et al.[11] reported the application of Congo-red doped silver (CR@Ag). The synthesis of the material occurred in water by reducing $AgNO_3$ in the presence of Congo-red using sodium hypophosphite as the reducing agent. The final material was used in the methanol oxidation reaction, yielding formaldehyde, and was compared with bare silver and a catalyst comprising Congo-red adsorbed on silver.

The experiments showed that, while the adsorption of the molecule resulted in lower yield and selectivity in all the conditions tested, CR@Ag gave much better results: at 320 °C, it reached 90% methanol conversion, while the other catalysts did not reach 50%. Silver catalyst needed to reach 400° C to reach a comparable conversion. CG@Ag is also characterized by a higher selectivity, affording 70% selectivity at 320°C, while Ag and CG/Ag (Congo-red adsorbed on silver surface) reached about 30% and 20% respectively.

In another work,[12] a material comprised of Nafion, a perfluorinated polymer bearing sulphonic groups, entrapped in palladium (Nafion@Pd) was synthesized *via* reducing $PdCl_2$ using Zn in a Nafion water/ethanol solution. The resulting material was studied in the dehydration of 1,2,3,4-tetrahydro-1-naphthol. They showed how this material is able to catalyze the reaction to obtain 1,2-dihydronaphthalene, which subsequently undergoes disproportion to obtain a 50:50 mixture of tetralin and naphthalene (**Figure I.2** a). Furthermore, under H_2 flow, after the dehydration step, the

material catalyzed the selective hydrogenation to tetralin with unitary conversion and selectivity (**Figure I.2** b).

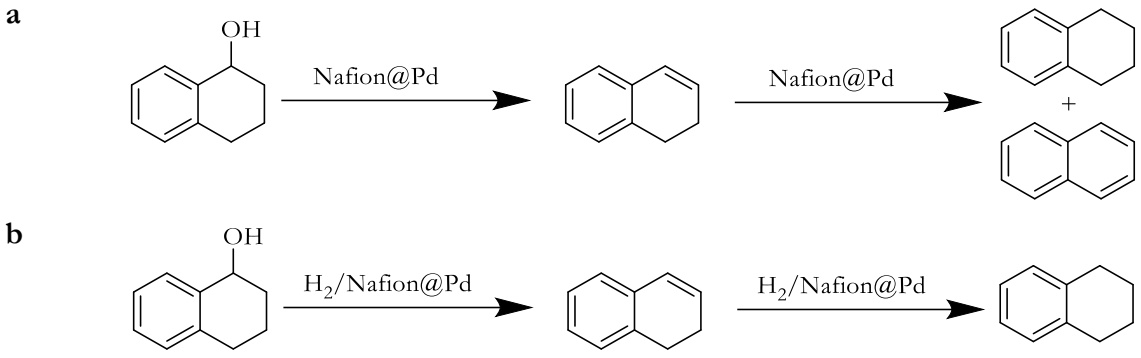

Figure I.2. Reaction scheme of Nafion@Pd reactivity on tetrahydronaphtol in the absence (a) and presence (b) of hydrogen.

The same procedure was also applied to other substrates (**Figure I.3**), like 1-phenyl-2-propanol, to obtain 1-phenylpropane through dehydration of the first reagent, giving 1-phenyl-2-propene, followed by hydrogenation. They also demonstrated that the two components alone are inactive in any of the conditions tested, being inactive in the first step of the catalytic chain.

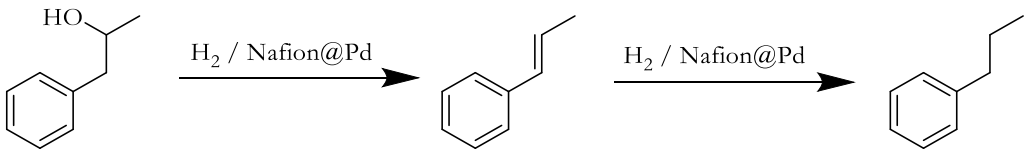

Figure I.3. Reaction scheme of Nafion@Pd with 1-phenyl-2-propanol and hydrogen.

Gold Nanoparticles

The term gold nanoparticles indicates particles composed of gold of nanometric dimensions. The definition of nanoparticles is given by some organizations. According to the norm ISO80004-1:2023,[13] nanoparticles are all the particles with all three dimensions within the 1-100 nm interval. According to the American Society for Testing and Materials, to be defined as nanoparticles, they can have two or three dimensions in the 1-100 nm interval.

While Michael Faraday described the first scientific synthesis of gold nanoparticles (AuNPs) in 1857,[14] their use predates this discovery by centuries. "Soluble gold, " usually a deep red solution, was historically used to stain glass, ceramics, and fabrics, and it even had medicinal applications. "Potable gold" solutions were recommended for various ailments, including the plague, epilepsy, diarrhea, and syphilis. Colloidal gold remained in medical diagnostics until the 20th century. Although the term "nanoparticle" was not used until much later, early scientists had an intuitive understanding of their nature. In the 17th century, German chemist Johann Kunckel suggested that drinkable gold contained particles "not visible to the human eye."

A historical example of the use of colloidal gold is the Lycurgus Cup (**Figure I.4**), the only known artifact made from a special type of glass called dichroic glass. This glass changes color depending on the source of light: it appears green under reflected light but becomes translucent red when illuminated from within. This unusual optical property is due to the presence of gold and silver nanoparticles in a molar ratio of approximately 1:14, which gives the glass its characteristic color-changing effect.

Figure I.4. Pictures of the Lycurgus Cup showing the different colors based on the different illumination. Left, illuminated from outside; right, illuminated from inside.

Another example from old times is the pigment called purple of Cassius, named after one of the main scientists who studied it, which is produced by the reduction of gold salts in the presence of stannous

chloride.[15] Despite its association with Cassius, which derives from a 1676 study, this pigment is much older, appearing as a red color in the stained glass of some churches.

Figure I.5. Red glass object colored employing Cassius purple.

In modern times, gold nanoparticles find applications across fields such as bioimaging, photothermal therapy, and catalysis. The high surface area makes them highly effective for catalytic processes. In biomedical contexts, they are particularly valuable for light-triggered drug delivery. However, bare AuNPs tend to aggregate and precipitate as metallic gold, compromising their functionality. In order to make them more stable, various types of ligands can be employed for surface stabilization, such as thiols, phosphines, amines, and citrates.

In particular, the most interesting application for the results presented in this work is their use as catalysts. Gold nanoparticles can be applied to various reactions, ranging from reductions to oxidations and C-C cross-coupling, often achieving high levels of conversion and selectivity. A disadvantage is that they tend to aggregate in suspension, leading to a loss of catalytic activity. Stabilization through ligands to keep a stable suspension or deposition on a support is necessary to maintain high efficiency.

This point was effectively demonstrated by Comotti et al.[16] in their study of the aerobic oxidation of glucose. They showed that, among the tested metals, unprotected gold nanoparticles were the most active in the oxidation process, but after a few minutes, the reaction rate slowed to almost a stop. They also detected the growth of nanoparticles during the reaction, attributing the loss in reaction rate to this phenomenon. To avoid deactivation, they supported the as-synthesized nanoparticles on activated carbon *via* sol deposition. Supported nanoparticles performed initially in the same way as gold sol, without decreasing catalytic activity over time, thus leading to almost unitary yield.

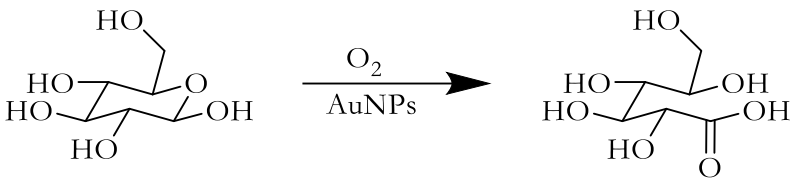

Figure I.6. Reaction scheme for glucose oxidation from Comotti's work.

NHC-functionalized Gold Nanoparticles

A new class of emerging ligands for metal nanoparticles and surfaces is that of Arduengo carbenes, also known as N-heterocyclic carbenes (NHCs). The first example, reported by Arduengo,[17] originates from an N,N-diadamantyl-substituted imidazolium. Deprotonation of such a molecule, using NaH in anhydrous THF solution, leads to the synthesis of a species with the C2 atom having formally six electrons (**Figure I.7**). This unusual molecule is stabilized both from the electronic point of view, being the hypovalent carbon atom in the middle of two nitrogen atoms that can donate electronic density, and from the steric hindrance of the adamantyl substituents.

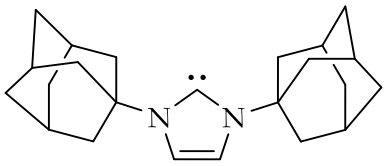

Figure I.7. The first example of N-heterocyclic carbenes synthetized by Arduengo.

Starting from this first example, multiple NHCs have been synthesized, varying both the carbon backbone and N-substituents (**Figure I.8**). The presence of two nitrogen atoms is not an absolute prerequisite to the stability of NHCs, and one of them can be substituted by sulfur, oxygen, or carbon. Because of this, different backbones have been applied in the synthesis of NHCs, such as N-substituted oxazole, N-substituted thiazole, and 1,2,3,5-tetrasubstituted imidazole.

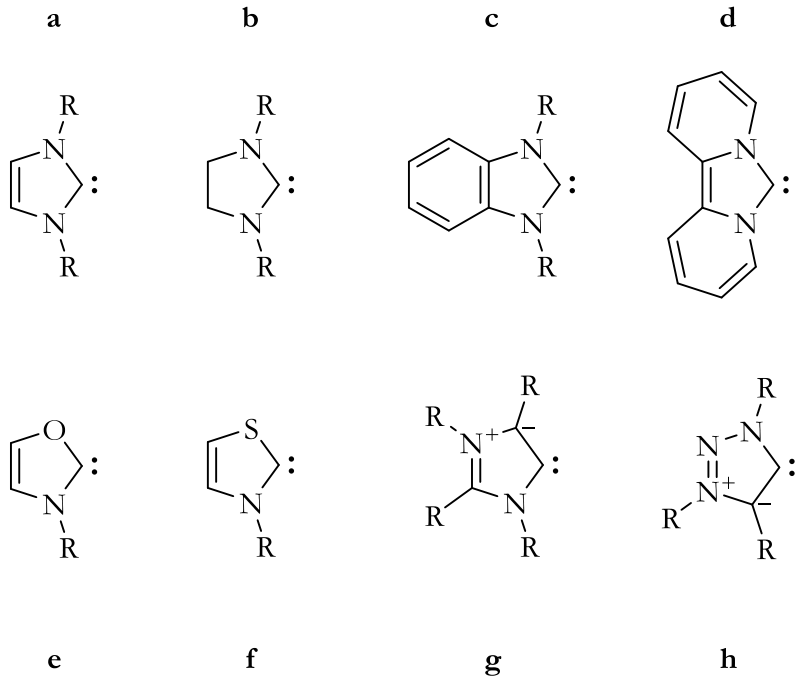

Figure I.8. General structures of different types of N-heterocyclic carbenes: a) imidazol-2-ylidene; b) imidazolin-2-ylidene; c) benzimidazol-2-ylidene; d) dipyrido[a]imidazol-2-ylidene; e) oxazol-2-ylidene; f) thiazol-2-ylidene; g) imidazol-4-ylidene; h) 1,2,3-triazol-5-ylidene.

NHCs are nucleophilic species that act as sigma-donors and bind to a wide range of metallic and non-metallic species. Examples of NHC complexes exist for all transition metals[18] as well as for a range of main group elements.[19]

First thought to be very similar to phosphines, NHCs have shown a chemistry of their own. As NHCs are typically more electron-donating than phosphines, they tend to form shorter and stronger bonds with metals.[20]

NHC-stabilized gold nanoparticles are expected to be more stable than their thiol-stabilized counterparts. A study of NHC self-assembled monolayer (SAM) on gold[21] measured the desorption energy of NHCs to be 158 ± 10 kJ·mol^{-1}, while the desorption energy of thiols was measured at 126 kJ·mol^{-1}.

Overall, NHC SAMs presented much better stability than their thiol counterparts, which are known to be unstable in ambient conditions over time.[22] Moreover, when NHCs were introduced on dodecyl sulfide (DDS) and dodecanethiol (DDT) SAMs, they were able to displace all the thioether and about 50% of the thiol. However, when DDS and DDT were introduced in NHC SAMs, no displacement occurred, and no sulfur could be detected by X-ray Photoelectron Spectroscopy (XPS).

Different groups studied the binding of NHC to gold surfaces from both experimental and theoretical perspectives.[23] While the strength of the bond between gold and NHCs appears to disfavor mobility, Scanning Tunneling Microscopy (STM) analysis showed that NHCs were bound to adatoms that could move along the surface in a ballbot-like motion. Despite this mobility, the SAM remains stable at high temperatures. Measurements at low temperature indicate a free rotation around a single bond between the NHC carbon and an Au atom. Density Functional Theory (DFT) calculations revealed that IMe (N,N-dimethylimidazolydene) has a significant impact on the surface as it "pulls" the gold atom it is bonded to away from the surface. The presence of NHC strongly favors the formation of adatoms on the surface, decreasing the energy barrier by ten times. The surface vacancy is occupied with a gold atom from the second layer of gold.

There are two main routes for the synthesis of NHC-functionalized nanoparticles:[24] the first is called a bottom-up approach (**Figure I.9** left), involving the synthesis of nanoparticles starting from a gold (I) carbene complex, achieving the direct synthesis of NHC-functionalized nanoparticles; the second is the top-down approach (**Figure I.9** right), consisting of the pre-formation of protected nanoparticles employing a sacrificial ligand such as sulfides or thiophenes, thereafter exchanging the ligands with carbenes generated *in situ* or *ex situ*.

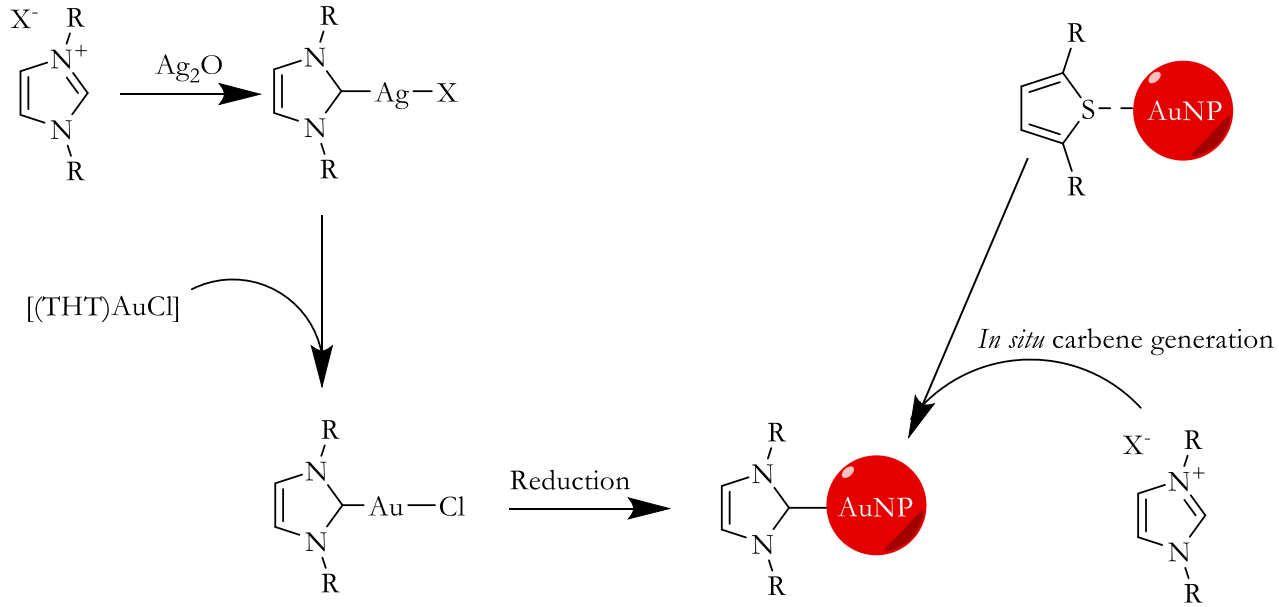

Figure I.9. Schemes of the synthetic procedures for NHC-functionalized gold nanoparticles. Left, bottom-up approach; right, top-down approach.

Due to the wide variability of NHCs, many strategies have been adopted to achieve different effects.

Bulky aryl substituents like mesityl (Mes) and 2,6-diisopropylphenyl (Dipp) provide rigidity and π-interactions with surface gold atoms.[25] The reduced packing density on the nanoparticle surface allows more exposed active sites, while π-stacking stabilizes the ligand shell. Catalytic studies show that such rigid wingtips enhance activity in hydrogenation and hydroamination reactions.

Long alkyl chains improve dispersity and colloidal stability. PEGylated NHCs confer water solubility, which is essential for biomedical applications and green catalysis. PEG chains also reduce nonspecific aggregation, enabling catalysis in aqueous environments.

The presence of charged substituents introduces electrostatic stabilization and pH-responsive behavior.[26-27] The presence of a carboxylic group (**Figure I.10**) makes nanoparticles stable in basic media, where the groups are deprotonated and repulsion between nanoparticles is high. Adding acetic acid to protonate the groups causes the nanoparticles to aggregate, as evidenced by the change in the absorption spectra.

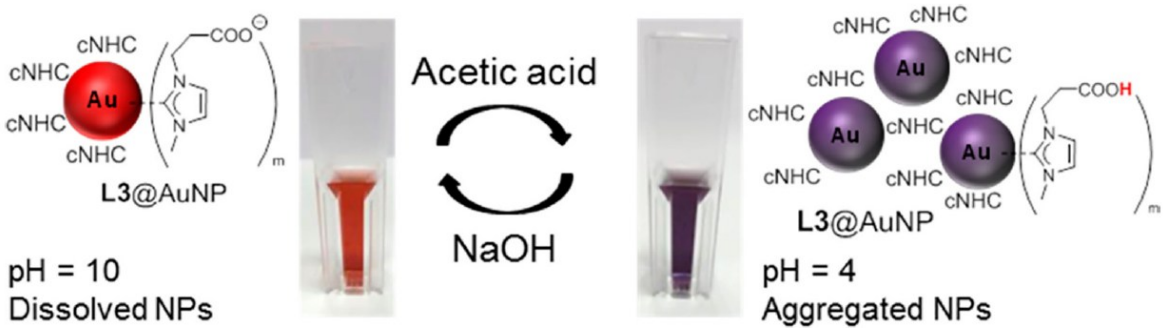

Figure I.10. The different behavior of carboxyl-functionalized gold nanoparticles at pH 4 and 10, demonstrating how deprotonated carboxylic groups can increase the repulsion between nanoparticles. Imager from Ferry et al.[26]

By introducing different substituents at the N1 and N3 positions, asymmetric NHCs can be designed. These allow incorporation of donor groups, such as additional NHCs, which provide chelation and further stabilize the AuNP surface.[27]

The electrochemical conversion of CO_2 into value-added products such as CO, formate, methanol, and hydrocarbons is a central goal in sustainable catalysis. Cao et al.[28] reported the first NHC@AuNP catalyst for CO_2 reduction, based on IMes-stabilized AuNPs prepared *via* a top-down ligand-exchange from oleylamine@AuNP. The catalyst displayed faradaic efficiencies strongly dependent on the steric demand of the NHC substituents. Zhang et al.[29] demonstrated that polymeric NHC ligands improved

selectivity and prevented nanoparticle aggregation, highlighting the role of multidentate binding. Comparative studies showed that NHC-functionalized AuNPs reached FE values up to 83%, with a 7.6-fold increase in current density compared to NHC-free AuNPs.

The reduction of 4-nitrophenol serves as a benchmark reaction for evaluating nanocatalyst stability and activity. NHC@AuNPs supported on aminopropyl-modified silica[30] or conductive polymer networks[31] exhibited excellent stability in aqueous media and high catalytic activity. Zhang et al. confirmed that NHC presence reduces aggregation and enhances recyclability,[29] allowing multiple catalytic cycles without loss of performance.

NHC@AuNPs with rigid aryl substituents (Mes, Dipp) have shown superior activity in hydrogenation and hydroamination reactions: π-stacking interactions among aryl backbones, gold surfaces, and support can stabilize the ligand shell and improve activity.[32] NHC@AuNPs supported on graphene displayed enhanced stability and selectivity in the intramolecular hydroamination of terminal alkynes to indoles.[33] Atomically precise NHC@AuNCs (Au_{11}, Au_{25}, Au_{29}) further revealed substrate selectivity, offering molecular-level insights into structure-activity relationships.[34-35]

NHC@Au_{13} clusters are also active in the catalytic hydrochlorination of alkynes. However, bidentate NHC ligands can block reactive sites, lowering activity. This case highlights the importance of ligand design: excessive surface coverage can compromise the accessibility of catalytic sites, underscoring the need to balance stability and reactivity.

The incorporation of chiral NHCs has opened pathways to asymmetric heterogeneous catalysis: dendrimer-encapsulated NHC@AuNPs[36] catalyzed the lactonization of allenic carboxylic acids, achieving enantioselectivities up to 16% enantiomeric excess. They also reported asymmetric induction in lactonization reactions using chiral NHC-ligated AuNPs. Also, examples of Pd, Ru, and Pt NPs with chiral NHCs are reported for the asymmetric synthesis of α-aryl ketones, achieving enantiomeric excesses of up to 85%.[37] Although enantioselectivities for AuNPs remain modest, these studies demonstrate the potential of NHC functionalization in stereoselective heterogeneous catalysis.

Triimidazotriazines

The molecule called triimidazo[1,2-*a*:1',2'-*c*:1'',2''-*e*][1,3,5]triazine (TT)[38] or, more briefly, cyclic triimidazole, is a molecule known from the 70s of the 19th century.[39] Anyway, because of the small scale it is obtained, it was not further studied for decades.

In 2011, a new methodology for its synthesis was developed,[40] involving the high vacuum decomposition of a copper diimidazolate polymer. In this way, it is possible the synthesis on a larger scale, obtaining a few grams of product per synthesis. In this way, together with TT, one isomer is obtained in lower yield (**Figure I.11**). This other molecule, namely triimidazo[1,5-*a*:1',2'-*c*:1'',2''-*e*][1,3,5]triazine (abbreviated with iso-TT), is characterized by the presence of a twisted imidazole ring.

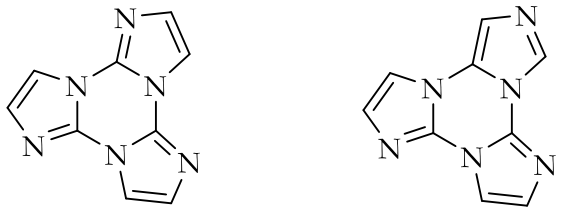

Figure I.11. Structures of TT (left) and iso-TT (right).

TT is a molecule characterized by aggregation-induced emission (AIE), a phenomenon consisting of the appearance of luminescent emission in aggregated states, such as the solid state or high-concentration solutions.[38] While non-emissive in solution, the solid state of TT is characterized by the formation of H-aggregates, granting strong emission characterized by a blue fluorescence and a green ultralong phosphorescence with lifetimes up to 1 s.

Over the years, this molecule has been functionalized in different ways: halide derivatives[41-43] were initially prepared, showing structure-related emission behaviors. From these first derivatives, other functional groups were introduced, such as pyrenes, pyridines, and thiophenes.

Beyond their emissive properties, substituted TT also found applications in various fields (**Figure I.12**). Pyrene-substituted TT was studied as a sensor for nitroaromatic compounds and as a photoluminescent dye in bioimaging. Pyridine derivatives, together with TT, were studied as organic building blocks for the synthesis of emissive metal-organic frameworks. Thiophene derivatives showed intriguing electrochromic properties. N-methylated pyridine derivatives were investigated as G-quadruplex stabilizers for anticancer treatment.

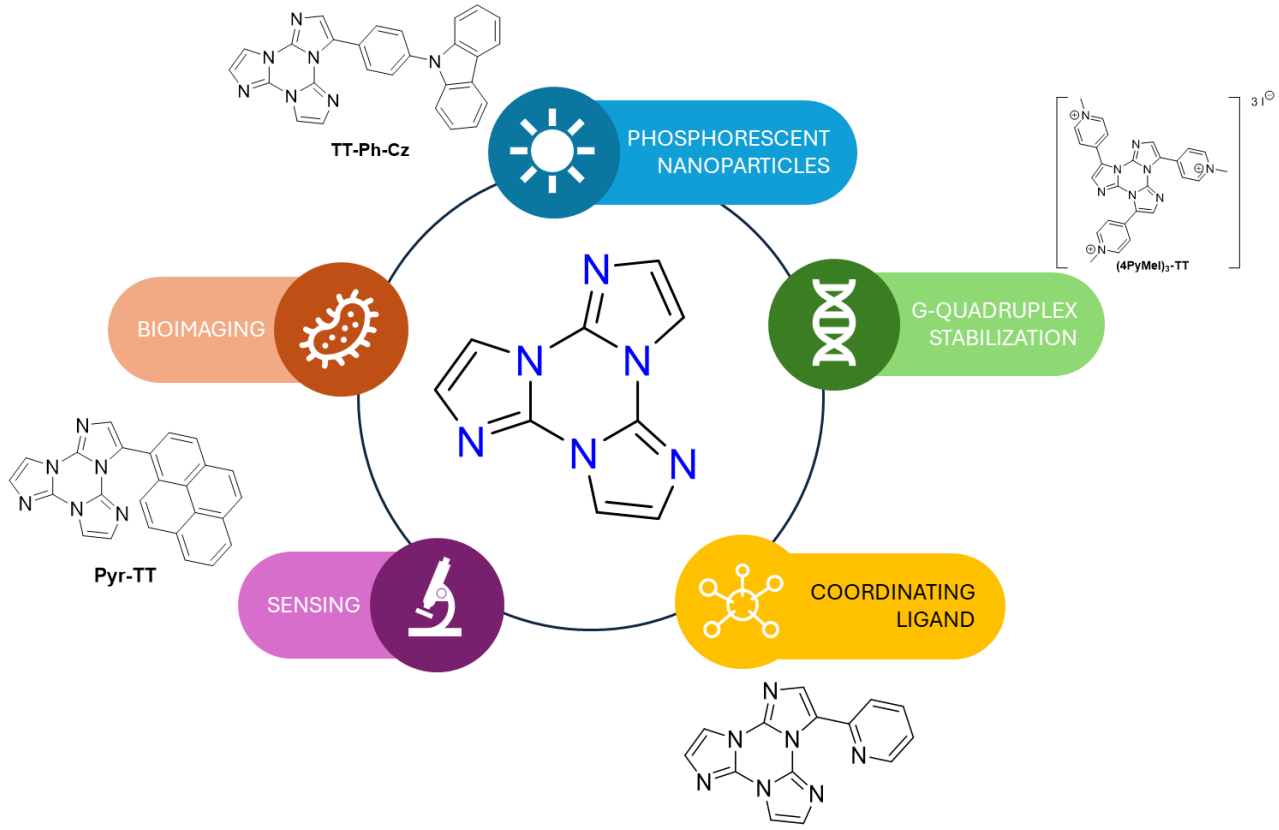

Figure I.12. A brief overview of various TT derivatives applications.

Despite the high variety of studies starting from TT, iso-TT is a poorly studied molecule. A work by Buck and Kunz[44] reports the use of an N-substituted iso-TT to explore the coordination chemistry of this carbene with different metals. In silver complexes, they observed unusually large Ag-C coupling constants, indicating strong orbital interactions. With rhodium (**Figure I.13**), the ligand revealed remarkable versatility: it could act as a simple monodentate donor, adopting a chelating mode, or even bridging between metal centers. In the solid state, the rhodium complexes assembled into trimers stabilized by anion-π interactions with tetrafluoroborate, an unusual structural motif that underscores the electron-poor nature of the triazine ring.

They also studied the carbene bond employing DFT calculations, FT-IR, and ^{77}Se-NMR. The results of calculations, together with a deshielded signal of selenium in NMR and a Tolman electronic parameter of 2055 cm^{-1}, show that the electron-poor π-system of the triazine leads to a pronounced π-acceptor ability.

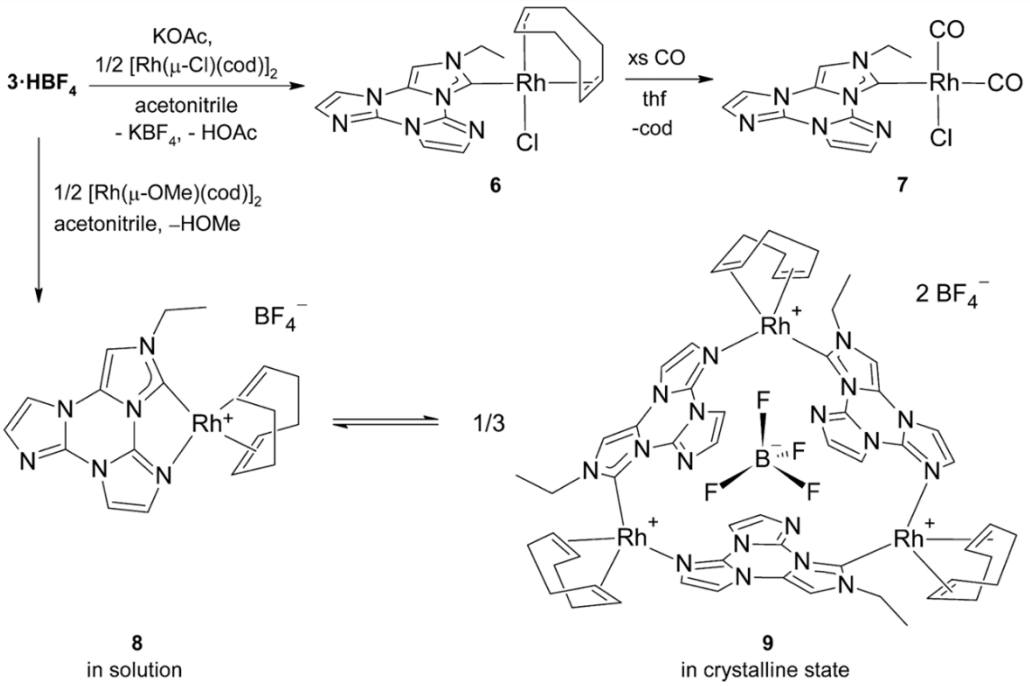

Figure I.13. Scheme for the synthesis of iso-TT-derived NHC complexes from the work by Buck and Kunz.

Inspired by these intriguing results, we decided to explore the use of triimidazotriazines as Arduengo-carbene precursor, and, hence, as ligands for gold nanoparticles.

Hydrogen Spillover

The term *hydrogen spillover* lacks a universally accepted definition in the literature. In the present work, we adopt the definition proposed by Prins,[45] according to which hydrogen spillover refers to the migration of highly mobile H-atom equivalents onto the catalyst surface. These H atom equivalents originate from the dissociation of H_2 molecules on metal active sites, which subsequently migrate onto the catalyst support surface.

More specifically, H atoms are split into H^+ species on the support surface, which migrate via surface hydroxyl groups, while the corresponding electrons move through the conduction band of the semiconductor support (**Figure I.14**). Since the migrating species involved in spillover is not a real hydrogen atom, it is more accurately described as a *hydrogen atom equivalent* or a *proton-electron couple*, and it is often denoted as H*. Although some studies have reported hydrogen spillover onto non-reducible supports, these findings remain a subject of debate within the scientific community.

In materials able to activate molecular hydrogen and generate spillover, three different phenomena can be observed:

1. Hydrogen activation and dissociation at the metal-support interface (MSI) or on the metal surface;
2. Hydrogen spillover, that is, migration of highly mobile hydrogen equivalents onto the support surface;
3. Reduction of metal atoms within the support induced by activated hydrogen.

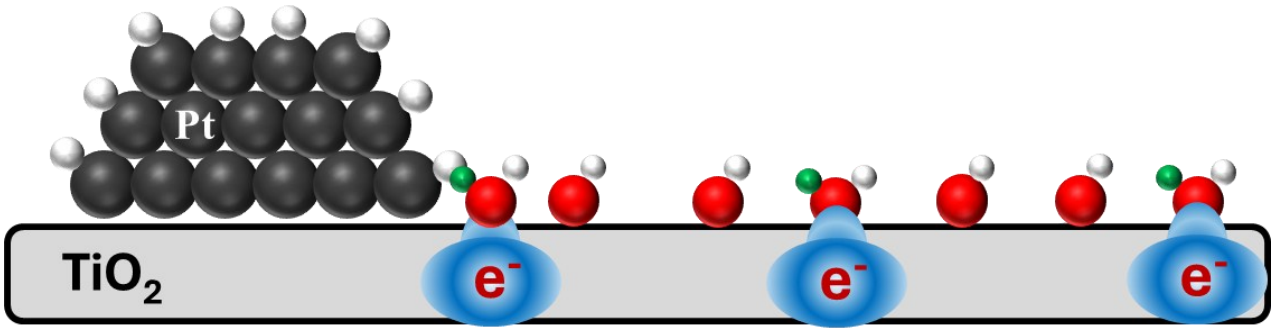

Figure I.14. Schematic representation of hydrogen spillover from a platinum nanoparticle to a titania surface. Color code: black, platinum atoms; red, oxygen atoms; white, hydrogen atoms; green, H^+ ions; blue, electrons in the titania conduction band.

To facilitate the understanding, hydrogen spillover can be regarded as a 2D analogue of the Grotthuss mechanism[46-47] for proton transport in aqueous environments. According to this mechanism, H^+ ions can

move in water through a hydrogen-bond network, by successive hopping from one molecule to another in a concerted chain mechanism. Analogously, surface oxygen atoms act as proton acceptors on the metal oxide surface, enabling proton hopping and thus high proton mobility across the surface.

Two key conditions must be fulfilled for hydrogen spillover to occur:

1) The presence of a metal capable of activating molecular hydrogen, such as platinum;
2) The presence of suitable acceptor sites for H* species on the support surface.

Since hydrogen spillover involves the transfer of H*from the metal surface to the support, metal-support interactions are intrinsically required.

Metal effect

In hydrogen spillover, the metal component plays a crucial role since it serves as the source of H* and also governs its interaction with the support. To increase contact between metal nanoparticles and support, Lachawiec et al.[48] employed Pd/C and carbon nanotubes as an effective material for hydrogen spillover. By carbonizing glucose, in order to create carbon bridges between the metal and the support, they increased the hydrogen adsorption capacity.

Noble metals such as Pd, Pt, and Ru are widely recognized as the most effective for promoting hydrogen spillover.[49] For instance, nanoclusters of Al-$CeZrO_4$ loaded with platinum[50] exhibited a 84% increase in NO_x reduction activity, while nickel-based systems showed negligible enhancement.

Similarly, a comparative study of Ru-, Pt-, and Ni-supported activated carbon catalysts[51] revealed that ruthenium-based catalysts adsorbed the largest amount of hydrogen, while nickel-based catalyst was the least active, underscoring the influence of metal identity on spillover efficiency from the metal to the support.

Support effect

Reducible supports

Typical supports for hydrogen spillover materials are reducible metal oxides such as WO_3, CeO_2, and TiO_2. In these materials, hydrogen spillover manifests as H^+ migration along the surface, while electrons can be transferred along the material through the conduction band and/or defect-induced edge states below the conduction band.

Since H* species can migrate across the entire support surface, spatial separation between metal particles and reactive sites does not limit catalytic performance. This concept was demonstrated by Karim et al.[52] who studied how the distance between platinum and iron oxide nanoparticles can affect iron

reduction. Using electron beam lithography, they prepared model catalysts with controlled iron oxide - platinum nanoparticle separations, spanning from 45 nm to overlapping configurations. They monitored the oxidation state of iron oxide nanoparticles *via* space-resolved *in situ* single-nanoparticles X-ray absorption spectroscopy measurements before and after flowing low pressure of H_2 ($1 \cdot 10^{-5}$ mbar). In this way, they showed that the extent of iron oxide reduction was independent of nanoparticle separation, proving that H* are free to move on the titania surface. Remarkably, even an isolated iron oxide nanoparticle located approximately 1 nm from the nearest Pt particle exhibited maximal reduction. (**Figure I.15**).

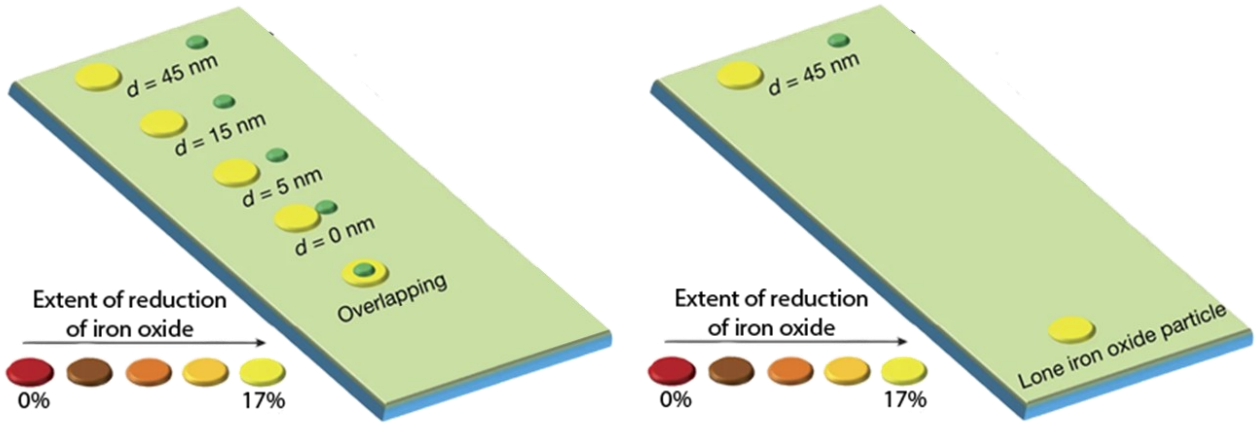

Figure I.15. Schematic representation of the work from Karim et al. on anatase support. Dark green, platinum nanoparticles; from red to yellow, iron oxide nanoparticles. The color of iron oxide nanoparticles depends on the extent of reduction after flowing hydrogen, as shown in the scheme.

Non-reducible supports

The occurrence of hydrogen spillover on non-reducible metal oxides remains controversial. While supports such as Al_2O_3 and SiO_2 are usually considered unable to sustain hydrogen spillover, recently, some studies have reported evidence to the contrary.[53-54] DFT suggests that surface defects may lower the energy barrier for the H* migration.[53] Nonetheless, spillover on defect-free non-reducible surfaces appears to be severely limited.

Using a similar experimental approach, Karim et al.[52] also investigated the possibility of hydrogen spillover on a Pt/Al_2O_3 system. In contrast to TiO_2-supported catalysts, a significant reduction of iron oxide occurred only when Pt nanoparticles were deposited directly on iron oxide nanoparticles. As the interparticle distance increased, the extent of reduction diminished, becoming undetectable beyond

15 nm (**Figure I.16**). Subsequent DFT studies[55] confirmed that while H* species are highly mobile on TiO_2 surface, they remain localized near the metal nanoparticles on Al_2O_3.

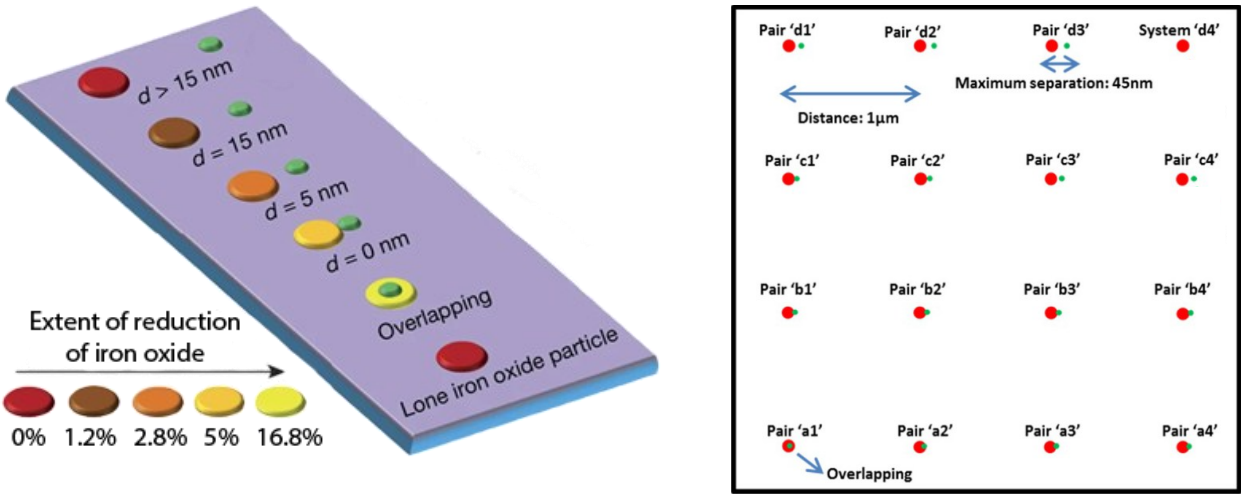

Figure I.16. Left, schematic representation of the work from Karim et al. on alumina support. Green, platinum nanoparticles; from red to yellow, iron oxide nanoparticles. The color of iron oxide nanoparticles depends on the extent of reduction after flowing hydrogen, as shown in the scheme. Right, the scheme of the sample reactor they built for the study.

Carbon supports

Carbon-based supports can also act as an acceptor for activated hydrogen. H* can migrate from the metal surface onto graphene,[56] forming C-H bonds, and on unsaturated carbon supports.

Carbon nanotubes, in particular, can not only act as efficient H* acceptors but have attracted interest for high-density hydrogen storage in light solid materials under near-ambient conditions, due to their high surface area and pore volume.[57] Zacharia et al.[58] reported that incorporating Pt nanoparticles into carbon nanotubes resulted in a nearly 40-fold increase in hydrogen uptake compared to pristine carbon nanotubes under the same conditions, an effect attributed to hydrogen spillover from Pt to carbon nanotubes.

Analytical techniques

techniques have been employed to investigate hydrogen spillover, such as *in situ* Surface-Enhanced Raman spectroscopy (SERS), Transmission Electron Microscopy (TEM), H_2- Temperature-Programmed Reduction (H_2- TPR), Electron Paramagnetic Resonance (EPR), and UV-vis spectroscopy. Worth noting, all these analytical techniques typically provide indirect evidence of hydrogen spillover by detecting the products of reduction, whether involving the support or adsorbed molecular species.

SERS, for example, enables real-time monitoring of catalytic reactions as well as hydrogen migration across interfaces,[59] as demonstrated in layered model catalysts comprised of a TiO_2 layer on a platinum surface covered with gold nanoparticles. In this system, p-nitrophenol adsorbed on gold nanoparticles served as a SERS substrate for monitoring reduction.

Temperature-programmed reduction has been used to quantify spillover-enhanced reduction, as in the case of Pt nanoparticles on the surface of a Cu-ZnO sample, where the presence of Pt significantly lowered the reduction temperature of CuO.[60] Temperature-programmed desorption was used to monitor the loss of adsorbed hydrogen from the materials, further revealing how different metals influence both the quantity and stability of adsorbed.[61]

UV-vis spectroscopy has been employed to monitor support reduction in three-dimensionally ordered microporous (3DOM) H_xWO_3/Pt/CdS heterojunction,[62] by tracking absorbance changes associated with hydrogen incorporation into the WO_3 lattice. X-ray techniques, including XRPD and XAS, have also been employed to probe structural changes induced by H* incorporation[62] and to investigate the oxidation state of copper in a Pt/CNT/CuO catalyst.[63]

The research group led by Professor Bert Chandler (Penn State University, USA) has developed an alternative approach. Using in situ FT-IR, they demonstrated that electrons generated during hydrogen spillover can be excited from defect-induced edge states into the conduction band. The resulting

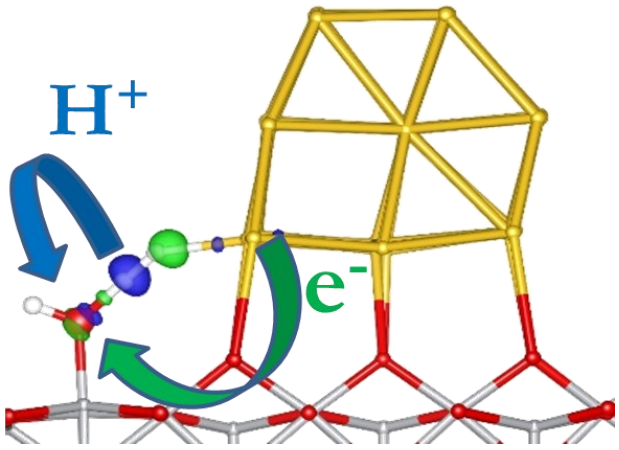

Figure I.17. Schematic representation of H_2 molecule coordination in the MSI on a Au/TiO_2 catalyst. Yellow, gold atoms; red, oxygen atoms; grey, titanium atoms; white, hydrogen atoms. Blue areas indicate electron-depletion areas, while green ones indicate electron-accumulation areas. Arrows indicate the proton-coupled electron transfer during the H-H bond cleavage for H^+ (blue) and e^- (green).

absorbance spectrum shows a characteristic increase in baseline absorbance, which they call broad background absorbance (BBA).

Notably, this group employed gold as the active metal. While most metals activate H_2 *via* strong dissociative chemisorption at their surfaces, dissociation on gold surface is characterized by a high activation energy.[64-65] Consequently, H_2 dissociation on the metal surface is avoided, thus favoring activation at the metal-support interface (MSI) through a concerted mechanism with a proton-coupled electron transfer (PCET), producing two H* on the support surface.[65-68]

During H_2 activation in a FT-IR cell using Au/TiO_2-P25 catalyst, they also detected the growth of two new bands, situated at 3300 and 1580 cm^{-1}, and a negative peak around 3628 cm^{-1}. All this is contemporaneous with the growth of BBA. They concluded that the new bands arise from the presence of protonated hydroxyl groups at the MSI and can be attributed to the stretching and scissoring vibrational modes. The negative peak was assigned to the depletion of non-protonated Ti–OH groups due to protonation.

Moreover, they synthesized four different catalysts with varying gold loadings. By combining TEM-based nanoparticle size and distribution analysis with calculations of perimeter site density, the number of gold atoms present at MSI was quantified., that is the active sites. In the end, tandem experiments with volumetric chemisorption and FT-IR measurements were conducted to correlate hydrogen uptake with the amount of $_{MSI}Ti\text{-}OH_2^+$ species under saturation conditions.

A linear relationship with unitary slope was observed when plotting the amount of $_{MSI}TiOH_2^+$ versus the amount of perimetral gold for each catalyst,. Being the peak area proportional to the amount of perimetral gold, this provides further confirmation that the new peaks derive from $_{MSI}Ti\text{-}OH$ and that each perimetral gold atom corresponds to one proton-accepting site.

The versatility of FT-IR measurements allows systematic variation of experimental conditions, such as temperature and hydrogen flow. When combined with volumetric chemisorption, this approach enables calibration of BBA signals by collecting isotherms under the same conditions. With this setup, both thermodynamic and kinetic data can be collected, allowing the extrapolation of different parameters for the hydrogen activation reaction. As a result, it provides a powerful framework for investigating how catalyst composition and structural modifications influence the hydrogen activation step.

Bibliography

1. Atkins, P.; de Paula, J., *Atkins' Physical Chemistry*. Oxford University Press: 2014.
2. Palmisano, G.; Augugliaro, V.; Ciriminna, R.; Pagliaro, M., NanoMORALs - Metal nanoparticles doped with organic molecules. *Canadian Journal of Chemistry* **2009,** *87* (5), 673–677.
3. Behar-Levy, H.; Avnir, D., Entrapment of Organic Molecules within Metals: Dyes in Silver. *Chemistry of Materials* **2002,** *14* (4), 1736–1741.
4. Behar-Levy, H.; Avnir, D., Silver Doped with Acidic/Basic Polymers: Novel, Reactive Metallic Composites. *Advanced Functional Materials* **2005,** *15* (7), 1141–1146.
5. Ben-Efraim, Y.; Avnir, D., Entrapment of organic molecules within binary metal alloys. *Journal of Materials Chemistry* **2012,** *22* (34), 17595–17603.
6. Yosef, I.; Avnir, D., Metal-Organic Composites: the Heterogeneous Organic Doping of the Coin Metals-Copper, Silver and Gold. *Chemistry of Materials* **2006,** *18*, 5890–5896.
7. Sinai, O.; Avnir, D., Electrolytical Entrapment of Organic Molecules within Metals. *The Journal of Physical Chemistry B* **2009,** *113* (42), 13901–13909.
8. Nesher, G.; Marom, G.; Avnir, D., Metal−Polymer Composites: Synthesis and Characterization of Polyaniline and Other Polymer@Silver Compositions. *Chemistry of Materials* **2008,** *20* (13), 4425–4432.
9. Nesher, G.; Marom, G.; Avnir, D., An $Fe(CO)_5$-Thermolysis-Based Process for the Preparation of Polymer@Iron Composite Powders with High Corrosion Resistance. *European Journal of Inorganic Chemistry* **2012,** *2012* (32), 5276–5281.
10. Ben-Efraim, Y.; Avnir, D., Organic Ag–Hg amalgam composite materials. *Acta Materialia* **2013,** *61* (19), 7381–7391.
11. Shter, G. E.; Behar-Levy, H.; Gelman, V.; Grader, G. S.; Avnir, D., Organically Doped Metals—A New Approach to Metal Catalysis: Enhanced Ag-Catalyzed Oxidation of Methanol. *Advanced Functional Materials* **2007,** *17* (6), 913–918.
12. Shapiro, L.; Avnir, D., Multiple One-Pot Reaction Steps using Organically Doped Metallic Hybrid Catalyst. *ChemCatChem* **2013,** *5* (8), 2195–2198.
13. ISO 80004-1:2023 - Nanotechnologies - Vocabulary - Part 1: Core vocabulary.
14. Faraday, M., The Bakerian Lecture: Experimental Relations of Gold (and Other Metals) to Light. *Philosophical Transactions of the Royal Society of London* **1857,** *147*, 147–181.
15. Habashi, F., Gold – An Historical Introduction. In *Gold Ore Processing*, 2016; pp 1–20.
16. Comotti, M.; Della Pina, C.; Matarrese, R.; Rossi, M., The catalytic activity of "naked" gold particles. *Angewandte Chemie International Edition* **2004,** *43* (43), 5812–5.
17. Arduengo III, A. J.; Harlow, R. L.; Kline, M., A Stable Crystalline Carbene. *Journal of the American Chemical Society* **1991,** *113* (1).
18. Hahn, F. E.; Jahnke, M. C., Heterocyclic carbenes: synthesis and coordination chemistry. *Angewandte Chemie International Edition* **2008,** *47* (17), 3122–72.
19. Nesterov, V.; Reiter, D.; Bag, P.; Frisch, P.; Holzner, R.; Porzelt, A.; Inoue, S., NHCs in Main Group Chemistry. *Chemical Reviews* **2018,** *118* (19), 9678–9842.
20. Hopkinson, M. N.; Richter, C.; Schedler, M.; Glorius, F., An Overview of N-Heterocyclic Carbenes. *Nature* **2014,** *2510*, 485–496.
21. Crudden, C. M.; Horton, J. H.; Narouz, M. R.; Li, Z.; Smith, C. A.; Munro, K.; Baddeley, C. J.; Larrea, C. R.; Drevniok, B.; Thanabalasingam, B.; McLean, A. B.; Zenkina, O. V.; Ebralidze, II; She, Z.; Kraatz, H. B.; Mosey, N. J.; Saunders, L. N.; Yagi, A., Simple direct formation of self-assembled N-heterocyclic carbene monolayers on gold and their application in biosensing. *Nature Communications* **2016,** *7*, 12654.
22. Li, Z.; Narouz, M. R.; Munro, K.; Hao, B.; Crudden, C. M.; Horton, J. H.; Hao, H., Carboxymethylated Dextran-Modified N-Heterocyclic Carbene Self-Assembled Monolayers on Gold for Use in Surface Plasmon Resonance Biosensing. *ACS Applied Materials & Interfaces* **2017,** *9* (45), 39223–39234.

23. Wang, G.; Ruhling, A.; Amirjalayer, S.; Knor, M.; Ernst, J. B.; Richter, C.; Gao, H. J.; Timmer, A.; Gao, H. Y.; Doltsinis, N. L.; Glorius, F.; Fuchs, H., Ballbot-type motion of N-heterocyclic carbenes on gold surfaces. *Nature Chemistry* **2017,** *9* (2), 152–156.
24. Eisen, C.; Chin, J. M.; Reithofer, M. R., Catalytically Active Gold Nanomaterials Stabilized by N-heterocyclic Carbenes. *Chemistry - An Asian Journal* **2021,** *16* (20), 3026–3037.
25. Tang, Q.; Jiang, D.-e., Comprehensive View of the Ligand–Gold Interface from First Principles. *Chemistry of Materials* **2017,** *29* (16), 6908–6915.
26. Ferry, A.; Schaepe, K.; Tegeder, P.; Richter, C.; Chepiga, K. M.; Ravoo, B. J.; Glorius, F., Negatively Charged NHeterocyclic Carbene Stabilized Pd and Au Nanoparticles and Efficient Catalysis in Water. *ACS Catalysis* **2015,** *5* (9), 5414–5420.
27. Thomas, S. R.; Yang, W.; Morgan, D. J.; Davies, T. E.; Li, J. J.; Fischer, R. A.; Huang, J.; Dimitratos, N.; Casini, A., Bottom-up Synthesis of Water-Soluble Gold Nanoparticles Stabilized by N-Heterocyclic Carbenes: From Structural Characterization to Applications. *Chemistry* **2022,** *28* (56), e202201575.
28. Cao, Z.; Kim, D.; Hong, D.; Yu, Y.; Xu, J.; Lin, S.; Wen, X.; Nichols, E. M.; Jeong, K.; Reimer, J. A.; Yang, P.; Chang, C. J., A Molecular Surface Functionalization Approach to Tuning Nanoparticle Electrocatalysts for Carbon Dioxide Reduction. *Journal of the American Chemical Society* **2016,** *138* (26), 8120–5.
29. Zhang, L.; Wei, Z.; Thanneeru, S.; Meng, M.; Kruzyk, M.; Ung, G.; Liu, B.; He, J., A Polymer Solution To Prevent Nanoclustering and Improve the Selectivity of Metal Nanoparticles for Electrocatalytic CO(2) Reduction. *Angewandte Chemie International Edition* **2019,** *58* (44), 15834–15840.
30. Crespo, J.; Guari, Y.; Ibarra, A.; Larionova, J.; Lasanta, T.; Laurencin, D.; Lopez-de-Luzuriaga, J. M.; Monge, M.; Olmos, M. E.; Richeter, S., Ultrasmall NHC-coated gold nanoparticles obtained through solvent free thermolysis of organometallic Au(i) complexes. *Dalton Transactions* **2014,** *43* (42), 15713–8.
31. Song, S. G.; Satheeshkumar, C.; Park, J.; Ahn, J.; Premkumar, T.; Lee, Y.; Song, C., N-Heterocyclic Carbene-Based Conducting Polymer–Gold Nanoparticle Hybrids and Their Catalytic Application. *Macromolecules* **2014,** *47* (19), 6566–6571.
32. Ventura-Espinosa, D.; Martín, S.; Mata, J. A., The non-innocent role of graphene in the formation/immobilization of ultra-small gold nanoparticles functionalized with N-heterocyclic carbene ligands. *Journal of Catalysis* **2019,** *375*, 419–426.
33. Ventura-Espinosa, D.; Martín, S.; García, H.; Mata, J. A., Ligand effects in the stabilization of gold nanoparticles anchored on the surface of graphene: Implications in catalysis. *Journal of Catalysis* **2021,** *394*, 113–120.
34. Shen, H.; Deng, G.; Kaappa, S.; Tan, T.; Han, Y. Z.; Malola, S.; Lin, S. C.; Teo, B. K.; Hakkinen, H.; Zheng, N., Highly Robust but Surface-Active: An N-Heterocyclic Carbene-Stabilized Au(25) Nanocluster. *Angewandte Chemie International Edition* **2019,** *58* (49), 17731–17735.
35. Shen, H.; Xiang, S.; Xu, Z.; Liu, C.; Li, X.; Sun, C.; Lin, S.; Teo, B. K.; Zheng, N., Superatomic Au13 clusters ligated by different N-heterocyclic carbenes and their ligand-dependent catalysis, photoluminescence, and proton sensitivity. *Nano Research* **2020,** *13* (7), 1908–1911.
36. Ye, R.; Zhukhovitskiy, A. V.; Kazantsev, R. V.; Fakra, S. C.; Wickemeyer, B. B.; Toste, F. D.; Somorjai, G. A., Supported Au Nanoparticles with N-Heterocyclic Carbene Ligands as Active and Stable Heterogeneous Catalysts for Lactonization. *Journal of the American Chemical Society* **2018,** *140* (11), 4144–4149.
37. Ranganath, K. V.; Kloesges, J.; Schafer, A. H.; Glorius, F., Asymmetric nanocatalysis: N-heterocyclic carbenes as chiral modifiers of Fe_3O_4/Pd nanoparticles. *Angewandte Chemie International Edition* **2010,** *49* (42), 7786–9.
38. Lucenti, E.; Forni, A.; Botta, C.; Carlucci, L.; Giannini, C.; Marinotto, D.; Previtali, A.; Righetto, S.; Cariati, E., H-Aggregates Granting Crystallization-Induced Emissive Behavior and Ultralong Phosphorescence from a Pure Organic Molecule. *The Journal of Physical Chemistry Letters* **2017,** *8* (8), 1894–1898.

39. Kirk, K. L.; Nagai, W.; Cohen, L. A., Photochemistry of Diazonium Salts. II. Synthesis of 2-Fluoro-L-histidine and 2-Fluorohistamine, and the Halogen Lability of 2-Fluoroimidazoles. *Journal of the American Chemical Society* **1973,** *95* (25), 8389–8392.
40. Schubert, D. M.; Natan, D. T.; Wilson, D. C.; Hardcastle, K. I., Facile Synthesis and Structures of Cyclic Triimidazole and Its Boric Acid Adduct. *Crystal Growth & Design* **2011,** *11* (3), 843–850.
41. Lucenti, E.; Forni, A.; Botta, C.; Carlucci, L.; Giannini, C.; Marinotto, D.; Pavanello, A.; Previtali, A.; Righetto, S.; Cariati, E., Cyclic Triimidazole Derivatives: Intriguing Examples of Multiple Emissions and Ultralong Phosphorescence at Room Temperature. *Angewandte Chemie International Edition* **2017,** *56* (51), 16302–16307.
42. Lucenti, E.; Forni, A.; Botta, C.; Carlucci, L.; Colombo, A.; Giannini, C.; Marinotto, D.; Previtali, A.; Righetto, S.; Cariati, E., The Effect of Bromo Substituents on the Multifaceted Emissive and Crystal-Packing Features of Cyclic Triimidazole Derivatives. *ChemPhotoChem* **2018,** *2* (9), 801–805.
43. Lucenti, E.; Forni, A.; Botta, C.; Giannini, C.; Malpicci, D.; Marinotto, D.; Previtali, A.; Righetto, S.; Cariati, E., Intrinsic and Extrinsic Heavy-Atom Effects on the Multifaceted Emissive Behavior of Cyclic Triimidazole. *Chemistry* **2019,** *25* (10), 2452–2456.
44. Buck, D. M.; Kunz, D., Triazine Annelated NHC Featuring Unprecedented Coordination Versatility. *Organometallics* **2015,** *34* (21), 5335–5340.
45. Prins, R., Hydrogen spillover. Facts and fiction. *Chem Rev* **2012,** *112* (5), 2714–38.
46. Grotthuss, C. J. T., Sur la décomposition de l'eau et des corps q'uelle tient en dissolution à l'aide de l'électricité galvanique. *Annales de Chimie* **1806,** *LVIII*, 54–74.
47. Cukierman, S., Et tu, Grotthuss! and other unfinished stories. *Biochimica et Biophysica Acta* **2006,** *1757*, 876–885.
48. Lachawiec, A. J.; Qi, G.; Yang, R. T., Hydrogen Storage in Nanostructured Carbons by Spillover: Bridge-Building Enhancement. *Langmuir* **2005,** *21* (24), 11418–11424.
49. Geng, Z.; Wang, D.; Zhang, C.; Zhou, X.; Xin, H.; Liu, X.; Cai, M., Spillover enhanced hydrogen uptake of Pt/Pd doped corncob-derived activated carbon with ultra-high surface area at high pressure. *International Journal of Hydrogen Energy* **2014,** *39* (25), 13643–13649.
50. Peng, Z.; Li, Z.; Liu, Y. Q.; Yan, S.; Tong, J.; Wang, D.; Ye, Y.; Li, S., Supported Pd nanoclusters with enhanced hydrogen spillover for NO(x) removal via H(2)-SCR: the elimination of "volcano-type" behaviour. *Chemical Communications* **2017,** *53* (44), 5958–5961.
51. Wang, L.; Yang, R. T., Hydrogen Storage Properties of Carbons Doped with Ruthenium, Platinum, and Nickel Nanoparticles. *The Journal of Physical Chemistry C* **2008,** *112* (32), 12486–12494.
52. Karim, W.; Spreafico, C.; Kleibert, A.; Gobrecht, J.; VandeVondele, J.; Ekinci, Y.; van Bokhoven, J. A., Catalyst support effects on hydrogen spillover. *Nature* **2017,** *541* (7635), 68–71.
53. Bettahar, M. M., The hydrogen spillover effect. A misunderstanding story. *Catalysis Reviews* **2020,** *64* (1), 87–125.
54. Choi, M.; Yook, S.; Kim, H., Hydrogen Spillover in Encapsulated Metal Catalysts: New Opportunities for Designing Advanced Hydroprocessing Catalysts. *ChemCatChem* **2015,** *7* (7), 1048–1057.
55. Spreafico, C.; Karim, W.; Ekinci, Y.; van Bokhoven, J. A.; VandeVondele, J., Hydrogen Adsorption on Nanosized Platinum and Dynamics of Spillover onto Alumina and Titania. *The Journal of Physical Chemistry C* **2017,** *121* (33), 17862–17872.
56. Li, J.; Jin, C.; Qian, R.; Wu, C.; Wang, Y.; Yan, Y.; Chen, Y., Hydrogen absorption-desorption cycle decay mechanism of palladium nanoparticle decorated nitrogen doped graphene. *Progress in Natural Science: Materials International* **2021,** *31* (4), 514–520.
57. Shang, S.; Yang, X.; Tao, X.-m., Easy synthesis of carbon nanotubes with polypyrrole nanotubes as the carbon precursor. *Polymer* **2009,** *50* (13), 2815–2818.
58. Zacharia, R.; Rather, S.-u.; Hwang, S. W.; Nahm, K. S., Spillover of physisorbed hydrogen from sputter-deposited arrays of platinum nanoparticles to multi-walled carbon nanotubes. *Chemical Physics Letters* **2007,** *434* (4-6), 286–291.
59. Murakami, K.; Sekine, Y., Recent progress in use and observation of surface hydrogen migration over metal oxides. *Physical Chemistry Chemical Physics* **2020,** *22* (40), 22852–22863.

60. Hu, B.; Yin, Y.; Liu, G.; Chen, S.; Hong, X.; Tsang, S. C. E., Hydrogen spillover enabled active Cu sites for methanol synthesis from CO_2 hydrogenation over Pd doped CuZn catalysts. *Journal of Catalysis* **2018,** *359*, 17–26.
61. Yao, Y.; Goodman, D. W., Direct evidence of hydrogen spillover from Ni to Cu on Ni–Cu bimetallic catalysts. *Journal of Molecular Catalysis A: Chemical* **2014,** *383-384*, 239–242.
62. Yan, X.; Xu, B.; Yang, X.; Wei, J.; Yang, B.; Zhao, L.; Yang, G., Through hydrogen spillover to fabricate novel 3DOM-H_xWO_3/Pt/CdS Z-scheme heterojunctions for enhanced photocatalytic hydrogen evolution. *Applied Catalysis B: Environmental* **2019,** *256*.
63. Briggs, N. M.; Barrett, L.; Wegener, E. C.; Herrera, L. V.; Gomez, L. A.; Miller, J. T.; Crossley, S. P., Identification of active sites on supported metal catalysts with carbon nanotube hydrogen highways. *Nature Communications* **2018,** *9* (1), 3827.
64. Sault, A. G.; Madix, R. J., Adsorption of oxygen and hydrogen on gold(110)-(1 × 2). *Surface Science* **2018,** *169*, 347–356.
65. Whittaker, T.; Kumar, K. B. S.; Peterson, C.; Pollock, M. N.; Grabow, L. C.; Chandler, B. D., H_2 Oxidation over Supported Au Nanoparticle Catalysts: Evidence for Heterolytic H_2 Activation at the Metal-Support Interface. *Journal of the American Chemical Society* **2018,** *140* (48), 16469–16487.
66. Mahdavi-Shakib, A.; Kumar, K. B. S.; Whittaker, T. N.; Xie, T.; Grabow, L. C.; Rioux, R. M.; Chandler, B. D., Kinetics of H_2 Adsorption at the Metal-Support Interface of Au/TiO_2 Catalysts Probed by Broad Background IR Absorbance. *Angewandte Chemie International Edition* **2021,** *60* (14), 7735–7743.
67. Mahdavi-Shakib, A.; Rich, L. C.; Whittaker, T. N.; Chandler, B. D., Hydrogen Adsorption at the Au/TiO_2 Interface: Quantitative Determination and Spectroscopic Signature of the Reactive Interface Hydroxyl Groups at the Active Site. *ACS Catalysis* **2021,** *11* (24), 15194–15202.
68. Sravan Kumar, K. B.; Whittaker, T. N.; Peterson, C.; Grabow, L. C.; Chandler, B. D., Water Poisons H_2 Activation at the Au-TiO_2 Interface by Slowing Proton and Electron Transfer between Au and Titania. *Journal of the American Chemical Society* **2020,** *142* (12), 5760–5772.

II. GO- AND RGO-BASED MORALs

This section covers the first of two distinct classes of catalysts on which my doctoral work focused, that is, Graphene Oxide- and Reduced Graphene Oxide-based Metal-ORganic ALloys (GO- and RGO-based MORALs), with particular emphasis on their performance in the nitrobenzene reduction to aniline under mild conditions. These catalysts represent the evolution of MORALs, a family of catalysts invented by Avnir in 2002[1] based on organic molecules 3D-embedded in metal particles. While previous studies have demonstrated the encapsulation of small molecules, enzymes, and polymers, this work aims to explore how a macromolecule with an extended π-conjugated system, such as GO and RGO, can influence the catalytic behavior of group 10 transition metals.

Graphene has been widely studied as a reinforcing material in different metal/graphene composite materials, generally made by mixing, compacting, and sintering or by extrusion.[2] For instance, graphene coated on both sides of a Cu foil *via* chemical vapor deposition, followed by stacking and hot pressing numerous layers of numerous Gr/Cu/Gr foils, affords copper having an electrical conductivity up to 117% higher than that of pure copper.[3] Other applications include the use of graphene oxide as a support for palladium nanoparticles,[4] or for single metal atoms[5] for catalytic applications.

For this work, we took inspiration from a study by Shapiro et al.[6] reporting the preparation of a MORAL comprised of palladium incorporating Nafion, a perfluorinated polymer functionalized with sulphonic groups. This material exhibited diverse reactivity under various conditions for one-pot reactions. Considering such interesting results, we wondered how the incorporation of a macromolecule characterized by an extended π-system could impact the reactivity of metals widely used in catalysis, such as palladium and nickel.

In this context, the encapsulation of graphene oxide within palladium nanoparticles (GO@nPd) represents the introduction of a new class of functional materials. Initially, the study focused on the synthesis and characterization of GO@nPd, and was subsequently extended to include the reduced form, RGO@nPd, to further investigate the influence of graphene oxidation state on the catalytic properties of the resulting new MORALs in the nitrobenzene reduction to aniline under mild conditions. Encouraged by the promising catalytic performance, particularly the excellent reusability of palladium-based systems, the study was extended to the development of analogous, cost-effective materials based on nickel. This transition aimed to explore whether similar structural and functional benefits could be achieved using a more economical and sustainable metal, such as nickel.

Neither graphene oxide nor reduced graphene oxide is, semantically, an organic material, as the latter should contain C-H bonds. The use of the MORAL (metal-organic alloy) acronym is retained only to refer that the MORAL approach to composite organics@Metal was followed in all material synthetic routes employed. As such, it is an extension of the concept to carbon-based materials (reduced graphene oxide and graphene oxide), which, semantically and also in practical terms, are not organic materials

Synthesis of the Materials

Following the protocol reported by Shapiro et al.,[6] $PdCl_2$ was suspended in a 1:1 water-ethanol mixture, to which a GO suspension was subsequently added. Zinc powder was then introduced as the reducing agent, and the mixture was stirred for 24 hours to complete the reduction.

The resulting material, denoted as GO@nPd, was filtered and washed with diluted HCl to remove excess zinc, followed by thorough rinsing with water. This material served both as the first catalyst for the study and as the precursor for a second material.

Following a procedure employing thiophene as a reducing agent for GO, the material GO@nPd was modified by suspending it in a water-thiophene biphasic mixture at 80°C for 24 hours under nitrogen atmosphere.[7] The final material was then filtered and washed with methanol to remove all the residual organic molecules. The scheme for the preparation of palladium-based MORALs is reported in **Figure II.1**. More details can be found in the experimental section (Chapter VII).

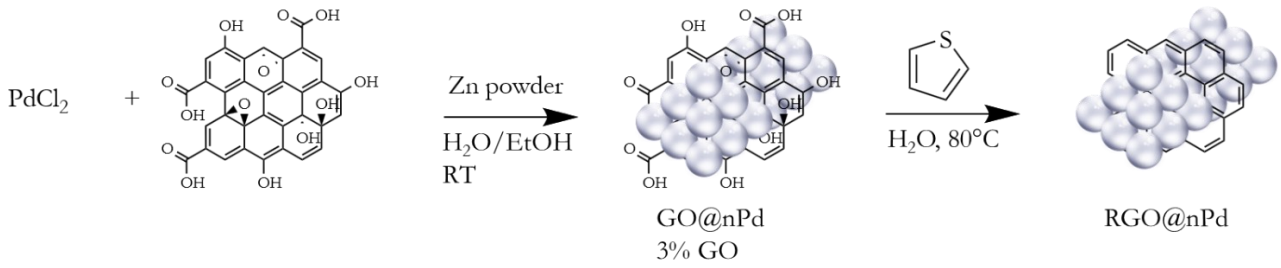

Figure II.1. Scheme for the preparation of palladium-based MORALs GO@nPd and RGO@nPd.

Based on the same preparation protocol, two analogous nickel-based materials were synthesized. In this case, due to the higher oxidation sensitivity of metallic nickel owing to its lower reduction potential with respect to palladium, the synthesis of the first material, GO@Ni, was carried out in methanol under nitrogen atmosphere. Moreover, zinc powder was revealed not to be a suitable reducing agent to obtain the precipitation of nickel and was therefore substituted with sodium borohydride. The second step, the reduction of GO to RGO, was performed under nitrogen employing methanol as solvent, too.

Characterization

XRPD

The XRD diffractogram of GO@nPd reported in **Figure II.2** provides evidence that the material consists of graphene oxide entrapped in Pd nanoparticles. Well-defined peaks around 40° and 46° in the diffractogram correspond to the (111) and (200) crystal planes, and Rietveld analysis indicates the presence of Pd nanoparticles approximately 9 nm in diameter (calculation performed with Profex software). The entrapped GO platelets are revealed by the diffraction peak at 13°, visible upon magnification of the diffraction pattern. Accordingly, the XRPD spectrum for GO shows a peak at 13° and a broad band centered at 24° associated with the A-B stacking order, corresponding to the (002) reflection. The large full-width at half maximum of this reflection suggests a relatively low number of layers in the GO sample.[5]

The pattern of RGO@nPd does not show significant differences.

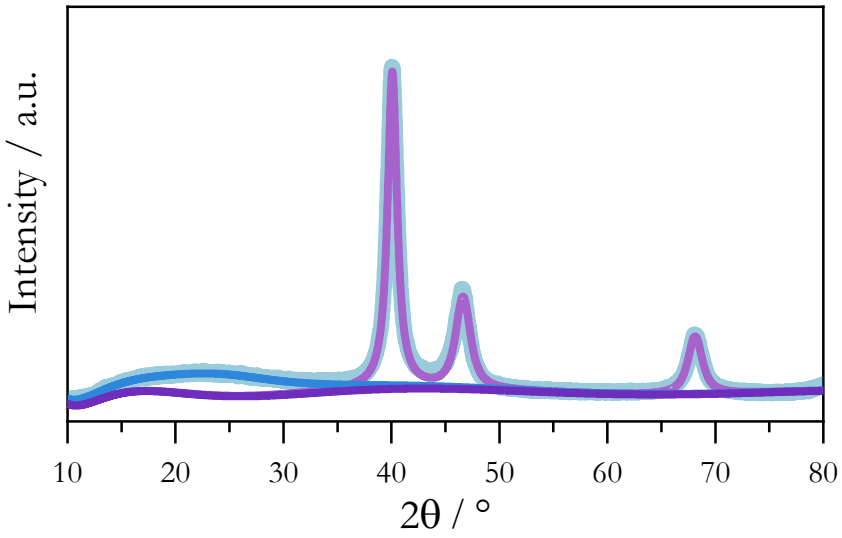

Figure II.2. XRPD diffractogram of GO@nPd, reporting the typical peaks of palladium. Light blue, raw data: in purple, background; in violet, palladium pattern; in blue, the broad band deriving from GO.

The XRD pattern of GO@Ni (in **Figure II.3** a) clearly shows that this material has an amorphous structure. However, overlapping with the diffraction peak of Ni and NiO reveals enhanced signals in those regions of the GO@Ni pattern. The XRPD pattern of GO@Ni after employment of the material to mediate the nitrobenzene reduction with hydrazine in five consecutive catalytic runs (**Figure II.3** b)

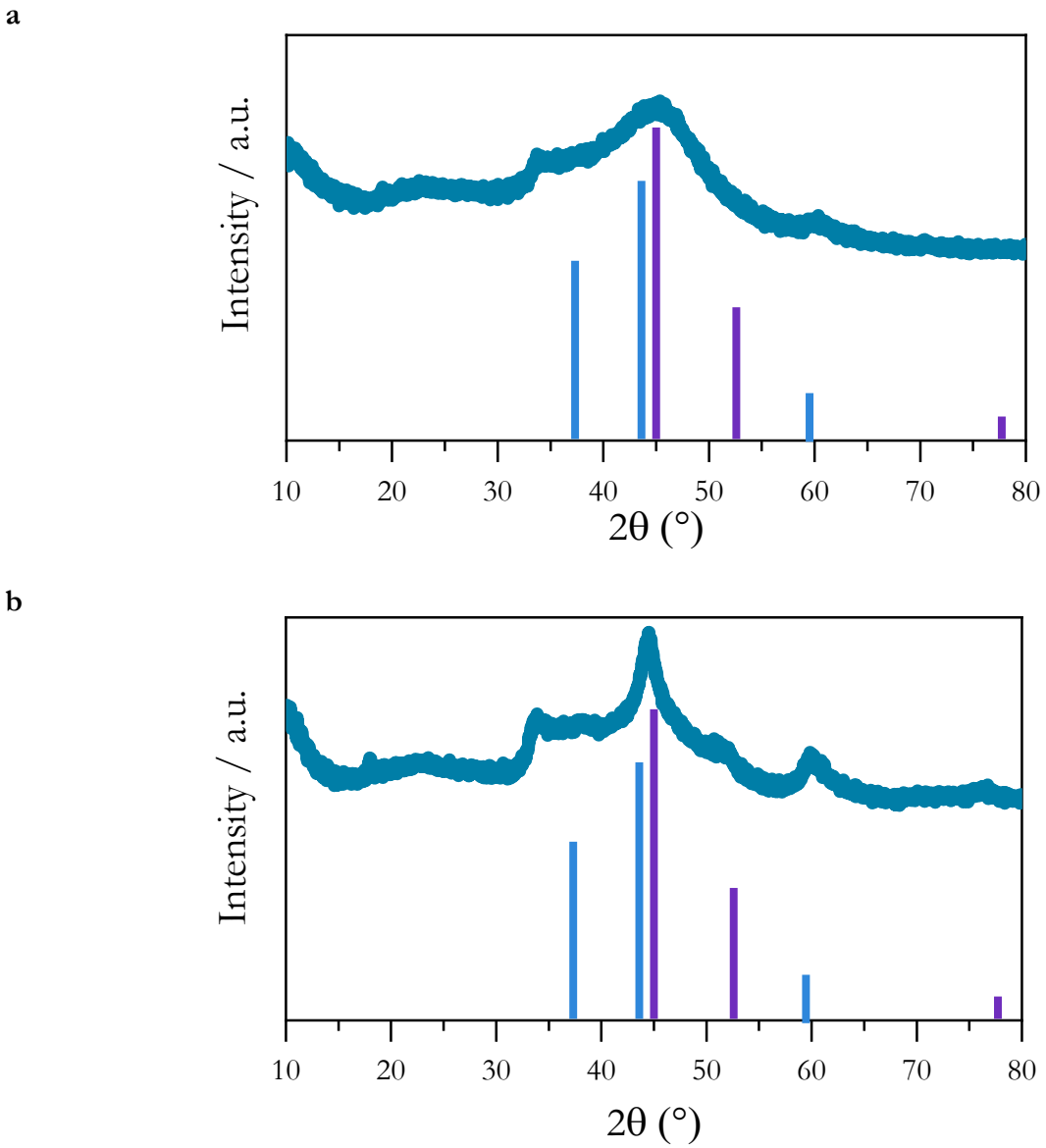

Figure II.3. XRPD diffractograms of: a)fresh GO@Ni; b) used GO@Ni. Even if slightly different, both diffractograms suggest and amorphous structure. Blue bars are NiO peaks positions and intensities; purple bars are Ni peaks positions and intensities.

displays a pattern even more similar to that of Ni and NiO, though it retains the characteristic of an amorphous material.

The XRD pattern of RGO@Ni (**Figure II.4** a) shows that this material is an amorphous solid whose diffraction pattern presents enhanced peaks in proximity to the diffraction peaks of Ni and NiO. The XRPD profile of the same RGO@Ni material after five consecutive catalytic cycles in the reduction of nitrobenzene to aniline using hydrazine as reductant (**Figure II.4** b) displays that the material remains amorphous, though the aforementioned signals corresponding to Ni and NiO are further intensified.

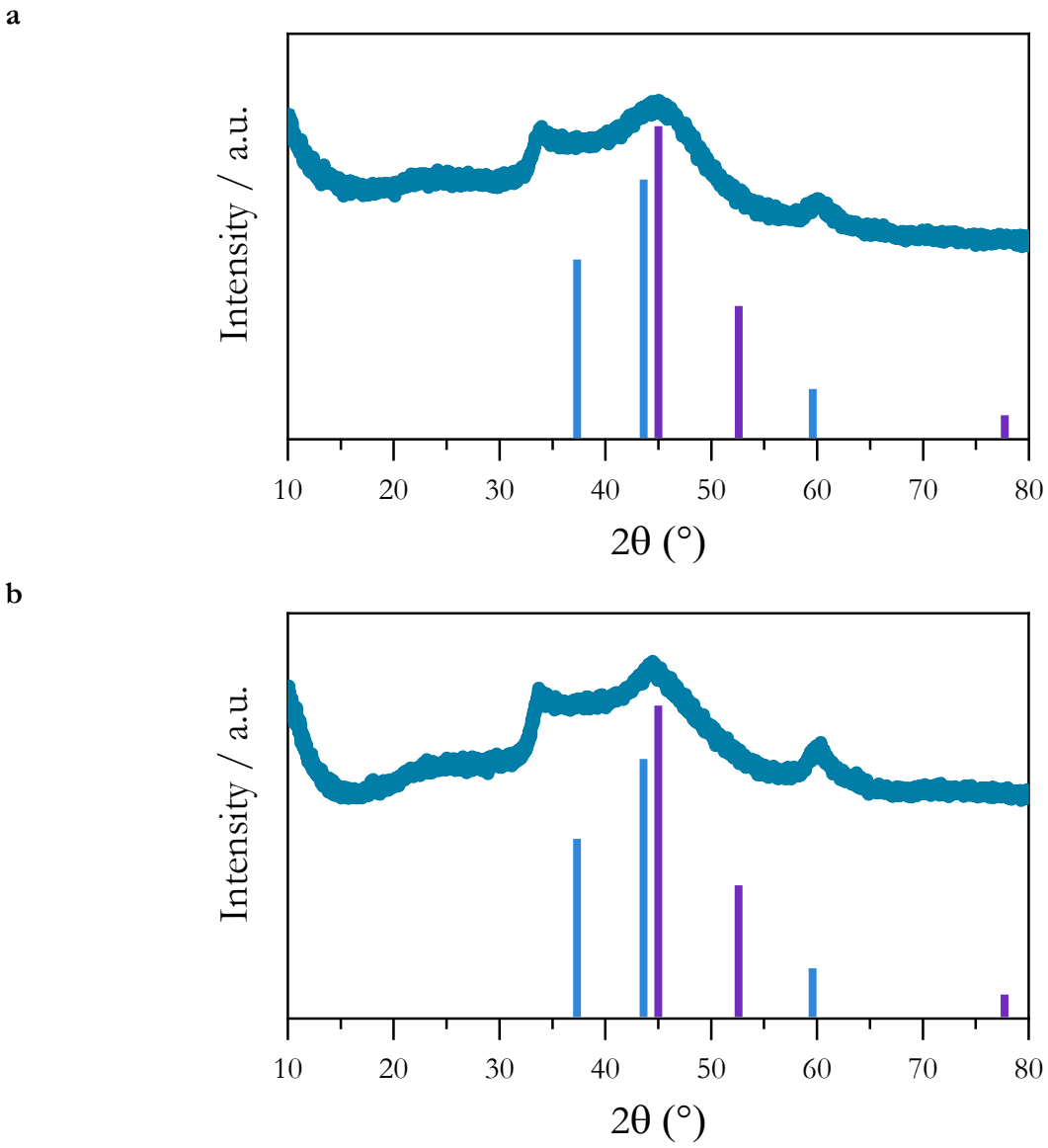

Figure II.4. XRPD diffractograms of: a)fresh RGO@Ni; b) used RGO@Ni. Even if slightly different, both diffractograms suggest and amorphous structure. Blue bars are NiO peaks positions and intensities; purple bars are Ni peaks positions and intensities.

We attempted to recrystallize RGO@Ni by heating a sample under N_2 atmosphere at 200 °C for 2 h, followed by slow cooling, in order to promote the growth of the crystal lattice driven by favored thermodynamics. The XRD pattern suggests that partial recrystallization actually occurred, although the MORAL remained substantially amorphous (**Figure II.5**).

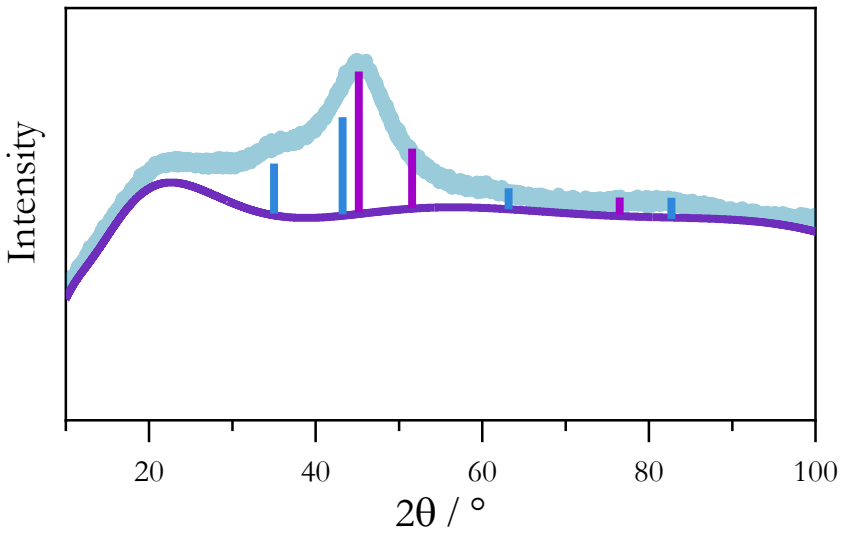

Figure II.5. XPRD pattern of fresh RGO@Ni after recrystallization by heating at 200°C. Rietveld refinement was performed on the raw data (light green), and a pattern background (dark purple) was modelled from an experimental spectrum of the sample holder. Blue bars are NiO peaks positions and intensities; purple bars are Ni peaks positions and intensities.

FT-IR Analysis

Successful encapsulation of the GO layers is shown by the typical infrared "fingertip" bands in the FTIR spectra (**Figure II.6** and **Figure II.7**). The spectra of GO@nPd and commercial GO present at 3424 and 3442 cm^{-1} the O-H group stretching vibration peaks. The carboxylic C=O stretching signal of GO at 1721 cm^{-1} disappears in the GO@nPd spectrum, whereas the signal at 1637 cm^{-1} for GO@nPd is due to the ketone group (C=O) shifted to slightly higher wavenumber than in pristine GO (1627 cm^{-1}).[8] The asymmetric and symmetric stretching vibrations of CH_2 bonds at 2919 and 2849 cm^{-1}, the C-OH bond stretching frequency at 1380 cm^{-1} (and 1384 cm^{-1} for GO@nPd) and the shoulder peak at 1227 cm^{-1} ascribed to the C-O-C (epoxy group) stretching mode in GO,[9] present in both spectra, all point to successful entrapment of GO within the Pd nanoparticles (**Figure II.6**).

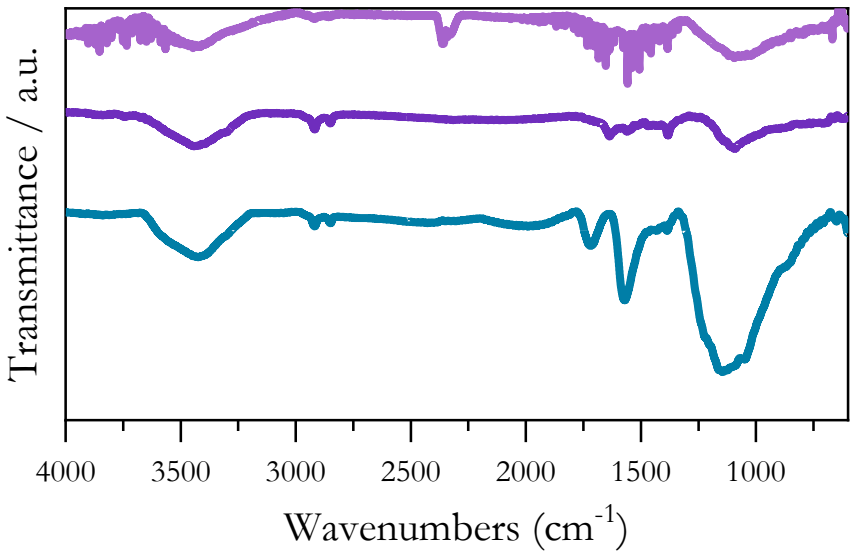

Figure II.6. FT-IR spectra of GO (green), GO@nPd (purple), and RGO@nPd (violet).

In the spectrum of RGO@Ni, the carboxylic C=O stretching signal at 1632 cm^{-1}, the carboxylic acid O-H stretching at 3400 cm^{-1}, and the C=O carbonyl signal at 1350 cm^{-1} evident in the spectrum of GO@Ni, either disappeared or are very weak (**Figure II.7**). Though weak, the stretching signal of non-reduced graphene C-O-C ether bonds at 1047 cm^{-1} is clearly present. This confirms that GO in the MORAL has actually been reduced to reduced graphene oxide.

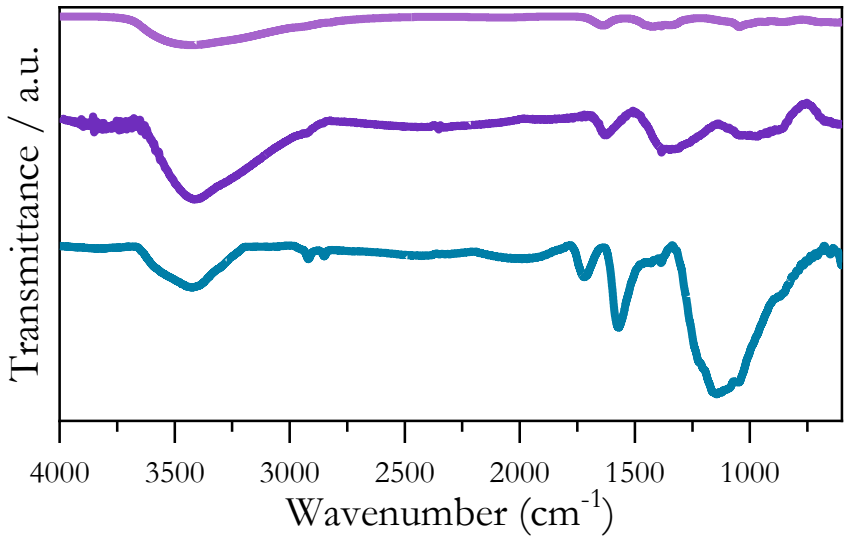

Figure II.7. FT-IR spectra of GO (green), GO@Ni (purple), and RGO@Ni (violet).

XPS Analysis

XPS analysis was performed on fresh and used GO@nPd to detect a possible interaction between the components that would modify the electronic structure. The photoelectron signal of Pd 3d consists of a Pd $3d_{5/2}$ and Pd $3d_{3/2}$ doublet, with well-separated spin-orbit components (Δ= 5.29 eV) in a 3:2 intensity ratio. The deconvolution of the Pd 3d spectrum in fresh GO@nPd reveals a major Pd $3d_{5/2}$ component located at BE = 335.7 eV, originating from metallic Pd, and a second component at BE = 336.9 eV assigned to PdO due to the surface partial oxidation (**Figure II.8**).

After the catalytic tests (see Catalytic Application paragraph), the Pd 3d spectrum of used GO@nPd confirmed the existence of two oxidation states of Pd on the surface with the lower binding energy component at BE = 334.5 eV. The amount of metallic Pd increased from 71.2% to 82.5%, while that of PdO decreased from 28.8% to 17.5%. The signal for metal Pd, furthermore, shifted to 1.2 eV lower binding energy due to the fact that in metals like Pd, in which the d-band is more than half full, the surface atoms acquire a net negative charge relative to the bulk, which translates into a surface component in the Pd $3d_{5/2}$ signal appearing at lower binding energy.[2]

In addition, a size increase in palladium NPs upon catalysis would translate into a negative shift of 3d core-level electrons.[10] TEM images did not detect any change in the Pd nanoparticle average size after employment of GO@nPd as a catalyst in nitrobenzene reduction, in comparison to fresh GO@nPd.

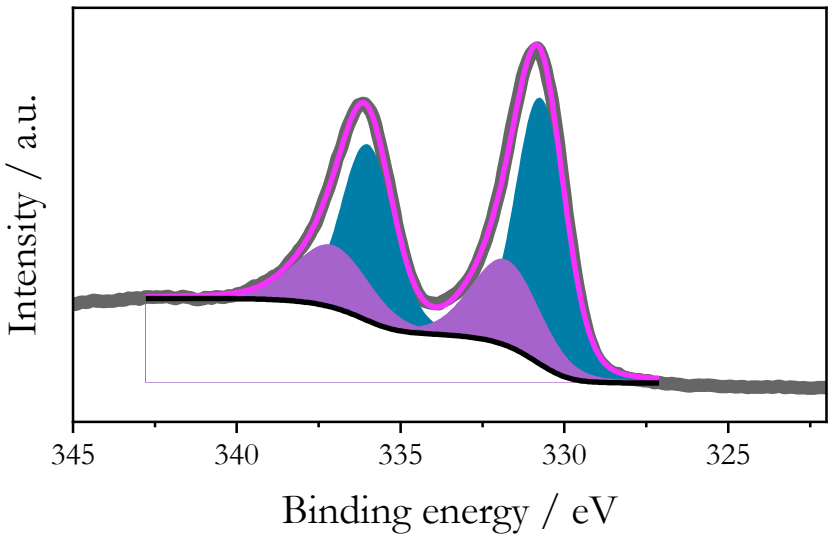

Figure II.8. XPS spectrum of fresh GO@nPd. In blue, Pd signals. In violet, PdO signals. The pink line represents the sum of the contributions, which overlaps with the raw data reported in grey.

Since XPS analysis on this sample did not reveal incontrovertible signs of interactions between the components, this analysis was not carried out on the other materials.

Electron Microscope Analysis

Both SEM analyses were performed on the four materials synthesized to investigate their morphology and structural features, together with TEM analysis performed on GO@nPd and RGO@Ni.

SEM revealed that all samples consist of micrometric aggregates. Elemental mapping *via* SEM-EDS (**Figure II.9**) confirmed the homogeneous distribution of palladium and nickel across the surfaces of their respective materials. Interestingly, the elemental maps for carbon and oxygen display similar spatial patterns. While surface oxidation of both Pd and Ni is expected upon air exposure, this observation suggests that a significant portion of the detected oxygen originates from the GO or RGO framework.

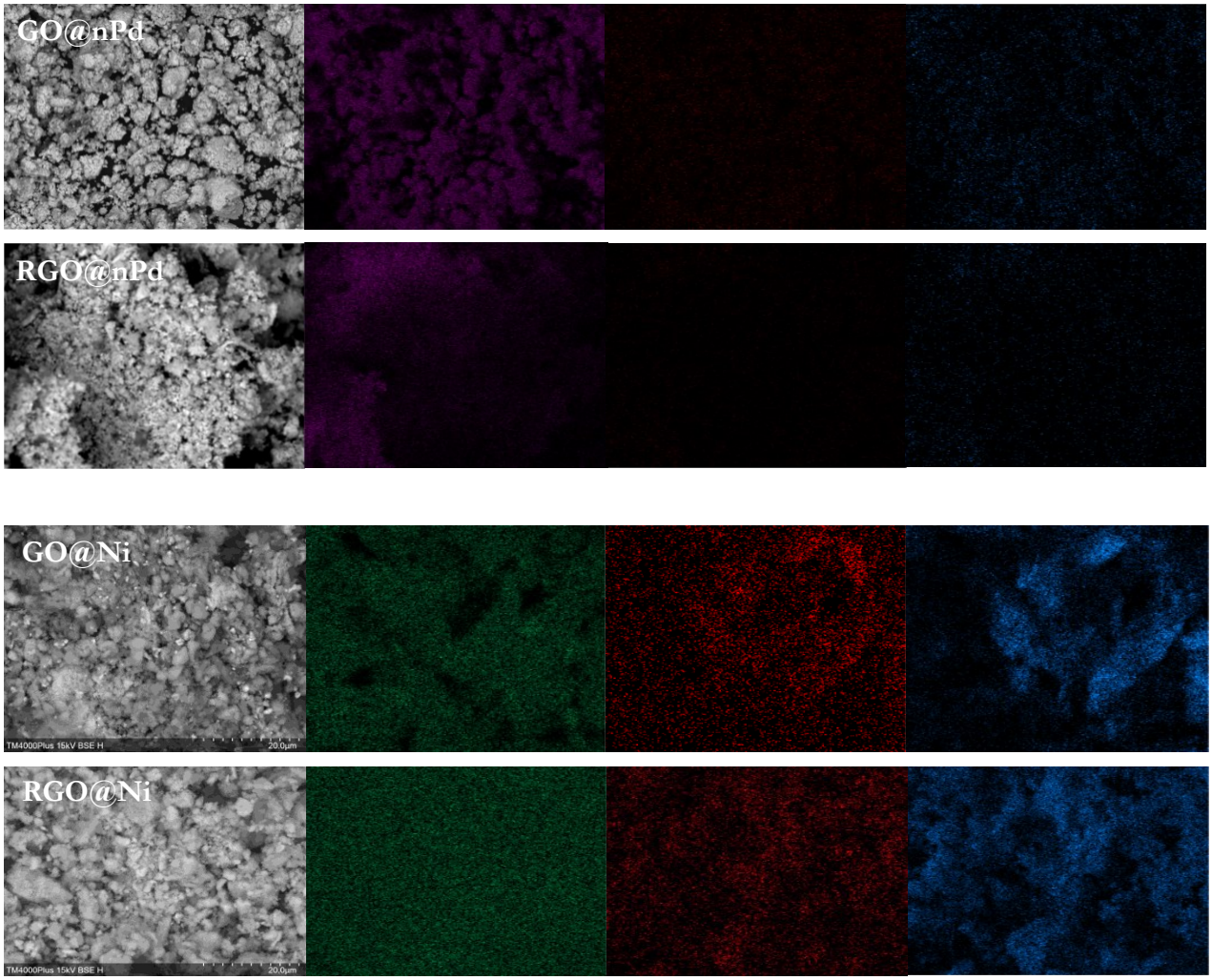

Figure II.9. SEM images and elemental maps obtained from EDS analysis of the four MORALs. Purple, Pd; green, Ni; red, C; blue, O.

The TEM images of GO@nPd in **Figure II.10** show that the material is comprised of aggregated palladium nanoparticles (**Figure II.10** a, b, and c), some of which clearly reveal the presence of glassy GO layers on the edge of the aggregated NPs (**Figure II.10** b). In both fresh and used samples, the Pd

aggregated nanoparticles are tightly intertwined with GO regions (Figure II.10 b, e, and f). Following the use of GO@nPd as a catalyst to mediate the nitrobenzene reduction to aniline with hydrazine at room temperature (see Catalytic Application chapter), the material retains its structural features. The regions comprised of tightly aggregated Pd nanoparticles with evidence of graphene-like layers are still clearly visible, along with others in which more dispersed Pd nanoparticles are deposited over GO aggregated layers. This is probably due to the disaggregation of some catalyst grain, compatible with the slight loss of activity we see from the catalytic.

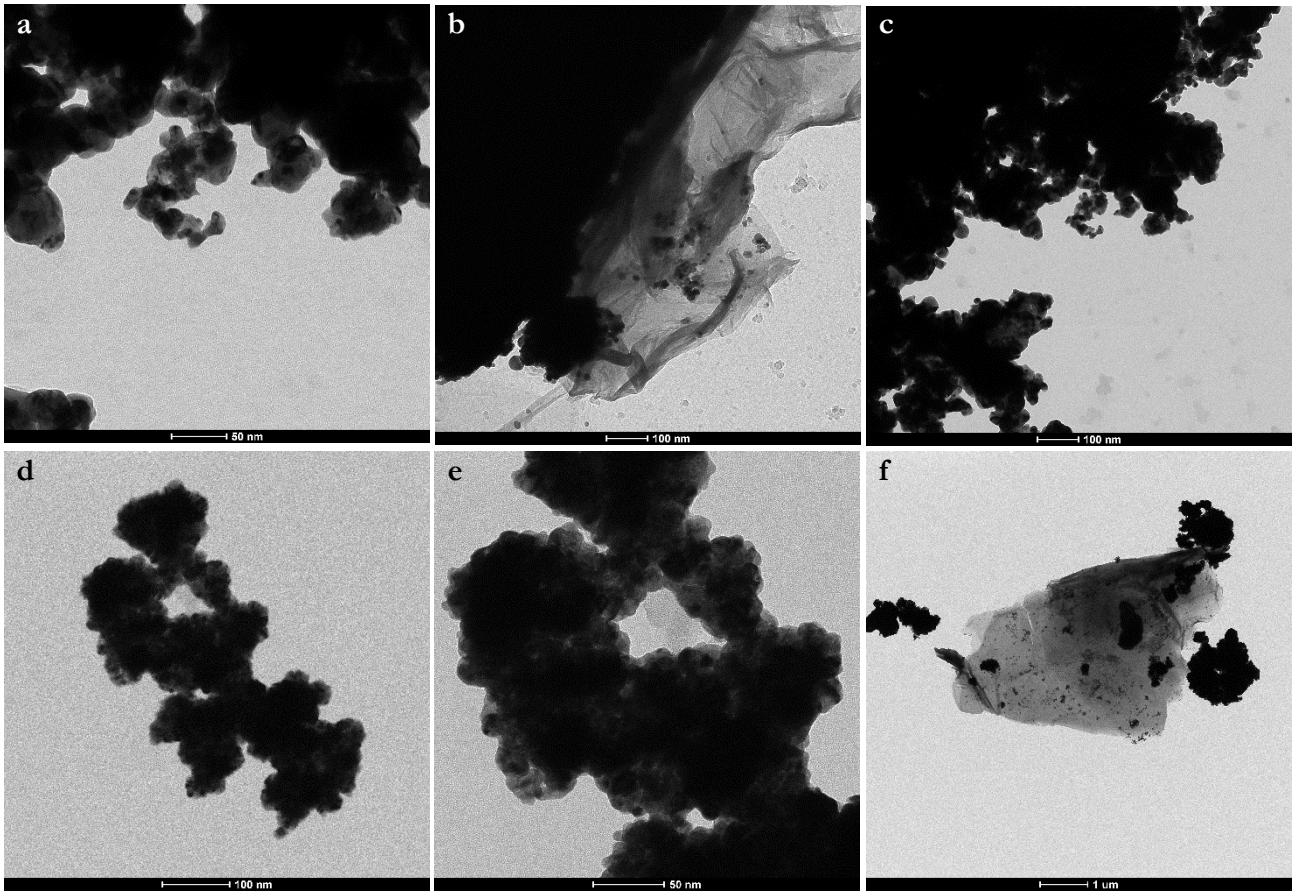

Figure II.10: TEM images of fresh GO@nPd (a, b, c) and after employment in nitrobenzene reduction (d, e, f).

For RGO@Ni, TEM images at different magnification degrees in **Figure II.11** a, b, and c show evidence that RGO@Ni consists of nickel agglomerates where graphene layers are disorderly entrapped within the metal structure and not wrapped around the Ni nanoparticles or regularly entrapped within said particles.

Additional evidence that RGO@Ni is amorphous is given by the diffraction pattern of the electron beam of the TEM instrument (**Figure II.11** f). No circular diffraction pattern with well-defined peaks is

observed, as it happens with crystalline materials, but rather concentric halos lacking any well-defined diffraction signal.

The outcomes of the energy-dispersive X-ray spectroscopy (EDS) analysis conducted with the same TEM instrument (**Figure II.12**) confirms that RGO@Ni chiefly consists of Ni (the copper signal is due to the copper mesh supporting the RGO@Ni sample).

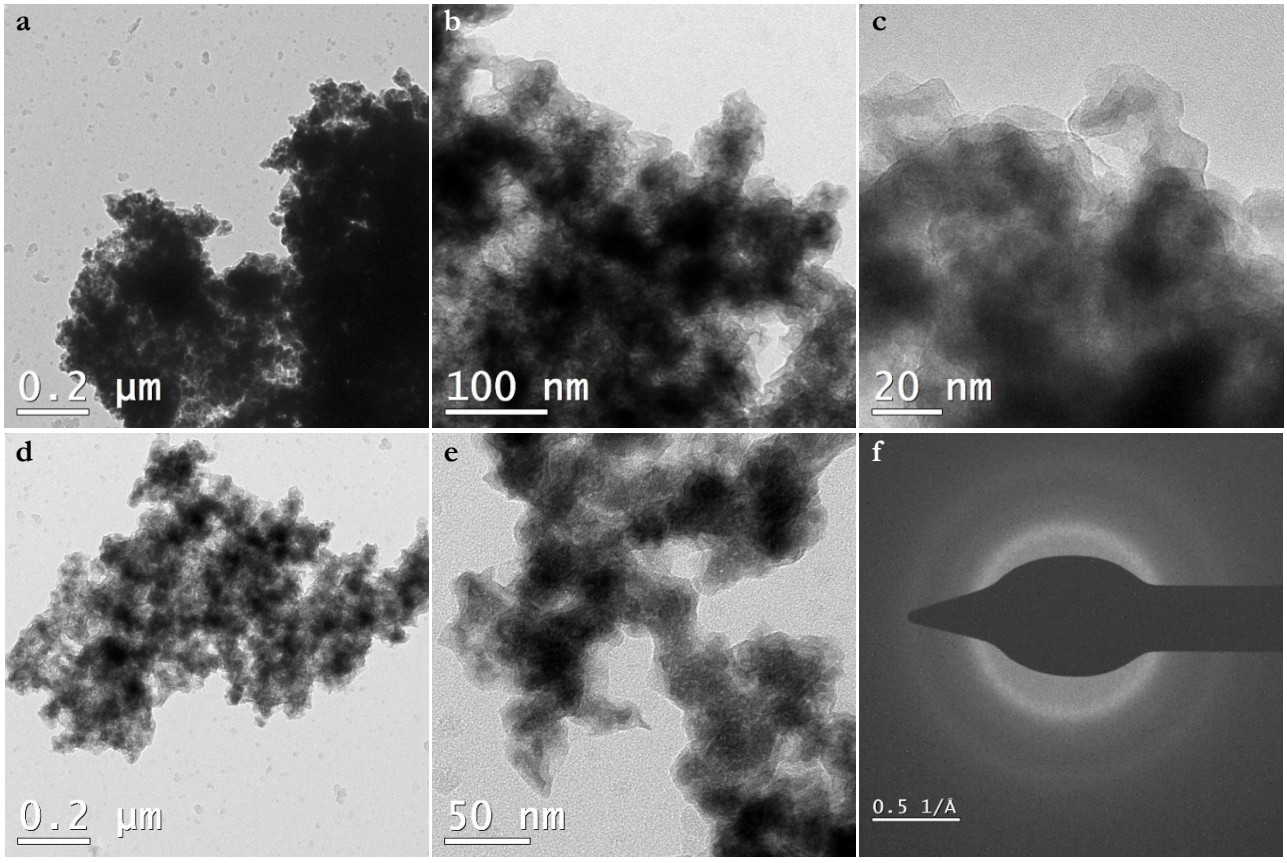

Figure II.11. a, b, c, d, e) TEM images at different magnifications of RGO@Ni; f) electron diffraction image of the material obtained from the area reported in image e, showing no proper diffraction images.

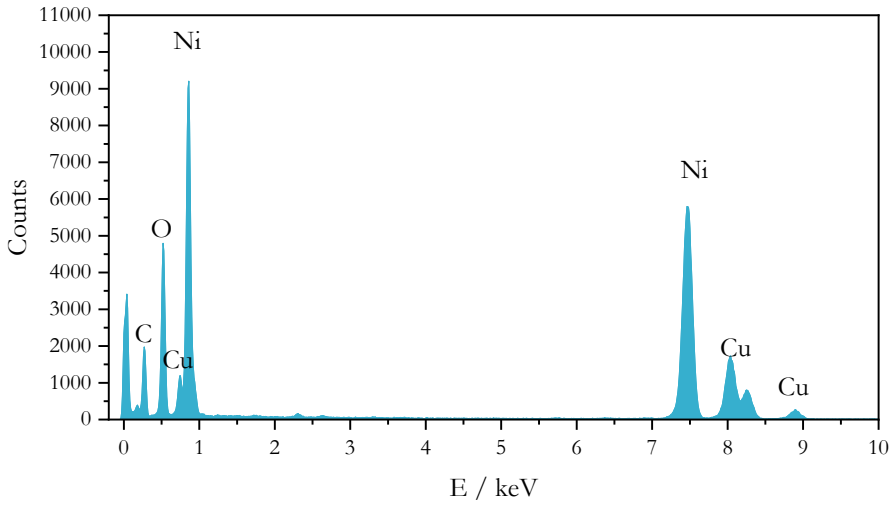

Figure II.12. EDS analysis of RGO@Ni acquired during the TEM analysis. Copper signals derive from the copper sample holder.

Catalytic Application

All the materials prepared were tested as catalysts in the probe liquid phase reaction of nitrobenzene reduction to aniline under mild conditions.[11-12] Aniline is an important bulk chemical used as a valuable intermediate for polyurethanes, dyes, pharmaceuticals, phytochemicals, and explosives, which is commercially produced via nitrobenzene hydrogenation, usually in >99% yield, in very large amounts (over 7 million tons in 2022). The catalytic process is highly favored, being highly exothermic with a ΔH = -544 kJ/mol at 200 °C and a ΔG = 520 kJ/mol for gas phase reaction with H_2.[13] Employing hydrazine at room temperature, the ΔG value is around 500 kJ/mol from NIST data, corresponding to an equilibrium constant of around 10^{88}. The industrial production can be carried out both in the vapor phase, with a high molar excess of hydrogen at 250-300 °C, and in the liquid phase at 90 °C. In both cases, certain chemical companies use heterogeneous catalysts based on palladium or palladium-platinum.

More than this, nitrobenzene reduction is a widely diffused probe reaction to test the catalytic activity of newly synthesized catalysts. As a reproducible test reaction, nitrobenzene reduction allows straightforward quantification of activity, selectivity (aniline vs. partially reduced or condensed byproducts), and stability (deactivation under hydrogen or in the presence of solvent and impurities). It is also adaptable to thermal, electrocatalytic, and photocatalytic evaluations, enabling cross-comparison of supported metals, core–shell architectures, and photocatalysts under both batch and flow conditions, supporting different possible reducing agents, such as molecular hydrogen, sodium borohydride, and hydrazine.

Palladium-Based Catalysts

Palladium-based catalysts were employed at room temperature and ambient pressure, employing 33% excess of hydrazine as reducing agent and 5% in moles of palladium with methanol as solvent (**Figure II.13**). Reaction mixtures were stirred for one hour and then filtered to eliminate the catalysts in order to stop any possible reaction. More details can be found in the experimental section (Chapter VII).

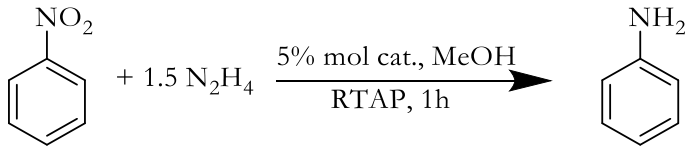

Figure II.13. Scheme for nitrobenzene reduction reporting conditions used for palladium-based catalysts.

Both GO@nPd and RGO@nPd exhibited high selectivity, obtaining aniline as the only product with no byproduct detected. However, a notable difference emerged in the conversion parameter: while GO@nPd achieved a conversion (and yield) of 74%, RGO@nPd overcame this result with 97% conversion.

Under the same conditions, the reaction was also conducted using more conventional palladium-based catalysts for comparative purposes. Accordingly, a commercial palladium on carbon (Pd/C) from Engelhart and a home-made palladium black were chosen. These materials demonstrated a selective conversion to aniline too, but with marked differences: while palladium black is the least-performing material, with only 46% yield, Pd/C afforded unitary yield, overcoming also the result obtained with RGO@nPd.

Time-course studies, here reported in **Figure II.14**, were conducted to highlight differences in the reaction rates. Pd/C led to complete conversion after 15 minutes, while palladium black reached a plateau after about 60 minutes. Data also show that palladium black is the slowest catalyst, while both GO@nPd and RGO@nPd are more active, although less than Pd/C. In particular, it is evident that RGO@nPd achieved the same yield as Pd/C, but only after 60 minutes, compared to 15 minutes for the commercial catalyst.

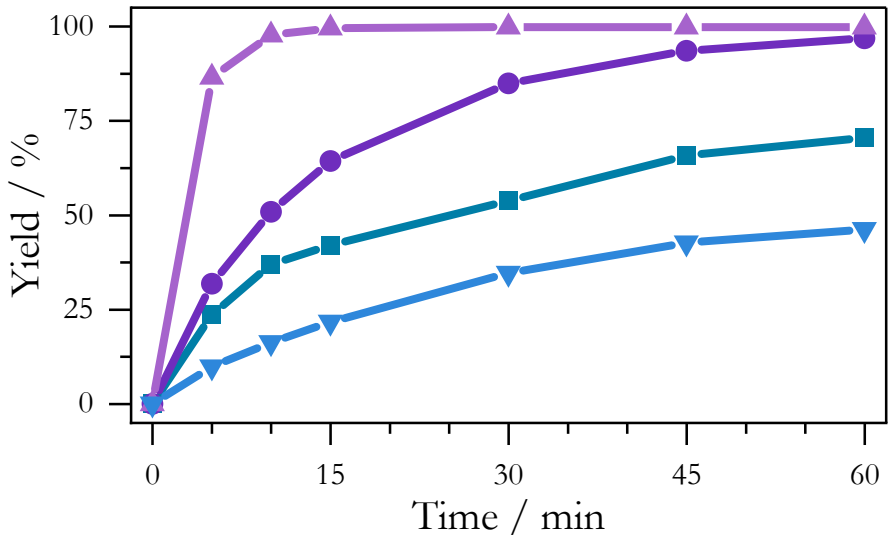

Figure II.14. Time course study for the palladium-based catalysts, highlighting the different performances of the tested catalysts. The reported data are the yield in aniline. Color code: green, GO@nPd; purple, RGO@nPd; violet, Pd/C; blue, palladium black.

To assess the robustness of the catalysts after use, their performance was compared in five reaction runs. Although all the catalysts led to aniline as the sole detected product, palladium black was found to

be the worst catalyst, deactivating during all reuse tests and achieving only 8% yield after the fifth reaction run. A similar behavior was observed by RGO@nPd, rapidly dropping below 20% yield after the second reaction run, then reaching only 10% yield after the fifth one. Better results were obtained with Pd/C, which slightly loses its performance during the second and third reaction runs (93% and 92% yields, respectively), further lowering yields to 66% and 27% after the fourth and fifth runs, respectively. GO@nPd revealed to be the most robust catalyst in terms of reuse, showing no detectable deactivation over the five reaction runs.

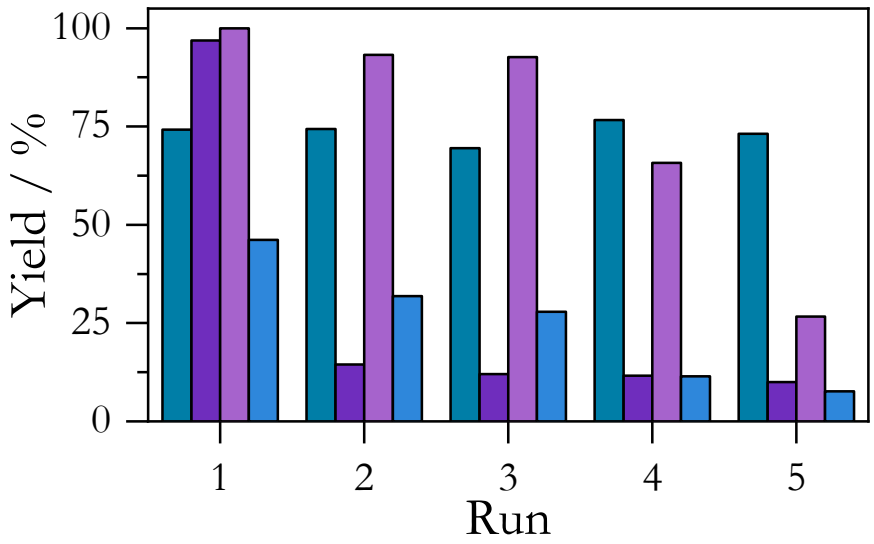

Figure II.15. Comparison in aniline yield among the palladium-based catalysts over five consecutive reaction runs. The reported data are after one hour of reaction. Color code: green, GO@nPd; purple, RGO@nPd; violet, Pd/C; blue, palladium black.

A deeper time-course study was performed on GO@nPd to better assess its robustness over five consecutive reaction runs. (**Figure II.16** top). It was possible to see how, during the second and third reaction runs, the catalytic activity slightly decreased, but this did not influence the final result. On the other hand, from the data collected during the second reaction run catalyzed by RGO@nPd, the activity decreased significantly (Figure II.16, bottom).

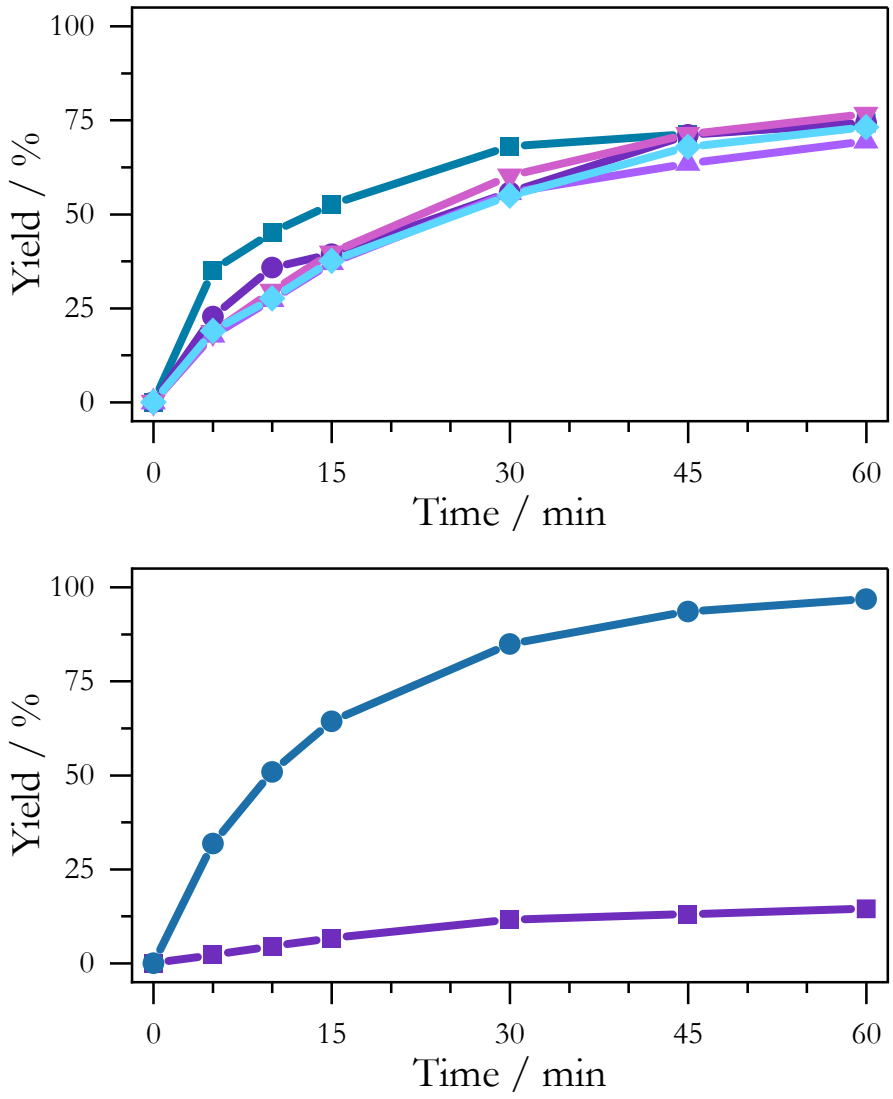

Figure II.16: Top, time-course study for the five consecutive uses of GO@nPd; from 1st to 5th use, blue, purple, violet, pink, light blue. After the first use, the slight loss of activity is evident. Bottom, time-course study of RGO@nPd; in green, 1st use; in purple, 2nd use. The plot displays the significant deactivation of the catalyst.

Nickel-Based Catalysts

Unlike palladium-based catalysts, a preliminary optimization was carried out to identify the best experimental conditions for the nickel-based catalysts. Temperature, aliquots of the reducing agent (hydrazine), kind and aliquots of solvent (water vs methanol), and atmosphere (air vs nitrogen) were systematically varied. The choice of the solvents is based on the different solubility of nitrobenzene: while it is largely soluble in methanol, its solubility in water is lower (1.9 g/L)[14] also if not negligible. On the other hand, both hydrazine and aniline, the main product, are widely soluble in both solvents. Employing nickel-based catalysts, in fact, led to side products, which were identified as nitrosobenzene, azobenzene, and azoxybenzene, as reported in **Figure II.17**.

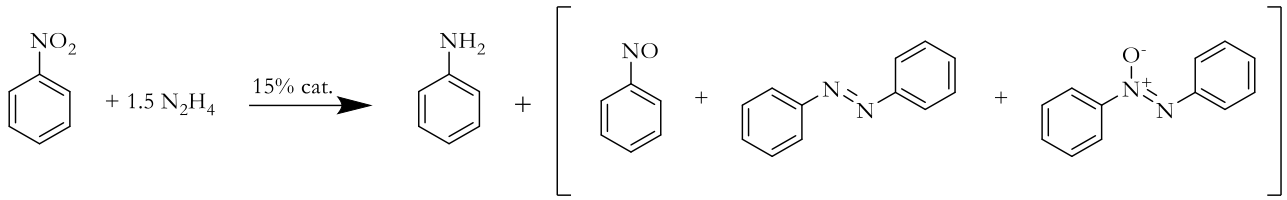

Figure II.17. Scheme for nitrobenzene using nickel-based catalysts. The identified byproducts are also reported.

Table II.1. A brief summary of the experimental optimization tests for nickel-based catalysts.

Entry	Catalyst	Solvent	Atm.	T / °C	Hydrazine eq.	Yield / %
1	GO@Ni	MeOH	N_2	35	1.1	6
2	RGO@Ni	MeOH	Air	35	1.1	7
3	GO@Ni	H_2O	N_2	35	1.1	61
4	RGO@Ni	H_2O	Air	35	1.1	82
5	RGO@Ni	H_2O	N_2	20	1.1	99
6	RGO@Ni	H_2O	N_2	35	1.1	>99
7	RGO@Ni	H_2O	N_2	50	1.1	68
8	GO@Ni	H_2O	N_2	35	1.4	70
9	GO@Ni	H_2O	N_2	35	1.7	83

Table II.1 reports some of the experimental optimization tests carried out to find the best reaction conditions. The first two trials in methanol resulted in very low aniline yield, both for GO@Ni and RGO@Ni, either under nitrogen or air (6% or 7% yield in entries 1 and 2, respectively). Moving to water, yield notably increased, from 6% to 61% for GO@Ni under nitrogen at 35 °C with 1.1 equivalents of hydrazine (entry 3) and 82% for RGO@Ni in air (entry 4). On the other hand, increasing the temperature to 50 °C was not beneficial for RGO@Ni, since the yield decreased from 99% at 20 °C and 99% 35 °C (entries 5 and 6) to 68% at 50 °C (entry 7).

In brief, a nitrogen atmosphere was found to be the best environment to conduct the reaction, while water turned out to be the optimum solvent at low temperatures (20 °C or 35 °C). A slight excess of hydrazine was found to be enough to achieve complete reduction, and a higher excess resulted in just a small increase in aniline yield (e.g., from 70% to 83% by increasing hydrazine from 1.4 to 1.7 equivalents, entries 8 and 9). More details can be found in the experimental section (Chapter VII).

Also these catalysts underwent reuse tests to assess their robustness, and their performance was compared to a nickel powder precipitated under the same conditions (results reported in **Figure II.18**). 1.1 equivalents of hydrazine were employed in water at 35 °C under nitrogen with 15% mol of nickel. While both MORALs achieved yields higher than 99% after the first two reaction runs, nickel powder reached 97% after the first run and 99% after the second one. Major differences were noted starting from the third reaction run, where GO@Ni slightly lowered its performance (96% yield) and nickel powder

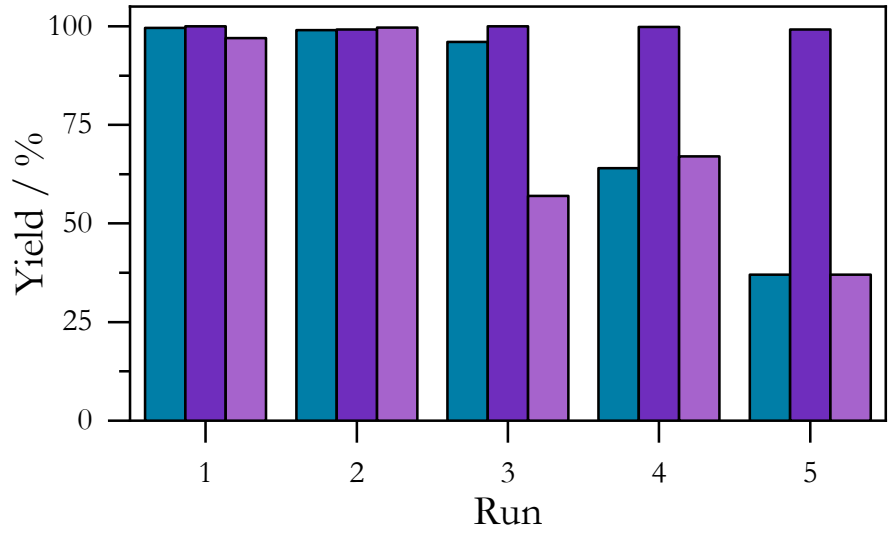

Figure II.18. Comparison in aniline yield among the palladium-based catalysts over five consecutive reaction runs. The reported data are after one hour of reaction. Green, GO@Ni; purple, RGO@Ni; violet, Ni.

reached only 57% yield, while RGO@Ni kept >99% yield. This behavior was observed over the next reaction runs, where Ni powder and GO@Ni further lowered aniline yield, dropping below 40% after the fifth run, while RGO@Ni showed no signs of performance loss.

Under the same conditions, a time-course study was performed employing the best catalyst, RGO@Ni (**Figure II.19**). It could be noted how the reaction proceeded in a selective way, yielding a very small amount of byproducts during the nitrobenzene reduction. At time = 90 min, the selectivity loss was due to the formation of the coupling products azobenzene and azoxybenzene.

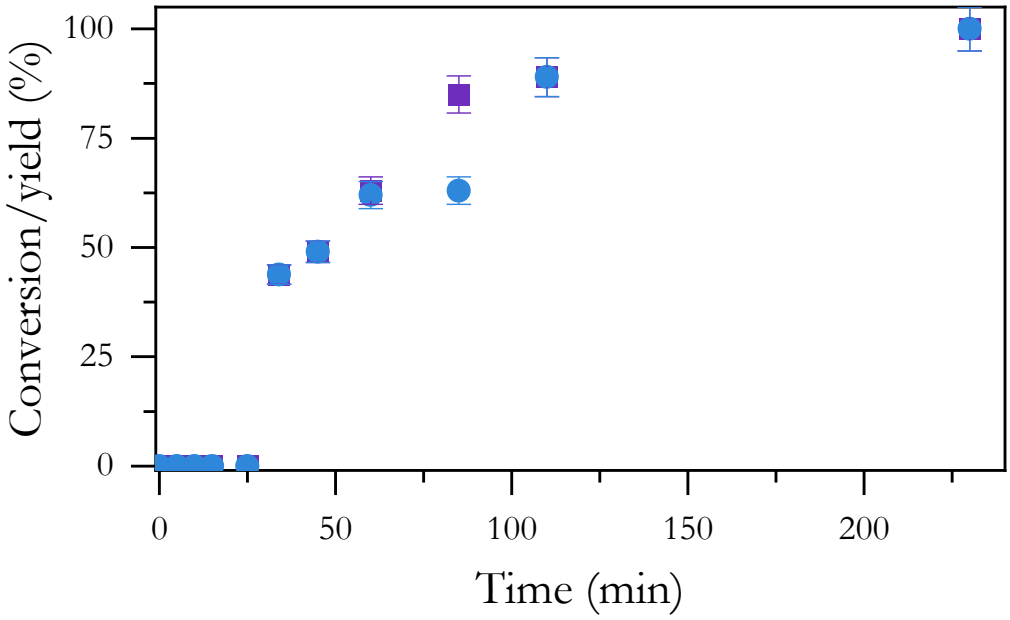

Figure II.19. Yield in aniline (blue circles) and substrate conversion (purple squares) in the reduction of nitrobenzene with hydrazine catalyzed by RGO@Ni (15 mol%) at 35 °C under N_2 atmosphere.

A final test on RGO@Ni was performed by decreasing the catalyst amount to improve the substrate-to-catalyst ratio. Results confirmed that the catalyst amount can be reduced to 7.5 % mol, without sacrificing the reaction yield. On the contrary, further decreasing the catalyst amount to 5.5% mol resulted in a lower yield (90%) (**Figure II.20**). While a further increase in catalyst amount would not achieve any benefit, since 100% yield is reached yet, it would have been interesting to test even lower amount of catalysts to confirm the expected linear relationship between catalyst amount and yield. Anyway, due to technical limitations (e.g., a too low amount of catalyst to add to the reaction mixture, or an excessive increase in the solvent volume for the used apparatus) it was not possible to carry out these tests.

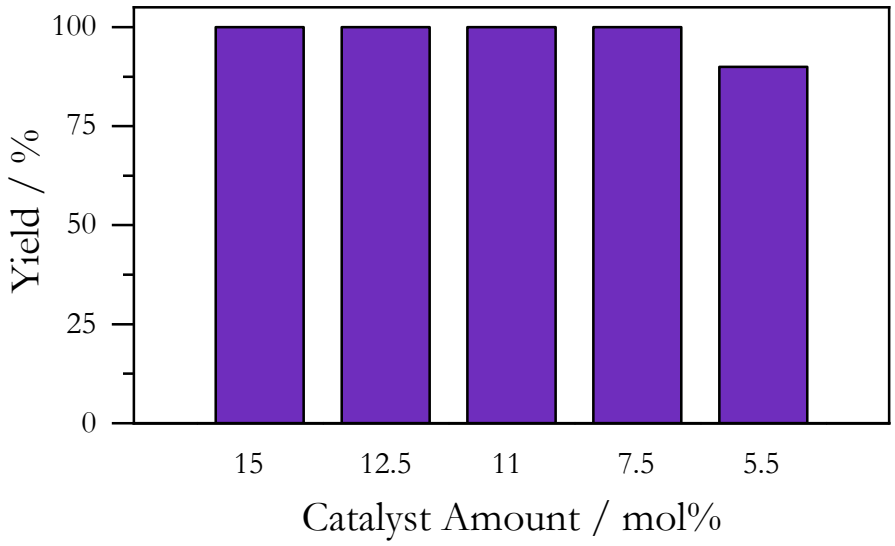

Figure II.20. Yield in aniline varying the amount of RGO@Ni catalyst.

Bibliography

1. Behar-Levy, H.; Avnir, D., Entrapment of Organic Molecules within Metals: Dyes in Silver. *Chemistry of Materials* **2002,** *14* (4), 1736–1741.
2. Güler, Ö.; Bağcı, N., A short review on mechanical properties of graphene reinforced metal matrix composites. *Journal of Materials Research and Technology* **2020,** *9* (3), 6808–6833.
3. Cao, M.; Xiong, D. B.; Yang, L.; Li, S.; Xie, Y.; Guo, Q.; Li, Z.; Adams, H.; Gu, J.; Fan, T.; Zhang, X.; Zhang, D., Ultrahigh Electrical Conductivity of Graphene Embedded in Metals. *Advanced Functional Materials* **2019,** *29* (17).
4. Chen, X.; Wu, G.; Chen, J.; Chen, X.; Xie, Z.; Wang, Z., Synthesis of "Clean" and Well-Dispersive Pd Nanoparticles with Excellent Electrocatalytic Property on Graphene Oxide. *Journal of the American Chemical Society* **2011,** *133* (11), 3693–3695.
5. Liu, J.-B.; Gong, H.-S.; Ye, G.-L.; Fei, H.-L., Graphene exide-derived single-atom catalysts for electrochemical energy conversion. *Rare Metals* **2022,** *41*, 1703–1726.
6. Shapiro, L.; Avnir, D., Multiple One-Pot Reaction Steps using Organically Doped Metallic Hybrid Catalyst. *ChemCatChem* **2013,** *5* (8), 2195–2198.
7. Some, S.; Kim, Y.; Yoon, Y.; Yoo, H.; Lee, S.; Park, Y.; Lee, H., High-quality reduced graphene oxide by a dual-function chemical reduction and healing process. *Sci Rep* **2013,** *3*, 1929.
8. Surekha, G.; Krishnaiah, K. V.; Ravi, N.; Padma Suvarna, R., FTIR, Raman and XRD analysis of graphene oxide films prepared by modified Hummers method. *Journal of Physics: Conference Series* **2020,** *1495*.
9. Rattana, T.; Chaiyakun, S.; Witit-anun, N.; Nuntawong, N.; Chindaudom, P.; Oaew, S.; Kedkeaw, C.; Limsuwan, P., Preparation and characterization of graphene oxide nanosheets. *Procedia Engineering* **2012,** *32*, 759–764.
10. Wertheim, G. K.; DiCenzo, S. B.; Buchanan, D. N. E., Noble- and transition-metal clusters: The d bands of silver and palladium. *Physical Review B* **1986,** *33* (8), 5384.
11. Formenti, M.; Ciriminna, R.; Della Pina, C.; Pagliaro, M., Reduced NiGraf: An effective hydrogenation catalyst of large applicative potential. *Next Materials* **2025,** *8*.
12. Formenti, M.; Pagliaro, M.; Della Pina, C.; Ciriminna, R., Graphene oxide in palladium nanoparticle (GrafeoPlad): A new class of functional materials. *Green Synthesis and Catalysis* **2025,** *6* (3), 297–301.
13. Kahl, T.; Schröder, K. W.; Lawrence, F. R.; Marshall, W. J.; Höke, H.; Jäckh, R., Aniline. In *Ullmann's Encyclopedia of Industrial Chemistry*, 2011.
14. Effect of water content on the stability of nitrobenzene solutions.

III. NHC-CAPPED GOLD NANOPARTICLES

A second topic I worked on during my PhD was the employment of new ligands to stabilize gold nanoparticles designed for catalytic applications. This project was carried out in collaboration with Dr. Daniele Malpicci and Prof. Elena Cariati at the Università degli Studi di Milano.

The choice of the ligand fell on derivatives of triimidazo[1,2-*a*:1',2'-*c*:1",5"-*e*][1,3,5]triazine, iso-TT, whose structure is reported in **Figure III.1** b. This molecule is poorly documented in the literature, being only reported by Buck and Kunz as a suitable precursor for Arduengo carbenes complexes[1] and by our collaborators as a building block for metal complexes[2-3] and in electrochemical studies.[4-5]

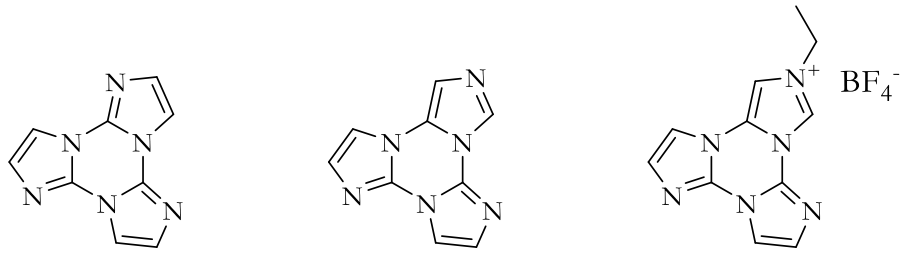

Figure III.1. Structures of (a) triimidazo[1,2-a:1',2'-c:1",2"-e][1,3,5]triazine (TT), (b) triimidazo[1,2-a:1',2'-c:1",5"-e][1,3,5]triazine (iso-TT), and (c) 10-ethyltriimidazo[1,2-a:1',2'-c:1",5"-e][1,3,5]triazin-10-ium tetrafluoroborate, the molecule from Buck's work

An additional motivation stems from the synthetic route itself. The isomer employed in this project is formed as a byproduct of the synthesis of triimidazo[1,2-*a*:1',2'-*c*:1",2"-*e*][1,3,5]triazine (**Figure III.1** a), a molecule that has been extensively investigated by our collaborators, who were interested in finding new applications. This is because the C_{3h} symmetric isomer demonstrated high versatility and applicability in different fields, being the scaffold suitable to be functionalized in various ways.

Based on this, the project was established with two major aims:

1. to investigate the use of a new ligand for the synthesis of gold nanoparticles stabilized by N-Heterocyclic Carbenes (NHC) and evaluating their catalytic performance;

2. to explore the incorporation of a molecule belonging to a family of photoluminescent compounds into biocompatible nanomaterials, assessing the potential emergence of photoluminescence..

Two different ligands derived from iso-TT were selected, but the resulting materials showed no photoluminescent behavior, thus leading the investigation to focus only on their catalytic application in the reduction of nitrobenzene. Comprehensive characterization was also performed using a wide set of analytical techniques in order to generate a robust dataset for future work.

Precursor Synthesis

The synthesis of triimidazo[1,2-*a*:1',2'-*c*:1",5"-*e*][1,3,5]triazine (iso-TT) followed the procedure reported in the literature.[6] Copper sulphate, sodium bicarbonate and imidazole were stirred in water at 80 °C, gradually leading to the precipitation of a blue copperdiimidazolate coordination polymer. The polymer was then filtered, dried, and sublimated under high vacuum to originate a mixture of imidazole, iso-TT, and its C_{3h} isomer triimidazo[1,2-*a*:1',2'-*c*:1",2"-*e*][1,3,5]triazine (TT). After recrystallization from hot toluene, the products were separated by preparative HPLC.

In the initial stage of the project, iso-TT was functionalized in order to obtain suitable precursors for the synthesis of Arduengo carbenes. N-alkylation was performed according to a modified protocol employing iodobenzene in toluene by refluxing overnight. The mixture was then cooled, and the product, namely 10-ethyltriimidazo[1,2-*a*:1',2'-*c*:1",5"-*e*][1,3,5]triazin-10-ium iodide (abbreviated as iso-TTEtHI, **Figure III.2** left), was obtained as a white precipitate. A toluene-water extraction was performed to separate the product from unreacted reagents, and purification by recrystallization from hot methanol yielded the pure product.

Following an analogous procedure, a second alkylated derivative bearing a benzyl substituent was synthesized by employing benzylbromide as the alkylating agent. The resulting molecule was 10-benzyltriimidazo[1,2-*a*:1',2'-*c*:1",5"-*e*][1,3,5]triazin-10-ium bromide (iso-TTBnHBr, **Figure III.2** right).

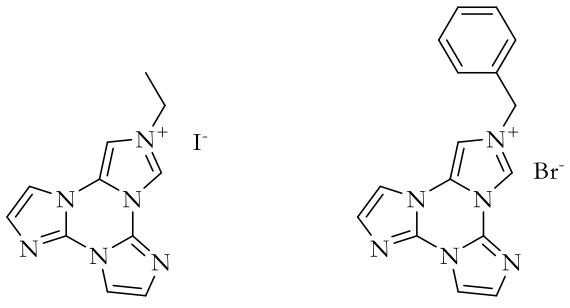

Figure III.2. Left, structure of 10-ethyltriimidazo[1,2-a:1',2'-c:1",5"-e][1,3,5]triazin-10-ium iodide (iso-TTEtHI); right, structure of 10-benzyltriimidazo[1,2-a:1',2'-c:1",5"-e][1,3,5]triazin-10-ium bromide (iso-TTBnHBr)

^{1}H-NMR spectra, here reported in **Figure III.3**, help confirm the successful functionalization. The spectrum of iso-TT displays six peaks in the 8.6 - 7.1 ppm region, two singlets associated with the 1,5-anellated imidazole and four doublets for the 1,2-anellated imidazole. After the alkylation, a marked shift is observed. One of the singlet peaks shifts at lower fields, more specifically, 10.40 ppm in the iso-TTEtHI spectrum and 10.64 ppm in that of iso-TTBnHBr. This strong deshielding effect is consistent with the introduction of a formal positive charge into the molecule. Simultaneously, new peaks attributable to the ethyl or benzyl substituents appear. In the iso-TTEtHI spectrum, a quadruplet centered at 4.52 ppm and a triplet at 1.57 ppm are detected, while iso-TTBnHBr exhibits a singlet at 5.75 ppm and a multiplet in the 7.35 - 7.6 ppm region.

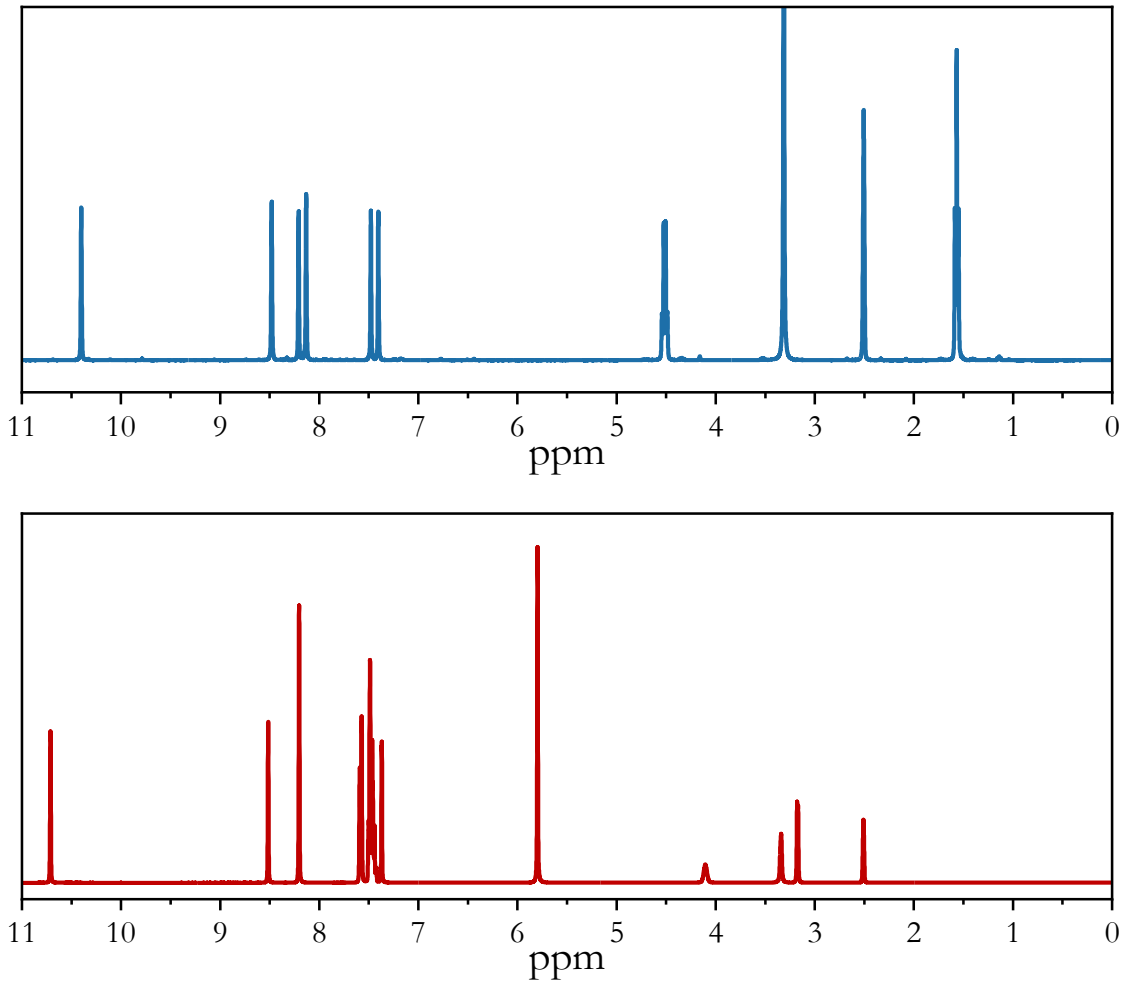

Figure III.3. ^{1}H-NMR spectra in DMSO-d6 of iso-TTEtHI (top) and iso-TTBnHBr (bottom). In both spectra, the highly deshielded signal over 10 ppm is attributed to the proton on the carbon atom generating the carbene.

Crystals suitable for XRD analysis were easily obtained by recrystallization of the newly synthesized compound, in order to determine the molecular structure. The compound crystallizes in the $P2_1/n$

punctual group, and the asymmetric unit is constituted of an iso-TTBnHBr molecule (**Figure III.4** left). The molecules assemble into dimers stabilized by π-anion interactions between the bromide anions and the cations. Furthermore, methanol molecules were found to be trapped in the crystal lattice with a non-homogeneous position.

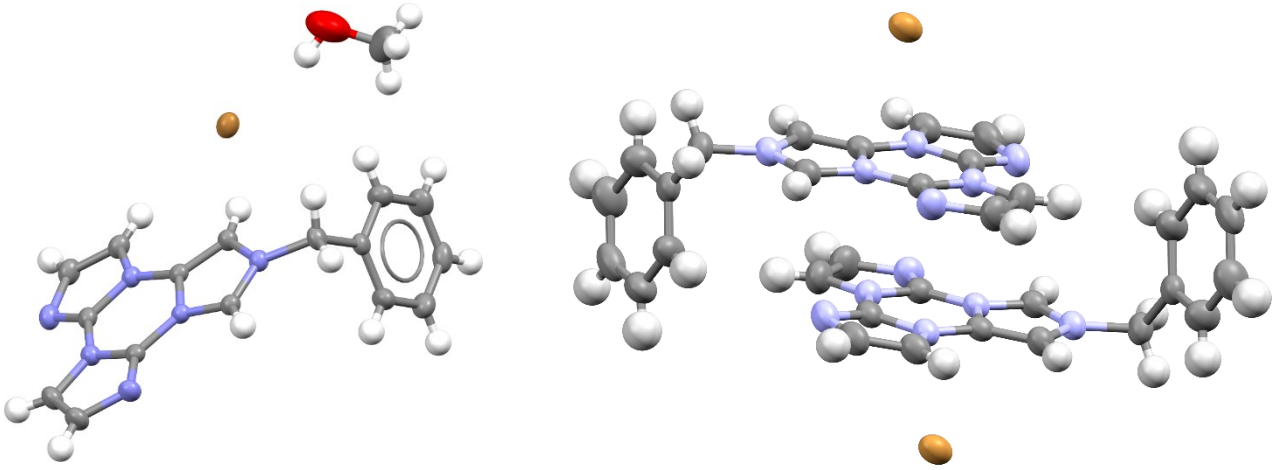

Figure III.4. Left, view of the asymmetric unit of iso-TTBnHBr. Right, packing of iso- TTBnHBr dimer.

To follow the nanoparticle synthesis procedure reported by Serpell et al.[7] for the preparation of NHC-stabilized palladium and gold nanoparticles, later applied by Bridonneau et al.[8] for broader studies on gold nanoparticles - substitution of the anion with tetrachloroaurate is needed. This procedure can be directly applied to iso-TTBnHBr, yielding iso-TTBnHAuCl$_4$. However, the same route cannot be followed for the iodide derivative iso-TTEtHI, as iodide possesses a strong reducing character capable of reducing Au(III) to Au(I), thereby leading to the precipitation of gold (I) chloride.

To overcome this issue, an ion exchange reaction with NH_4PF_6 was initially performed. This allowed the removal of iodide from the compound with the precipitation of iso-TTEtHPF$_6$, thus making it possible for $AuCl_4^-$ ions to coexist in solution with the triimidazotriazinium salt. A solution containing both the components was subsequently employed as a precursor mixture for the synthesis of gold nanoparticles.

Additional methods for iodide removal from the triimidazotriazinium salt were explored.

In the first strategy, $AgNO_3$ was employed to remove iodide as AgI from an aqueous solution of iso-TTEtHI, followed by the addition of $HAuCl_4$ for the precipitation of iso-TTEtHAuCl$_4$. Since no precipitation occurred, the solution was concentrated with a rotary evaporator and cooled overnight in the fridge to promote the precipitation. Also in this case, no precipitate was collected. To exclude the

possibility that the nitrate salt of iso-TTEtH$^+$ simply does not precipitate, iso-TTEtHI was mixed with $NaNO_3$. No precipitation occurred in this case either. This route was therefore deemed unsuccessful.

A second strategy (**Figure III.5**) involved the synthesis of an NHC-AuCl complex as a precursor for nanoparticle synthesis. In this method, tetrahydrothiophene (THT) was used both as ligand and reducing agent[9] to react with $HAuCl_4$, initially giving the complex [(THT)$AuCl_3$], which is then reduced to [(THT)AuCl]. Subsequent ligand substitution was performed in DMF using sodium acetate as deprotonating agent[10] to obtain the NHC-AuCl complex to be used as a precursor for iso-TTEt@AuNPs. The result of this procedure is illustrated in the following "Synthesis and Characterization of NHC-protected Gold Nanoparticles" paragraph.

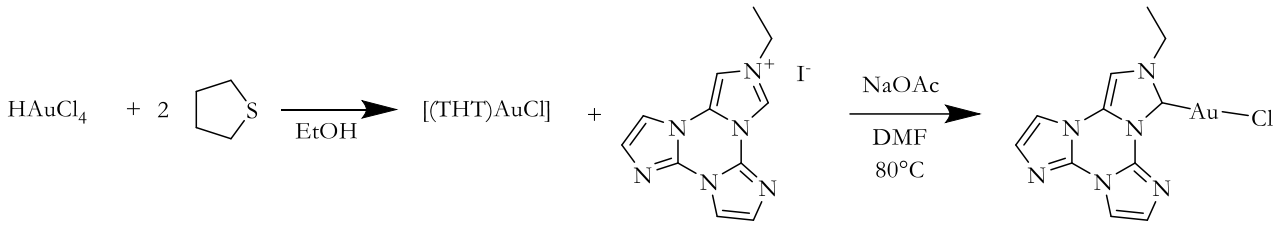

Figure III.5. Scheme for the synthesis of [(iso-TTEt)AuCl) complex.

A final strategy involved the use of a chloride-loaded ion-exchange resin (Amberlite) to exchange iodide with chloride. Amberlite was poured into a chromatographic column, and HCl was flushed to perform the mentioned exchange. A solution of iso-TTEtHI was then passed through the column, allowing conversion to iso-TTEtHCl, which was collected at the bottom of the column. This salt was further subjected to ion exchange with tetrachloroaurate to obtain iso-TTEtH$AuCl_4$ suitable as a precursor for iso-TTEt@AuNPs synthesis.

Synthesis and Characterization of NHC-protected Gold Nanoparticles

Conventional protocols for NHC-protected gold nanoparticles typically rely on sodium hydride to generate carbenes, either *in situ* or *ex situ*, followed by the reduction of a gold precursor in the presence of free carbenes. The method, first introduced by Serpell et al.,[7] in which sodium borohydride acts as a dual agent for carbene production and gold reduction, opened the door to a simplified synthetic route.

Reported methodologies usually employ a biphasic mixture, such as toluene/water or dichloromethane/water, where the organic phase dissolves the imidazolium salt and water dissolves $NaBH_4$. However, since our compounds are insoluble in both toluene and dichloromethane, modifications to these approaches were required.

Preliminary experiments employing iso-TTBnHAuCl$_4$ were performed, where both isopropanol and methanol were used as solvents for both iso-TTBnHAuCl$_4$ and NaBH$_4$. Even though TEM images confirmed nanoparticle formation in both cases, methanol was ultimately selected as the solvent due to different advantages: improved solubility of the precursor, enhanced dispersion of nanoparticles on the TEM sample holder, and a more homogeneous particle-size distribution. More details can be found in the experimental section (Chapter VII).

For the synthesis of iso-TTBn-functionalized gold nanoparticles (iso-TTBn@AuNPs), iso-TTBnHAuCl$_4$ was dissolved in methanol and reacted using 10 equivalents of NaBH$_4$. To prepare supported catalysts, the amount of support material necessary to obtain a nominal gold loading of 1% w/w was added to the suspension of nanoparticles. The resulting materials are indicated as iso-TTBn@AuNPs/support.

A similar procedure was used for the synthesis of iso-TTEt@AuNPs. Equimolar amounts of iso-TTEtHPF$_6$ and HAuCl$_4$ were added to methanol before reacting with 10 equivalents of NaBH$_4$. This is the procedure followed for the preparation of all the catalysts used for the catalytic tests.

Prior to support addition, samples suitable for TEM analysis were prepared by drop-casting the nanoparticles suspension onto a copper TEM grid.

XRPD Analysis

X-ray powder diffraction (XRPD) analysis was performed on gold particles suspensions dispersed in amorphous carbon (Vulcan XC72R) to confirm their successful formation in the nanoscale. Diffractograms of both iso-TTBn@AuNPs/Vulcan (**Figure III.6**) and iso-TTEt@AuNPs/Vulcan show the presence of a broad peak centered at 25° deriving from the amorphous carbon. Additional peaks sited at 38°, 44°, 65°, 78°, and 82° can be reconducted to the 111, 200, 220, 311, and 222 gold lattice planes, thus confirming the presence of crystalline gold particles.

Rietveld refinement was performed with Profex 5.2.5[11] to better analyze the peak shape and to obtain preliminary estimates of the nanoparticles size. Peak broadening was attributed to the nanoscale size of the gold crystallites. From the refinement, an average crystallite size of 6.7 nm was calculated for iso-TTBn@AuNPs/Vulcan, while this value was slightly higher (10.7 nm) for iso-TTEt@AuNPs/Vulcan.

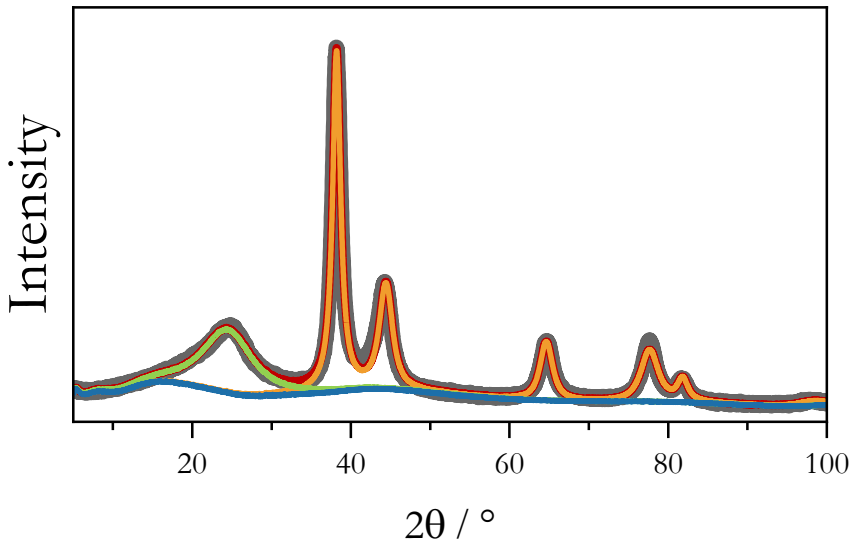

Figure III.6. XRPD diffractogram of iso-TTBn@AuNPs dispersed in amorphous carbon. Gray, raw data; blue, background; yellow, gold pattern; green, amorphous carbon band; red, sum of all the contributions.

UV-vis Analysis

UV-visible absorption spectra were obtained for the nanoparticle suspensions to characterize the plasmonic band of the gold nanoparticles.

Measurements were performed in transmittance on both iso-TTEt@AuNPs and iso-TTBn@AuNPs at 0.1 mg/mL and 0.01 mg/mL concentration (**Figure III.7**).

In all the samples, in the UV region, some absorption bands are present, consistent with the presence of the organic ligand.

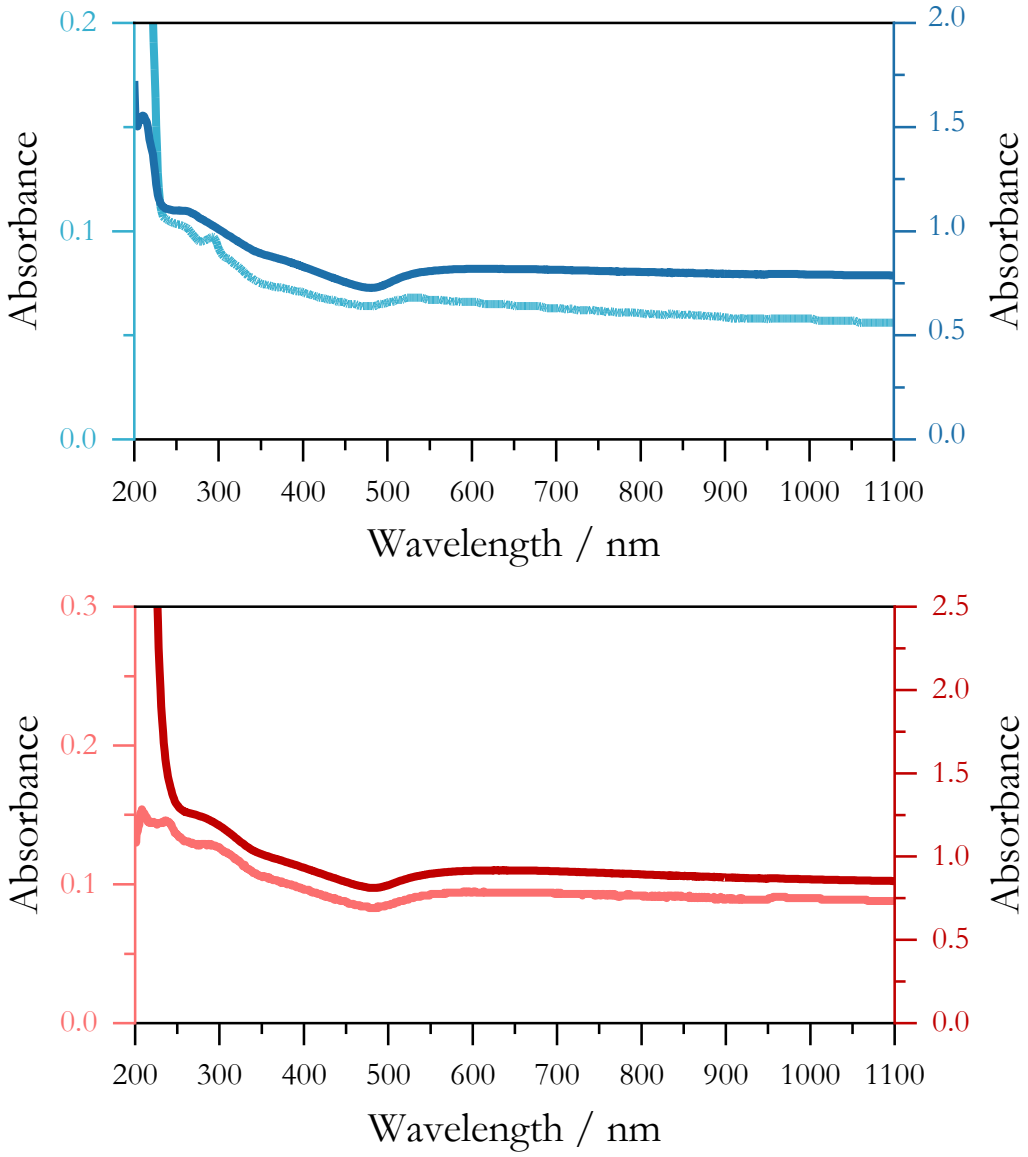

Figure III.7. UV-vis spectra of iso-TTEt@AuNPs (top) and iso-TTBn@AuNPs (bottom). Dark lines indicate 0.1 mg/mL suspensions, light lines indicate 0.01 mg/mL suspensions.

The visible region is characterized by the presence of a broad absorption band. In contrast, for iso-TTBn@AuNPs, this band shows no difference between the two concentrations; iso-TTEt@AuNPs spectra exhibit a different behavior.

While the 0.1 mg/mL suspension spectrum still presents a broad adsorption band centered at 612 nm, the 0.01 mg/mL suspension spectrum presents a sharper peak at 530 nm. This behavior suggests a lower-aggregation state, since the plasmonic band of aggregated nanoparticles behaves similarly to bigger nanoparticles because of the contemporaneous resonance of multiple nanoparticles.

This difference was also evident to the naked eye (**Figure III.8**): 24 hours after the preparation of suspensions, iso-TTEt@AuNPs suspension was still limpid, while iso-TTBn@AuNPs suspension presented big dark aggregates.

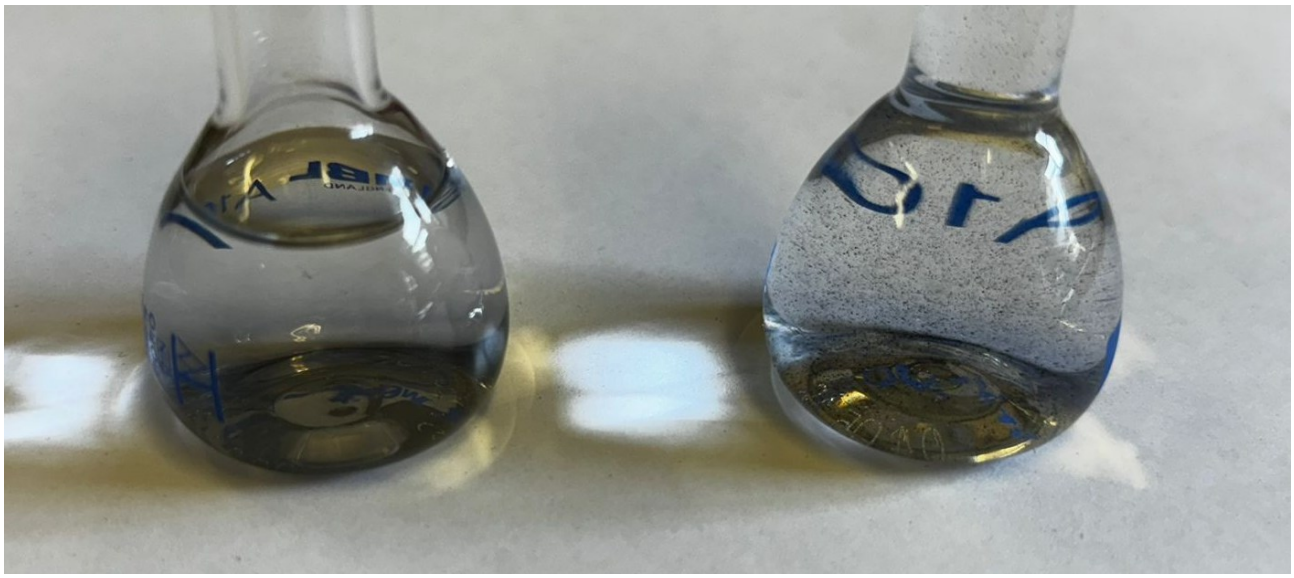

Figure III.8. Picture of 0.01 mg/mL suspensions 24 hours after the preparation. Left, iso-TTEt@AuNPs remaining limpid; right, iso-TTBn@AuNPs showing nanoparticles aggregates.

TEM Analysis

Transmission Electron Microscopy (TEM) was employed to investigate the morphology and size distribution of the synthesized nanoparticles. Comparative analysis of samples derived from iso-TTBnHAuCl$_4$ revealed differences in gold nanoparticles dispersion and aggregation depending on the solvent employed. The sample synthesized in isopropanol (**Figure III.9**) exhibited extensive aggregation, with isolated nanoparticles being rarely observed. Nevertheless, the individual nanoparticles retained well-defined shapes, enabling reliable diameter measurements for statistical analysis. In contrast, the methanol-derived sample (**Figure III.10**) showed lower aggregation and a higher amount of well-dispersed nanoparticles.

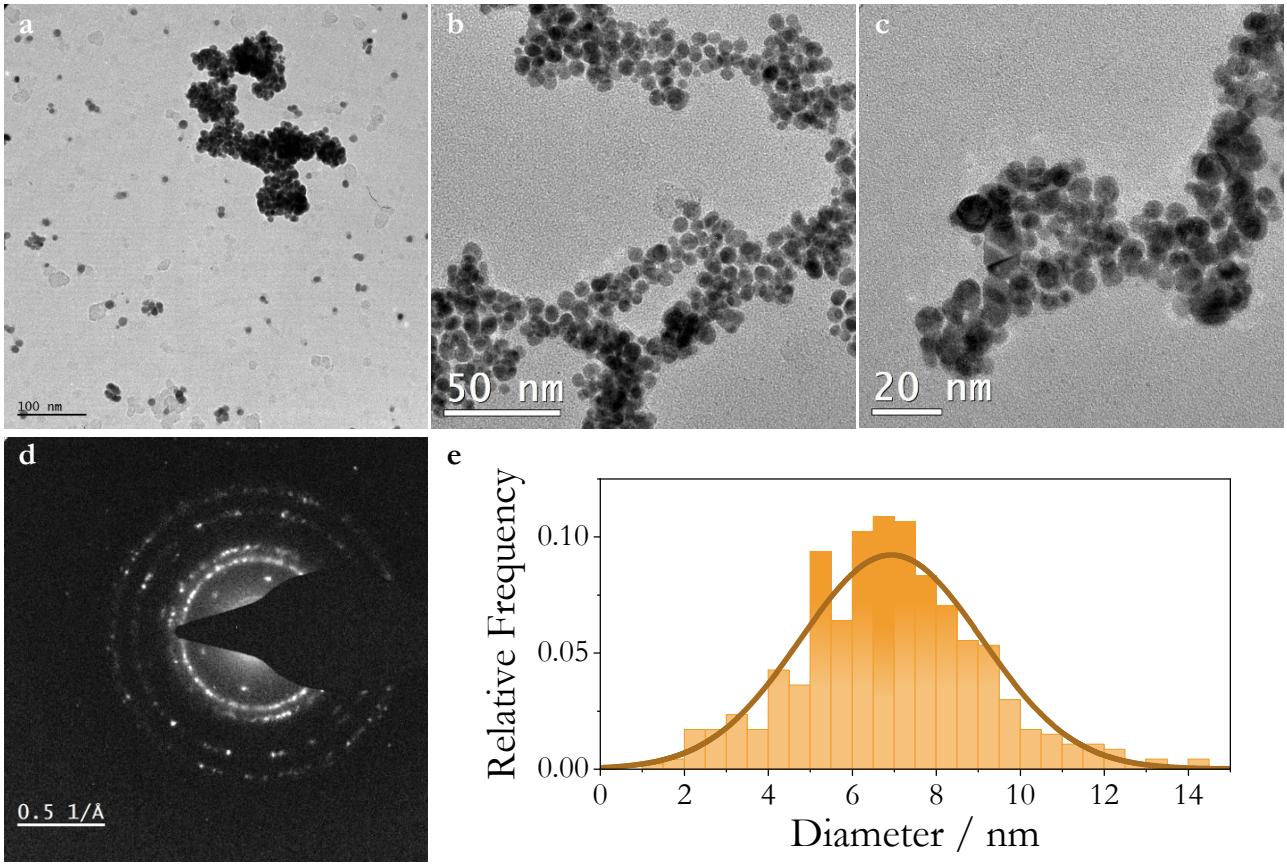

Figure III.9. a, b, c) TEM images at different magnifications of iso-TTBnHAuCl$_4$-derived gold nanoparticles from isopropanol solution. d) electron-diffraction image of the sample showing diffraction peaks of gold. e) distribution plot of nanoparticles diameter

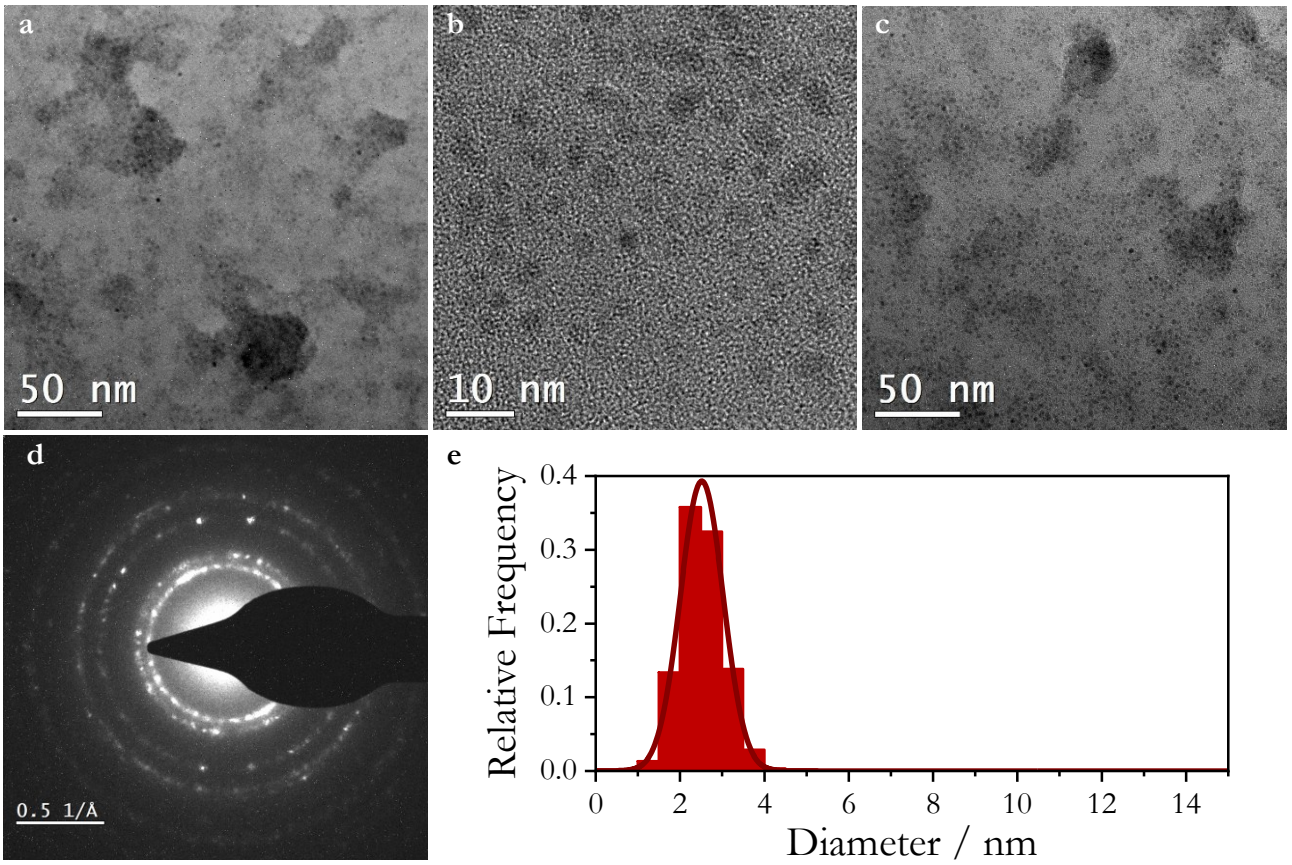

Figure III.10. a, b, c) TEM images at different magnifications of iso-TTBnHAuCl$_4$-derived gold nanoparticles from methanol solution. d) electron-diffraction image of the sample showing diffraction peaks of gold. e) distribution plot of nanoparticles diameter

Nanoparticles synthesized from iso-TTEtHPF$_6$ (**Figure III.11**) were found to be highly unstable under the TEM electron beam. During image acquisition, beam-induced melting was frequently observed. Despite this limitation, it was still possible to measure the diameters of several nanoparticles for statistical analysis.

Particle-size distributions were fitted using Gaussian functions, with dispersion analyses carried out in OriginLab2025 considering a bin size of 0.5 nm. Iso-TTBnHAuCl$_4$ in methanol led to the smallest nanoparticles size with a very narrow distribution (average diameter of 2.5 nm, FWHM = 2.8 nm), while the sample from isopropanol yielded significantly larger particles and distribution (average diameter of 6.9 nm, FWHM = 5.0 nm). Sample from iso-TTEtHPF$_6$ presented larger nanoparticles too, but with a narrower size distribution (average diameter of 7.9 nm, FWHM = 1.2 nm).

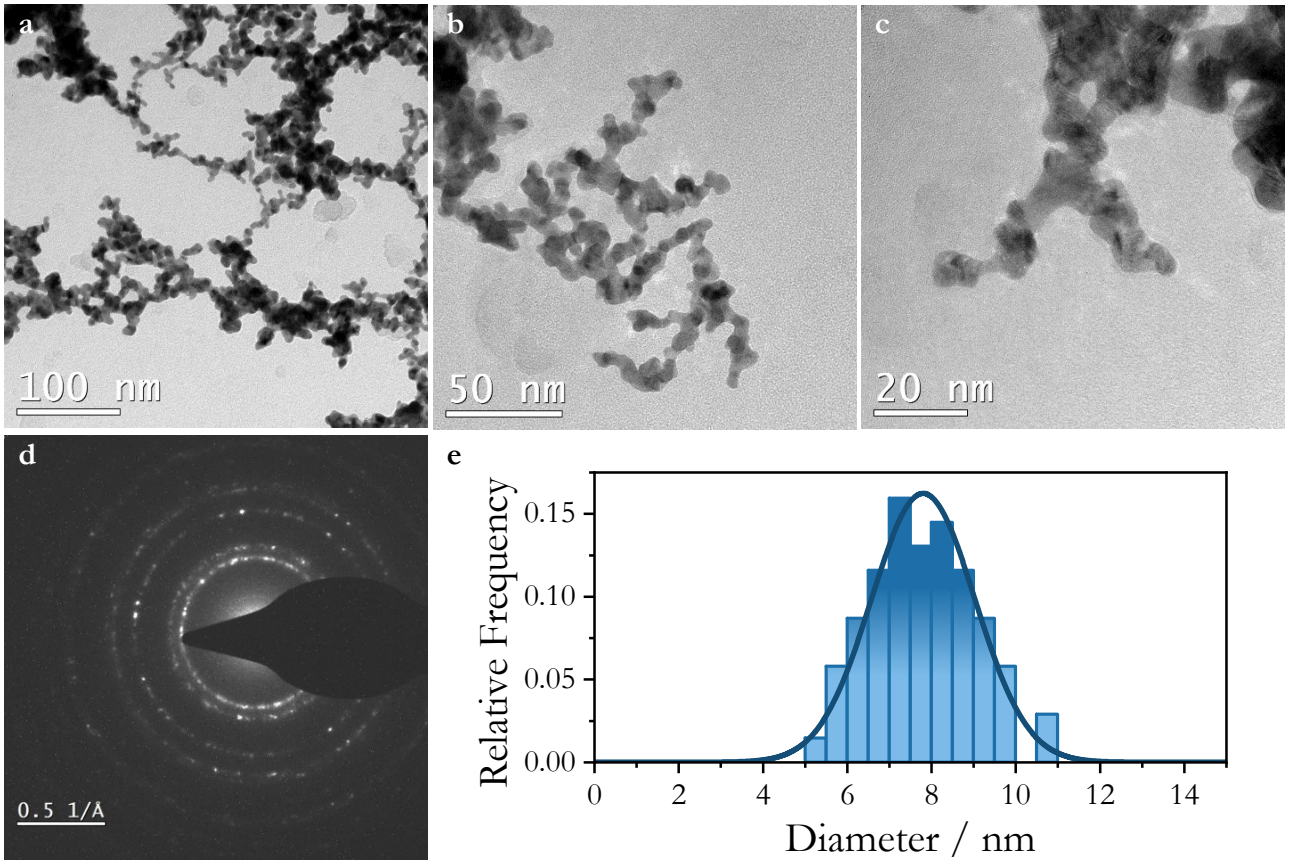

Figure III.11. a, b, c) TEM images at different magnifications of iso-TTEtHPF$_6$-derived gold nanoparticles. d) electron-diffraction image of the sample showing diffraction peaks of gold. e) distribution plot of nanoparticles diameter.

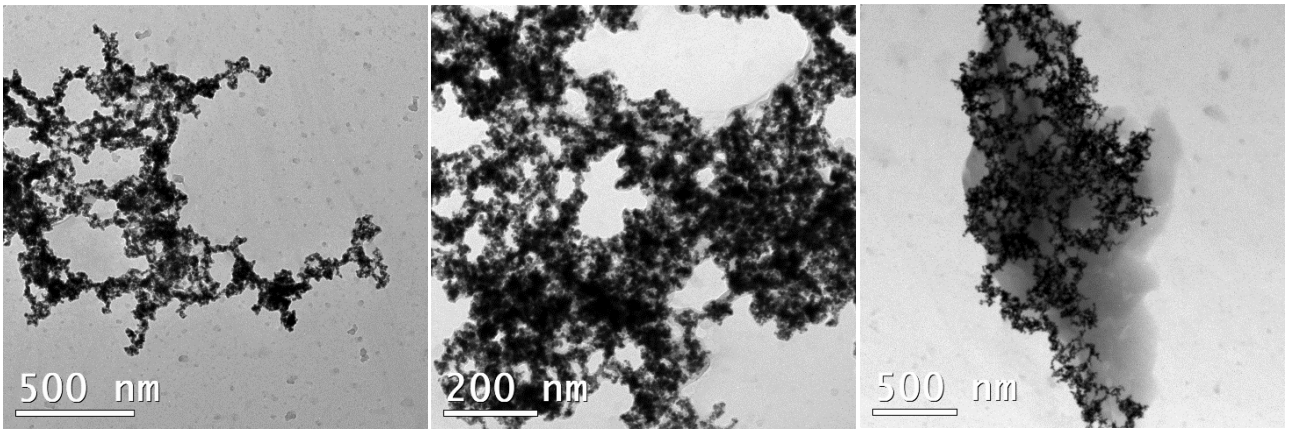

Figure III.12. TEM images at different magnifications of iso-TTBnHPF$_6$-derived gold nanoparticles.

Due to the marked difference in TEM beam stability, a test synthesis of iso-TTBn@AuNPs was performed by performing ion exchanging iso-TTBnHBr with PF_6^- to obtain iso-TTBnHPF$_6$, in order to

employ it for nanoparticles synthesis with $HAuCl_4$ to evaluate a possible influence of PF_6^-. TEM images (**Figure III.12**) confirmed that, also in this sample, nanoparticles are not stable and tend to form large aggregates. This suggests that PF_6^- may contribute to beam-induced melting and should therefore be avoided for samples intended for TEM analysis.

For this purpose, alternative synthetic pathways for iso-TTEt@AuNPs were explored. In the first approach, carbene complex [(iso-TTEt)AuCl] was prepared as a gold-containing nanoparticle precursor to undergo subsequent reduction using $NaBH_4$ in a THF/water mixture. TEM analysis of the final product (**Figure III.13**) revealed that nanoparticles were highly dispersed with low aggregation. While most of the nanoparticles resulted to be below 2 nm size, a minor population was present with diameter between 2 nm and 4 nm.

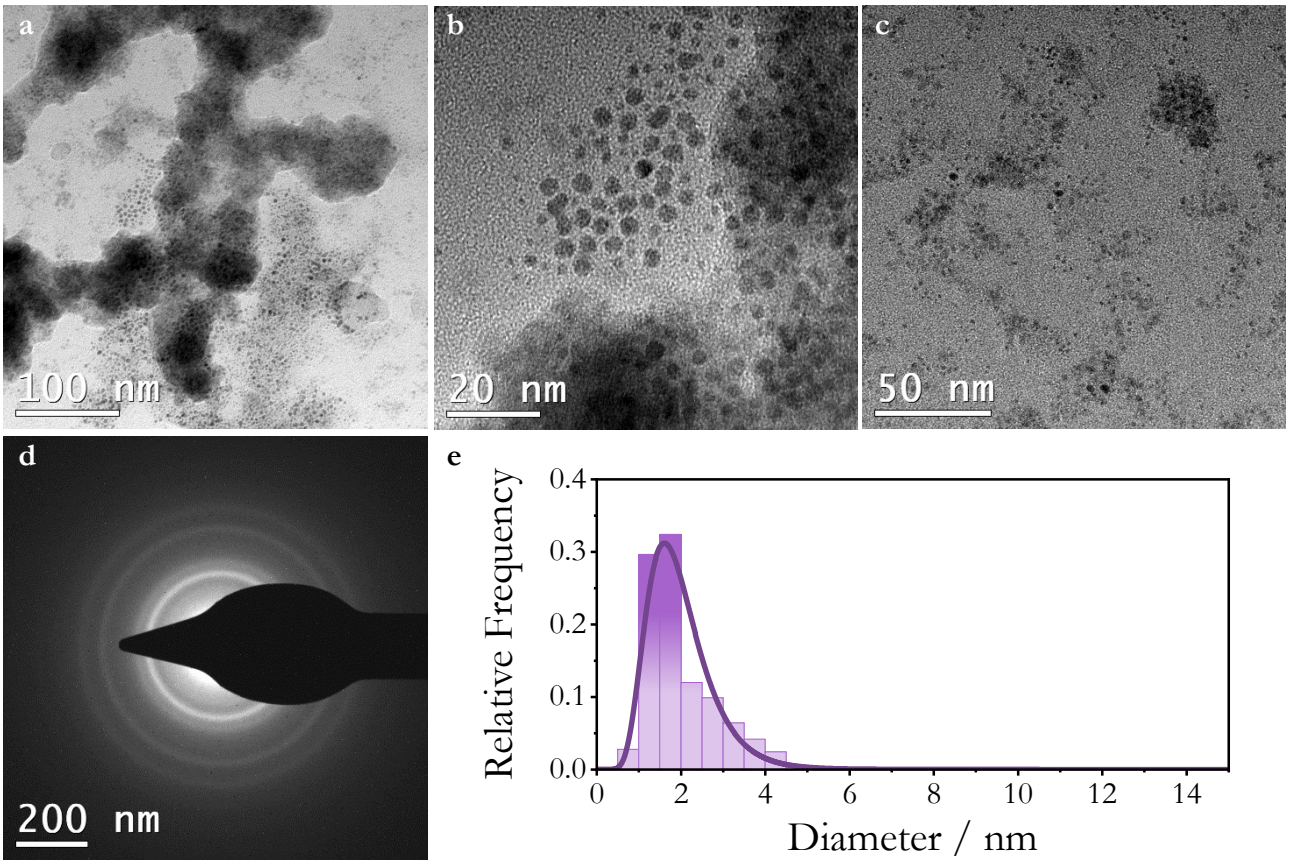

Figure III.13. a, b, c) TEM images at different magnifications of [(iso-TTEt)AuCl]-derived gold nanoparticles. d) electron-diffraction image of the sample showing diffraction peaks of gold. e) distribution plot of nanoparticles diameter.

A second route involved generating iso-TTEtHCl using an ion-exchange resin, followed by reaction with $AuCl_4^-$ and subsequent deprotonation/reduction with $NaBH_4$. The resulting nanoparticles were again

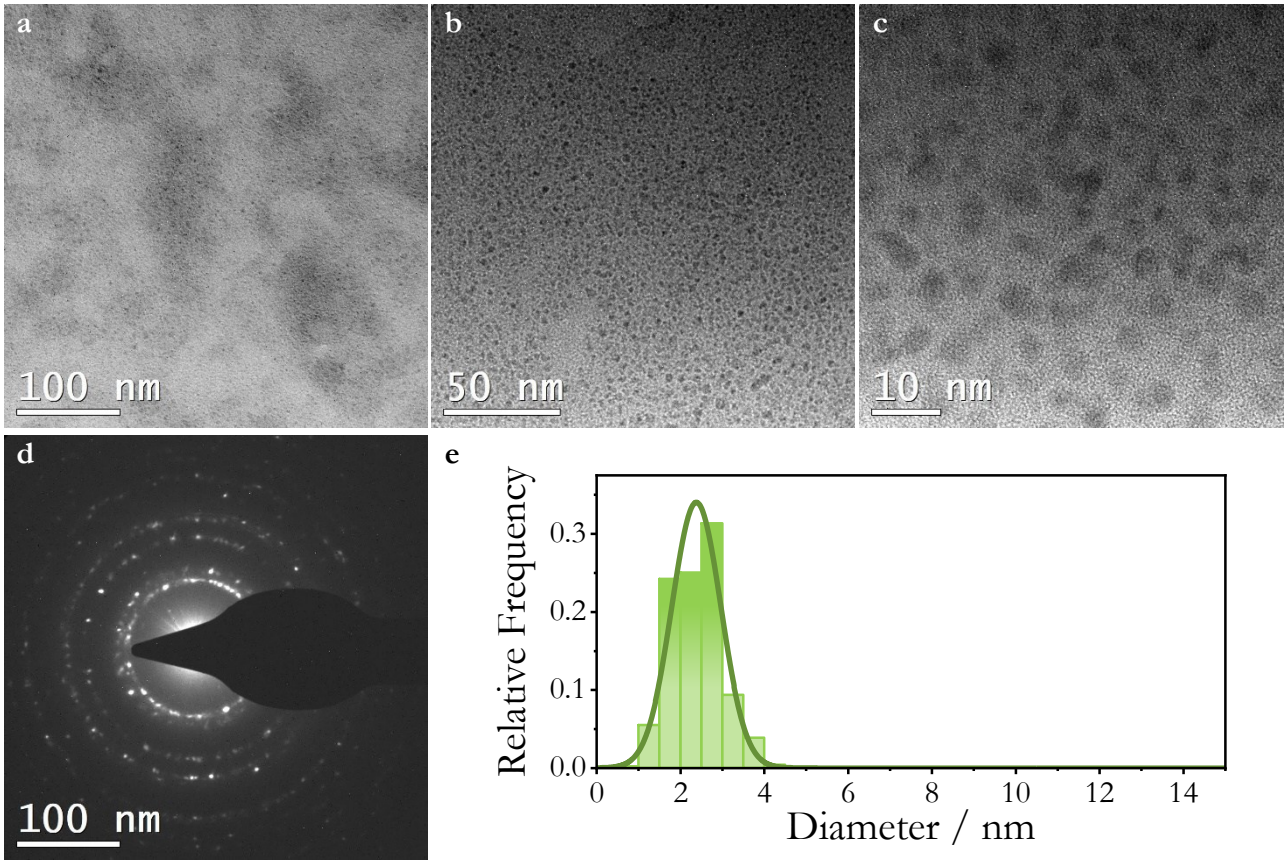

Figure III.14. a, b, c) TEM images at different magnifications of iso-TTEtHAuCl$_4$-derived gold nanoparticles. d) electron-diffraction image of the sample showing diffraction peaks of gold. e) distribution plot of nanoparticles diameter.

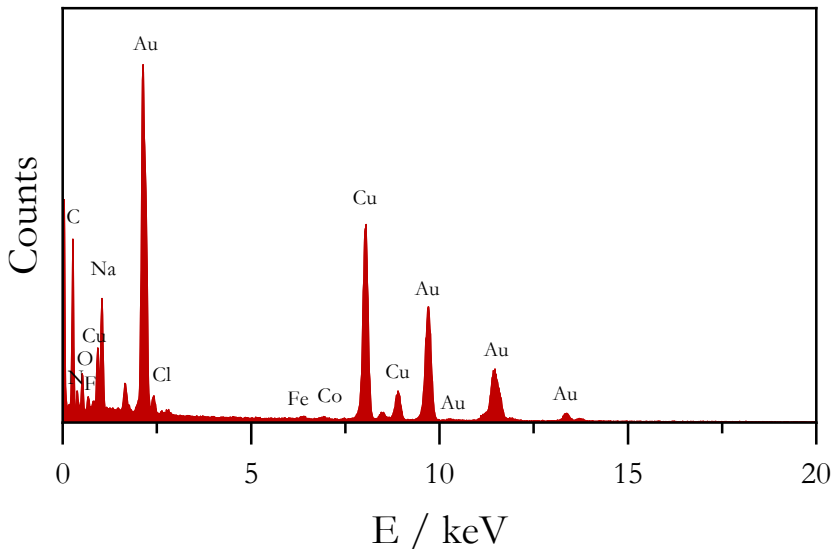

Figure III.15. Example of EDS spectra obtained during TEM analysis. Copper signals derive from the sample holder, while iron and cobalt derive from the magnetic elements of TEM instrument.

well dispersed (**Figure III.14**) with sizes comparable to those obtained from the iso-TTBnHBr-based synthesis.

To conclude, energy-dispersive X-ray spectroscopy (EDX) and electron diffraction images were also acquired on all the samples. EDX spectra (**Figure III.15**) confirmed the presence of gold, along with carbon originating from both the sample and the TEM copper grid. Detection of nitrogen, deriving from the ligand, sometimes failed, probably due to a combination of low loading of organic ligand on the nanoparticles surface and partial overlapping of nitrogen and oxygen signals. Electron diffraction showed the typical pattern of metallic gold in all the analyzed samples, thus confirming the identity of the gold nanoparticles.

FT-IR Analysis

Throughout the synthetic process, FT-IR spectroscopy was employed to monitor structural changes in the molecules and confirm the presence of carbene species on the nanoparticles surface. This technique was selected for its rapid execution, broad applicability, and effectiveness in characterizing surface-bound functional groups.

The spectrum of iso-TT is dominated by a structured band in the 1510-1670 cm^{-1} region, typical of C=C and C=N stretching, with three peaks sited at 1625, 1603, and 1586 cm^{-1}.

After alkylation, a new band emerged, sited at 1663 cm^{-1} in iso-TTBnHBr and at 1668 cm^{-1} in iso-TTEtHI, attributed to a vibration mainly involving the substituted imidazolic ring, while the other two bands are retained similarly to iso-TT at 1603 cm^{-1} and 1590 cm^{-1}. These findings align with literature reports,[12-13] where imidazolium cations show a vibration band usually sited between 1600 and 1650 cm^{-1}.

Ion exchange to PF_6^- or $AuCl_4^-$ induced only minor shifts in band positions and intensities.

Major changes, however, appear in the nanoparticles spectra. Despite extensive washing, centrifugation, and sonication, no FT-IR spectral features attributable to the ligand precursor remained, therefore providing a first confirmation of the successful functionalization. It is possible to note a global broadening of the experimental spectra, such that the bands of C=C and C=N stretching are broadened into a single band.

Examples in literature report that carbene formation eliminates IR absorption between 1500 and 1700 cm^{-1}. This is usually used to confirm carbene formation and coordination to the nanoparticle. This discrepancy with the spectra obtained could be attributed to the specific ligand used: while an imidazolium-derived carbenes strongly change their structure, being formed of just one imidazole ring, the change in triimidazotriazinium-derived carbenes can be more limited because of the larger aromatic

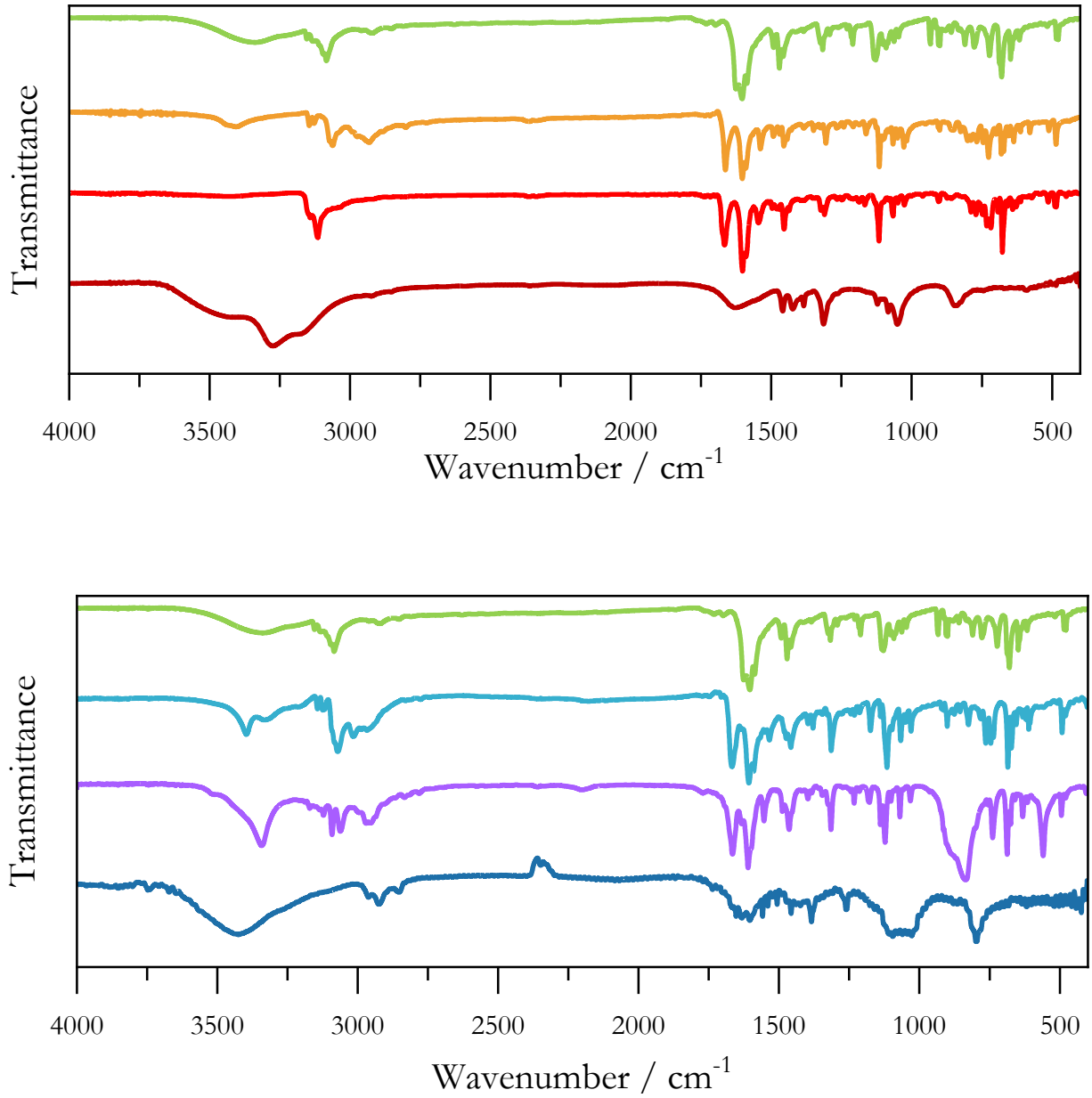

Figure III.16. FT-IR spectra of the molecules along the synthetic steps. In the top spectra, iso-TT (green), iso-TTBnHBr (orange), iso-TTBnHAuCl$_4$ (red), iso-TTBn@AuNPs (brown). In the bottom spectra, iso-TT (green), iso-TTEtnHI (azure), iso-TTEtHPF$_6$ (violet), iso-TTEt@AuNPs (blue).

backbone. This could explain the presence of bands attributed to aromatic C=C and C=N bonds. According to the literature, the effective formation of the C-Au bond can be detected with the presence of some new bands, e.g., around 1300 cm^{-1} or 800 cm^{-1}.[14] While spectra of both samples, reported in **Figure III.16**, present some new bands, the novelty of the ligand complicates unambiguous assignment.

Because of these discrepancies with IR spectra previously reported in the literature, theoretical calculations were performed to assist spectral interpretation.

DFT Simulations

Theoretical calculations were performed to simulate the IR vibrational spectra of the compounds throughout the entire synthetic procedure. DFT simulations of IR spectra were performed using Orca 6.0[15-16] at the r^{2}SCAN-3c level of theory.[17] An Au_{20} cluster served as a model for gold nanoparticles, as it is reported to be an efficient model to study vibrational modes of functionalized nanoparticles,[18] especially in combination with r^{2}SCAN-3c.[19] For each compound, conformer search was performed prior to structure optimization. UCSF ChimeraX 1.9[20-21] equipped with SEQCROW[22] plugin was used to calculate the Boltzmann averaged IR spectra at 298 K of the calculated conformers, applying a FWHM = 8 cm^{-1} and a frequency-scaling linear factor of $1.5 \cdot 10^{-2}$.

Comparing the experimental spectrum of iso-TT with the simulated one (**Figure III.17**) allowed the assignation of the bands around 1600 cm^{-1} to three different vibrational modes of the molecule (calculated at 1582, 1599, and 1602 cm^{-1}), mainly constituted by C=C and C=N stretching. Other intense computed bands, with the relative correspondence in the experimental spectrum, are at 1463 cm^{-1} (experimental 1471 cm^{-1}, C-C and C-N stretching) 1327 and 1317 cm^{-1} (experimental 1324 and 1317 cm^{-1}, on-plane bending) 1133 and 1128 cm^{-1} (experimental 1138 and 1110 cm^{-1}, on-plane bending) 718 and 659 cm^{-1} (experimental 722 and 679 cm^{-1}, out-of-plane bending).

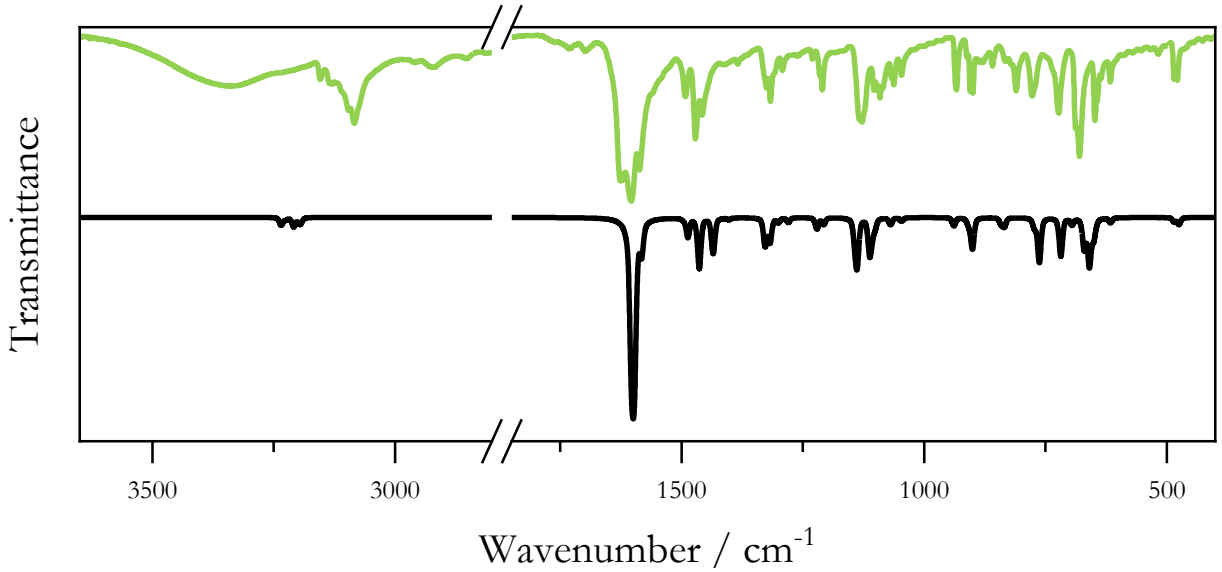

Figure III.17. Comparison of the experimental (green) and simulated (black) IR spectra of iso-TT.

The new band appearing upon N-alkylation, observed at 1663 cm^{-1} in the iso-TTBnHBr spectrum compared with the calculated value of 1664 cm^{-1}, can be attributed to a vibrational mode which mainly involves the substituted imidazolic ring (**Figure III.18**). Reporting herein the values observed for iso-TTBnHBr, additional intense bands are at 1452 cm^{-1} (experimental 1455 cm^{-1}, C-C and C-N stretching), 1306 and 1116 cm^{-1} (experimental 1305 and 1111 cm^{-1}, on-plane bending), 717 cm^{-1} (experimental 726 cm^{-1}, out-of-plane bending).

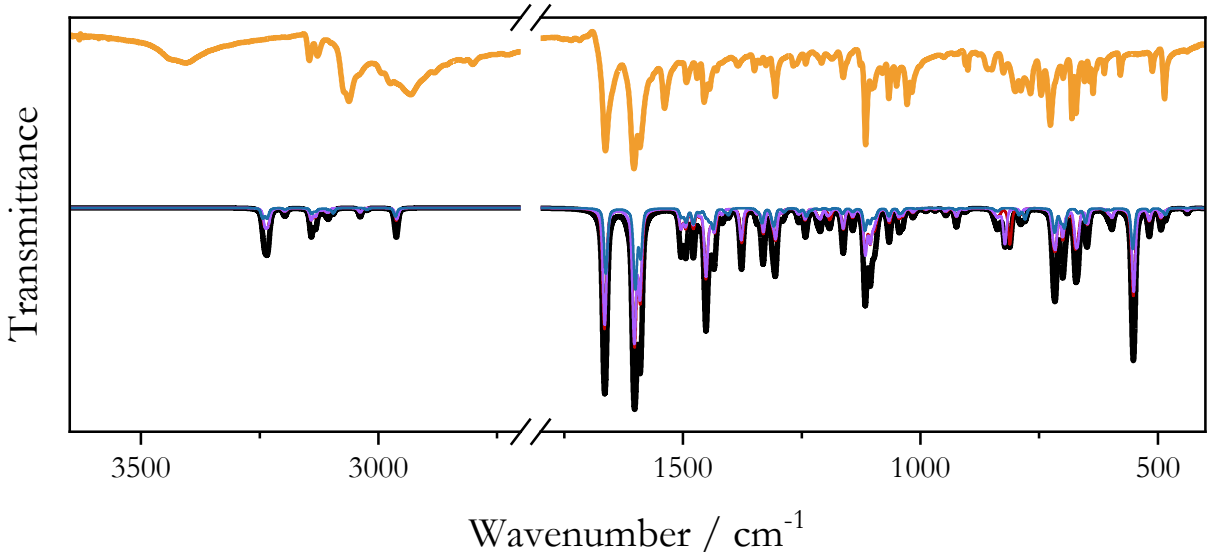

Figure III.18. Comparison of experimental (orange) and simulated (black) IR spectra of iso-TTBnHBr. In red, blue, and violet, the contributions of different conformers to the final simulated spectra.

In the nanoparticles spectrum (**Figure III.19**), the broad band centered at 1620 cm^{-1} can be traced back to three different vibrational modes, calculated at 1666, 1595, and 1566 cm^{-1}, involving the vibration of the iso-TT backbone. Searching for vibrational modes involving the C-Au bond, a strong contribution was detected in the following bands: 1036 cm^{-1} (experimental 1049 cm^{-1}), 1264 cm^{-1} (experimental 1261 cm^{-1}, quite weak) and 1426 cm^{-1} (experimental 1423 cm^{-1}, quite weak) involve C-Au bond stretching; 1391 cm^{-1} (experimental 1385 cm^{-1}) involves the carbenic carbon out of plane bending. Additional intense bands were calculated at 1322 cm^{-1} (experimental 1313 cm^{-1}, on-plane bending of iso-TT) and a broad band at 845 and 833 cm^{-1} (experimental 849 and 822 cm^{-1}, out-of-plane bending of iso-TT).

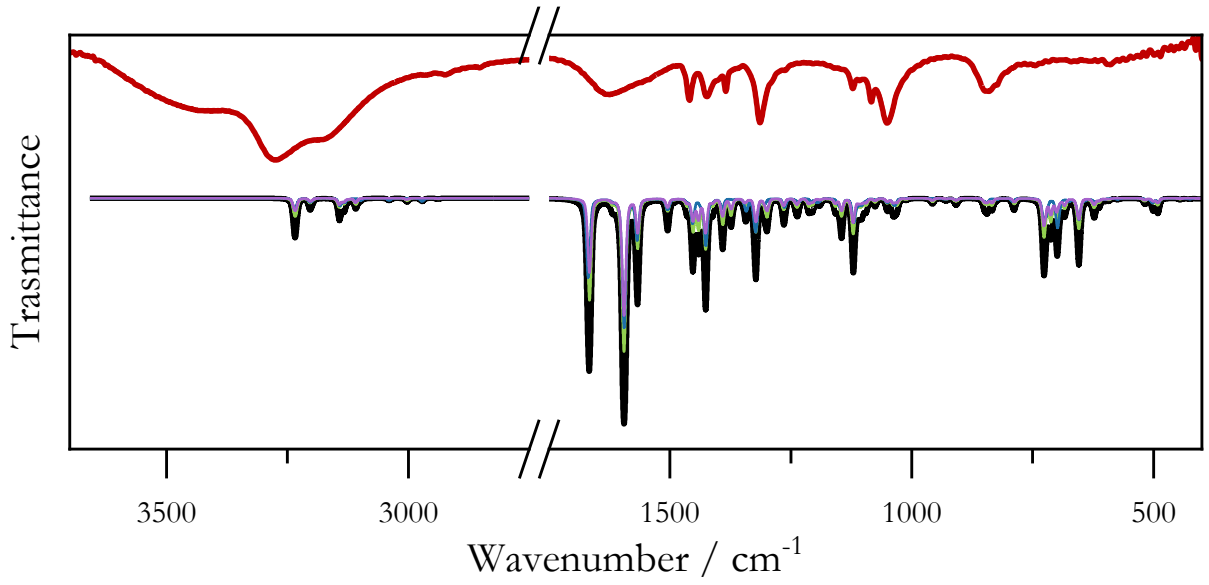

Figure III.19. Comparison of experimental (red) and simulated (black) IR spectra of iso-TTBn@AuNPs. In green, blue, and violet, the contributions of different conformers to the final simulated spectra.

Analogous features were identified for iso-TTEtHI and iso-TTEt@AuNPs (**Figure III.20**): upon N-alkylation, a new band appeared at 1668 cm^{-1}, attributed to the vibrational mode of the N-substituted imidazole ring; in the nanoparticles spectra, a contribution of the C-Au bond was found at 1039 and 1111 cm^{-1} (with a broad band in the experimental spectrum between 990 and 1140 cm^{-1}), 1272 cm^{-1} (experimental 1275 cm^{-1}, shoulder of another band), and 1425 cm^{-1} (experimental 1424 cm^{-1}) for the C-Au bond stretching. The carbenic carbon bending was calculated to have a strong contribution in the vibrations sited at 154, 476, and 610 cm^{-1}. While the first one is outside the range of the IR spectrum, the other two were calculated to be extremely weak. As a result, these bands were absent from the spectrum, where that region was dominated solely by noise.

In conclusion, FT-IR analysis combined with DFT simulations confirms ligand coordination of the nanoparticles surface, helping to clarify the structure of the molecule.

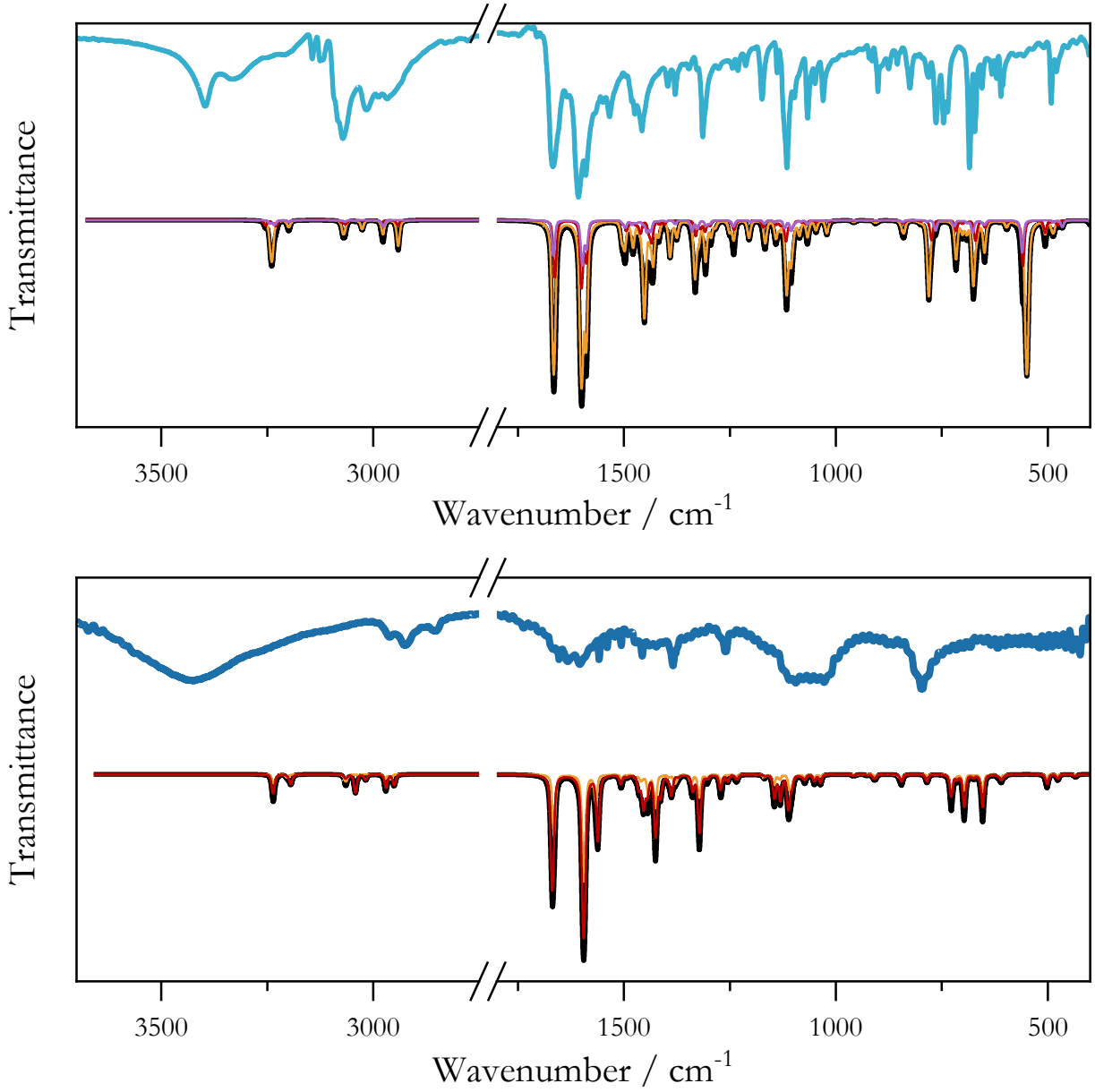

Figure III.20. Top, comparison between experimental (blue) and DFT-simulated (black) IR spectra of iso-TTEtHI. In red, orange, and violet, the contributions of different conformers to the final DFT-simulated spectrum; bottom, comparison between experimental (blue) and DFT-simulated (black) IR spectra of iso-TTEt@AuNPs. In red and orange, the contributions of different conformers to the final DFT-simulated spectrum.

XPS Analysis

X-ray photoelectron spectroscopy (XPS) was used to detect and further investigate the presence of molecules bound on the nanoparticles surface, too. Being a surface analytical technique, XPS is able to detect the presence of molecules bound to the surface of nanomaterials and to determine the chemical state of the analyzed surface. Hence, in the case of NHC-functionalized nanoparticles, XPS is well suited to confirm the presence of carbenes by examining both carbon and gold signals.

To prepare a sample suitable for the analysis, nanoparticles were washed multiple times, and a concentrated suspension was drop-casted onto a glass slide. Survey analysis revealed no detectable signal deriving from the presence of boron, halides, and phosphorous, thus confirming the absence of strong electrostatic interactions between the nanoparticles and ions, also supporting the neutral-charge nature of the ligand.

High-resolution spectra were analyzed with XPSPeak 4.1 to deconvolute the presence of multiple contributions. The typical doublet of f-type orbitals deriving from Au 4f electrons (**Figure III.21**), characterized by a spin-orbit coupling of 3.7 eV, can be properly fitted with three peaks. The resulting binding energies of Au $4f_{7/2}$ peak at 84.0 eV, 85.3 eV and 87.0 eV (referred to a graphitic C 1s binding energy of 295.0 eV) correspond to the contributions of Au^0, Au^+ and Au^{3+} species, respectively. While Au^0 contribution derives from the metallic nanoparticles, Au^+ signals is consistent with surface gold atoms interacting with NHC ligands, since the Au-carbene interaction can modify the gold oxidation

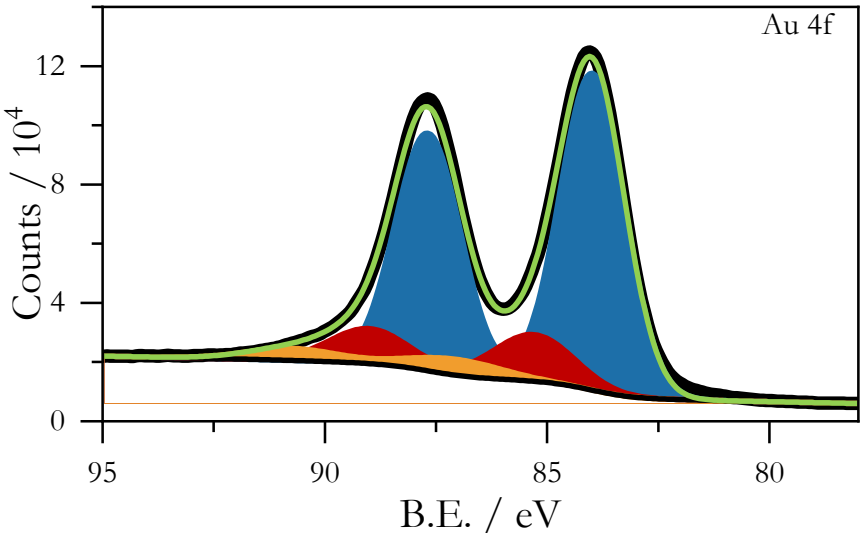

Figure III.21. High-resolution XPS spectrum of Au 4f of iso-ttBn@AuNPs. In black, raw data and background; blue, Au(0) contribution; red, Au(I) contribution; yellow, Au(III) contribution; green, sum of all the contributions.

state, as well documented in the literature.[23-24] Worth mentioning, survey spectra did not detect traces of chlorides, bromides, hexafluorophosphates, or any other possible anion working as a counterion of Au(I) species, thus excluding the presence of adsorbed Au(I)–carbene complexes. The last peak attributed to Au^{3+} likely arises from partial surface oxidation during exposure to the X-ray beam. **Table III.1** reports the binding energy values of the Au $4f_{7/2}$ peak detected on iso-TTEt@AuNPs and iso-TTBn@AuNPs.

Table III.1. Binding energies of Au $4f_{7/2}$ peak on iso-TTEt@AuNPs and iso-TTBn@AuNPs.

	Au $4f_{7/2}$ Binding Energy / eV	
Species	**iso-TTEt@AuNPs**	**iso-TTBn@AuNPs**
Au(0)	84.1	84.0
Au(I)	85.3	85.3
Au(III)	87.1	87.0

In the C 1s region, a dominant peak at 285.0 eV, deriving from the unsubstituted carbon atom, was accompanied by multiple contributions consistent with the different types of carbon atom present in the triimidazotriazine. Importantly, a low-binding-energy component (284.0 ± 0.1 eV) appeared in both

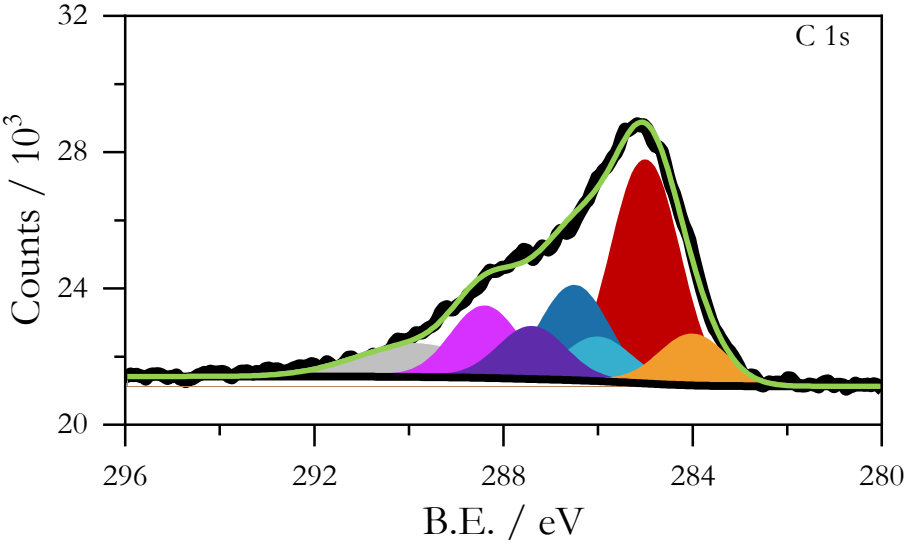

Figure III.22. High-resolution C1s spectra of iso-TTBn@AuNPs. In black, raw data and background; red, signal from graphitic carbon; orange, signal from the carbenic carbon; green, sum of all the contributions.

nanoparticle samples. This peak is typical of carbenic carbon, further confirming carbene coordination to the nanoparticles surface.

All the contributions and the respective binding energies present in the sample are reported in **Table III.2**

Table III.2. Binding energy of C 1s peak of iso-TT, iso-TTEt@AuNPs, and iso-TTBn@AuNPs.

	C 1s Binding Energy / eV		
Species	**iso-TT**	**iso-TTEt@AuNPs**	**iso-TTBn@AuNPs**
N_2-C-Au	/	284.0	284.0
C-C and C-H	285.0	285.0	285.0
C-N aliphatic	/	286.0	286.0
C-N aromatic	286.4	286.5	286.5
N-C-N aromatic	287.5	287.4	287.4
$C(N)_3$ melamine-like	288.4	288.4	288.4

Catalytic Application

As discussed in Chapter 0, the model reaction selected for catalytic evaluation was the reduction of nitrobenzene. Under the mild conditions examined, hydrazine proved to be ineffective as a reducing agent. Therefore, sodium borohydride, widely reported as suitable for Au-NP-catalysed nitrogroup reduction,[25-27] was employed.

Catalytic activity was initially assessed using unsupported functionalized nanoparticles in methanol, employing a substrate-to-reductant molar ratio of 1 : 10 and 1% mol in gold of catalyst. Prior to use, the nanoparticles suspension was centrifuged and redispersed in fresh methanol to remove residual byproducts. More details can be found in the experimental section (Chapter VII).

Results (**Table III.3**) show that both materials were highly active in the reduction of nitrogroup, even though with different performances. While iso-TTEt@AuNPs displayed declining selectivity and yield over consecutive runs, iso-TTBn@AuNPs maintained higher selectivity and yield, although some variability in conversion and selectivity was observed for both catalysts. To improve catalytic behaviour,

the carbene-functionalized nanoparticles were deposited onto various supports, including activated carbon (X40S), titania, alumina, and ceria.

Table III.3. Results of the catalytic test performed with the two types of unsupported nanoparticles.

Catalyst	Use	Conversion / %	Selectivity / %	Yield / %
iso-TTEt@AuNPs	1	93	56	52
	2	88	50	44
	3	85	54	46
	4	92	27	25
iso-TTBn@AuNPs	1	99	85	84
	2	>99	>99	>99
	3	89	35	31
	4	96	87	84

In this work, materials are named after the ligand type and support. Accordingly, nanoparticles functionalized with the ethyl-substituted iso-TT supported on titania are named iso-TTEt@AuNPs/TiO_2, while nanoparticles functionalized with the benzyl substituted iso-TT supported on ceria are labeled iso-TTBn@AuNPs/CeO_2.

While iso-TTEt@AuNPs performed best when supported on ceria or titania, iso-TTBn@AuNPs were best-performing when supported on carbon or titania. Other combinations resulted in materials achieving low conversion, selectivity, and yield from the first catalytic cycle.

Catalysts were then subject to five consecutive reuse cycles, washing the catalyst with methanol between runs. Both iso-TTEt@AuNPs/CeO_2 and iso-TTBn@AuNPs/X40S maintained good activity over the first three reaction runs, but lost performance thereafter. In contrast, both catalysts supported on titania exhibited no significant loss of activity across all five runs.

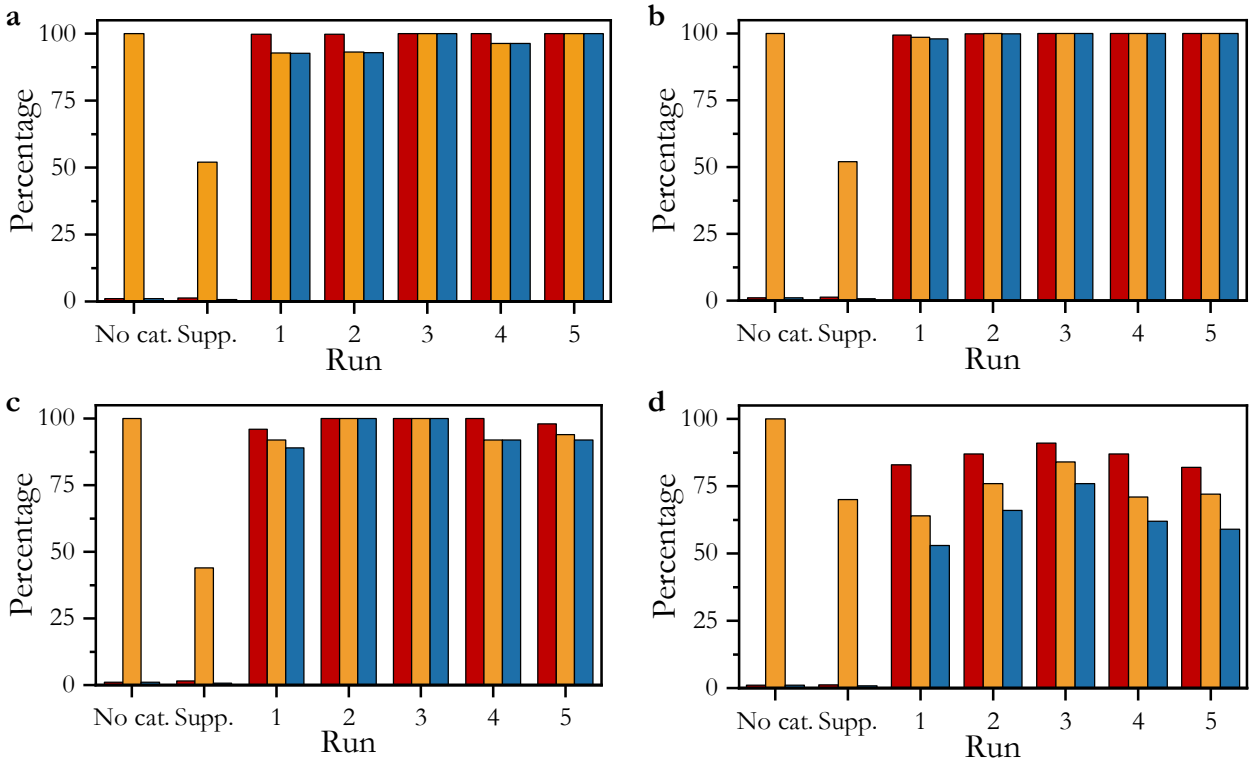

Figure III.23. Comparison of catalytic results of the most performing materials. a) iso-TTEt@AuNPs/TiO_2; b) iso-TTBn@AuNPs/TiO_2; c) iso-TTEt@AuNPs/CeO_2; d) iso-TTBn@AuNPs/X40S. Conversion in red, selectivity in yellow, yield in blue.

Control experiments performed without catalyst or with support alone showed negligible aniline formation, combined with less than 2% conversion of nitrobenzene, confirming the catalytic role of the gold nanoparticles (**Table III.4**).

Table III.4. Summary of the catalytic tests performed with the two types of functionalized nanoparticles, iso-TTEt@AuNPs and iso-TTBn@AuNPs, supported on activated carbon (X40S), titania, alumina, and ceria.

Catalyst	Use	Conversion / %	Selectivity / %	Yield / %
No cat.	/	1	>99	1
TiO_2	/	1	52	<1
X40S	/	1.2	70	<1
CeO_2	/	1.5	44	<1

Catalyst	Use	Conversion / %	Selectivity / %	Yield / %
iso-TTEt@AuNPs/X40S	1	81	20	16
	2	97	45	44
	3	98	47	46
	4	>99	33	33
	5	>99	92	92
iso-TTEt@AuNPs/CeO_2	1	96	92	89
	2	>99	>99	>99
	3	>99	>99	>99
	4	>99	92	92
	5	98	94	92
iso-TTEt@AuNPs/Al_2O_3	1	31	3	1
	2	2	80	2
	3	90	<1	<1
	4	36	8	3
	5	20	15	3
iso-TTEt@AuNPs/TiO_2	1	>99	93	93
	2	>99	93	93
	3	>99	>99	>99
	4	>99	96	96
	5	>99	>99	>99
iso-TTBn@AuNPs/X40S	1	83	64	53
	2	87	76	66
	3	91	84	76
	4	87	71	62
	5	82	72	59

Catalyst	Use	Conversion / %	Selectivity / %	Yield / %
iso-TTBn@AuNPs/CeO_2	1	79	69	54
	2	84	35	29
	3	88	30	27
	4	83	37	31
	5	83	38	32
iso-TTBn@AuNPs/Al_2O_3	1	96	24	24
	2	88	29	26
	3	87	27	23
	4	86	25	22
	5	95	14	13
iso-TTBn@AuNPs/TiO_2	1	>99	98	98
	2	>99	>99	>99
	3	>99	>99	>99
	4	>99	>99	>99
	5	>99	>99	>99

The stable and, at times, growing activity with subsequent reaction runs points to pronounced stability of the heterogeneous catalyst. As it happens for example with sol-gel entrapped organo-catalyst,[28] the entrapped Au-based nanoparticles upon use become even more accessible to external reactants which may explain the slight enhancement in reactivity of the heterogenized catalyst.

At last, a catalyst comprised of unprotected gold nanoparticles, synthesized by reducing $HAuCl_4$ with $NaBH_4$ without carbenes and supported on titania, was prepared and tested. Under identical conditions, this catalyst was slightly less performing than the catalysts with carbene, affording 92% yield in aniline when compared to 93% and 98% of iso-TTEt@AuNPs/TiO_2 and iso-TTBn@AuNPs/TiO_2, respectively. Further differences emerged by lowering the amount of the reducing agent. Passing from 10 to 5 equivalents of $NaBH_4$, the yield of non-functionalized nanoparticles dropped to 58%, whereas both carbene-functionalized versions retained yields above 90%. The complete results are reported in **Table III.5**.

Table III.5. Summary of the catalytic tests performed with non-functionalized AuNPs and functionalized nanoparticles, iso-TTEt@AuNPs and iso-TTBn@AuNPs, supported on titania, by varying the amount of reducing agent.

Catalyst	$NaBH_4$ eq.	Conversion / %	Selectivity / %	Yield / %
AuNPs/TiO_2	10	>99	92	92
	5	99	58	58
	2	86	2	2
	1	50	<1	<1
iso-TTEt@AuNPs/TiO_2	10	>99	96	96
	5	>99	97	97
	2	99	15	15
	1	59	<1	<1
iso-TTBn@AuNPs/TiO_2	10	>99	>99	>99
	5	>99	>99	>99
	2	86	1	1
	1	67.8	<1	<1

Comparison with some work from the literature reveals that the catalysts developed here are generally more efficient. Thomas et al.[25] report that unsupported gold nanoparticles functionalized with 1-butyl-3-propylsulphonate imidazole can reduce p-nitrophenol in water with 100% conversion by employing 100 equivalents of $NaBH_4$. Under similar conditions, Eisen et al.[29] achieved 99% conversion with 15 equivalents of $NaBH_4$ using gold nanoparticles bound in an NHC-functionalized hyper-crosslinked polymer. Fountoulaki et al.[27] reported 95% nitrobenzene conversion with 6 equivalents of $NaBH_4$ employing gold nanoparticles supported on mesoporous titania. In contrast, the catalysts developed in this work achieved 99% conversion using only 5 equivalents of $NaBH_4$, demonstrating substantially

enhanced efficiency. It is also worth to mention, data reported from other works refer to the conversion parameter. Most of the papers monitor the nitrobenzene depletion employing UV-vis, calculating the conversion via the disappearing of one nitrobenzene absorption peak. With this methodology, no analysis of possible byproducts is performed, giving no information about the selectivity of the reaction. In comparison, when supported on titania, NHC-functionalized gold nanoparticles are highly selective toward aniline with high recyclability, without losing catalytic performances.

Bibliography

1. Buck, D. M.; Kunz, D., Triazine Annelated NHC Featuring Unprecedented Coordination Versatility. *Organometallics* **2015,** *34* (21), 5335–5340.
2. Melnic, E.; Kravtsov, V. C.; Lucenti, E.; Cariati, E.; Forni, A.; Siminel, N.; Fonari, M. S., Regulation of π···π stacking interactions between triimidazole luminophores and comprehensive emission quenching by coordination to Cu(II). *New Journal of Chemistry* **2021,** *45* (20), 9040–9052.
3. Fonari, M. S.; Kravtsov, V. C.; Bold, V.; Lucenti, E.; Cariati, E.; Marinotto, D.; Forni, A., Structural Landscape of Zn(II) and Cd(II) Coordination Compounds with Two Isomeric Triimidazole Luminophores: Impact of Crystal Packing Patterns on Emission Properties. *Crystal Growth & Design* **2021,** *21* (7), 4184–4200.
4. Magni, M.; Lucenti, E.; Previtali, A.; Mussini, P. R.; Cariati, E., Electrochemistry of cyclic triimidazoles and their halo derivatives: A casebook for multiple equivalent centers and electrocatalysis. *Electrochimica Acta* **2019,** *317*, 272–280.
5. Malpicci, D.; Araneo, S. R.; Arnaboldi, S.; Cariati, E.; Forni, A.; Grecchi, S.; Lucenti, E.; Marinotto, D.; Maver, D.; Mussini, P. R., Electrochemical insight on the nitrogen-rich, weakly aromatic cyclic triimidazole multifunctional system expanded with pyridine or thiophene terminals. *Electrochimica Acta* **2023,** *469*.
6. Schubert, D. M.; Natan, D. T.; Wilson, D. C.; Hardcastle, K. I., Facile Synthesis and Structures of Cyclic Triimidazole and Its Boric Acid Adduct. *Crystal Growth & Design* **2011,** *11* (3), 843–850.
7. Serpell, C. J.; Cookson, J.; Thompson, A. L.; Brown, C. M.; Beer, P. D., Haloaurate and halopalladate imidazolium salts: structures, properties, and use as precursors for catalytic metal nanoparticles. *Dalton Transactions* **2013,** *42* (5), 1385–93.
8. Bridonneau, N.; Hippolyte, L.; Mercier, D.; Portehault, D.; Desage-El Murr, M.; Marcus, P.; Fensterbank, L.; Chaneac, C.; Ribot, F., N-Heterocyclic carbene-stabilized gold nanoparticles with tunable sizes. *Dalton Transactions* **2018,** *47* (19), 6850–6859.
9. Uson, R.; Laguna, A.; Laguna, M.; Briggs, D. A.; Murray, H. H.; Fackler, J. P., (Tetrahydrothiophene)Gold(I) or Gold(III) Complexes. In *Inorganic Syntheses*, 1989; pp 85–91.
10. Mather, J. C.; Wyllie, J. A.; Hamilton, A.; Soares da Costa, T. P.; Barnard, P. J., Antibacterial silver and gold complexes of imidazole and 1,2,4-triazole derived N-heterocyclic carbenes. *Dalton Transactions* **2022,** *51* (32), 12056–12070.
11. Doebelin, N.; Kleeberg, R., Profex: a graphical user interface for the Rietveld refinement program BGMN. *Journal of Applied Crystallography* **2015,** *48* (5), 1573–1580.
12. Mao, L.; Pan, W.; Fu, Y.; Chen, L.; Xu, M.; Ren, Y.; Feng, W.; Yuan, L., Reversibly Tunable Lower Critical Solution Temperature Behavior Induced by H-Bonded Aromatic Amide Macrocycle and Imidazolium Host-Guest Complexation. *Organic Letters* **2017,** *19* (1), 18–21.
13. Nicholls, T. P.; Jia, Z.; Chalker, J. M., Electrochemical Synthesis of Gold-N-Heterocyclic Carbene Complexes. *Chemistry* **2024,** *30* (2), e202303161.
14. Jensen, I. M.; Chowdhury, S.; Hu, G.; Jensen, L.; Camden, J. P.; Jenkins, D. M., Seeking a Au-C stretch on gold nanoparticles with ^{13}C-labeled N-heterocyclic carbenes. *Chemical Communications* **2023,** *59* (98), 14524–14527.
15. Neese, F., The ORCA program system. *WIREs Computational Molecular Science* **2012,** *2* (1), 73–78.
16. Neese, F., Software update: the ORCA program system, version 5.0. *WIREs Computational Molecular Science* **2022,** *12* (1), e1606.
17. Grimme, S.; Hasen, A.; Helert, S.; Mewes, J.-M., r^{2}SCAN-3c: A "Swiss army knife" composite electronic-structure method. *The Journal of Chemical Physics* **2021,** *154*.
18. Jensen, L.; Aikens, C. M.; Schats, G. C., Electronic structure methods for studying surface-enhanced Raman scattering. *Chemical Society Reviews* **2008,** *37* (5), 1061–1073.
19. Kuster, L.; Belanger-Bouliga, M.; Shaw, T. E.; Jurca, T.; Nazemi, A.; Frenette, M., Insight into the nature of carbon-metal bonding for N-heterocyclic carbenes in gold/silver complexes and

nanoparticles using DFT-correlated Raman spectroscopy: strong evidence for pi-backbonding. *Nanoscale* **2024,** *24*, 11052–11068.
20. Goddard, T. D.; Huang, C. C.; Meng, E. C.; Pettersen, E. F.; Couch, G. S.; Morris, J. H.; Ferrin, T. E., UCSF ChimeraX: Meeting modern challenges in visualization and analysis. *Protein Science* **2018,** *27* (1), 14–25.
21. Meng, E. C.; Goddard, T. D.; Pettersen, E. F.; Couch, G. S.; Pearson, Z. J.; Morris, J. H.; Ferrin, T. E., UCSF ChimeraX: Tools for structure building and analysis. *Protein Science* **2023,** *32* (11), e4792.
22. Schaefer, A. J.; Ingman, V. M.; Wheeler, S. E., SEQCROW: A ChimeraX bundle to facilitate quantum chemical applications to complex molecular systems. *Journal of Computational Chemistry* **2021,** *42* (24), 1750–1754.
23. Young, A. J.; Sauer, M.; Rubio, G.; Sato, A.; Foelske, A.; Serpell, C. J.; Chin, J. M.; Reithofer, M. R., One-step synthesis and XPS investigations of chiral NHC-Au(0)/Au(I) nanoparticles. *Nanoscale* **2019,** *11* (17), 8327–8333.
24. Ye, R.; Zhukhovitskiy, A. V.; Kazantsev, R. V.; Fakra, S. C.; Wickemeyer, B. B.; Toste, F. D.; Somorjai, G. A., Supported Au Nanoparticles with N-Heterocyclic Carbene Ligands as Active and Stable Heterogeneous Catalysts for Lactonization. *Journal of the American Chemical Society* **2018,** *140* (11), 4144–4149.
25. Thomas, S. R.; Yang, W.; Morgan, D. J.; Davies, T. E.; Li, J. J.; Fischer, R. A.; Huang, J.; Dimitratos, N.; Casini, A., Bottom-up Synthesis of Water-Soluble Gold Nanoparticles Stabilized by N-Heterocyclic Carbenes: From Structural Characterization to Applications. *Chemistry* **2022,** *28* (56), e202201575.
26. Eisen, C.; Chin, J. M.; Reithofer, M. R., Catalytically Active Gold Nanomaterials Stabilized by N-heterocyclic Carbenes. *Chemistry - An Asian Journal* **2021,** *16* (20), 3026–3037.
27. Fountoulaki, S.; Daikopoulou, V.; Gkizis, P. L.; Tamiolakis, I.; Armatas, G. S.; Lykakis, I. N., Mechanistic Studies of the Reduction of Nitroarenes by $NaBH_4$ or Hydrosilanes Catalyzed by Supported Gold Nanoparticles. *ACS Catalysis* **2014,** *4* (10), 3504–3511.
28. Ciriminna, R.; Bolm, C.; Fey, T.; Pagliaro, M., Sol-Gel Ormosils Doped with TEMPO as Recyclable Catalysts for the Selective Oxidation of Alcohols. *Advanced Synthesis & Catalyis* **2002,** *344* (2).
29. Eisen, C.; Ge, L.; Santini, E.; Chin, J. M.; Woodward, R. T.; Reithofer, M. R., Hyper crosslinked polymer supported NHC stabilized gold nanoparticles with excellent catalytic performance in flow processes. *Nanoscale Advances* **2023,** *5* (4), 1095–1101.

IV. CATALYSTS FOR HYDROGEN SPILLOVER

The NHC-protected gold nanoparticles developed in the previous Chapter 0 were also employed in the functionalization of materials designed for the investigation of hydrogen spillover. This part of the research was conducted in collaboration with Professor Bert Chandler and his group at Penn State University, Pennsylvania, USA, where I spent 6 months.

As better explained in the Introduction chapter (Chapter I), hydrogen spillover is a phenomenon consisting of highly movable hydrogen atom equivalents moving on the surface of the catalyst. the catalyst. Hydrogen activation and spillover phenomena are routinely studied by the Chandler group using in situ FT-IR spectroscopy. The primary catalyst used in this study consisted of gold nanoparticles supported on titania (rutile phase), although a comparison with a gold-on-alumina catalyst was also performed.

Their selection was motivated by fundamental differences in their capacity to host spillover hydrogen. Among the different types of titania available, rutile is the one that can accept a higher amount of hydrogen spillover. In contrast, γ-Al_2O_3 does not promote hydrogen migration, thereby serving as a non-spillover reference system. Gold was selected as the active metal owing to its intrinsically high barrier for homolytic H_2 dissociation on metallic Au sites. Nevertheless, previous studies have demonstrated that heterolytic dissociation can occur at the MSI, thereby generating activated hydrogen species capable of migrating onto suitable support surfaces.

The combination of these materials gives origin to two catalysts: Au/TiO_2, able to activate hydrogen at the MSI and to generate hydrogen spillover on the support surface; Au/Al_2O_3, able to activate hydrogen at the MSI but unable to generate hydrogen spillover, thereby confining activated hydrogen in the MSI.

Synthesis and Characterization

Since the presence of MSI is fundamental for hydrogen activation,[1-2] a synthetic strategy different from that previously reported for NHC@AuNPs (Chapter III) was adopted. The deposition of pre-formed, ligand-stabilized nanoparticles onto a support does not guarantee the formation of strong metal-support interactions nor a high number of MSI atoms.

Therefore, both Au/TiO_2 and Au/Al_2O_3 catalysts were synthesized via the urea-assisted precipitation-deposition method, which promotes intimate metal–support contact. Tetrachloroauric acid was used as gold source and combined with the chosen support in aqueous suspension, following the standard

procedure illustrated in **Figure IV.1**. Heating this mixture at 80 °C caused the slow decomposition of urea, releasing ammonia and CO_2. The pH increase by ammonia formation triggered the precipitation of Au(III) hydroxide onto the support surface.

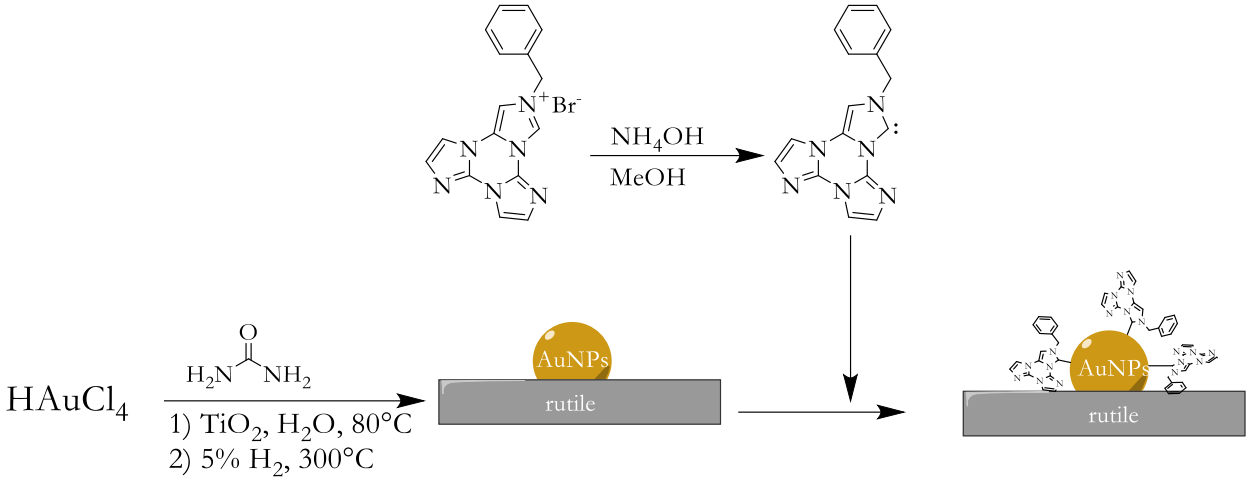

Figure IV.1. Scheme for the preparation of carbene-functionalized catalyst.

Once the precipitation was concluded, the solid was recovered by centrifugation and washed multiple times with MilliQ water, to ensure complete removal of chloride ions. This is necessary because chloride is known to inhibit hydrogen activation by binding strongly at MSI sites. The absence of chloride in the supernatant was confirmed via $AgNO_3$ test. The washed solid was subsequently reduced in a tube furnace under 5% H_2 in Ar at 300 °C to generate metallic Au nanoparticles.

Starting from the Au/TiO_2 catalyst, five different materials were studied: the pristine catalyst obtained after gold reduction, three NHC-functionalized catalysts with different carbene loadings, and a control catalyst subjected to the same functionalization procedure in the absence of the carbene precursor.

For carbene grafting, the precursor iso-TTBnHBr was dissolved in methanol, and thereafter degassed under nitrogen. Ammonia was then added, followed by the proper amount of pristine catalyst. Adsorption progress was monitored by UV-vis spectroscopy of the supernatant (**Figure IV.2**).

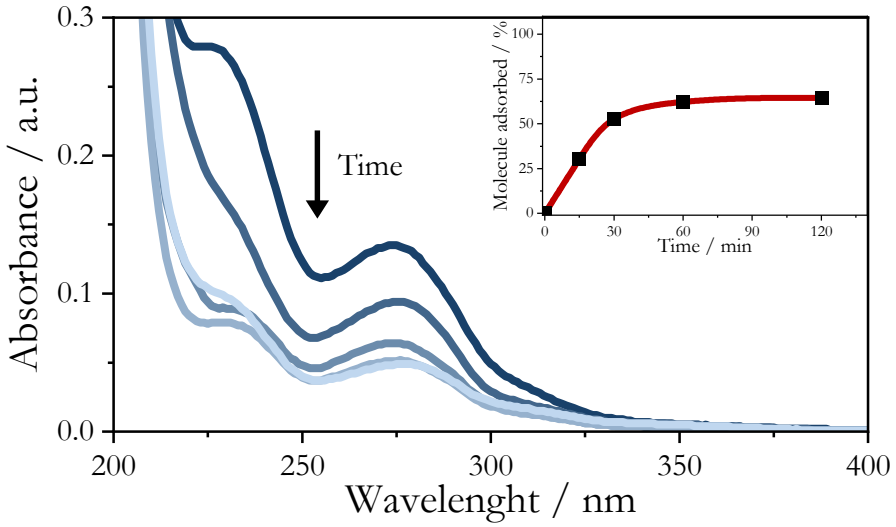

Figure IV.2. Monitoring of carbene adsorption from the solution employing UV-vis spectroscopy; from dark blue, spectrum of initial solution, to light blue, spectrum after one and a half hours. Inset, amount of carbene adsorbed over time.

Once the absorption was complete, the solid was centrifuged and washed repeatedly with water to remove bromide anions. Again, $AgNO_3$ test was performed to check for the presence of bromide. During the first three washing steps, UV-vis spectra of the supernatants were collected to verify that no carbene species detached from the functionalized catalysts. No traces were found.

The amount of adsorbed carbene was calculated from the difference between the initial ligand concentration and that remaining after the first centrifugation. The final carbene loadings on the three different catalysts are 0.095 %, 0.032 % and 0.013 % w/w.

The use of ammonia as deprotonating agent for generating carbenes is quite unusual. Anyway, it is proven that also acetate,[3-4] another unconventional deprotonating agent, enables the synthesis of Arduengo carbene complexes. Having $pK_b = 4.74$, ammonia is a stronger base than acetate ($pK_b = 9.25$), thus ensuring efficient precursor deprotonation.

Two control experiments were carried out to verify the effective adsorption of carbene species onto the gold surface.

In the first one, a sample of rutile was suspended in methanol with ammonia and iso-TTBnHBr. After two hours, no loss of ligand from the solution is detected, showing that the presence of gold is fundamental for the binding of carbenes, and no adsorption occurs on the rutile surface.

In the second one, the adsorption procedure was attempted without ammonia to avoid carbene formation and to check whether iso-TTBnHBr, as well, can bind to gold nanoparticles . Already after 15 minutes, ligand consumption was detected. The broadening of the absorption peaks was also observed, shifting the shape of the absorption spectra to the one previously observed in basic solutions. We attribute this behavior to the presence of basic sites on rutile surface.

More into the details, the rutile used[5] has a surface area of 34 m^2/g, an acidic hydroxyls density of 1.16 $_a$Ti-OH/nm^2 and a basic hydroxyls density of 1.34 $_b$Ti-OH/nm^2. Together, it gives $4.56 \cdot 10^{19}$ $_b$Ti-OH/g. The experiment was performed on 100 mg of rutile ($7.57 \cdot 10^{-6}$ mol $_b$ and $5.06 \cdot 10^{-7}$ mol of ligand precursor. This gives a ligand-to-basic-site ratio of about 1:15.

The rutile used has a measured pK_b of $_b$Ti-OH equal to 9.28, comparable with the pK_b of acetate (9.25). Given the large excess of basic sites, it is reasonable to attribute the observed ligand adsorption to the deprotonation of the ligand precursor by the basic sites on rutile.

Having ascertained this, ammonia was anyway retained in all syntheses to avoid pH-induced spectral modifications that would compromise accurate ligand quantification..

The gold on titania catalyst was analyzed at the TEM to calculate the nanoparticles' diameter distribution. The analysis of over 700 nanoparticles gives an average diameter of 4.4 ± 1.5 nm. Starting from the diameter distribution of nanoparticles, and assuming a cuboctahedra nanoparticle shape, the fraction of perimetral gold atoms and, therefore, the number of potential active sites in the MSI was computed. The equation used is the following:

$$\%Au_{per} = \frac{24 m_{au}}{5 D_p^2 \cdot r_{Au} \cdot \rho_{Au} \cdot \sqrt{2}} \cdot 100 \qquad \textit{Equation IV.1}$$

In a similar way, the amount of surface gold can be calculated with the following equation:

$$\%Au_{surf} = \frac{12 m_{Au} \cdot (3 + \sqrt{3})}{5 \pi D_p \cdot r_{Au}^2 \cdot \rho_{Au} \cdot \sqrt{2}} \cdot 100 \qquad \textit{Equation IV.2}$$

Where:

- m_{Au} is the mass of a single Au atom ($3.27 \cdot 10^{-25}$ kg/atom)
- D_p is the circumsphere diameter of a cuboctahedral particle (in meters, from TEM)
- r_{Au} is the atomic radius of Au ($1.66 \cdot 10^{-10}$ m/atom)
- ϱ_{Au} is the bulk density of Au (19300 kg/m^3)

Calculating such parameters using the mean nanoparticle diameter from a broad distribution of nanoparticles introduces significant errors due to the non-linear relationship between $\%Au_{per}$, $\%Au_{surf}$, and D_p. Hence, these parameters are calculated across the entire nanoparticle size histogram, considering more than 400 nanoparticles in each sample. For the perimeter site density determination, a bin size of 0.25 nm was used, with parameters calculated based on the center of each bin. These values were then multiplied by their respective bin counts and averaged to estimate the weighted average $\%Au_{per}$ and $\%Au_{surf}$ of the sample.

From these values, the amount of perimetral and surface gold atoms in moles per gram of catalyst was calculated using the following equations:

$$Au_{per} = \frac{\%Au \cdot \%Au_{per} \cdot 10^{-6}}{MW_{Au}} \qquad \textit{Equation IV.3}$$

$$Au_{surf} = \frac{\%Au \cdot \%Au_{surf} \cdot 10^{-6}}{MW_{Au}} \qquad \textit{Equation IV.4}$$

The results for Au/TiO_2 and Au/Al_2O_3 catalysts are reported in **Table IV.1**.

Table IV.1. Au_{per} and Au_{surf} parameters calculated for Au/TiO_2 and Au/Al_2O_3 catalysts.

Catalyst	**Au_{per} / %**	**Au_{per} / mol/g_{cat}**	**Au_{surf} / %**	**Au_{surf} / mol/g_{cat}**
3.5% Au/TiO_2	2.54	$4.52 \cdot 10^{-6}$	39.3	$6.99 \cdot 10^{-5}$
5% Au/Al_2O_3	7.38	$1.87 \cdot 10^{-6}$	68.2	$1.22 \cdot 10^{-4}$

Using these values, the ratio of carbene molecules to gold surface atoms was estimated. For the 0.095% carbene loading sample, one carbene molecule per 21 surface gold atoms was calculated.

For comparison, unsupported nanoparticles were synthesized in the same way as discussed in Chapter 0. After washing them with methanol and evaporating the solvent to dryness, TGA was performed to measure the mass loss due to decomposition of the carbenes on the surface (**Figure IV.3**). Performing a similar data analysis, one carbene molecule every 24 gold surface atoms was calculated.

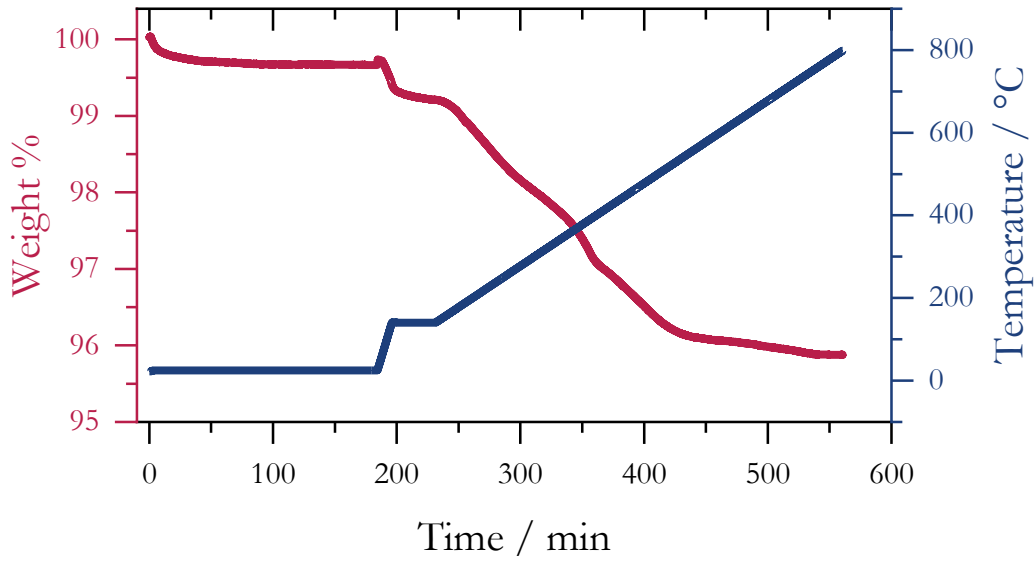

Figure IV.3. TGA trace of unsupported iso-TTBn@AuNPs. Purple, weight variation over time; blue, temperature variation over time.

Noteworthy, these values are quite similar to the supported systems, suggesting an intrinsic upper limit to carbene coverage .

In terms of number of carbene molecules per nanoparticle, the loading corresponds to approximately eight NHC molecule per nanoparticle. This number looks quite low, even though the molecules are quite bulky. This may be consistent with preferential binding to undercoordinatedcorner atoms,[6] rather than to all surface sites. Accordingly, the possible binding sites are only a fraction of all surface gold atoms.

To detect carbene species on the functionalized materials, two different analytical approaches were adopted: diffuse-reflectance UV-vis and FT-IR. The first one was used to search for differences in the absorption spectra of the catalyst before and after carbene adsorption. In this case, only few differences in the UV-region , were observed., more specifically in correspondence with the absorption band of rutile. Consequently, discriminating between rutile and carbene contributions was particularly difficult. Because of this, the use this technique did not prosecute.

Even FT-IR spectra proved challenging, due to both low carbene loading and signal overlapping with the catalyst itself, such as the crystal lattice vibrations, adsorbed water, hydrocarbons adsorbed from the atmosphere, and carbonates. These bands overlap with those of carbenes, making it complicated to understand their origin.

Heating a catalyst pellet from room temperature to 120°C, and using the pellet spectrum as a background, the clearest evidence of carbene retention emerged (**Figure IV.4**). Upon dehydration and thermal equilibration, new bands were observed. Comparing this spectrum with isoTTBnHBr and isoTTBn@AuNPs ones, the same pattern as carbene functionalized gold nanoparticles was observed, which is completely different from the carbene precursor spectrum. This not only provides further evidence for the presence of a carbene, but also confirms that the species bound to the catalyst is the carbene rather than the imidazolium salt.

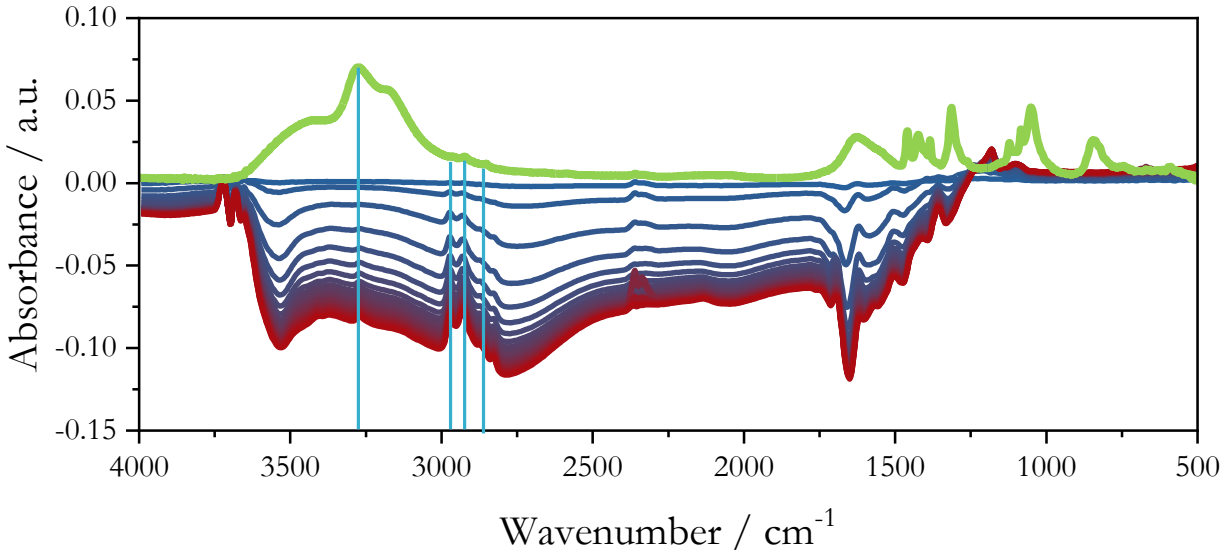

Figure IV.4: Variation of absorption spectra of carbene-functionalized catalyst while heating up from 30 °C (blue) to 120 °C (red). In green, absorption spectrum of iso-TTBn@AuNPs, showing correlations among the peak positions for the two samples.

Arrhenius Analysis

The catalytic materials were first evaluated through Arrhenius analysis to measure kinetic constants for hydrogen activation and to extrapolate the corresponding apparent activation energy .

As detailed in the experimental section (Chapter VII), before any measurement, each pellet underwent a standardized pretreatment to remove strongly adsorbed oxygen species (SAO) from the titania surface. Following this step, the sample was cooled down to the target temperature, and held under inert gas until the equilibration of surface water was achieved. This procedure is critical for ensuring data reproducibility, as the presence of surface water significantly influences the measured apparent activation energy[7-8] obtained from the measurements. The hydrogen adsorption measurement procedure was previously optimized by colleagues for Penn State University who concluded that, with a 40 mL/min gas flow, the process is not limited by mass transfer effect.

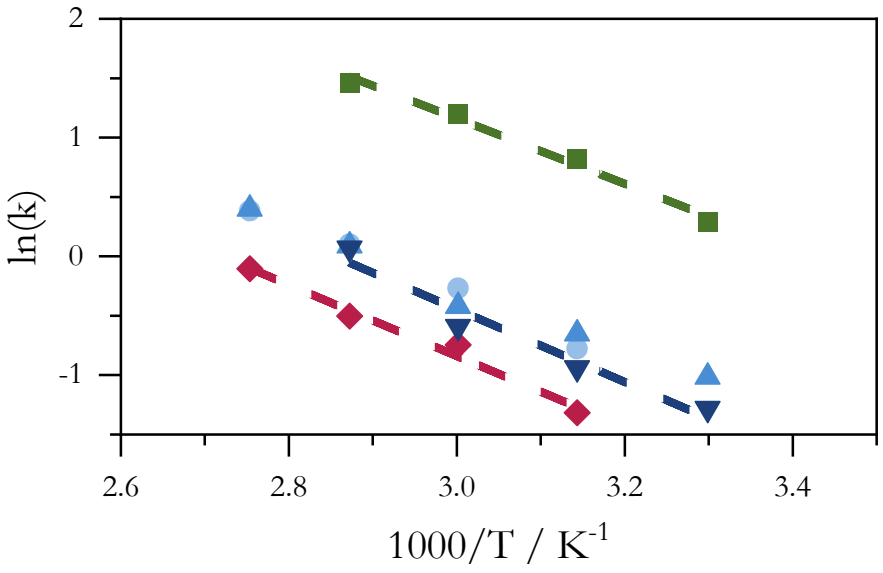

Figure IV.5. Arrhenius plot for the five catalysts studied. Green, pristine catalyst; purple, ammonia-treated catalyst; light blue, blue, and dark blue, carbene-functionalized catalysts at increasing loadings. Regression lines for pristine, ammonia-treated treated and 0.095 % w/w carbene loading catalysts are also reported.

Starting from the unfunctionalized catalyst as a reference for H_2 activation kinetic constants and apparent activation energies, it was observed that exposure to ammonia led to a substantial reduction in the hydrogen activation rate, lowering the kinetic constants by approximately a factor of eight (**Figure IV.5**).

Subsequent functionalization with NHC ligands partially restored the reaction rate , increasing the kinetic constants by approximately 70 %. Surprisingly, this enhancement was essentially independent of the carbene loading over the tested range (0.015 % - 0.095 % w/w), and no significant variation in kinetic constants was observed across different carbene concentrations or within the temperature interval studied (30 – 90 °C). The kinetic constants for all materials and temperatures are reported in **Table IV.2**

Another parameter obtained from this analysis is the apparent activation energy of the process (**Table IV.3**). Extrapolated values show the activation energy does not undergo significant changes with the modifications occurring when treating the catalyst with ammonia or functionalizing it with carbenes.

Table IV.2. Measured kinetic constants for the different catalysts at various temperatures.

	k / H*/Au_{per}·min·$atm^{0.5}$				
			Carbene loading / w/w		
T / °C	**Pristine**	**NH_3 treat.**	**0.015%**	**0.032%**	**0.095%**
30	1.339			0.362	0.278
45	2.277	0.264	0.459	0.521	0.390
60	3.312	0.468	0.764	0.657	0.553
75	4.325	0.594	1.110	1.094	1.069
90		0.887	1.466	1.491	

Table IV.3. Apparent activation energies extrapolated from the Arrhenius plot.

			Carbene loading / w/w		
	Pristine	**NH_3 treat.**	**0.015%**	**0.032%**	**0.095%**
E.a. / kJ/mol	23 ± 2	25 ± 4	24 ± 2	23 ± 1	25 ± 4

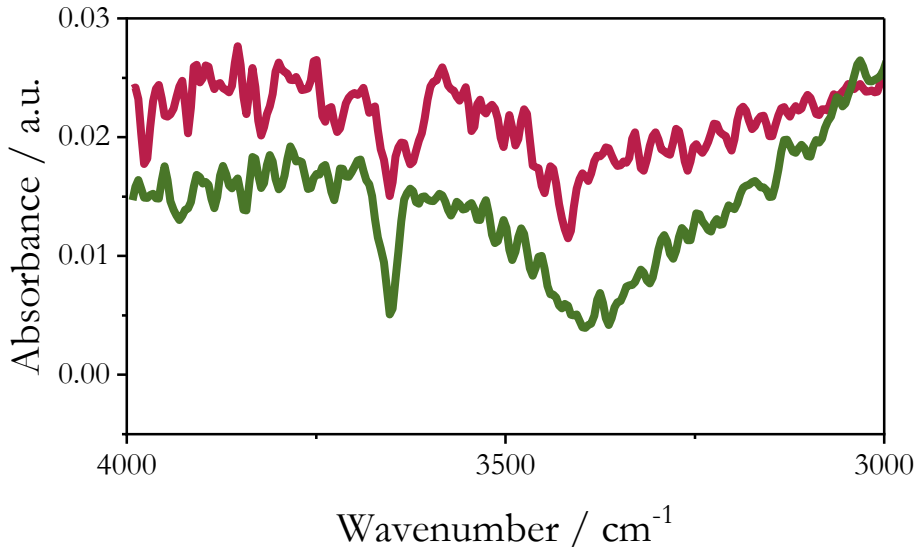

Figure IV.6. FT-IR spectra of pristine (green) and ammonia-treated (red) catalysts showing the hydroxyl loss during the heating process from 140 °C to 170 °C.

To rationalize the pronounced decrease in kinetic constants after the ammonia treatment, we initially hypothesized that ammonia could introduce some surface modifications or electronic effects that hinder the activation process. To better investigate this, two pellets of material, one pristine and one ammonia-treated, were equilibrated at 120 °C and gradually heated up to 400 °C while monitoring surface dehydroxylation by FT-IR spectroscopy (**Figure IV.6**).

The FT-IR spectra of both pellets show two main losses: one band at high energy (about 3650 cm^{-1}) and one at a lower energy (about 3390-3420 cm^{-1}). While the high-energy one does not significantly change position, it is worth noting that after the treatment with ammonia, this band presents a shoulder at lower energy (3622 cm^{-1}). On the other hand, the low-energy band shifts from 3390 cm^{-1} on the pristine catalyst to 3418 cm^{-1} on the ammonia-treated one, and becomes markedly sharper.

These spectral changes suggest that treating the catalyst with ammonia disrupts the hydrogen bond network across the titania surface, producing stronger, less hydrogen-bonded O-H groups, thus causing the band shift at higher energy. Stronger O-H bonds are associated with slower proton mobility across the surface, consistent with a longer lifetime of Ti-OH species, and it is reflected in the narrowing of the corresponding IR band.

Although this interpretation remains tentative due to the complexity of hydroxyl species on titania and the challenges in assigning their IR signatures, it provides a plausible framework. A more comprehensive study would be required to definitively identify the affected species and elucidate the precise nature of their modification. Nonetheless, these observations seem to support the conclusion that ammonia treatment induces surface modifications that hinder hydrogen activation and spillover.

$_{MSI}$Ti-OH Peaks Position

During the hydrogen activation process, a comparison of FT-IR spectra for the pristine, ammonia-treated and 0.095% carbene functionalized catalysts revealed systematic differences in the vibrational features associated with MSI hydroxyl groups. Spectra are reported in **Figure IV.7**.

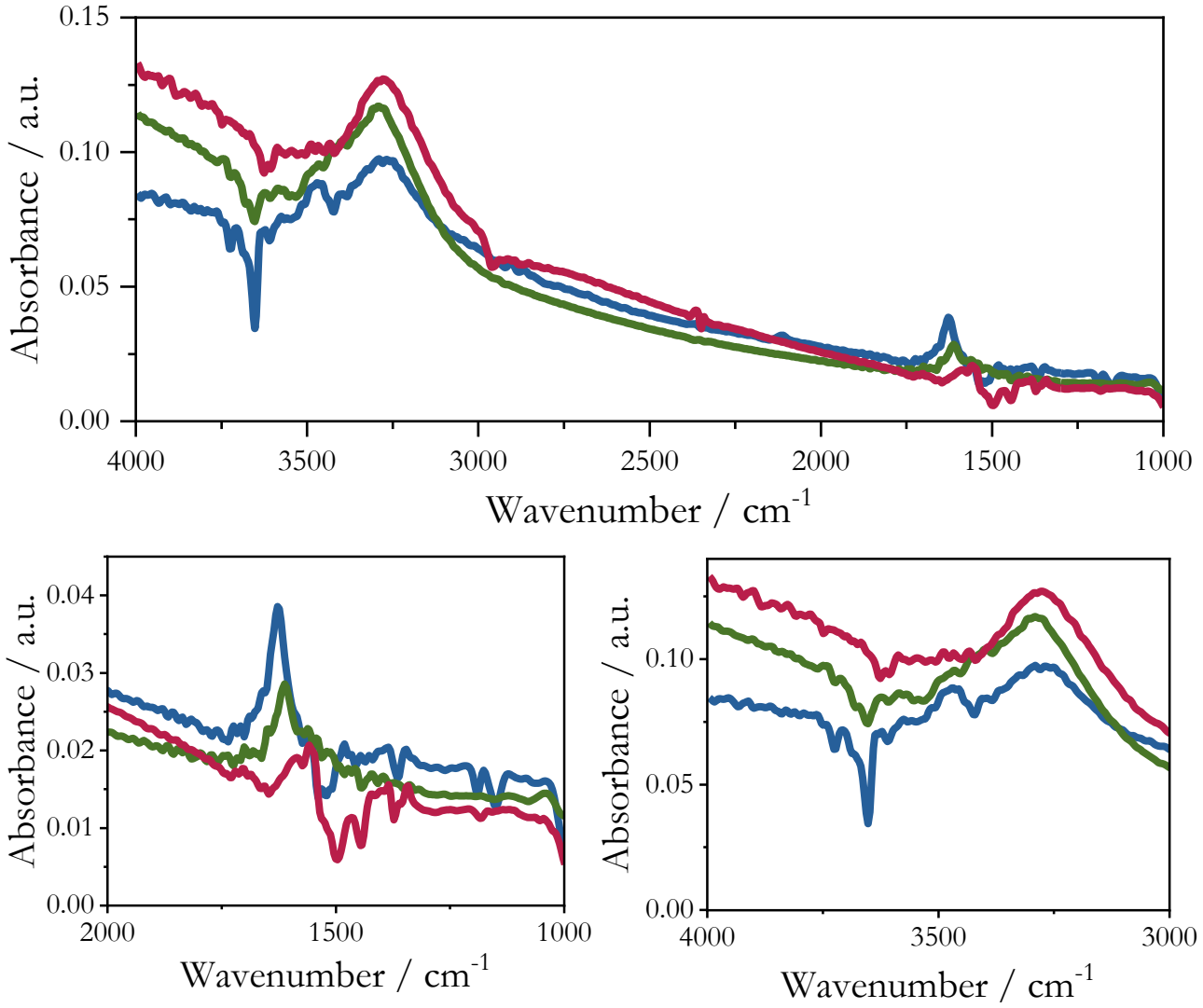

Figure IV.7. Top, FT-IR spectra of pristine catalyst (green), ammonia-treated catalysts (purple), and 0.095% carbene loading catalysts (blue) under hydrogen flow. Bottom left, magnification of the 2000-1000 cm^{-1} area showing the $_{MSI}OH_2^+$ scissoring mode peaks. Bottom right, magnification of the 4000-3000 cm^{-1} area showing the $_{MSI}OH_2^+$ and $_{MSI}OH$ stretching mode peaks.

Since the stretching bands of newly formed protonated MSI hydroxyls, $_{MSI}$Ti-OH_2^+, are broad, and also considering they are overlapped with the broad background absorption (BBA), it is risky to determine the band absorbance maximum with high confidence. It is much easier to focus on the loss of

unprotonated $_{MSI}$Ti-OH, which occurs due to their protonation, whose band maximum can be located with greater confidence.

The maximum of this band shifts from 3652 cm^{-1} in the pristine catalyst to 3625 cm^{-1} on the ammonia-treated catalyst, with the appearance of a shoulder at 3606 cm^{-1}. Remarkably, in the presence of carbenes, this band moves back to 3652 cm^{-1}.

A similar trend can be detected on the $_{MSI}$Ti-OH_2^+ scissoring band: being originally sited at 1612 cm^{-1}, upon ammonia treatment it shifts to lower energy (1585 cm-1 with a shoulder at 1558 cm-1), whereas carbene functionalization restores the band to higher energy (1627 cm^{-1}).

These spectral shifts are consistent with electronic perturbations at the MSI. Since the $_{MSI}$Ti-OH are in close contact with the nanoparticle, changes in Au electron density are expected to influence the MSI their vibrational properties. It is demonstrated[3] that this type of Arduengo carbenes are electron-withdrawing ligands. Their coordination to gold can plausibly decrease the electron density of the nanoparticle and the MSI active site. The shifts at higher energies can be due to this electronic effect.

On the other hand, the shifts at lower energies after treatment with ammonia should consequently be attributed to the increased electron density on the nanoparticles. This suggests that ammonia treatment causes not only some changes at the support surface but also at the material active sites.

To validate this hypothesis, an analogous analysis was performed on the Au/Al_2O_3 catalysts, pristine, ammonia-treated, and carbene-functionalized.

As expected for a non-conductive support, no BBA was observed during hydrogen activation. Anyway, in this case, vibrational signatures of hydrogen activation were detected because of the increase of $_{MSI}OH_2^+$ peaks along with bands disappearing in the $_{MSI}$OH region.

For the $_{MSI}$OH loss band, the principal peak remained constant at 3764 cm^{-1} across all samples, though the ammonia-treated material exhibited an additional shoulder at 3733 cm^{-1}, mirroring the behavior observed on the rutile sample.

For the $_{MSI}OH_2^+$ scissoring mode, while the pristine catalyst displayed a peak at 1605 cm^{-1}, the treatment with ammonia produced two bands at 1646 and 1600 cm^{-1}, which shifted to 1650 cm^{-1} for the carbene-functionalized catalyst.

From these data, it is difficult to rationalize the changes occurring in the materials. The $_{MSI}$OH loss peak does not undergo significant changes, except for the appearance of a new unexplained band. The $_{MSI}OH_2^+$ scissoring peak changed its maximum position, but, looking at the band shape, in the pristine catalyst (peak maximum at 1605 cm-1), a shoulder appears at around 1650 cm^{-1}. Conversely, for the

carbene-functionalized sample (peak maximum at 1650 cm^{-1}), a shoulder was observed at lower energy(around 1600 cm^{-1}).

A hypothesis for this behavior is a greater recalcitrance of alumina to undergo electronic modification because of its non-conductive nature, so it does not totally reflect the changes observed on rutile. Another method is needed to better investigate how the treatment with ammonia and the presence of carbenes affect the electronic properties of the catalytic sites.

CO Adsorption Analysis

To obtain a more direct assessment of the electron density on gold nanoparticles in the different systems, CO adsorption analysis was performed using *in situ* FT-IR spectroscopy. This is because carbon monoxide is an optimal probe of metal electronic structure. When CO binds to a metal atom, it establishes two different interactions: the first one is a σ-donation from CO to the metal; the second one is a π-backdonation from the metal into the CO π* orbitals, as shown in **Figure IV.8**. The stretching energy of bonded CO depends consequently on the magnitude of backdonation, therefore the modulation of the metal energy levels alters the stretching frequency. Accordingly, increasing the energy levels of metal orbitals results in an increased contribution of CO π* orbitals in the bonding, thus lowering the bond order and, consequently, the stretching frequency. Reducing the energy level of metal orbitals results in a diminished contribution of CO π* orbitals in the bonding, increasing the bond order and the stretching frequency.

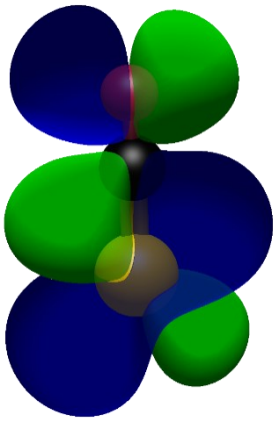

Figure IV.8. Representation of π-backdonation in Au-CO interaction. Gold in yellow; carbon in black; oxygen in red.

The same principle can be extended to gold nanoparticles. In this case, describing the system in terms of molecular orbitals is less straightforward, being composed of a few hundred atoms. Instead, the effect

could be rationalized in terms of a modulation of the Fermi level: an increase in the Fermi level leads to enhanced π-backdonation, whereas a decrease has the opposite effect.

CO adsorption measurements were performed using *in situ* FT-IR at low CO pressure (< 0.05 atm) since it is known that higher pressure of CO leads to the reconstruction of the gold surface.[9] Moreover, at low CO pressure, CO binds to low-coordinated corner atoms producing well-defined vibrational signatures, while at high CO pressure, the competitive adsorption on nanoparticles faces occurs, characterized by a different vibrational frequency and also subject to dipolar coupling, making the overall spectra complicated for the interpretation.

For the pristine Au/TiO_2 catalyst, CO adsorption resulted in a single band centered at 2109 cm^{-1} (Figure IV.9). After ammonia treatment, this band shifted to lower energy (2104 cm^{-1}), confirming that this treatment increases the electron density on gold nanoparticles, while slightly modifying the titania surface. In contrast, CO adsorption on the 0.095% carbene-functionalized catalyst surprisingly yielded no detectable CO band. Since the calculated carbene loading of 0.095% is really low (corresponding to around 8 molecules per nanoparticle, as determined in the Synthesis and Characterization section), the absence of adsorbed CO indicates that these bulky ligands compete effectively for corner sites, blocking CO adsorption even at low coverage. Analyzing the 0.032 % loading sample, a CO band was detected at 2116 cm^{-1} after subtraction of the gas-phase CO contribution. This substantial upshift demonstrates that even minimal carbene functionalization withdraws electron density from the gold nanoparticles, thus lowering their Fermi level.

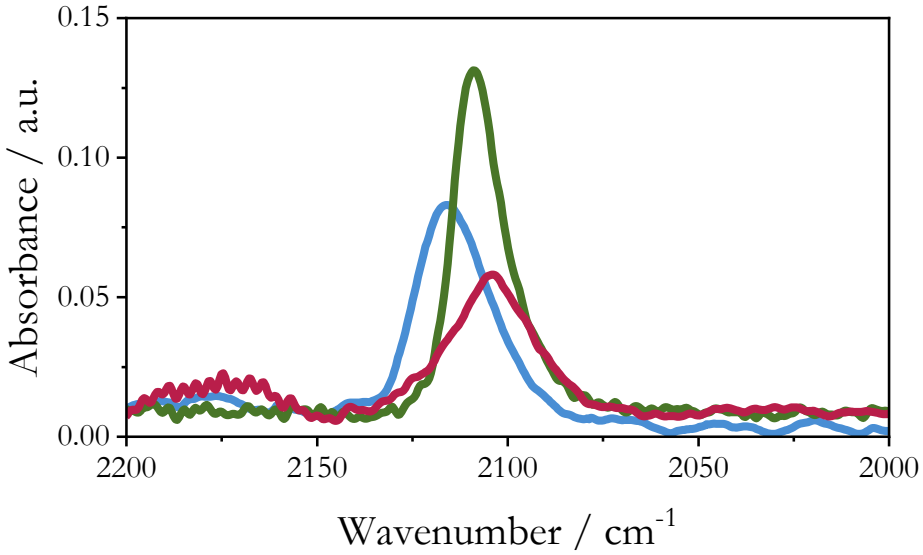

Figure IV.9. FT-IR spectra of CO adsorbed on three different catalysts. Pristine catalyst in green, ammonia treated in red, and 0.032% carbene loading in blue.

In short, these CO adsorption results validate the trends inferred from MSI vibrational analysis and kinetic data, underlining how much electron density impacts on the kinetics of the process. Specifically, treatment with ammonia slows down the process, not only by causing modifications of titania surface, but also by increasing the electrondensity of gold nanoparticles (probed by the shift of adsorbed CO peak from 2109 cm^{-1} to 2104 cm^{-1}), together with $_{MSI}$Ti-OH weaker stretching and scissoring vibrations. On the other hand, the presence of carbenes decreases the electrondensity of the gold nanoparticles (**Figure IV.10** a), confirmed by the shift of adsorbed CO from 2104 cm^{-1} to 2116 cm^{-1}, together with $_{MSI}$Ti-OH stronger stretching and scissoring vibrations.

To explain how these electronic perturbations extend to the $_{MSI}$Ti-OH vibrational modes, we must consider the change in polarity of the O-H bond. In a more electron-dense MSI, the electron-withdrawing property of oxygen atoms is mitigated by a larger availability of electrons in the system. The O-H bond, naturally a $O^{\delta-}$-$H^{\delta+}$ dipole, displays therefore lower polarity, resulting in lower stretching energy. Also, the scissoring mode of the protonated species is lower since a weaker dipole results in longer bond, thereby decreasing repulsion during the vibration. In an electron-poor MSI, oxygen atoms compensate for the lack of electrons by withdrawing electrondensity from the hydrogen atoms. As a consequence, $O^{\delta-}$-$H^{\delta+}$ becomes a stronger dipole, resulting in a shorter bond and a stretching vibration at higher energy

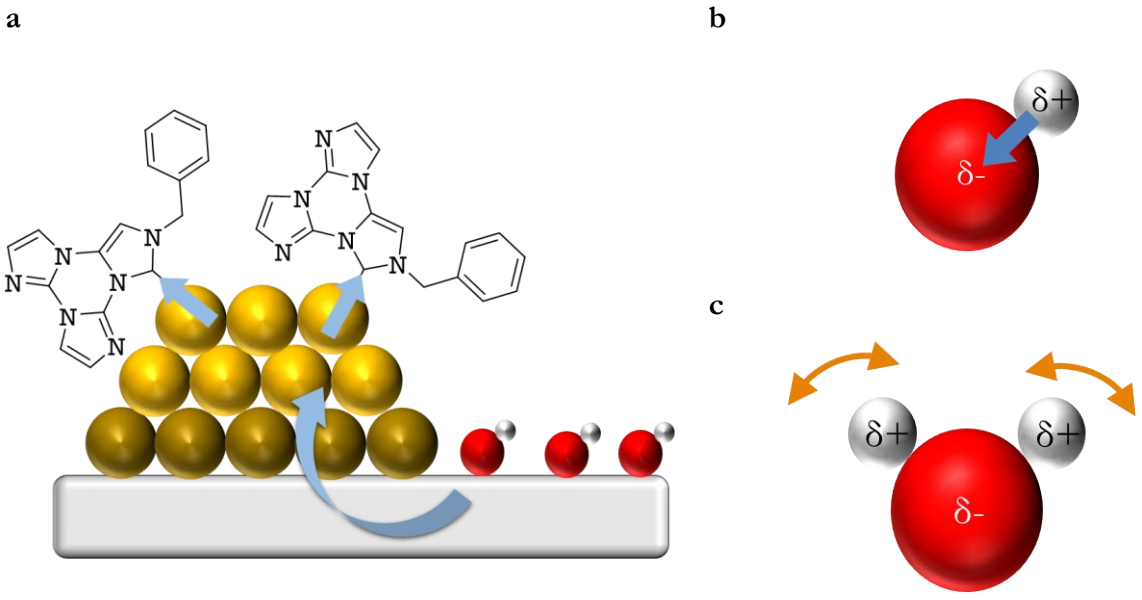

Figure IV.10. a) Schematic representation of carbene-functionalized catalyst; the light blue arrow indicates the electron-withdrawing path. b) Representation of O-H stretching. c) Representation of H-O-H scissoring.

(**Figure IV.10** b). In the same way, scissoring of the protonated species occurs at higher energies because of closer $H^{\delta+}$ and higher charge repulsion due to the increased dipole (**Figure IV.10** c).

A similar rationale applies to the kinetics of hydrogen activation, in which the transition state of H_2 molecule dissociation must be considered. DFT calculations[10] suggest a quasi-heterolytic dissociation pathway, characterized by a transition state in which the H_2 molecule is coordinated from the gold nanoparticle and an $_{MSI}$Ti-OH site. In this state, the hydrogen molecule is characterized by a charge separation, with computed partial charges of +0.30 on the hydroxyl-coordinated H and -0.18 on the gold-coordinated hydrogen.

In the dissociation process, a proton-coupled electron-transfer (PCET)-like mechanism occurs.[8] During proton transfer to a basic support hydroxyl group, electron density is distributed through the gold nanorod and partially localized on the protonated support hydroxyl group. In the final state, the OH-bound hydrogen carries a charge of +0.94, while the gold-bound hydrogen exhibits a charge of –0.09. This charge asymmetry reflects the inherent instability of gold hydride species.[11] In broad terms, the distribution of negative charge is about 1/4 of an electron and remains distributed between the hydride and the Au nanoparticle, while about 1/2 of an electron is localized on the HO_{cus}, and about 1/4 of an electron is distributed across the rest of the support (Ti and O atoms). The gold-bound hydrogen is transferred to a neighboring Ti–OH site in an almost thermoneutral process.

Variations in electron density on the gold nanoparticle can significantly influence the charge distribution during the H_2 activation process. An increase in electron density tends to destabilize the gold hydride species, enhancing the negative character of the hydrogen atom coordinated to gold. Conversely, a decrease in electron density, such as that induced by the presence of a carbene ligand, can stabilize the gold hydride.

Reaction Order Determination

To further elucidate potential modifications to the reaction mechanism, induced by ammonia treatment or carbene functionalization, the reaction order with respect to hydrogen was determined for each catalyst. Reaction order measurements, in fact, offer insight into the nature of the rate-determining step and the involvement of hydrogen in the transition state.

For the pristine catalyst, the average reaction order obtained from three independent measurements was 0.48 ± 0.08. This value is in agreement with the expected value of 0.5 for quasi-heterolytic scission *via* PCET mechanism, since the chemical equation for the reaction is:

$$\frac{1}{2}H_2 + {}_{MSI}Au + {}_{MSI}Ti-OH \rightarrow \quad {}_{MSI}Au + {}_{MSI}Ti-OH_2$$

The ammonia-treated catalyst exhibited a nearly identical reaction order of 0.46 ± 0.07. Despite the substantial reduction in reaction rate caused by ammonia, the unchanged reaction order indicates that the fundamental mechanism of H_2 activation remains the same. In contrast, the catalyst functionalized with 0.095% carbene exhibited a markedly increased reaction order of 0.71 ± 0.13. This deviation from the expected value suggests a meaningful alteration of the transition state or intermediate stabilization.

A plausible explanation involves enhanced stabilization of the negative charge associated with the heterolytic cleavage of H_2. Since NHCs are electron-withdrawing ligands, they can delocalize electron density from the nanoparticle, both in the transition state, increasing the charge separation, and in the final state after the bond cleavage. In the transition state, this may promote a more pronounced heterolytic dissociation, while in the final state, the stabilization of the hydride could lower the energy of the intermediate and potentially raise the barrier for the subsequent hydrogen transfer step. A more pronounced heterolytic character in the transition state would manifest as a higher reaction order.

At this step of the work, colleagues from Rice University (TX) are performing theoretical calculations to better understand the mechanisms involved, but additional insights were obtained by examining IR spectra collected during the kinetic experiments (**Figure IV.11**). When these spectra were overlaid with the ones of NHC-functionalized Au nanoparticles, reproducible features emerged in the 2800 - 3000 cm^{-1} region. Specifically, negative signals appeared at frequencies characteristic of carbene C-H stretching vibrations, accompanied by the growth of positive bands at lower energies.

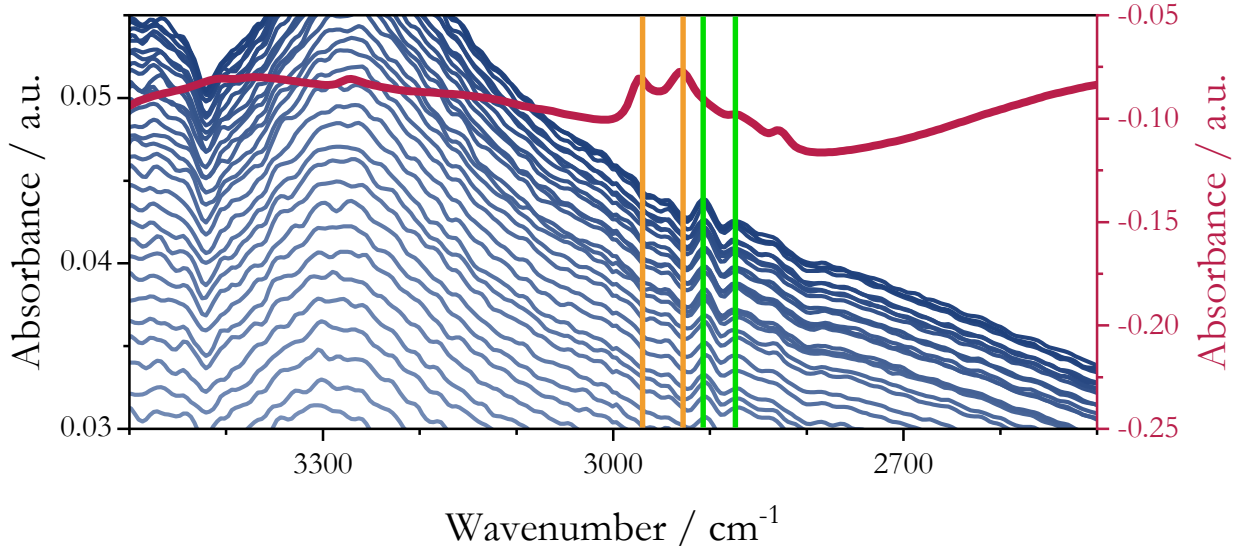

Figure IV.11. In blue, magnification of BBA growth during hydrogen adsorption. In red, adsorption spectrum of the carbene-functionalized catalyst. Highlighted in yellow, the decrease of BBA in correspondence with carbene-deriving peaks. Highlighted in green, the new positive bands appearing at lower energies.

Given that the reference spectrum was recorded under argon on an equilibrated pellet, this pattern indicates a transformation occurring on the pellet surface: the system lost features present in the reference (negative peaks) but acquired new ones (positive peaks), suggesting that the species are not removed by the gas flow but are rather altered.

Since this modification occurs during the hydrogen activation process, when the system is enriched in electrons deriving from activated hydrogen, the data suggests the weakening of some bonds on the carbene molecules. This can be explained as an increased π-backdonation from the electron-enriched Au nanoparticle to the carbene under reaction conditions. This causes a higher population of antibonding molecular orbitals, resulting in a weaker bond with lower vibrational energy. This supports the hypothesis that carbene ligands actively participate in modulating charge distribution during H_2 activation, contributing to the observed increase in reaction order.

To verify this increased π–backdonation, experiments combining CO adsorption with hydrogen activation were attempted in order to detect the CO stretching vibration energy decrease. Since CO adsorption works better on the untreated catalyst, this latter was used to avoid interference from carbene.

However, flowing CO over the catalyst and then flowing H_2 to enrich the system in electrons resulted in almost no BBA growth. Even doing the opposite, the H_2-after-CO sequence, did not yield interpretable CO adsorption signals. This likely reflects the well-known high activity of Au/TiO_2 for CO hydrogenation even at mild temperatures.[12] Yet at 30°C, activated hydrogen rapidly reacts with CO, precluding its detection. Thus, combined CO/H_2 adsorption cannot serve as a diagnostic tool for electronic changes during hydrogen activation in this system.

Kinetic Isotopic Effect

To probe more deeply the mechanistic features of hydrogen activation, Kinetic Isotope Effect (KIE) was measured on selected catalysts. Both primary KIE (ratio between H_2 and D_2 activation on $_{MSI}$Ti-OH active site) and secondary KIE (ratio between H_2 activation on $_{MSI}$Ti-OH active site and $_{MSI}$Ti-OD active site) were studied.

Initial measurements performed on the pristine catalyst and the 0.095% carbene loading one showed no differences, with a primary KIE of 2.5 and 2.6, respectively (**Figure IV.12** left). Different results were found for the secondary KIE, leading to 0.89 and 1.05, respectively (**Figure IV.12** right). The result related to pristine catalyst, however, was quite different from the previously achieved within the research group (4.1 for primary KIE and 1.19 for inverse secondary KIE). Anyway, in that case, they were

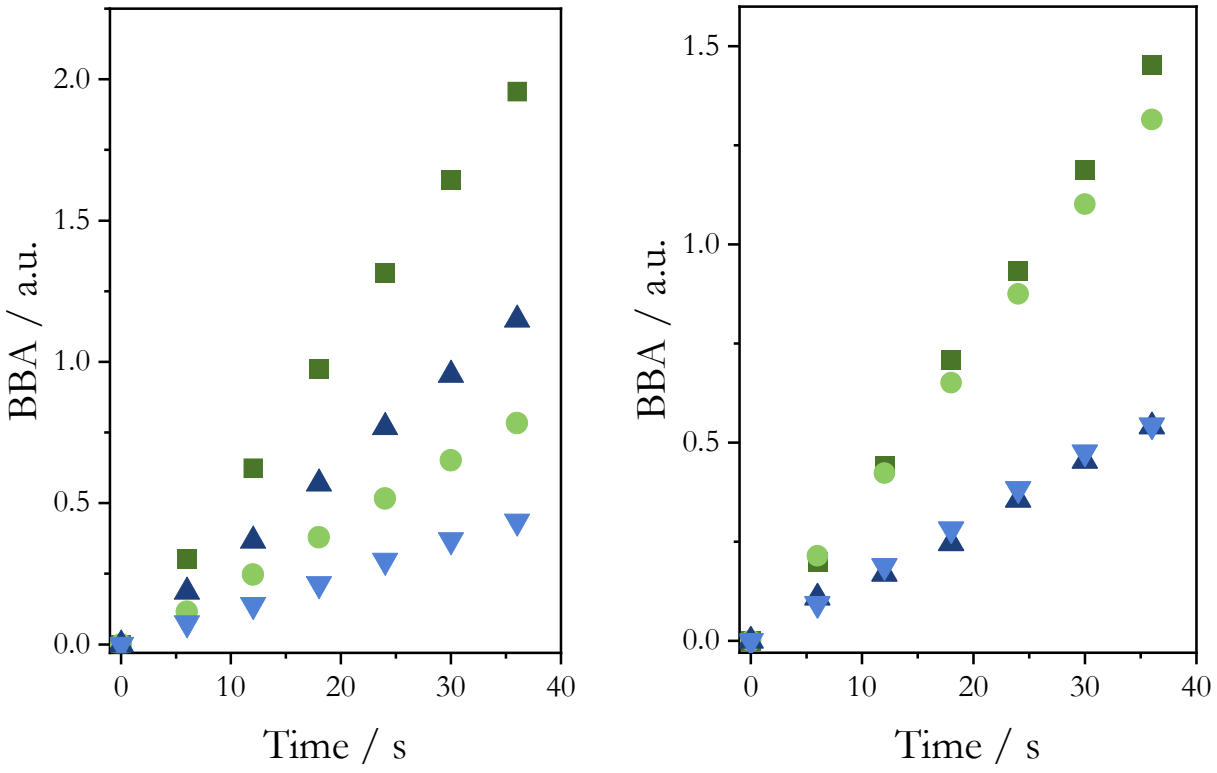

Figure IV.12. Evolution of BBA with time for KIE measurements. Left, data for primary KIE; dark and light green, kinetics data of H_2 and D_2 on the pristine catalyst; dark and light blue, kinetics data of H_2 and D_2 on the 0.095% carbene loading catalyst. Right, data for secondary KIE; dark and light green, kinetics data of D_2 on the pristine and deuterated surface of pristine catalyst; dark and light blue, kinetics data of D_2 on the pristine and deuterated surface of 0.095% carbene loading catalyst.

employing Au/P25 catalyst (not TiO_2 rutile), performing pre-treatment before measurement at different temperatures (carbonate removal and SAO treatment at 150°C instead of 120°C).

To explore this, an Au/P25 sample was treated using the same conditions applied in the present work. Under these conditions, the values obtained were 3.5 for primary KIE and 0.98 for inverse secondary KIE. 120°C, the primary and secondary KIEs increased to 4.0 and 1.34,respectively, thus aligning closely with the expected values(**Figure IV.13**).

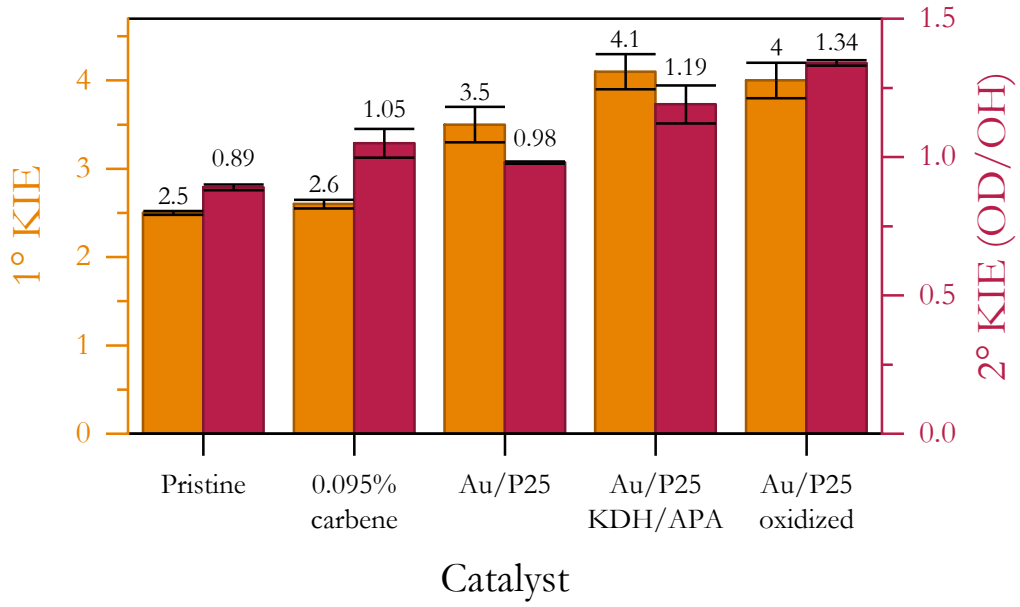

Figure IV.13. Values for primary (orange) and inverse secondary (purple) kinetic isotopic effect (KIE). The dataset called "Au/P25 KDH/APA" reports data previously obtained within the research group following a different pretreatment.

These differences demonstrate that surface carbonates can measurably influence isotopic measurements. Since carbene-functionalized catalysts are unstable under the conditions required for carbonate removal, reliable KIE measurements on these materials were not feasible.

Reduction of p-nitrophenol

As a final application of the synthesized catalysts, their ability to mediate the reduction of nitroaromatic compounds via hydrogen spillover was evaluated. In this context, p-nitrophenol was selected as the model substrate in place of nitrobenzene. (**Figure IV.14**). This choice was motivated by considerations of volatility and physical state. Since the reduction was conducted in the thermostatically controlled FT-IR cell under a 40 mL/min gas flow, the main concern was to avoid the compound evaporation or sublimation during the analysis, or at least to make it negligible.

The calculated vapor pressure of nitrobenzene at 120°C *via* the Antoine equation is 66.7 hPa[13], compared with a reported one of 0.8 hPa for p-nitrophenol. Moreover, at 120 °C, p-nitrophenol is present in its liquid phase, while in the temperature range used for the study (60-90 °C) it is still in the solid phase. Finally, heating a pellet of the sample for one hour and monitoring the IR spectrum revealed no loss of compound, after a slight change in the IR absorbance during thermal equilibration.

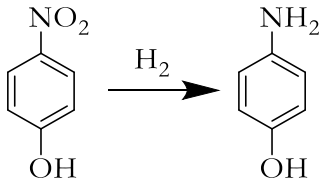

Figure IV.14. Scheme of p-nitrophenol reduction reaction.

Once the pellet was equilibrated, spectra were acquired at 10 s intervals to monitor the reaction progress. In the final data collection, three principal time intervals were identified (**Figure IV.15**).

In the first one, comprised between 0 min and 2.5 min, BBA started increasing as H_2 reached the FT-IR cell. Concurrently, minor perturbations appeared in the spectral regions associated with p-nitrophenol vibrations (1000-1700 cm^{-1} and 2800-3700 cm^{-1}), indicating the onset of p-nitrophenol reduction.

Over the second time interval, between 2.5 min and 5.66 min, the BBA stopped increasing and remained almost constant. During this interval, major changes were registered in the regions of the organic molecule: pronounced negative bands corresponding to the depletion of p-nitrophenol emerged, accompanied by new bands likely associated with reaction intermediates.

During the third time interval, after 5.66 min, BBA resumed its increase while the other spectral changes diminished, ultimately reaching an equilibrium state after about 30-35 minutes.

To quantify the reaction rate, the asymmetric -NO_2 stretching band of p-nitrophenol was integrated in the 1565-1600 cm^{-1} region, and the resulting peak area was plotted vs time. In this plot, it is easy to

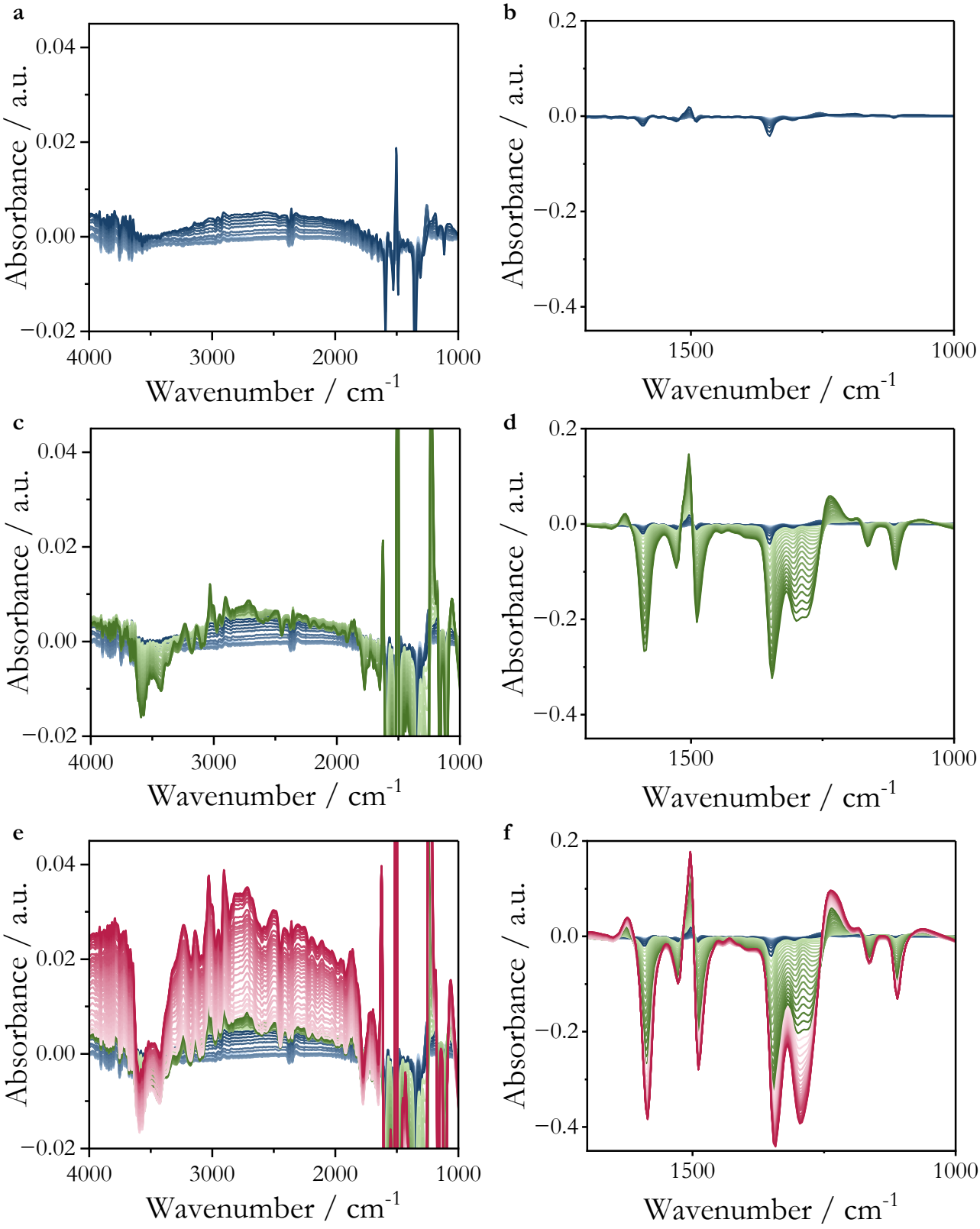

Figure IV.15. Left, magnification of BBA during p-nitrophenol reduction; right, variation of organic compounds peaks during p-nitrophenol reduction. a, b) 0.00 – 2.50 min interval (blue); c, d) 2.50 – 5.66 min interval (green); e, f) 5.66 – 20.00 min interval (purple).

identify a region where the variation in peak area is linear at the same time BBA is in a stationary state (**Figure IV.16**, green region), thus allowing to perform kinetic analysis.

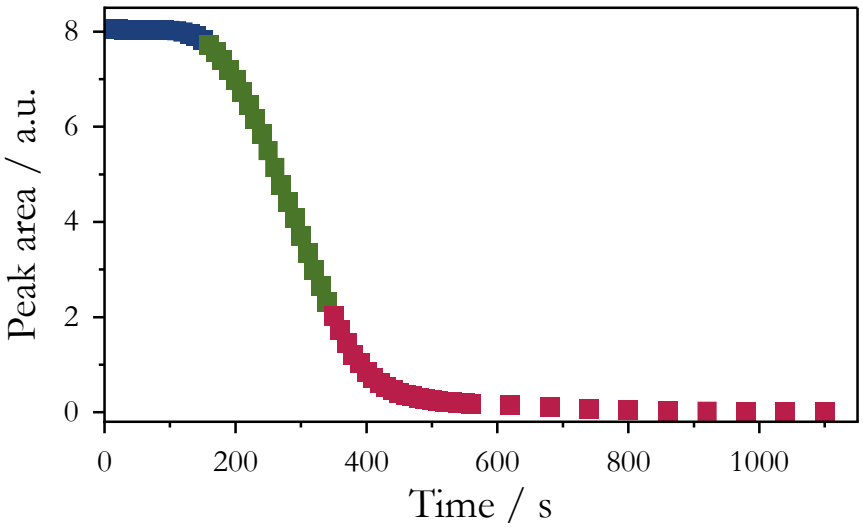

Figure IV.16. Example of variation of -NO_2 asymmetric stretching peak area over time. 0.00 – 2.50 min interval, blue; 2.50 – 5.66 min interval, green; 5.66 – 20.00 min interval, purple.

Arrhenius analysis was performed on both the ammonia-treated catalyst and the 0.095% carbene loading catalyst. Across the temperature range examined (60, 70, 80, and 90 °C), both catalysts exhibited comparable kinetic constants. The apparent activation energies, derived from linear fits to the Arrhenius plots, were 44.0 and 44.5 kJ/mol, respectively. These results are consistent with the data found in the literature for analogous reductions (34 and 68 kJ/mol).[14-16] Also if reference are referred to the same process, conditions are different. References work with sodium borohydride[14-15] or hydrazine[16] as reducing agent, carrying out the tests in aqueous solutions, while for these experiments hydrogen was used. Although all the considered compounds possess their relative advantages and disadvantages about stability, toxicity and transport, the employment of *in situ* generated H_2 highly reduce the risks. Also, UV-vis absorption is employed as measurement to monitor the reduction. The employment of FT-IR is an improvement, since absorption bands of organic molecules are usually narrower than in UV-vis. Moreover, IR signals derive from specific functional groups, making easier to monitor the depletion of a specific functional group.

The reason for the similarity in the obtained activation energies can be found in the specific spatial separation between the sites of hydrogen activation and the sites of p-nitrophenol reduction. While NHC ligands are located on gold nanoparticles, thus affecting the hydrogen activation step, the reaction

between activated hydrogen, H*, and p-nitrophenol occurs on the support, ideally far away from gold nanoparticles and, therefore, from carbenes.

A final consideration must be made about the reduction mechanism: at this point of the work, it is not known. For simplicity, a rough approximation of three H_2 reacting with one p-nitrophenol molecule is considered, in order to determine kinetic constants. Anyway, values are obtained from a -NO_2 stretching band, so the step of p-nitrophenol reduction to p-nitrosophenol with only one H_2 is enough for the disappearance of the peak. Although the apparent activation energy does not change, the absolute values of kinetic constants will undergo a big change when considering one or three H_2 molecules.

Also, calculations are performed using the pressure of gaseous hydrogen, and this is wrong because gaseous hydrogen does not directly react with p-nitrophenol. Instead, hydrogen molecules are activated at the catalyst MSI, then hydrogen spillover occurs, thus allowing H* to migrate on the surface up to react with p-nitrophenol. Hence, only H* species generated via spillover are chemically relevant. Therefore, a rigorous kinetic study should employ the steady-state concentration of H* (rather than gas-phase H_2 pressure) in the rate law.

Accurate measurements require pellet-by-pellet calibration, but for this type of experiment, pellets are single-use since once the nitrocompound is reduced, it is no longer possible to reuse the pellet. Between one pellet and another, the calibration factor can be subject to large changes in value, as demonstrated by the initial -NO_2 peak area usually spanning between 3 and 9 a.u.. While -NO_2 peak is internally calibrated on a single pellet since its amount is known, this is not possible for BBA calibration.

Because of this, for a correct approximation of the H* amount on the catalyst surface, each pellet should be calibrated after its use, a procedure that would require a lot of time. In this way, it would be possible to determine the reaction order with respect to H*. Such a reaction order value should then be inserted in the equation to calculate the kinetic constants for the Arrhenius analysis.

To address these limitations, a generalized calibration strategy was developed to transpose the full calibration of one pellet to all the others, based on the -NO_2 peak area.

Starting from the Lambert Beer law, absorbance is defined as:

$$A_\lambda = \epsilon_\lambda \cdot c \cdot l \qquad \textit{Equation IV.5}$$

Applying this equation to a sample pellet, "ϵ" is the ϵ value of the species we observe (e.g., NO_2 group), *"c"* is the concentration of the species, and *"l"* is the pellet thickness. The pellet is not perfectly uniform; therefore, we can define it as an integral of the thickness along the pellet area subject to the measure.

As demonstrated by the calibration factor for -NO_2 obtained during nitrogroup reduction experiments, different pellets of the same materials can have very different calibration factors. Although the species concentration is the same, this causes the variation of the initial-NO_2 peak area in values between 3 and 9 a.u.. Since the observed species is the same, the "ϵ" values are the same for all the pellets. Being different pellets prepared from the same material obtained by the same synthesis batch and studied under identical conditions, the *"c"* values are also the same. It means that any variations arise solely from differences in the spatial distribution of the material within the measured area of the pellet, leading to different values for *"l"*.

Importantly, the precise determination of the absolute "*l*" value for each pellet is not required. For the subsequent data analysis, only the ratio between the "*l*" value of the reference pellet and that of the pellet under measurement is relevant.

In all the following equations, the absorbance values do not correspond to a single wavelength, but to the peak area or BBA area. This is because the area represents the integral of the absorbance over the selected wavelength range. Accordingly, the ϵ values also correspond to the integral of ϵ over the same range. All the integral symbols are omitted for simplicity.

For the asymmetric -NO_2 stretching band on the reference pellet, absorbance can be expressed as:

$$A_{NO_2\ pellet_{ref}} = \epsilon_{NO_2} \cdot c_{NO_2} \cdot l_{pellet_{ref}} \qquad \textit{Equation IV.6}$$

For a sample pellet, the absorbance of the same peak will be:

$$A_{NO_2\ pellet_{sample}} = \epsilon_{NO_2} \cdot c_{NO_2} \cdot l_{pellet_{sample}} \qquad \textit{Equation IV.7}$$

When flowing hydrogen, BBA increases on the same pellet, and the absorbance for BBA on the reference and sample pellets is, respectively:

$$A_{BBA\ pellet_{ref}} = \epsilon_{H^*} \cdot c_{H^*} \cdot l_{pellet_{ref}} \qquad \textit{Equation IV.8}$$

$$A_{BBA\ pellet_{sample}} = \epsilon_{H^*} \cdot c_{H^*} \cdot l_{pellet_{sample}} \qquad \textit{Equation IV.9}$$

Calculating the ratio between absorbance of the NO_2 peak for reference and sample, thus *Equation IV.6* divided by *Equation IV.7*, we can obtain:

$$\frac{A_{NO_2\ pellet_{ref}}}{A_{NO_2\ pellet_{sample}}} = \frac{\epsilon_{NO_2} \cdot c_{NO_2} \cdot l_{pellet_{ref}}}{\epsilon_{NO_2} \cdot c_{NO_2} \cdot l_{pellet_{sample}}} \qquad \textit{Equation IV.10}$$

The observed species is the same and therefore also the concentration of the nitro compound is. *Equation IV.10* can then be simplified in:

$$\frac{A_{NO_2\ pellet_{ref}}}{A_{NO_2\ pellet_{sample}}} = \frac{l_{pellet_{ref}}}{l_{pellet_{sample}}} \qquad \textit{Equation IV.11}$$

Since the value of *"l"* is the only parameter affecting the calibration factor, this ratio is called *"r_f"*, the calibration factor ratio.

$$r_f = \frac{A_{NO_2\ pellet_{ref}}}{A_{NO_2\ pellet_{sample}}} = \frac{l_{pellet_{ref}}}{l_{pellet_{sample}}} \qquad \textit{Equation IV.12}$$

The same elaboration can be carried out for the BBA area:

$$\frac{A_{BBA\ pellet_{ref}}}{A_{BBA\ pellet_{sample}}} = \frac{\epsilon_{H^*} \cdot c_{H^*_{ref}} \cdot l_{pellet_{ref}}}{\epsilon_{H^*} \cdot c_{H^*_{sample}} \cdot l_{pellet_{sample}}} \qquad \textit{Equation IV.13}$$

Again, the *"ϵ"* values are the same; however, in this case, the concentration of H* may differ, since we are considering experiments conducted under different conditions, such as varying temperatures or hydrogen flow, that affect the amount of adsorbed hydrogen at the equilibrium:

$$\frac{A_{BBA\ pellet_{ref}}}{A_{BBA\ pellet_{sample}}} = \frac{c_{H^*_{ref}} \cdot l_{pellet_{ref}}}{c_{H^*_{sample}} \cdot l_{pellet_{sample}}} \qquad \textit{Equation IV.14}$$

At this point, it is possible to rewrite *Equation IV.14* to calculate the value of $c_{H^*_{sample}}$

$$c_{H^*_{sample}} = \frac{c_{H^*_{ref}} \cdot l_{pellet_{ref}}}{l_{pellet_{sample}}} \cdot \frac{A_{BBA\ pellet_{sample}}}{A_{BBA\ pellet_{ref}}} \qquad \textit{Equation IV.15}$$

Since $\frac{l_{pellet_{ref}}}{l_{pellet_{sample}}}$ value is the *"r_f"* calculated from the nitrocompound peak following *Equation IV.12*:

$$c_{H^*_{sample}} = c_{H^*_{ref}} \cdot r_f \cdot \frac{A_{BBA\ pellet_{sample}}}{A_{BBA\ pellet_{ref}}} \qquad \textit{Equation IV.16}$$

In the reference sample, $c_{H^*_{ref}}$ can be calculated at any moment by multiplying the BBA area by the calibration factor f_c:

$$c_{H^*_{sample}} = A_{BBA\ pellet_{ref}} \cdot f_{c_{ref}} \cdot r_f \cdot \frac{A_{BBA\ pellet_{sample}}}{A_{BBA\ pellet_{ref}}} \qquad \textit{Equation IV.17}$$

Simplifying:

$$c_{H^*_{sample}} = f_{c_{ref}} \cdot r_f \cdot A_{BBA\ pellet_{sample}} \qquad \textit{Equation IV.18}$$

Given this last equation, all the data needed for the calculation can be collected.

Starting with the reference pellet, data for nitro group reduction are acquired, allowing the peak area of the asymmetric -NO_2 stretching mode ($A_{NO_2\ pellet_{ref}}$) to be determined.

Once the reduction is completed, hydrogen is desorbed, and the same pellet is subsequently used to collect calibration isotherms. From these datasets, the calibration factor for the BBA of the reference pellet ($f_{c_{ref}}$) can be calculated.

For the sample pellet, data are collected for the kinetics of nitro group reduction. Once the reduction is completed, the peak area of the asymmetric -NO_2 stretching mode($A_{NO_2\ pellet_{sample}}$) can be determined.

According to *Equation IV.12*, the *"r_f"* factor can then be calculated, and *Equation IV.18* can be used to convert all BBA values into an accurate estimation of the amount of H* present on the catalyst at any given time.

With a reliable quantification of H*, it becomes possible to determine the reaction order for nitro group reduction and to achieve more accurate kinetic constants calculation, as well as activation energy values.

Bibliography

1. Mahdavi-Shakib, A.; Whittaker, T. N.; Yun, T. Y.; Sravan Kumar, K. B.; Rich, L. C.; Wang, S.; Rioux, R. M.; Grabow, L. C.; Chandler, B. D., The role of surface hydroxyls in the entropy-driven adsorption and spillover of H_2 on Au/TiO_2 catalysts. *Nature Catalysis* **2023,** *6* (8), 710–719.
2. Mahdavi-Shakib, A.; Rich, L. C.; Whittaker, T. N.; Chandler, B. D., Hydrogen Adsorption at the Au/TiO_2 Interface: Quantitative Determination and Spectroscopic Signature of the Reactive Interface Hydroxyl Groups at the Active Site. *ACS Catalysis* **2021,** *11* (24), 15194–15202.
3. Buck, D. M.; Kunz, D., Triazine Annelated NHC Featuring Unprecedented Coordination Versatility. *Organometallics* **2015,** *34* (21), 5335–5340.
4. Mather, J. C.; Wyllie, J. A.; Hamilton, A.; Soares da Costa, T. P.; Barnard, P. J., Antibacterial silver and gold complexes of imidazole and 1,2,4-triazole derived N-heterocyclic carbenes. *Dalton Transactions* **2022,** *51* (32), 12056–12070.
5. Yun, T. Y.; Chandler, B. D., Surface Hydroxyl Chemistry of Titania- and Alumina-Based Supports: Quantitative Titration and Temperature Dependence of Surface Bronsted Acid-Base Parameters. *ACS Applied Materials and Interfaces* **2023,** *15* (5), 6868–6876.
6. Rodriguez-Castillo, M.; Lugo-Preciado, G.; Laurencin, D.; Tielens, F.; van der Lee, A.; Clement, S.; Guari, Y.; Lopez-de-Luzuriaga, J. M.; Monge, M.; Remacle, F.; Richeter, S., Experimental and Theoretical Study of the Reactivity of Gold Nanoparticles Towards Benzimidazole-2-ylidene Ligands. *Chemistry* **2016,** *22* (30), 10446–58.
7. Yun, T. Y.; Battiste, A. M.; Pathickal Abraham, A.; Hart, K. D.; Chandler, B. D., Surface Entropy Mediated Hydrogen Spillover on Au/TiO_2: Influences of Strongly Adsorbed Water on H_2 Adsorption Thermodynamics. *Journal of the American Chemical Society* **2025,** *147* (33), 29908–29918.
8. Sravan Kumar, K. B.; Whittaker, T. N.; Peterson, C.; Grabow, L. C.; Chandler, B. D., Water Poisons H_2 Activation at the $Au\text{-}TiO_2$ Interface by Slowing Proton and Electron Transfer between Au and Titania. *Journal of the American Chemical Society* **2020,** *142* (12), 5760–5772.
9. Roze, E.; Quinet, E.; Caps, V.; Bianchi, D., Experimental Microkinetic Approach of the Surface Reconstruction of Gold Particles during the Adsorption of CO at 300 K on 1% Au/Al_2O_3. *Journal of Physical Chemistry C* **2009,** *113* (19), 8194–8200.
10. Whittaker, T.; Kumar, K. B. S.; Peterson, C.; Pollock, M. N.; Grabow, L. C.; Chandler, B. D., H_2 Oxidation over Supported Au Nanoparticle Catalysts: Evidence for Heterolytic H_2 Activation at the Metal-Support Interface. *Journal of the American Chemical Society* **2018,** *140* (48), 16469–16487.
11. Wijzenbroek, M.; Helstone, D.; Meyer, J.; Kroes, G. J., Dynamics of H_2 dissociation on the close-packed (111) surface of the noblest metal: H_2 + Au(111). *The Journal of Chemical Physics* **2016,** *145* (14), 144701.
12. Sakurai, H.; Haruta, M., Carbon dioxide and carbon monoxide hydrogenation over gold supported on titanium, iron, and zinc oxides. *Applied Catalysis A: General* **1995,** *127*, 93–105.
13. Brown, I., Liquid-Vapour Equilibria. III. The Systems Benzene-n-Heptane, n-Hexane-Chlorobenzene, and cycloHexane-Nitrobenzene. *Australian Journal of Scientific Research, Series A: Physical Sciences* **1952,** *5*, 530–540.
14. Arif, M.; Shahid, M.; Irfan, A.; Nisar, J.; Wu, W.; Farooqi, Z. H.; Begum, R., Polymer microgels for the stabilization of gold nanoparticles and their application in the catalytic reduction of nitroarenes in aqueous media. *RSC Adv* **2022,** *12* (9), 5105–5117.
15. Blanco, E.; Esteve-Adell, I.; Atienzar, P.; Casas, J. A.; Hernández, P.; Quintana, C., Cucurbit[7]uril-stabilized gold nanoparticles as catalysts of the nitro compound reduction reaction. *RSC Advances* **2016,** *6* (89), 86309–86315.
16. Monti, G. A.; Correa, N. M.; Falcone, R. D.; Silbestri, G. F.; Moyano, F., Water-soluble gold nanoparticles: recyclable catalysts for the reduction of aromatic nitro compounds in water. *RSC Adv* **2020,** *10* (26), 15065–15071.

V. CONCLUSION AND PERSPECTIVE

To conclude, this work focused on the design, preparation, characterization, and catalytic application of novel heterogeneous systems, spanning from metal-organic alloy materials (MORALs) to NHC-functionalized gold nanoparticles. These materials were studied using various analytical techniques and tested in the nitrogroup reduction reaction, primarily with nitrobenzene.

MORALs were first prepared through the incorporation of graphene oxide (GO) into palladium and nickel, followed by further modification via reduction to reduced graphene oxide (RGO). These materials were mainly studied using electron microscopy, FT-IR, and XRPD, which showed the presence of both the metal and GO or RGO; both IR absorption bands and diffraction patterns of the two species were observed in the spectra of the final materials. All the materials were also tested in the catalytic reduction of nitrobenzene, with results compared to pure metals and commercial catalysts. Palladium-based catalysts showed selective reduction to aniline, but at a slower rate than the commercial catalysts; however, the GO@nPd material outperformed all other catalysts in the reuse tests, with no loss in yield over five consecutive uses. Nickel-based materials can also perform selectively under the proper conditions, surpassing the performance of pure nickel. Among these catalysts, RGO@Ni was the best-performing, with no loss in yield over five consecutive uses.

NHC-functionalized gold nanoparticles were prepared to test the use of functionalized iso-TT as an NHC precursor. While XRPD, UV-vis, and TEM were employed to study the gold nanoparticles size, distribution, and plasmonic behavior, displaying how modifications in the synthesis and in the ligand can impact on the stability of nanoparticles and in their dimension. FT-IR and XPS analyses were performed to confirm the presence of organic molecules on the samples and to characterize them, thereby confirming the presence of the desired molecule. In parallel with FT-IR studies, DFT simulations were performed to allow a better interpretation of the spectra modifications. After immobilization on different supports, the catalysts were evaluated in nitrobenzene reduction. Tests revealed that the catalysts' performance is strictly related to the employed support, with titania providing the most effective systems. Gold nanoparticles supported on titania exhibited excellent recyclability, maintaining catalytic activity across multiple cycles.

During my research period at Penn State University (USA), the focus shifted to the functionalization of Au/TiO_2 catalysts with NHC ligands to investigate hydrogen spillover. TEM analysis was employed for the determination of nanoparticles dimension distribution and, via mathematical elaboration, to estimate the number of active sites. FT-IR was used to check the presence of organic molecules, while

UV-vis was used for their quantification. Physical-chemical studies were conducted to compare the functionalized catalyst with the unfunctionalized one and to collect data for Arrhenius analysis, reaction rate determination, and kinetic isotopic effects. Results show that functionalization increases the rate of hydrogen activation while leaving the activation energy unchanged. Also, the presence of carbenes alters the electronic properties of the active site, likely altering the activation pathway, as suggested by reaction rate measurements and CO adsorption analysis. This type of material was employed in nitrogroup reduction, too, this time employing nitrophenol as substrate. Even though this procedure is more complex and still needs some improvements, it was possible to monitor the reduction by the aim of spilled-over hydrogen and to extrapolate kinetic data.

Overall, this work demonstrates that controlled structural design and surface functionalization are powerful tools for modulating catalytic behavior. The incorporation of carbon-based components into MORAL systems significantly enhances catalyst stability, while NHC ligands provide a versatile platform for tuning the electronic properties of gold nanoparticles and influencing hydrogen activation mechanisms.

Although substantial progress has been achieved, several research directions remain open. Given the remarkable mechanical and chemical robustness of MORAL systems, their translation from batch conditions to continuous-flow reactors constitutes a particularly promising development. Implementing these materials into flow processes would not only enable more accurate evaluation of long-term stability and metal leaching but also provide insight into mass transport effects and catalyst productivity under industrially relevant conditions. Such studies will be essential to assess the true scalability and technological potential of these hybrid materials. In parallel, ongoing collaborations aimed at advanced structural investigations using synchrotron radiation will provide a deeper understanding of the metal-carbon interface. High-resolution techniques such as X-ray absorption spectroscopy (XAS) and related methods will be crucial to elucidate structure-activity relationships at the atomic level, clarifying how GO/RGO incorporation modifies metal dispersion, oxidation state, and electronic density.

Regarding NHC-functionalized gold nanoparticles, although their catalytic behavior was highly promising, their lack of emissive properties underscores the need for further molecular design. Future work will focus on identifying and incorporating suitable chromophoric ligands that preserve nanoparticle stability and catalytic activity while introducing controlled optical features. The development of multifunctional systems combining catalytic and luminescent properties could open new perspectives in biomedical applications.

Finally, the observed correlation between active-site electron density and hydrogen activation rate provides a strong conceptual basis for further systematic investigations. The deliberate introduction of

more electron-withdrawing NHC ligands represents a rational strategy to modulate the electronic environment of the metal surface and, consequently, the kinetics of hydrogen spillover. A combined experimental and computational approach will be essential to quantitatively correlate ligand electronic parameters with catalytic performance, enabling predictive control over hydrogen activation processes. Such studies could significantly advance the fundamental understanding of spillover phenomena and contribute to the broader field of supported metal catalysis.

VI. ACKNOWLEDGMENT

At the end of this work, I would first of all like to sincerely thank all the people I had the privilege to work with over these three years. This journey has been much more than a research project: it has been a period of intense growth, both professionally and personally, made possible by the people who shared it with me. This obviously does not include just my tutor, Cristina, and my co-tutor, Mario, whose support and trust allowed me to face challenges with confidence and to develop a more critical and independent approach to research, but also all the students who worked with me in the lab. Thank you, Elisa, Happee, Michele, Mario, Giulia, and Anna, not only for your commitment and hard work, but also for the enthusiasm and positive atmosphere you brought every day. I had the opportunity to learn far beyond the technical aspects of research.

Thanks also to Elena, Elena, Daniele, Daniele, Luca, and all my former group members for the fruitful and pleasant collaboration we shared. I am grateful for the many discussions, suggestions, and discussions. I would also like to extend my gratitude to all the friends and colleagues I had the pleasure to collaborate with at UniMi. A big thank you goes as well to all the professors and technicians who generously dedicated their time to teaching me how to use the new techniques required for this project.

A big thank you also to Bert for hosting me at Penn State and being a great teacher, and to his group, Angela, Audrey, Kelle, Mary, Mohammad, Musa, Rebekah, and Tae Yong, for keeping me company and for the great work environment. Another thank you to Angela for all the work we did together. You always told me you learned a lot from me, but I learned a lot from you, too. To Rebekah and Audrey, for game time and the all-American experience of tailgating. To Kelle and Nick, for all the extra-university activities: kayaking and baseball games, fireworks nights, and for accompanying me in exploring the Pennsylvania wilderness, and for all the time we spent together.

Thank you also to all the colleagues and friends I spent time with over the last few years, for the events at the university, the Friday nights at "birri", all the lunches together, and everything else.


PENN STATE
FOOTBALL

VII. EXPERIMENTAL SECTION

Instruments

Experiments Conducted at UniMi

For catalytic studies, reactions were monitored *via* high-performance liquid chromatography (HPLC) using a Shimadzu LC-10ADvp (Shimadzu Corporation, Kyoto, Japan) chromatograph equipped with a RID-10A detector and Restek Ultra BiPh 5 μm column (Restek, Cernusco sul Naviglio, Italy). A 60:40 mixture of methanol and water was used as the eluent. Analyses were conducted with a 1.0 mL/min flow, with the column heated at 45 °C.

FTIR spectra were acquired on a JASCO FT/IR 4100 spectrometer (Jasco, Japan). For data acquisition, 3 mg of the samples were dispersed in 150 mg of dry, highly pure KBr.

X-ray powder diffraction (XRPD) patterns were measured using a Rigaku Miniflex 600 spectrometer (Rigaku, Japan) using the Cu Kα (λ = 0.1541 nm) radiation. Data were acquired in the 2θ range 10-100° with a step size of 0.05 and a counting time of 8 s per step. Rietveld refinement on the pattern was performed with Profox 5.2.5, modelling the background starting from an experimental pattern of the sample holder

The scanning electron microscopy (SEM) photographs were taken using a SEM TM4000 PLUS II instrument (NanoVision, Japan) using an acceleration voltage of 15 kV. Samples were placed on a conductive carbon adhesive. For SEM-EDS maps, an accelerating voltage of 20 kV was used.

Transmission electron microscopy (TEM) images were acquired on samples deposited on a copper TEM grid with a carbon sept using a Thalos L120C instrument (Thermo Fischer Scientific, Waltham, MA, USA) operating at 120 kV.

X-ray pohotoelectron spectroscopy (XPS) spectra were acquired with a Surface Sciences Instruments (SSI) M-Probe apparatus equipped with a monochromatic Al Kα source ($h\nu$ = 1486.6 eV). A spot size of 200 ÷ 750 μm and a pass energy of 25 eV were used during data acquisition.

Nuclear magnetic resonance (NMR) spectra were acquired on a NMR Bruker Advance operating at 9.4 T (400 MHz).

Experiments Conducted at PSU

Hydrogen adsorption experiments were performed on a Micromeritics 3Flex instrument.

In situ FTIR spectra were collected on a Bruker Invenio-R FTIR spectrometer in a heated (20-500 °C) transmission flow cell (Harrick Instruments). Gas flows were controlled using mass flow controllers (Bronkhorst), which were calibrated for each gas using a soap and bubble flow meter. H_2O and oxygen in the feed gases were minimized with moisture and oxygen scavenging traps (Restek, USA).

Thermogravimetric analysis (TGA) experiments were performed on a TA Instruments Discovery TGA 550-WaterTM analysis instrument. A heating ramp under 99.999% nitrogen (40 mL/min, Linde) was used to quantify mass loss.

Gold nanoparticle sizes were determined by imaging with scanning/transmission electron microscopy (STEM) using a Talos F200X microscope at an accelerating voltage of 200 kV. To prepare each sample, a small amount of catalyst was crushed in an agate mortar and pestle, then dispersed in isopropanol. A Cu TEM grid (Ted Pella, Inc.) was dipped into this suspension and allowed to dry before analysis. The average Au nanoparticle diameter was determined using ImageJ from nanoparticle diameter measurements.

Reagents and Materials

Graphene oxide suspension 8 mg/mL was purchased from Nanografi. GO sheets have dimensions in the 1-5 μm range.

Palladium chloride (purity > 99.9%) was purchased from Sigma Aldrich.

Zinc powder (99% purity) was purchased from Carlo Erba Reagents.

Thiophene (purity ≥ 99%) was purchased from Sigma Aldrich.

Nickel chloride hexahydrate (purity ≥98%) was purchased from Fluka.

Sodium borohydride in powder (purity > 95%) was purchased from TCI.

Nitrobenzene (purity > 99%) was purchased from Sigma Aldrich.

Hydrazine hydrate solution (85% w/w in water) was purchased from Carlo Erba Reagents.

Commercial catalyst Pd/C 5% w/w was purchased from Engelhard.

Aniline (purity > 99.5%) was purchased from Sigma Aldrich.

Nitrosobenzene (purity > 97%) was purchased from Sigma Aldrich.

Azobenzene (purity > 98%) was purchased from Sigma Aldrich.

Azoxybenzene (purity > 90%) was purchased from Sigma Aldrich.

Bromobenzene (99% purity) was purchased from Sigma Aldrich.

Imidazole (purity > 99%) was purchased from Sigma Aldrich.

Copper sulphate (purity ≥ 98%) was purchased from Sigma Aldrich.

Sodium bicarbonate (purity ≥ 99.5%)was purchased from Sigma Aldrich.

Ethyl iodide (98% purity) was purchased from Sigma Aldrich.

Benzyl bromide (98% purity) was purchased from Sigma Aldrich.

Ammonium hexafluorophosphate (purity > 95%) was purchased from Sigma Aldrich.

Tetrachloroauric acid solution 50.8 mmol/L was prepared by dissolving highly pure gold sheets in aqua regia, evaporating the excess of nitric acid, and diluting with MilliQ water. The final concentration was assessed with ICP-AAS.

Tetrachloroauric acid trihydrate (purity > 99.9%) was purchased from Sigma Aldrich.

Tetrahydrothiophene (99% purity) was purchased from Sigma Aldrich.

Sodium acetate anhydrous was prepared by drying the trihydrate compound (99.8% purity) purchased from Sigma Aldrich.

Potassium bromide (purity ≥ 99%) was purchased from Sigma Aldrich.

Urea (purity > 99%) was purchased from Sigma Aldrich.

Titania (anatase phase) was purchased from Tronox.

Titania (rutile phase) was purchased from Sigma Aldrich.

Activated carbon X40S was purchased from CAMEL.

Activated carbon Vulcan XC 72R was purchased from CABOT.

γ-alumina was purchased from Sigma Aldrich.

Ceria was purchased from Grace.

Chlorohydric acid was acquired from Sigma Aldrich.

Acetone was purchaser from Carlo Erba

Methanol was purchaser from Carlo Erba

Ethanol was purchaser from Sigma Aldrich

Toluene was purchaser from Sigma Aldrich

Dichloromethane was purchaser from Sigma Aldrich

Acetonitrile was purchaser from Sigma Aldrich

DMF was purchaser from Sigma Aldrich

THF was purchaser from Sigma Aldrich

Diethyl ether was purchaser from Sigma Aldrich

Chapter II Experimental Procedures

Synthesis of GO@nPd

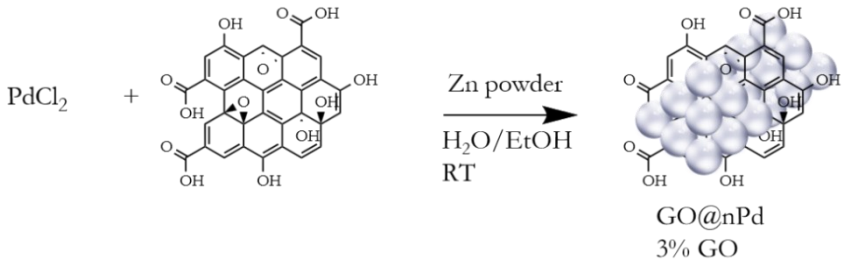

Reagent	V / µL	m / mg	MM / g/mol	n / mol	Eq.
$PdCl_2$	/	200.0	177.33	$1.14 \cdot 10^{-3}$	1
Zn	/	86.0	65.38	$1.32 \cdot 10^{-3}$	1.1
GO suspension 8 mg/mL	442.5	3.54	/	/	/

In a typical reaction, 12.5 mL of ethanol and 12.5 mL of MilliQ water are poured into a 50 mL round-bottom flask. Palladium chloride and GO suspension are added, and the mixture is sonicated for 30 minutes to disperse the GO sheets. Zinc powder is then added to the mixture under stirring, and the mixture is left to react for 24 h.

After 24 h, the stirring is stopped, and the product is decanted. The solid product is filtered on Hirsch and washed three times with a 0.1 M HCl solution to remove the excess of unreacted zinc, then with MilliQ to remove the traces of HCl.

XPS results

Sample	C 1s	Pd 3d	O 1s	N 1s	F 1s	Zn 2p	Cl 2p
GO@nPd fresh	44.2	15.5	37.0	/	/	1.8	1.5
GO@nPd used	7.3	3.1	18.6	2.6	3.1	0.3	/

XPS peak	Pd 3d B.E. / eV	Assignment	Peak area / %
GO@nPd fresh	335.7–341.0	Pd	71.2
	336.9–342.2	PdO	28.8
GO@nPd used	334.5–339.8	Pd	82.5
	336.3–341.6	PdO	17.5

Binding energy C1s [eV]	**284.6**	**285.6**	**286.8**	**289.4**
Assignment	**C sp^2 / %**	**C sp^3 / %**	**C-O-C / %**	**O-C=O / %**
GO@nPd fresh	13.0	58.4	23.8	4.8
GO@nPd used	7.5	36.1	34.7	21.7

Binding energy O1s [eV] Assignment	**530.5 PdO/O-C=O / %**	**532.3 C=O / %**	**533.8 C-O-C/C-OH / %**	**535.4 Adsorbed water / %**
GO@nPd fresh	5.7	47.1	39.7	7.5
GO@nPd used	6.1	40.1	35.7	18.1

Synthesis of RGO@nPd

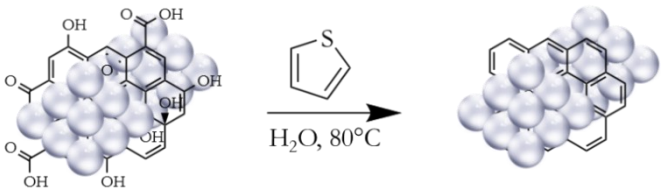

GO@nPd
3% GO

RGO@nPd

Reagent	V / mL	d / g/mL	m / mg	MM / g/mol	n / mol
GO@nPd	/	/	80.0	/	/
thiophene	1.000	1.05	1050	84.14	$1.25 \cdot 10^{-2}$

In a typical reaction, 80 mg of GO@nPd are suspended in 10 mL of MilliQ water in a round-bottom flask. Thiophene is then added, and the round-bottom flask is sealed under nitrogen atmosphere. The mixture is stirred for 24 h in an oil bath at 80 °C.

After 24 h, the mixture is filtered on Hirsch, washed with acetone, methanol, and DCM to remove thiophene and oligoolefins, and then dried in vacuum.

Synthesis of GO@Ni

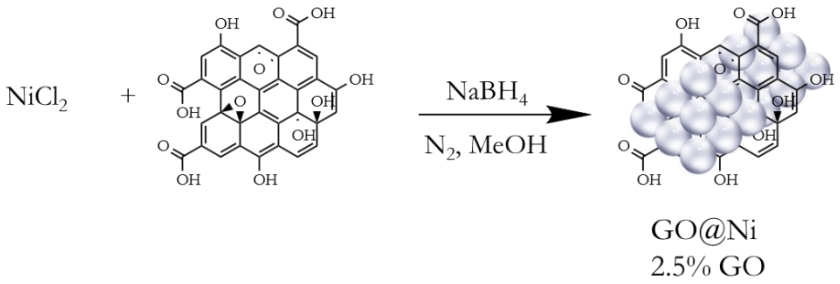

Reagent	V / µL	m / mg	MM / g/mol	n / mol	Eq-
$NiCl_2 \cdot 6H_2O$	/	167.0	237.69	$7.0 \cdot 10^{-4}$	1
$NaBH_4$	/	128	37.83	$3.38 \cdot 10^{-3}$	5
GO suspension 8 mg/mL	111.0	0.89	/	/	/

In a typical reaction, 25 mL of methanol are added to a 50 mL two-neck round-bottom flask. $NiCl_2$ and GO suspension are added, and the mixture is sonicated for 30 min to disperse the GO sheets. The system is then poured under nitrogen atmosphere, and $NaBH_4$ is added under nitrogen flow.

After 30 min, the solid product is filtered on Hirsh and washed with water and methanol. The product is then left to dry in the air.

Synthesis of RGO@Ni

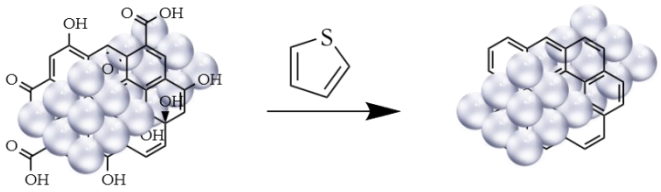

GO@Ni
2.5% GO

RGO@Ni

Reagent	V / mL	d / g/mL	m / mg	MM / g/mol	n / mol
GO@nPd	/	/	110.0	/	/
thiophene	1.000	1.05	1050	84.14	$1.25 \cdot 10^{-2}$

In a typical reaction, 80 mg of GO@nPd are suspended in 20 mL of methanol in a round-bottom flask. Thiophene is then added, and the round-bottom flask is sealed under nitrogen atmosphere. The mixture is stirred for 24 h in an oil bath at 80 °C.

After 24 h, the mixture is filtered on Hirsch, washed with acetone, methanol, and DCM to remove thiophene and oligoolefins, and then dried in vacuum.

Synthesis of palladium black

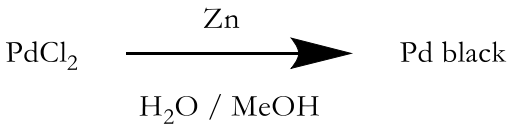

Reagent	m / mg	MM / g/mol	n / mol	Eq.
$PdCl_2$	200.0	177.33	$1.14 \cdot 10^{-3}$	1
Zn	86.0	65.38	$1.32 \cdot 10^{-3}$	1.1

In a typical reaction, 12.5 mL of ethanol and 12.5 mL of MilliQ water are poured into a 50 mL round-bottom flask. Palladium chloride is added, and the mixture is sonicated for 30 minutes. Zinc powder is then added to the mixture under stirring, and the mixture is left to react for 24 h.

After 24 h, the stirring is stopped, and the product is decanted. The solid product is filtered on Hirsch and washed three times with a 0.1 M HCl solution to remove the excess of unreacted zinc, then with MilliQ to remove the traces of HCl.

Synthesis of nickel powder

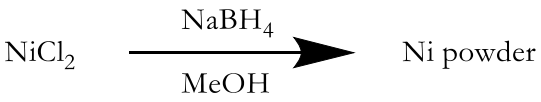

Reagent	V / µL	m / mg	MM / g/mol	n / mol	Eq.
$NiCl_2 \cdot 6H_2O$	/	167.0	237.69	$7.0 \cdot 10^{-4}$	1
$NaBH_4$	/	128	37.83	$3.38 \cdot 10^{-3}$	5

In a typical reaction, 25 mL of methanol are added to a 50 mL two-neck round-bottom flask. $NiCl_2$ is added. The system is then poured under nitrogen atmosphere, and $NaBH_4$ is added under nitrogen flow.

After 30 min, the solid product is filtered on Hirsh and washed with water and methanol. The product is then left to dry in the air.

Catalytic Reduction of Nitrobenzene – Pd-based catalysts

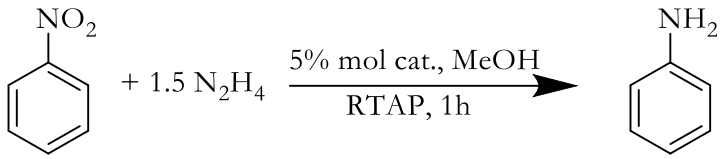

[only product]

Reagent	V / µL	d / g/mL	m / mg	MM / g/mol	n / mol	Eq.
Nitrobenzene	40.0	1.20	48.0	123.11	$3.90 \cdot 10^{-4}$	1
Hydrazine hydrate	44.6	1.03	39.0	50.06	$7.80 \cdot 10^{-4}$	2

In a typical reaction, 40 µL of nitrobenzene are dissolved in 6 mL of methanol. The catalyst is then added to the solution in the proper amount to achieve 5% mol Pt (e.g., 3 mg of GO@nPd, 63 mg for Pd/C). Hydrazine is added last to start the reaction.

After one hour, 20 µL of bromobenzene are added as internal standard, and the catalyst is removed *via* centrifugation. The solution is analyzed with HPLC for product identification and quantification.

For reuse tests, the catalyst is washed three times with fresh methanol and centrifuged prior to reuse.

The following table reports results of yield in aniline during the first-use time-course study.

Time / min	GO@nPd / %	RGO@nPd / %	Pd/C / %	Pd Black / %
0	0	0	0	0
5	35	32	87	10
10	45	51	98	16
15	53	64	>99	22
30	68	85	>99	35
45	71	94	>99	43
60	74	97	>99	46

Results of reuse tests:

Catalyst	Use	Conversion / %	Selectivity / %	Yield / %
GO@nPd	1	74	>99	74
	2	74	>99	74
	3	69	>99	69
	4	76	>99	76
	5	73	>99	73
RGO@nPd	1	97	>99	97
	2	14	>99	14
	3	12	>99	12
	4	12	>99	12
	5	10	>99	10
Pd/C	1	>99	>99	>99
	2	93	>99	93
	3	92	>99	92
	4	65	>99	65
	5	26	>99	26
Pd black	1	46	>99	46
	2	31	>99	31
	3	27	>99	27
	4	11	>99	11
	5	8	>99	8

Results of yields during time-course study for GO@nPd over five consecutive reaction runs:

Time / min	1st use	2nd use	3rd use	4th use	5th use
0	0	0	0	0	0
5	35	23	18	9	19
10	45	36	27	30	28
15	53	39	37	40	38
30	68	56	56	60	55
45	71	71	63	71	68
60	74	74	69	76	73

Results of yields during time-course study for RGO@nPd in two consecutive reaction runs:

Time / min	1st use	2nd use
0	0	0
5	32	2
10	51	5
15	64	7
30	85	12
45	94	13
60	97	14

Catalytic Reduction of Nitrobenzene – Ni-based catalysts

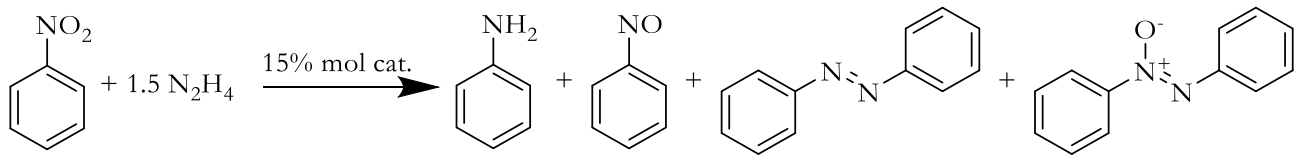

Reagent	V / µL	d / g/mL	m / mg	MM / g/mol	n / mol	Eq.
Nitrobenzene	40.0	1.20	48.0	123.11	$3.90 \cdot 10^{-4}$	1
Hydrazine hydrate	36.8	1.03	32.2	50.06	$6.44 \cdot 10^{-4}$	1.65

In a typical reaction, 40 µL of nitrobenzene are dissolved in 6 mL of methanol or water. The catalyst is then added to the solution in the proper amount to achieve 15% mol Ni (about 3 mg). Hydrazine is added last to start the reaction. The table reports the quantity for tests with 10% hydrazine excess. Also 40%, 70% and 100% hydrazine excess were tested.

After the reaction, 20 µL of bromobenzene are added as internal standard, and the catalyst is removed *via* centrifugation. For tests conducted in water, 6 mL of methanol are added prior to this step to solubilize the water-insoluble products. The solution is then analyzed with HPLC for product identification and quantification.

For reuse tests, the catalysts are washed three times with fresh methanol and centrifuged prior to reuse.

Entry	Catalyst	Solvent	Air / N_2	T / °C	Hydrazine eq.	Yield / %
1	RGO@Ni	Water	Air	35	1.1	82
2	RGO@Ni	Water	Air	35	1.4	98
3	RGO@Ni	Water	Air	35	1.7	>99
4	RGO@Ni	Water	Air	35	2.0	>99
5	RGO@Ni	Water	N_2	20	1.1	>99
6	RGO@Ni	Water	N_2	20	1.4	>99

Entry	Catalyst	Solvent	Air / N_2	T / °C	Hydrazine eq.	Yield / %
7	RGO@Ni	Water	N_2	20	1.7	93
8	RGO@Ni	Water	N_2	20	2.0	95
9	RGO@Ni	Water	Air	20	1.1	>99
10	RGO@Ni	Water	Air	20	1.4	>99
11	RGO@Ni	Water	Air	20	1.7	>99
12	RGO@Ni	Water	Air	20	2.0	97
13	GO@Ni	Water	N_2	20	1.1	99
14	GO@Ni	Water	N_2	20	1.4	98
15	GO@Ni	Water	N_2	20	1.7	>99
16	GO@Ni	Water	N_2	20	2.0	95
17	GO@Ni	Water	Air	20	1.1	25
18	GO@Ni	Water	Air	20	1.4	90
19	GO@Ni	Water	Air	20	1.7	>99
20	GO@Ni	Water	Air	20	2.0	>99
21	GO@Ni	Water	N_2	35	1.1	61
22	GO@Ni	Water	N_2	35	1.4	70
23	GO@Ni	Water	N_2	35	1.7	83
24	GO@Ni	Water	N_2	35	2.0.	92
25	RGO@Ni	Water	N_2	35	1.1	77
26	RGO@Ni	Water	N_2	35	1.4	85
27	RGO@Ni	Water	N_2	35	1.7	92
28	RGO@Ni	Water	N_2	35	2.0	>99
29	GO@Ni	Water	N_2	35	1.1	62

Entry	Catalyst	Solvent	Air / N_2	T / °C	Hydrazine eq.	Yield / %
30	GO@Ni	Water	N_2	35	1.4	>99
31	GO@Ni	Water	N_2	35	1.7	>99
32	GO@Ni	Water	N_2	35	2.0	>99
33	GO@Ni	MeOH	Air	35	1.1	7
34	GO@Ni	MeOH	N_2	35	1.1	6
35	GO@Ni	Water	N_2	50	1.1	20
36	RGO@Ni	Water	N_2	50	1.1	67
37	GO@Ni	MeOH	N_2	50	1.1	9
38	GO@Ni	MeOH	N_2	50	1.4	9
39	GO@Ni	MeOH	N_2	50	1.7	15
40	GO@Ni	MeOH	N_2	50	2.0	13
41	RGO@Ni	Water	Air	50	1.1	68

Comparison of the catalytical activity of GO@Ni, RGO@Ni and Ni over five consecutive reaction runs.

Catalyst	Use	Conversion / %	Selectivity / %	Yield / %
GO@Ni	1	>99	>99	>99
	2	>99	99	99
	3	97	99	96
	4	92	70	64
	5	61	61	37
RGO@Ni	1	>99	>99	>99
	2	>99	>99	>99
	3	>99	>99	>99
	4	>99	>99	>99
	5	>99	>99	>99

Catalyst	Use	Conversion / %	Selectivity / %	Yield / %
Ni	1	>99	97	97
	2	>99	>99	>99
	3	87	66	57
	4	91	74	67
	5	57	65	37

Time-course study of reaction catalyzed by RGO@Ni

Time / min	Conversion	Selectivity	Yield
0	0	/	0
5	0	/	0
10	0	/	0
15	0	/	0
25	0	/	0
34	44	>99	44
45	49	>99	49
60	63	98	62
85	85	74	63
110	89	>99	89
230	>99	>99	>99

Results of reaction catalyzed by different amount of RGO@Ni

Catalyst amount / %	Conversion	Selectivity	Yield
15.0	>99	>99	>99
12.5	>99	>99	>99
11.0	>99	>99	>99
7.5	>99	>99	>99
5.5	>99	90	90

Chromatography methods

In the following pages, a few chromatograms are reported as examples.

Reference for hydrazine

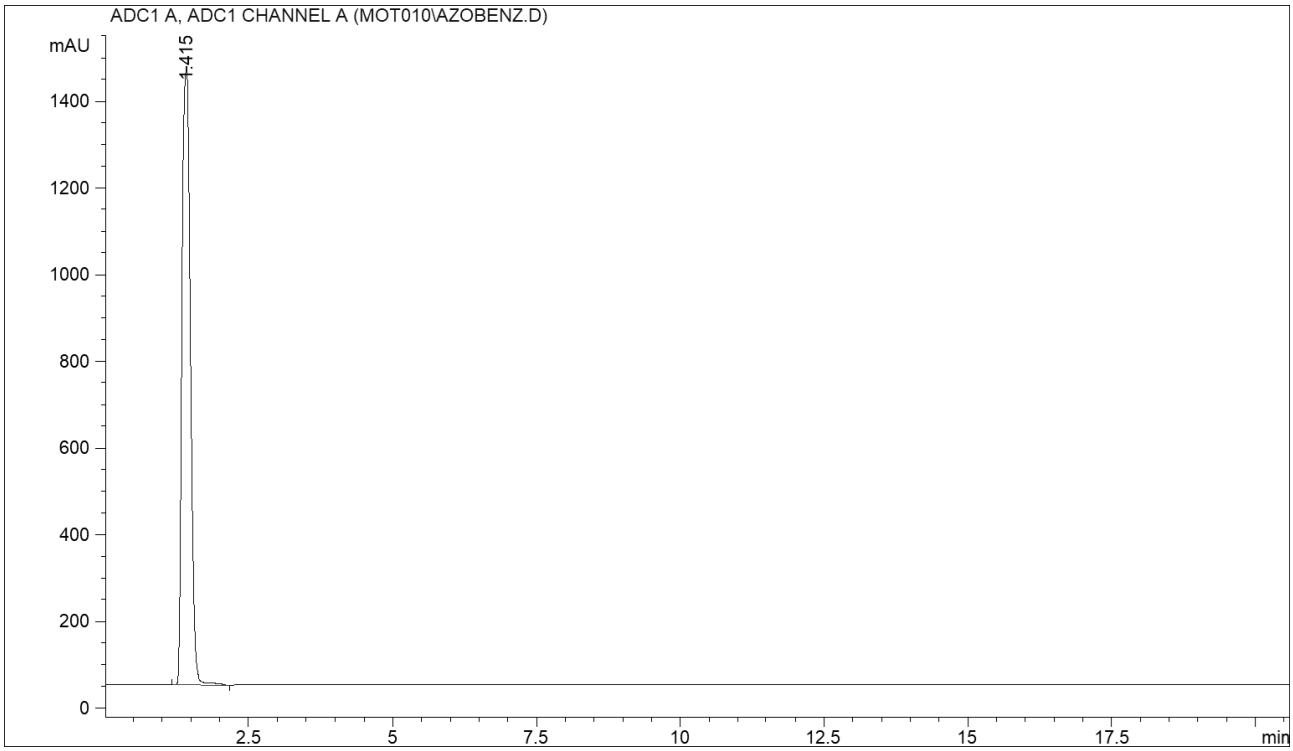

Reference for nitrobenzene

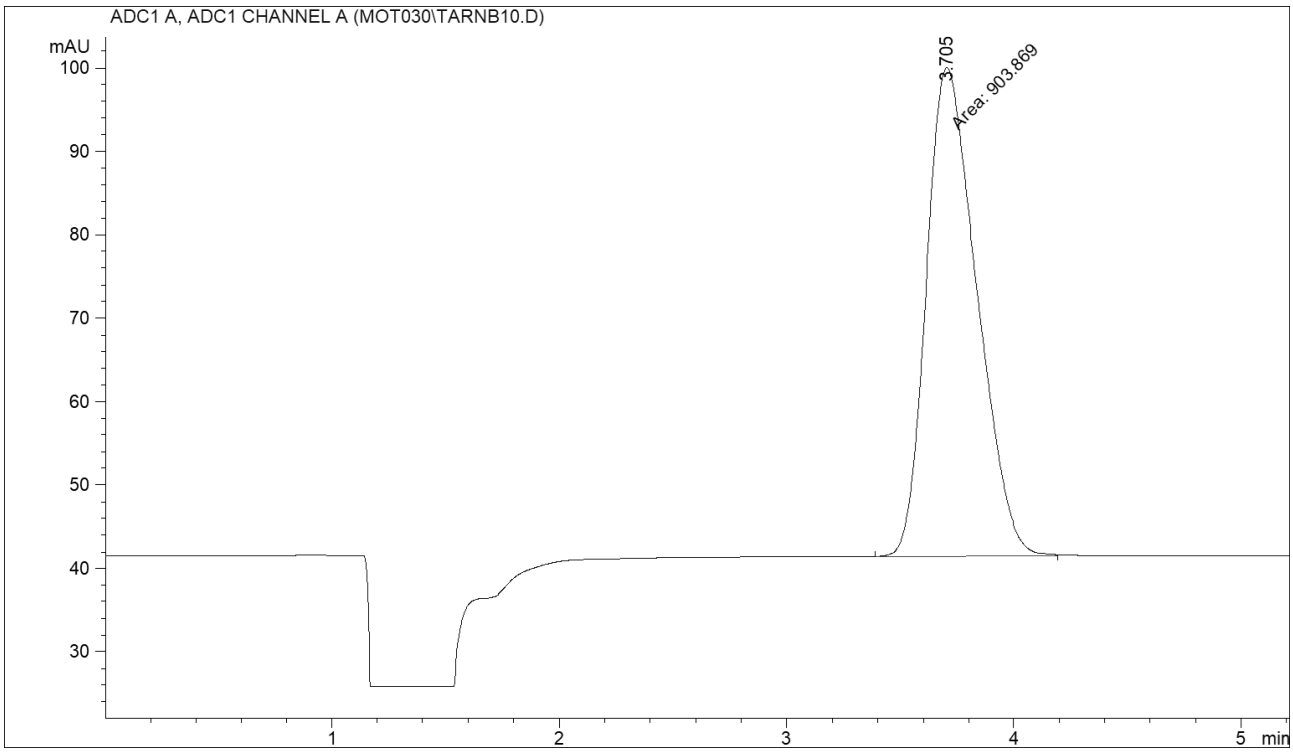

References for aniline (2 min), nitrobenzene (4 min), and bromobenzene (5.2 min)

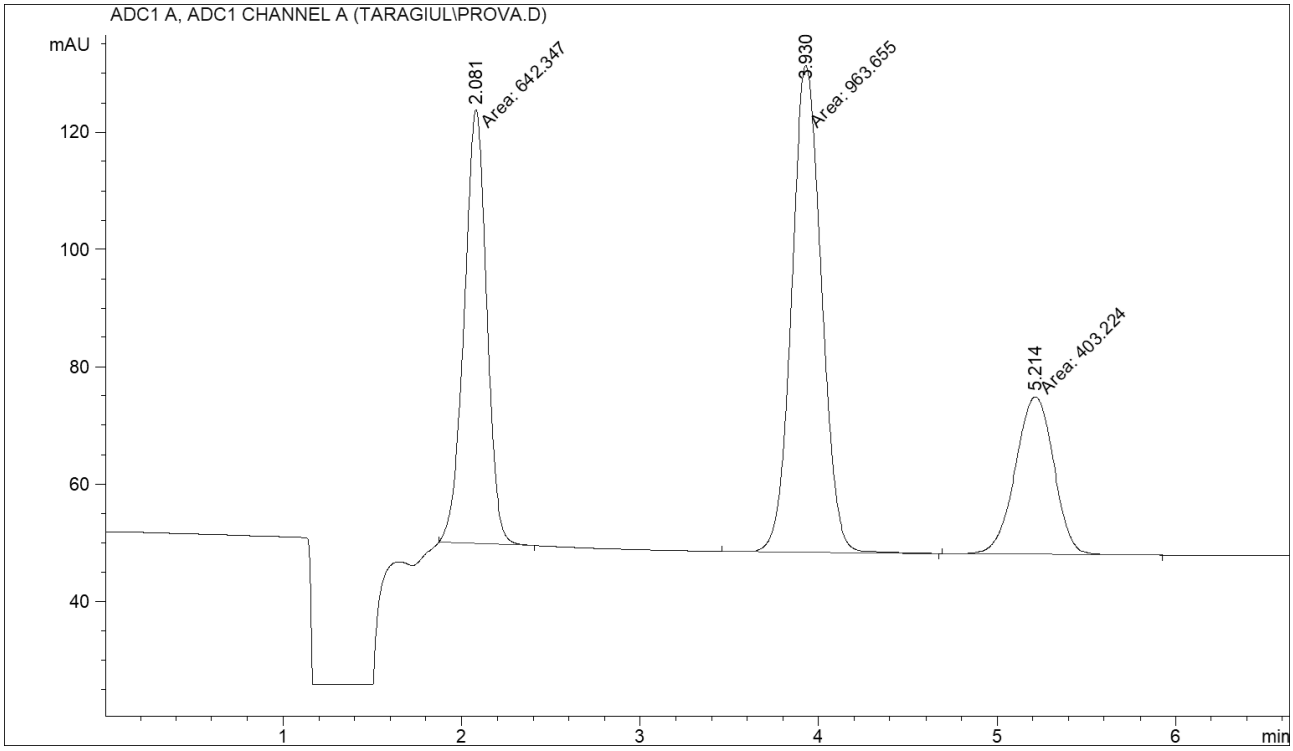

Reference for nitrosobenzene

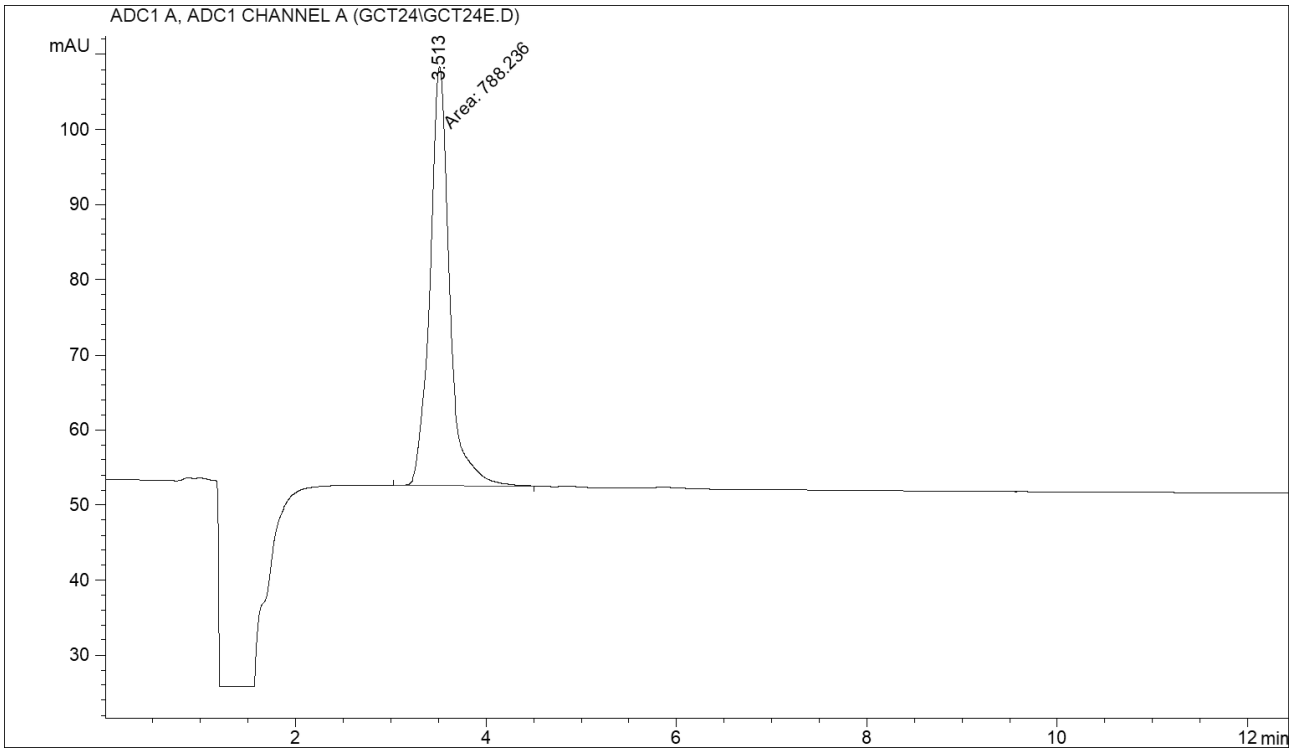

Reference for azobenzene

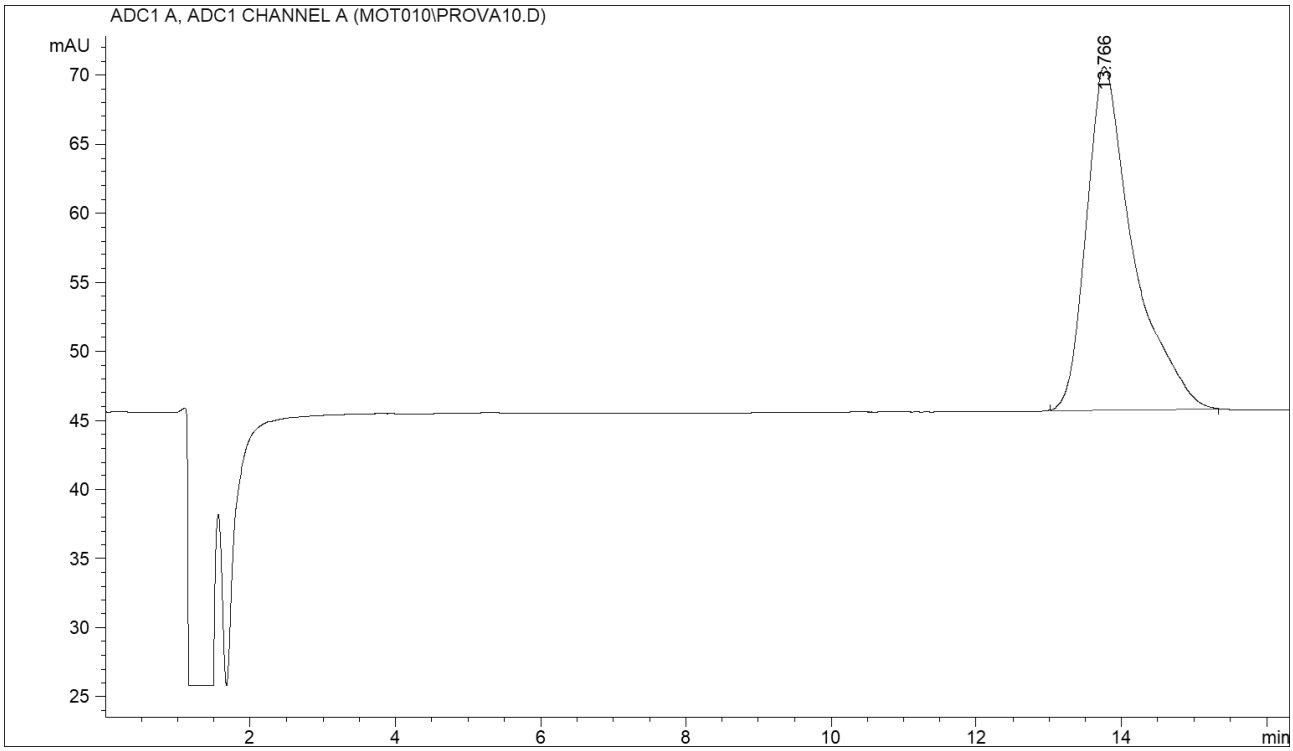

Reference for azoxybenzene

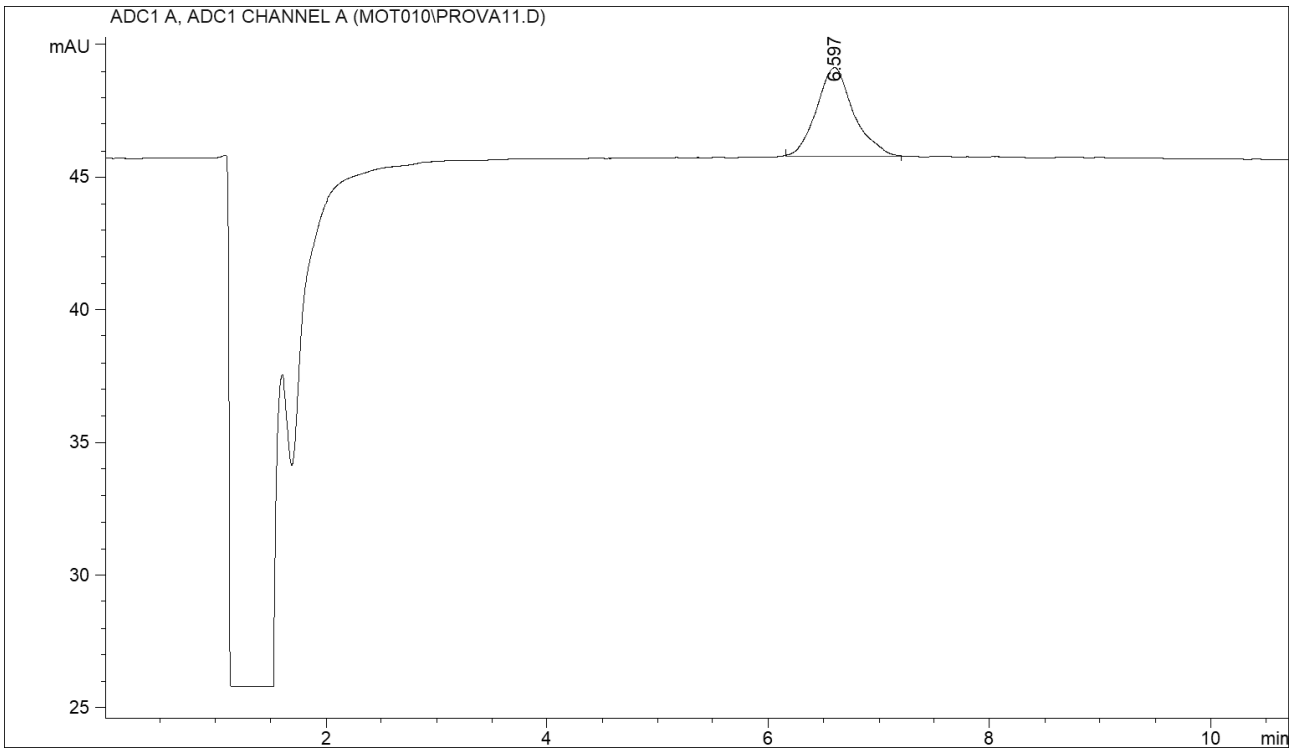

Example of chromatogram containing a mixture of products

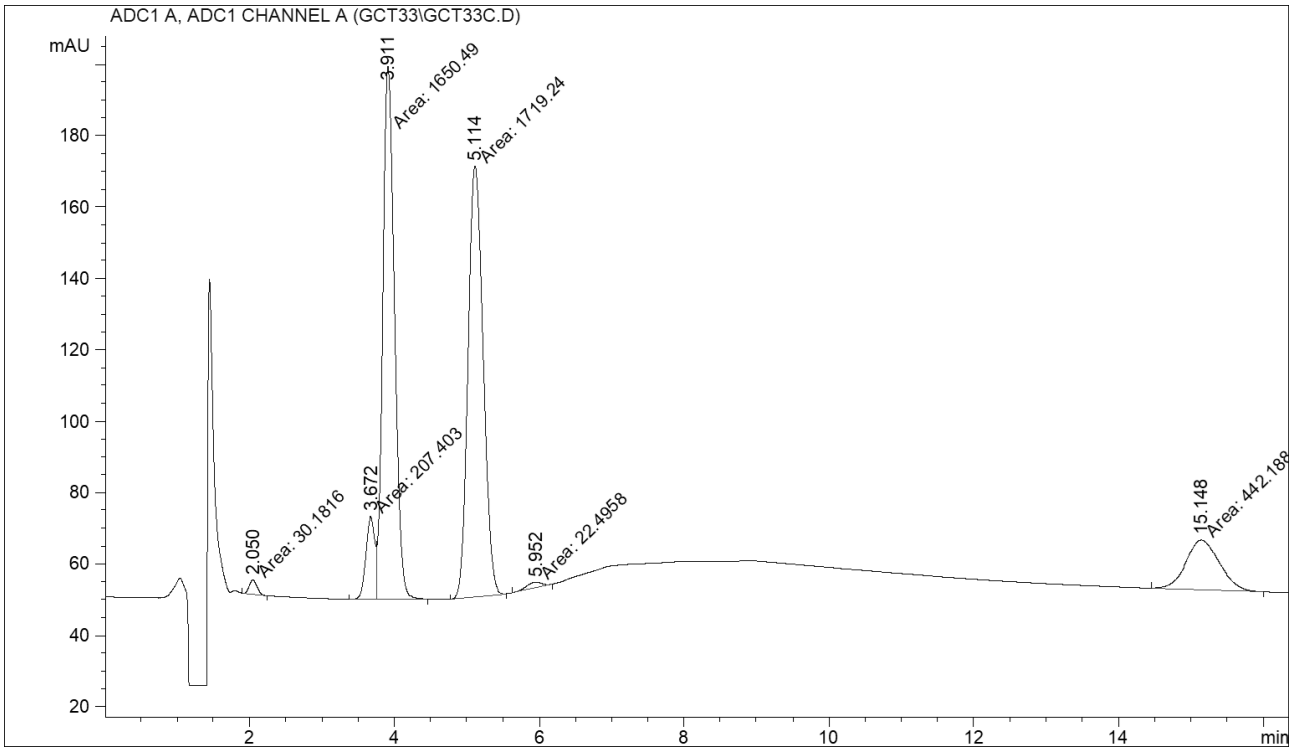

Example of chromatogram containing aniline, bromobenzene and a few traces of byproducts

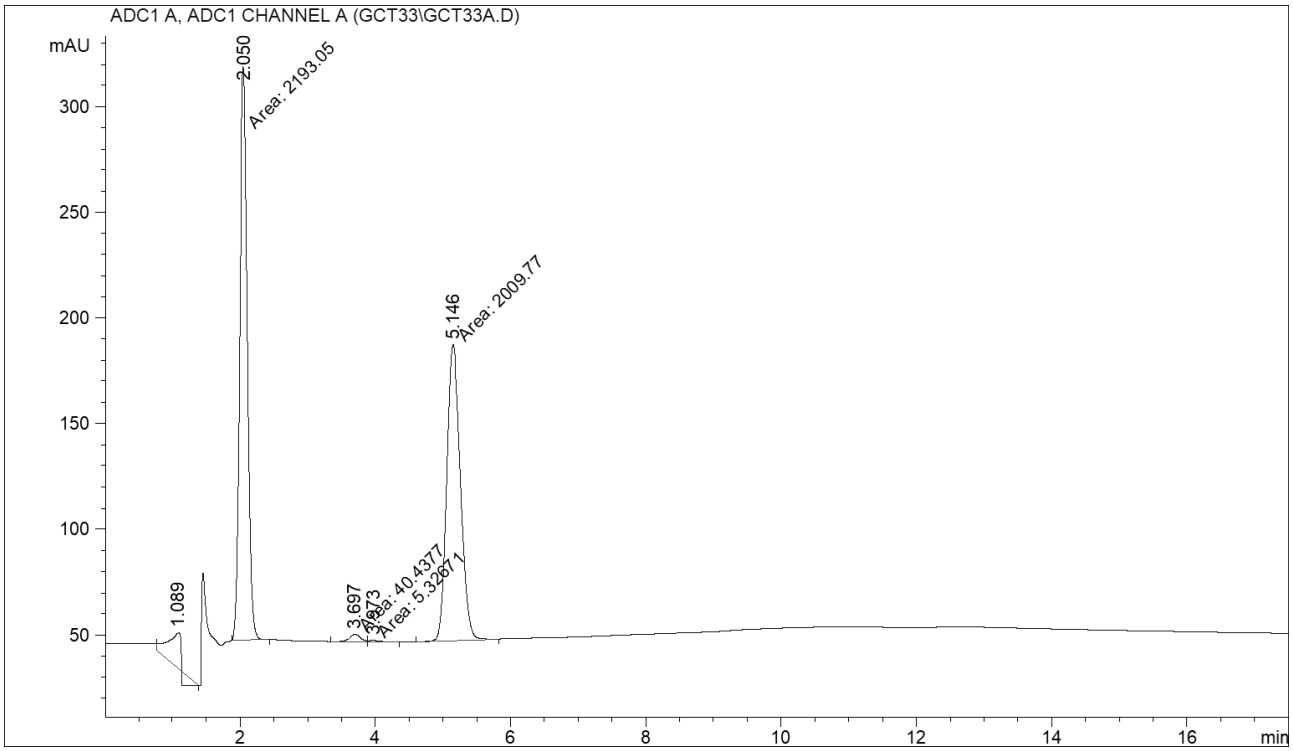

Chapter III Experimental Procedures

Synthesis of iso-TT

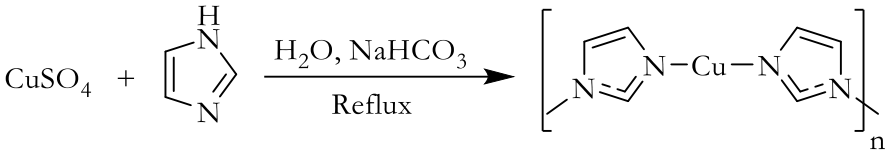

Reagents	m / g	MM / g/mol	n / mol	Eq.
Imidazole	56.33	68.08	0.827	3
$NaHCO_3$	185.67	80.01	2.317	8
$CuSO_4 \cdot 5H_2O$	68.61	249.69	0.275	1

In a typical reaction, imidazole and sodium bicarbonate are dissolved in a 3 L round-bottom flask with 2 L of MilliQ water. Thereafter, copper sulphate is dissolved in 500 mL of MilliQ and slowly added to the mixture. The mixture is stirred for five hours, then the copper diimidazolate polymer is filtered on Buchner funnel and dried in the oven for 48 h.

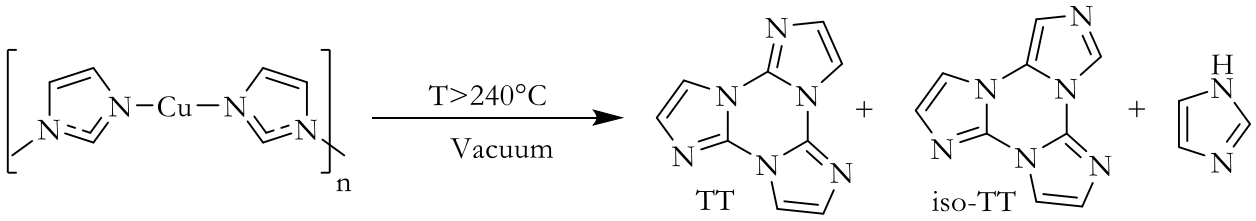

Once dry, the compound is poured into a 1 L round-bottom flask connected to a glass tube. The system is evacuated and heated with a temperature ramp of 230 °C – 260 °C – 280 °C – 300 °C, keeping each temperature steady for one hour. After three hours at 300 °C, the system is slowly cooled to room temperature. The sublimate in the glass tube is collected, dissolved in DCM, and filtered to remove impurities. The product is crystallized from hot methanol to get rid of unreacted imidazole. The product in toluene is evaporated to dryness and purified with preparative HPLC with the following gradient:

1 CV in 100% DCM, from 0% to 30% of ACN in 10 CV, from 30% to 35% of ACN in 4 CV.

The products were characterized by NMR spectroscopy.

^{1}H-NMR of TT in DMSO-d6

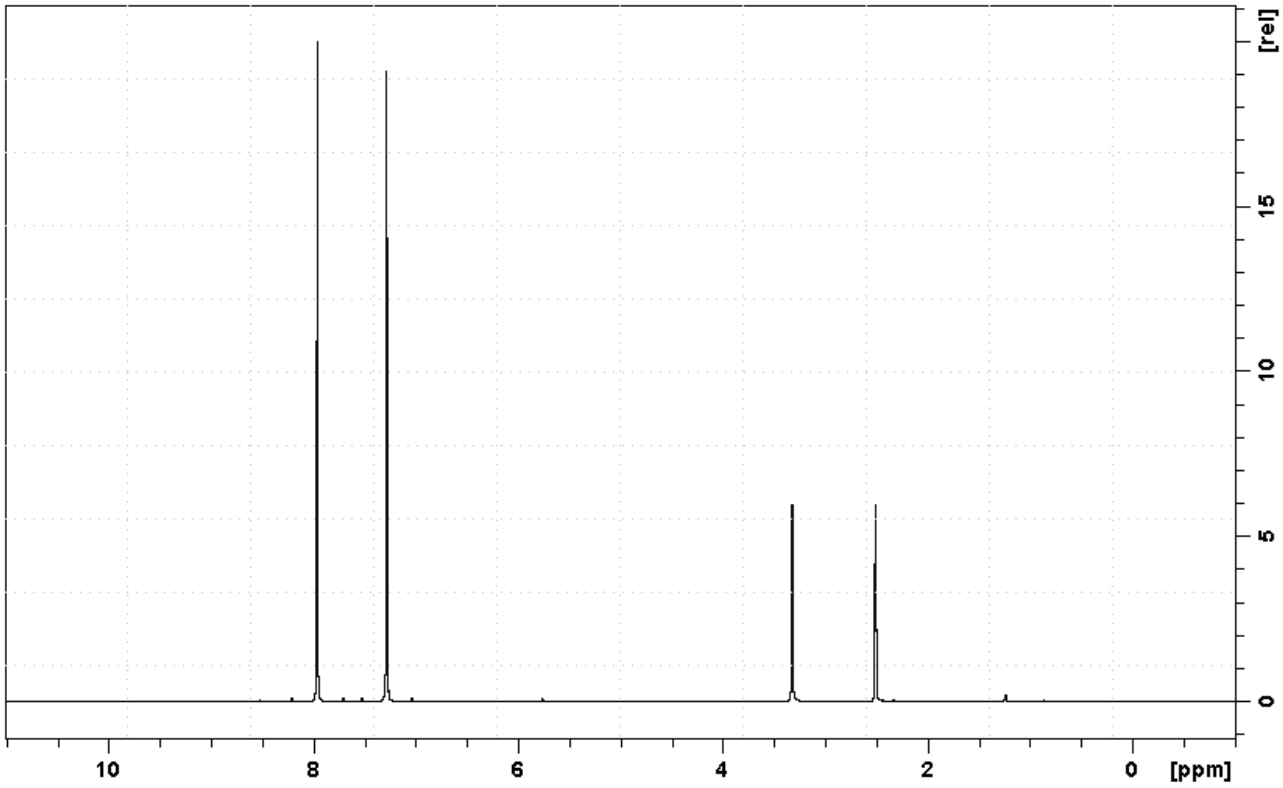

^{1}H-NMR of TT in DMSO-d6, magnification of the aromatic peaks. 7.96 ppm (d, 3H, J^{3} 2.68 Hz); 7.28 ppm (d, 3H, J^{3} 2.68 Hz).

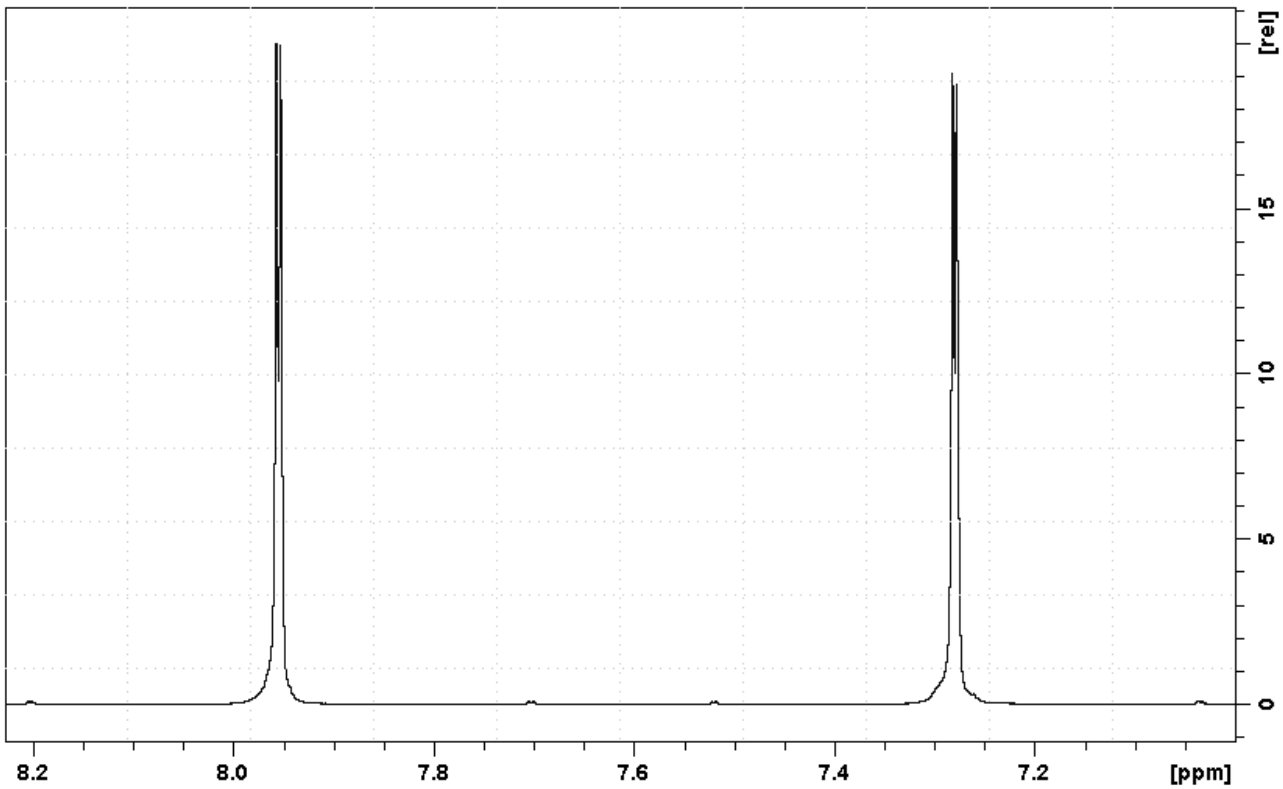

^{1}H-NMR of iso-TT in DMSO-d6

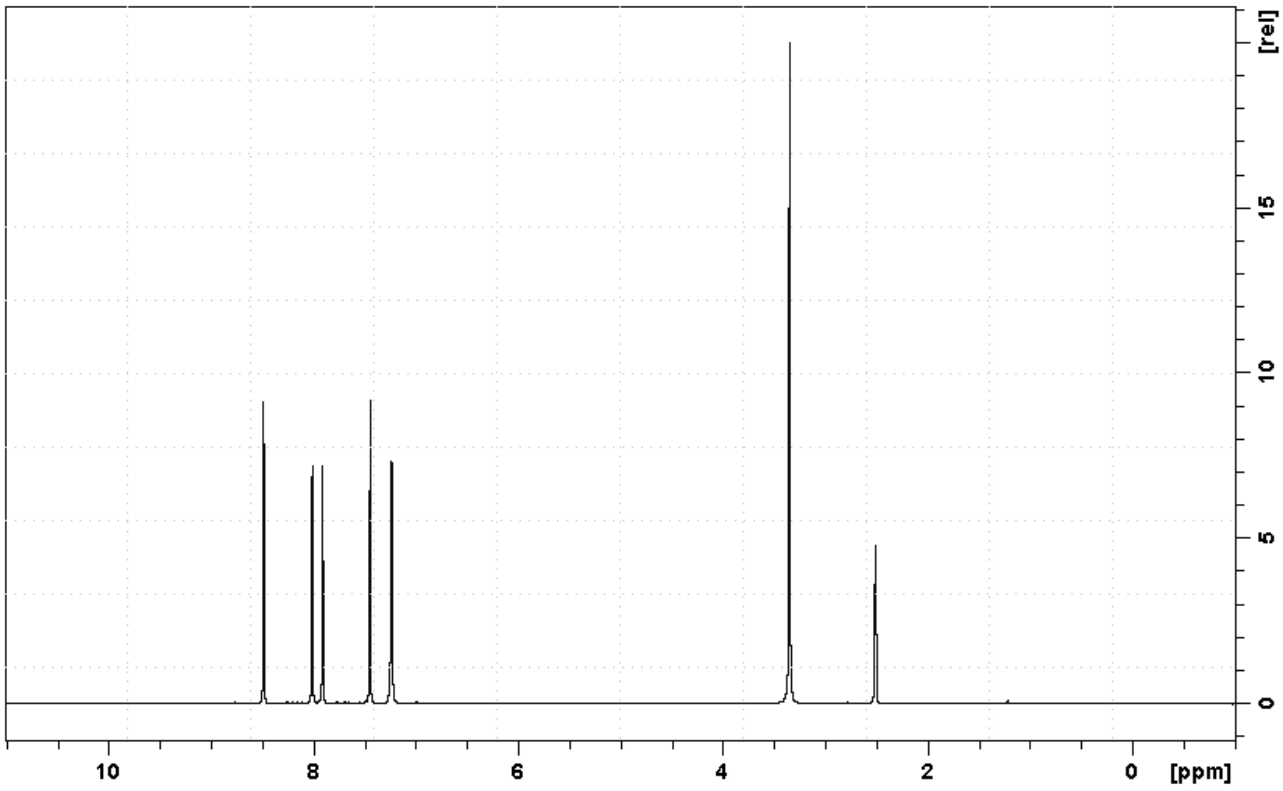

^{1}H-NMR of iso-TT in DMSO-d6, magnification of aromatic peaks. 8.48 ppm (s, 1H), 8.01 ppm (d, 1H, J^{3}1.34 Hz), 7.91 ppm (d, 1H, J^{3}1.51 Hz), 7.44 ppm (s, 1H), 7.24 ppm (d, 1H, J^{3} 1.46 Hz), 7.23 ppm (d, 1H, J^{3} 1.34 Hz)

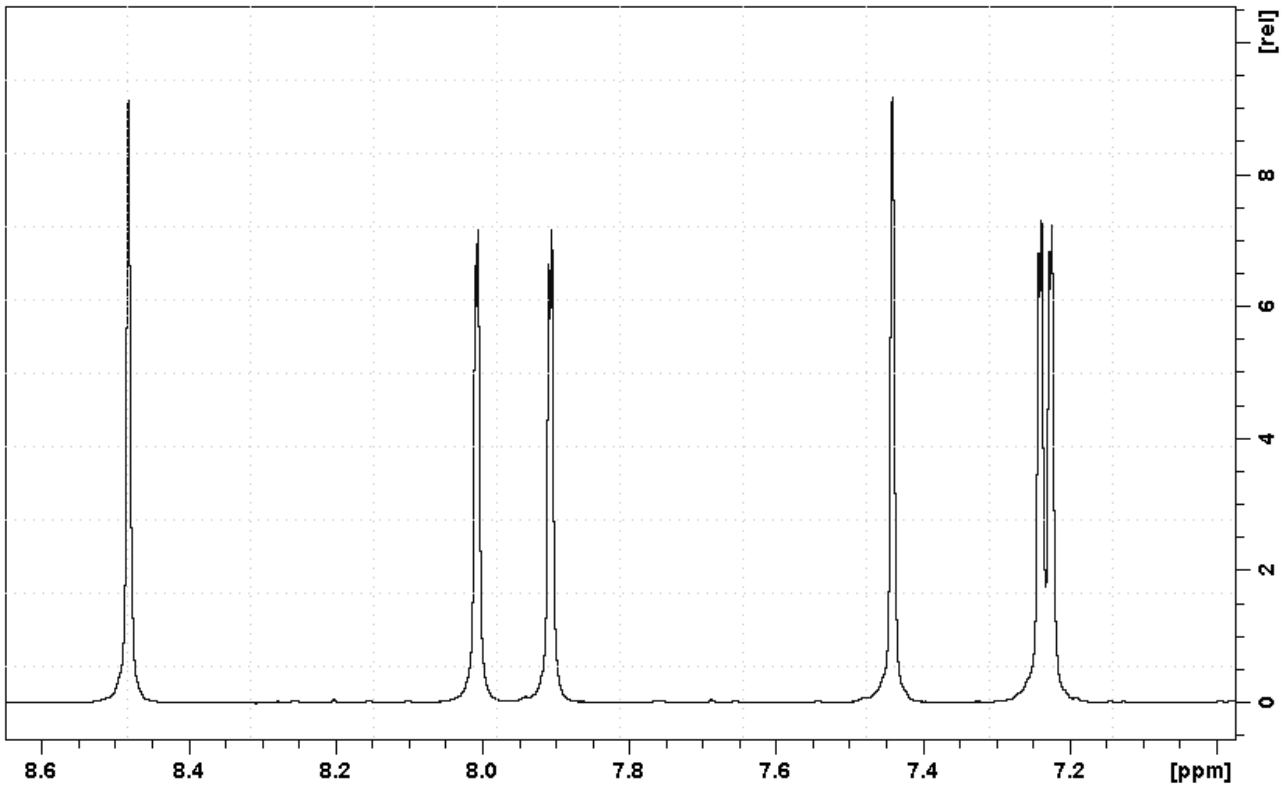

Synthesis of iso-TTEtHI

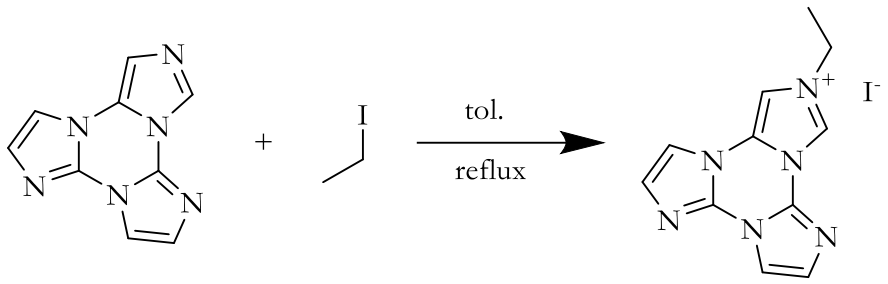

Reagents	V / µL	d / g/mL	m / g	MM / g/mol	n / mol	Eq.
iso-TT	/	/	1.000	198.19	$5.05 \cdot 10^{-3}$	1
Ethyl iodide	690.4	2.28	1.573	155.97	$1.01 \cdot 10^{-2}$	2

In a typical reaction, 1 g of iso-TT is dissolved in 30 mL of toluene in a pressure tube, then ethyl iodide is added. The system is placed in nitrogen atmosphere, and the mixture is refluxed for 48 hours and then cooled down to room temperature.

The product is isolated with water-toluene extraction, and the water fractions are evaporated to dryness to obtain iso-TTEtHI. Recrystallization from hot methanol allowed the product to be obtained with high purity.

The product was characterized by NMR spectroscopy.

^{1}H-NMR: 10.40 ppm (s, 1H), 8.48 ppm (s, 1H), 8.21 ppm (d, 1H), 8.13 ppm (d, 1H), 7.48 ppm (d, 1H), 7.40 ppm (d, 1H), 4.52 ppm (q, 2H), 1.57 ppm (t, 3H).

^{1}H-NMR of iso-TTEtHI in DMSO-d6

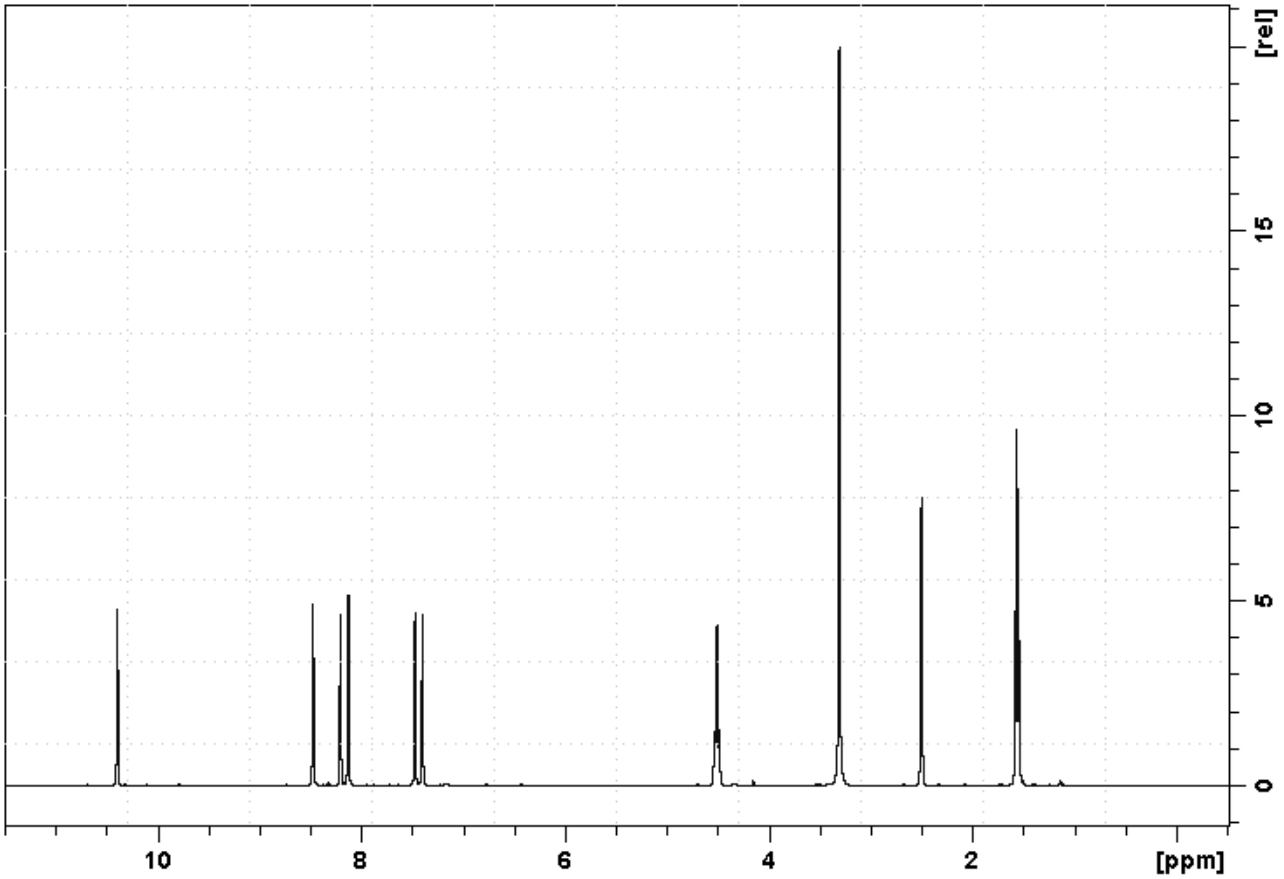

^{1}H-NMR of iso-TTEtHI in DMSO-d6, magnification of aromatic peaks.

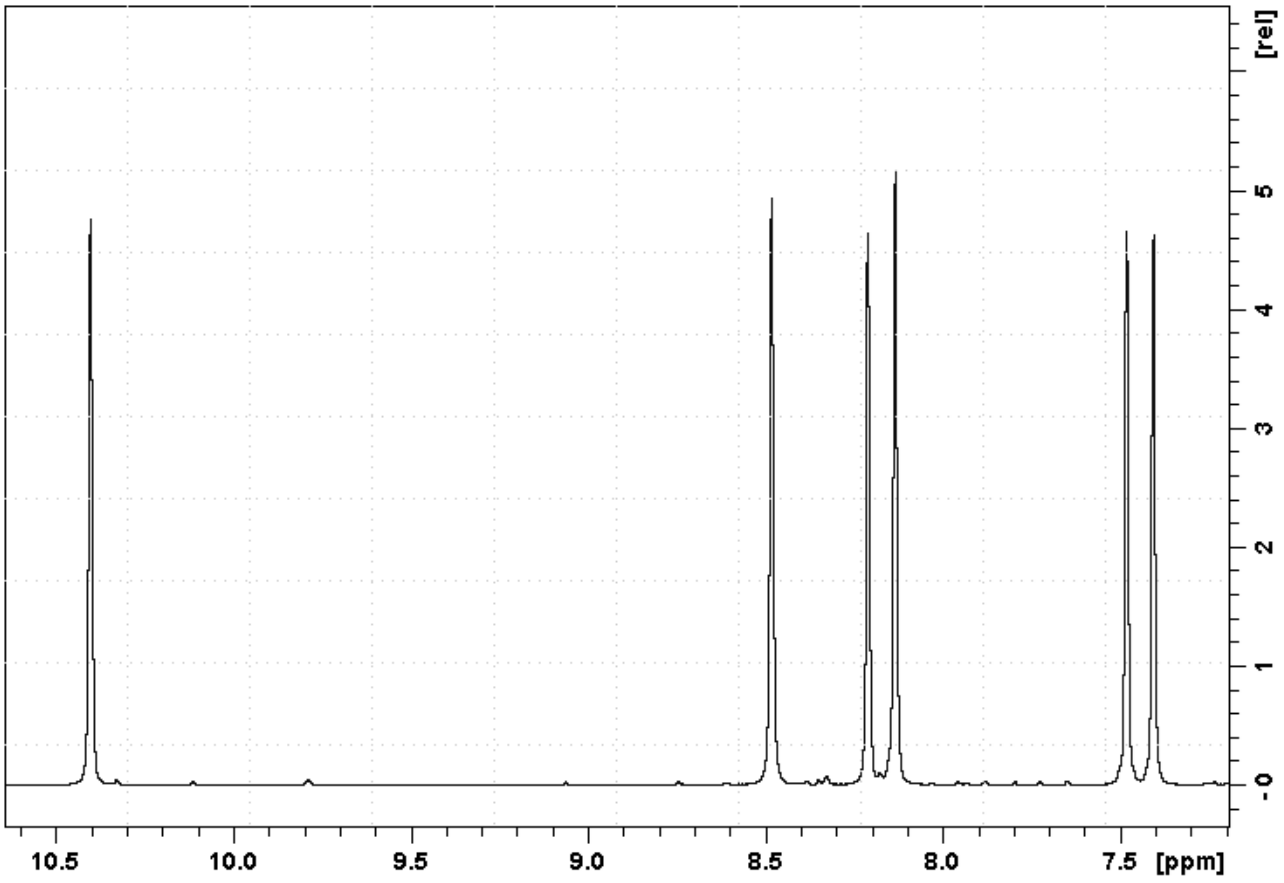

^{1}H-NMR of iso-TTEtHI in DMSO-d6, magnification of aliphatic peaks.

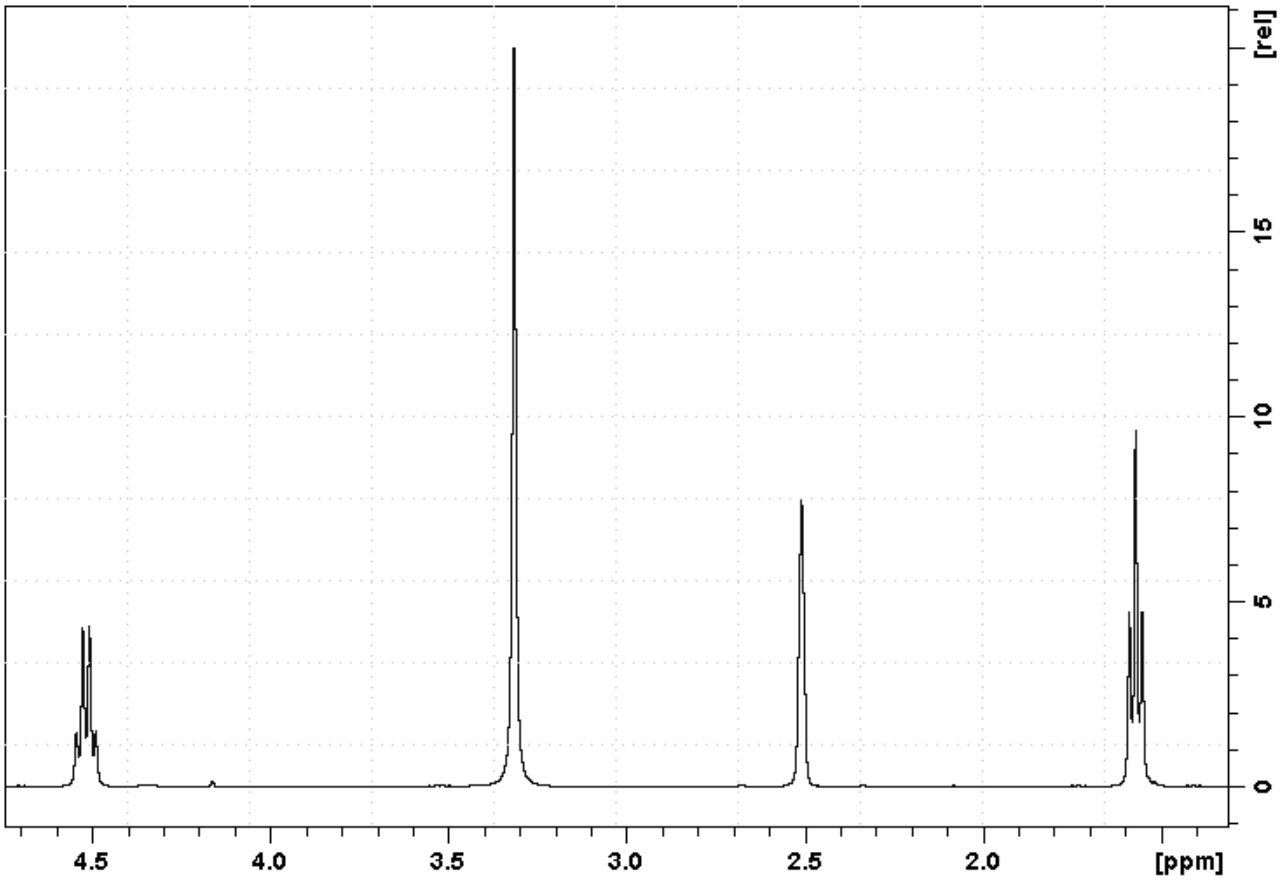

Synthesis of iso-TTBnHBr

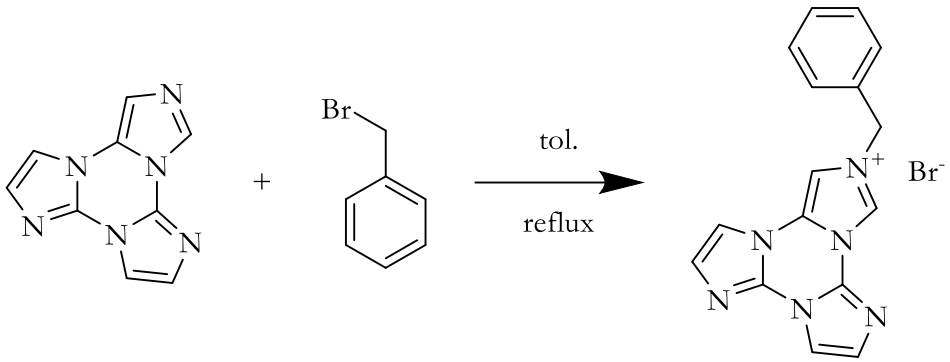

Reagents	V / μL	d / g/mL	m / g	MM / g/mol	n / mol	Eq.
iso-TT	/	/	1.000	198.19	$5.05 \cdot 10^{-3}$	1
Benzyl bromide	1,199	1.44	1.726	171.04	$1.01 \cdot 10^{-2}$	2

In a typical reaction, 1 g of iso-TT is dissolved in 30 mL of toluene in a pressure tube, then benzyl bromide is added. The system is placed in nitrogen atmosphere, and the mixture is refluxed for 48 hours and then cooled down to room temperature.

The product is isolated with water-toluene extraction, and the water fractions are evaporated to dryness to obtain iso-TTBnHBr. Recrystallization from hot methanol allowed the product to be obtained with high purity.

The product was characterized by NMR spectroscopy.

^{1}H: 10.71 ppm (d, 1H), 8.51 ppm (d, 1H), 8.21 ppm (m, 2H), 7.60-7.35 ppm (m, 7H), 5.80 (s, 2H)

^{13}C: 135.1, 134.5, 132.7, 129.6, 129.6, 129.5, 129.4, 129.1, 114.6, 114.2, 53.9, 49.1

^{1}H-NMR of iso-TTBnHBr in DMSO-d6

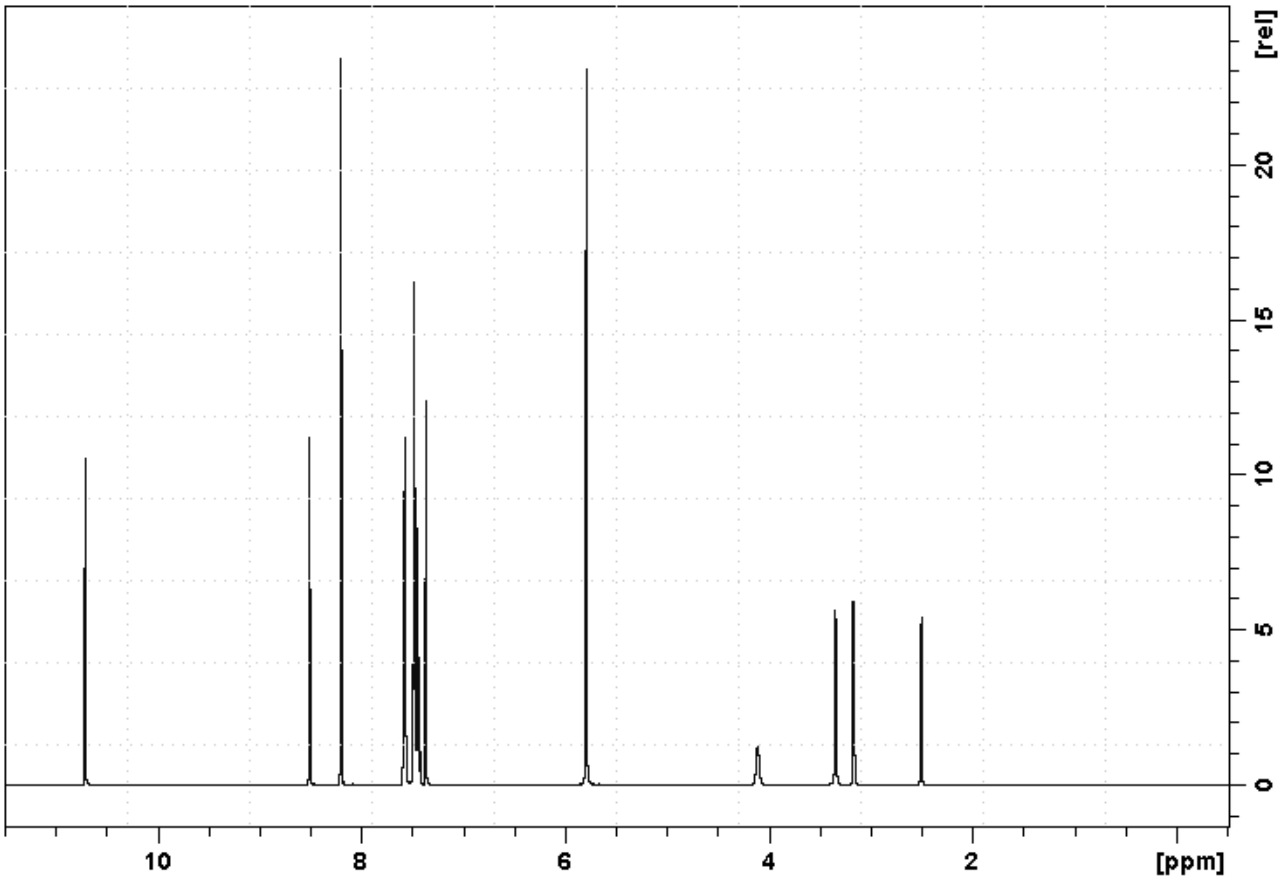

^{1}H-NMR of iso-TTBnHBr in DMSO-d6, magnification of the compound peaks.

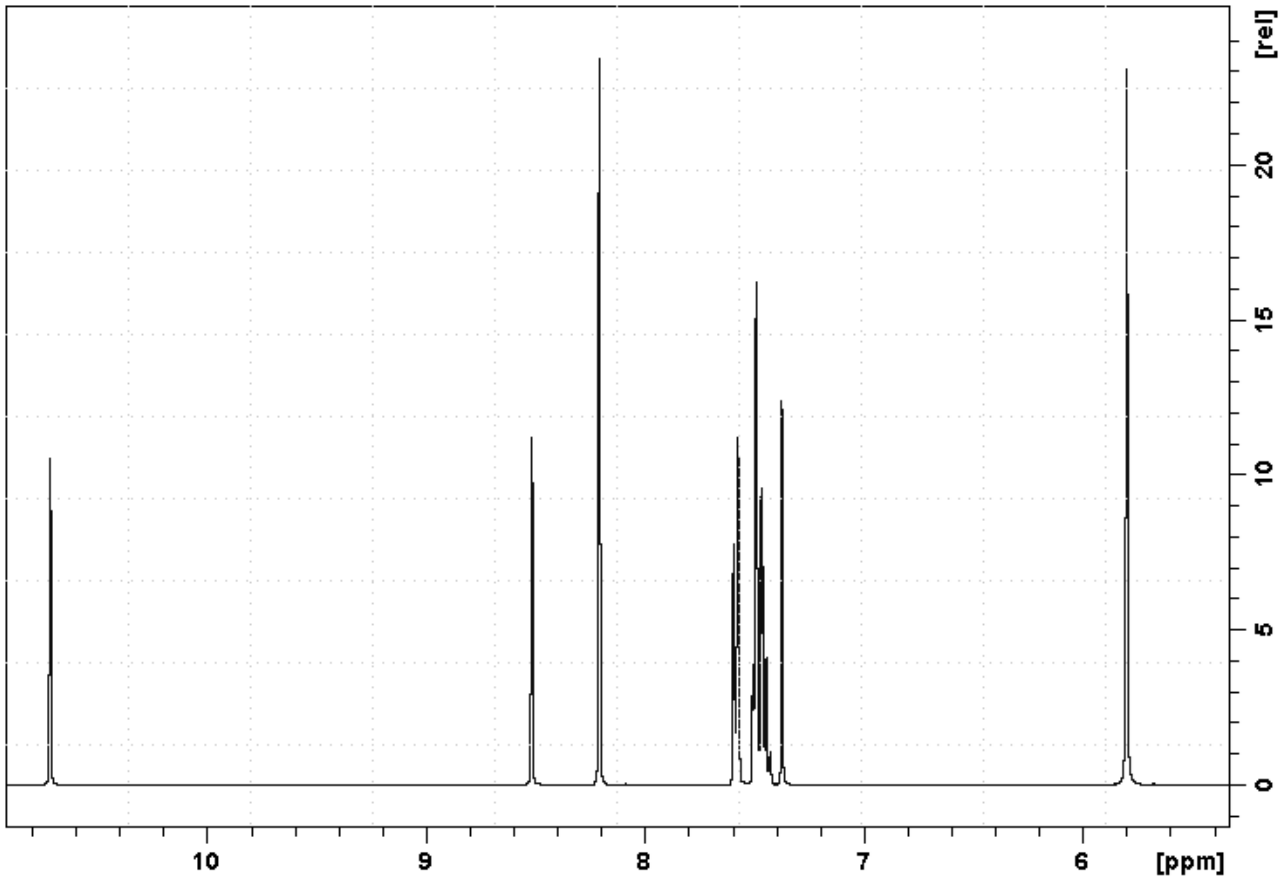

^{13}C-NMR of iso-TTBnHBr in DMSO-d6.

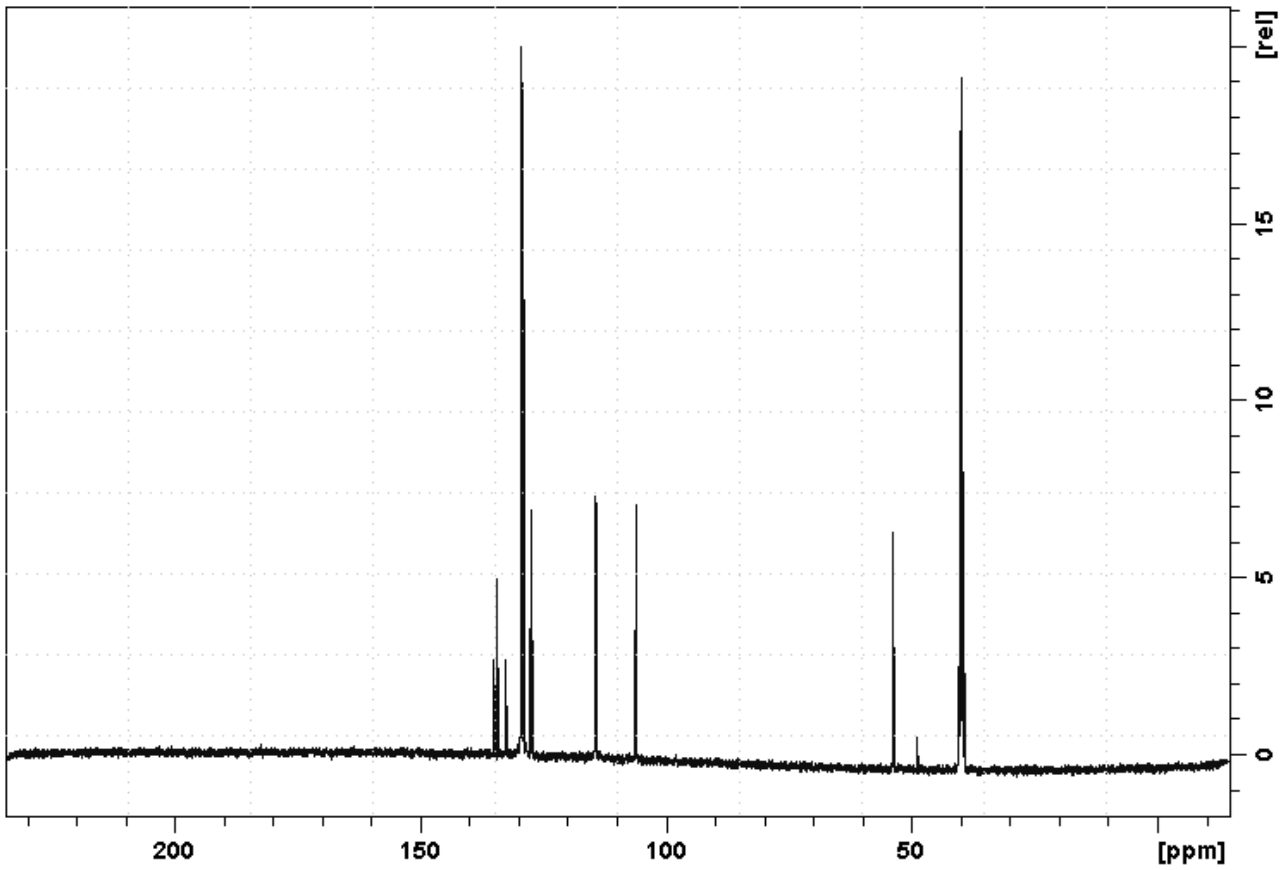

^{13}C-NMR of iso-TTBnHBr in DMSO-d6, magnification of the 137-105 ppm area.

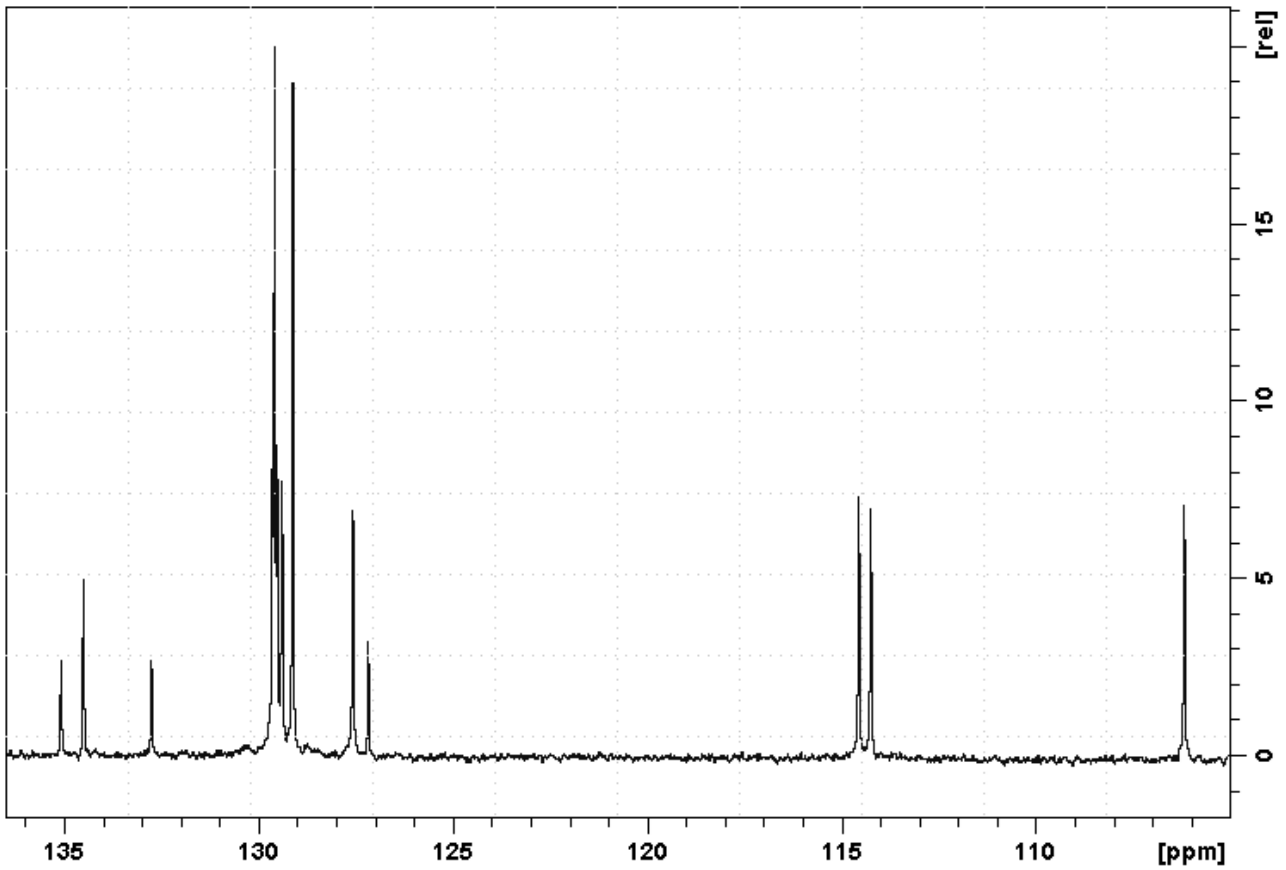

Synthesis of iso-TTEtHPF$_6$

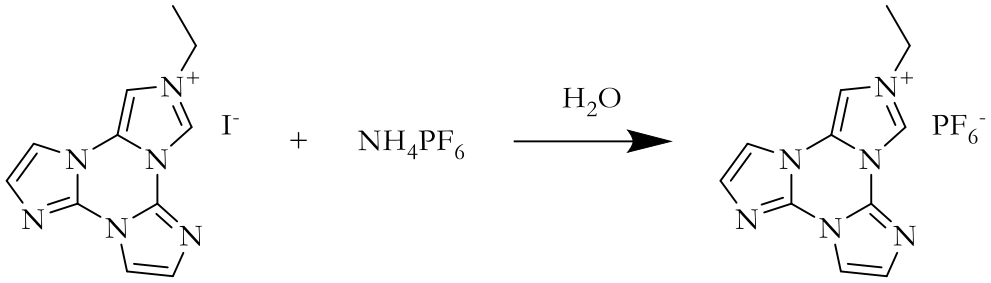

Reagents	m / mg	MM / g/mol	n / mol	Eq
iso-TTEtHI	100.0	354.16	$2.82 \cdot 10^{-4}$	1
NH_4PF_6	92.0	163.00	$5.65 \cdot 10^{-4}$	2

In a typical reaction, 100 mg of iso-TTEtHI are dissolved in 20 mL of MilliQ water in a round-bottom flask. In a vial, 92 mg of NH_4PF_6 are dissolved in 3 mL of MilliQ water. The latter solution is added dropwise into the iso-TTEtHI solution under vigorous stirring.

After a couple of hours, the product is filtered on Hirsch, washed with MilliQ water, and dried in vacuum.

The same procedure was followed to synthesize iso-TTBnHPF$_6$.

Synthesis of iso-TTBnHAuCl$_4$

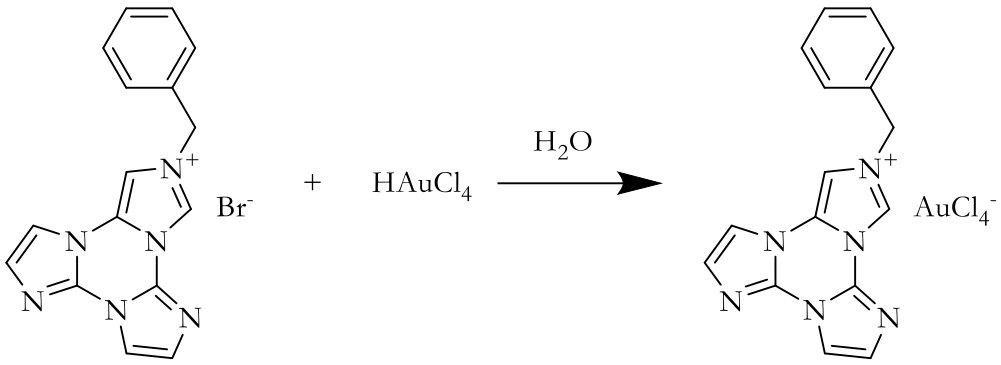

Reagents	V / mL	c/ mmol/L	m / mg	MM / g/mol	n / mol	Eq.
iso-TTBnHBr	/	/	100	369.23	$2.71 \cdot 10^{-4}$	1
HAuCl$_4$	5.86	50.8	101.23	339.77	$2.98 \cdot 10^{-4}$	1.1

In a typical reaction, 100 mg of iso-TTBnHBr are dissolved in 15 mL of MilliQ water. 5.86 mL of 50.8 mM HAuCl$_4$ solution are added dropwise under vigorous stirring.

After 30 minutes, the solid product is filtered on Hirsch and dried in vacuum.

The same procedure was used to synthesize iso-TTEtHAuCl$_4$.

The sample was characterized by NMR and mass spectrometry.

^{1}H-NMR: 10.61 ppm (d, 1H), 8.38 ppm (d, 1H), 8.21 ppm (d, 1H), 8.13 ppm (d, 1H), 7.60-7.40 ppm (m, 6H), 7.37 ppm (d, 1H), 5.74 ppm (s, 1H).

^{1}H-NMR of iso-TTBnHAuCl$_4$ in DMSO-d6.

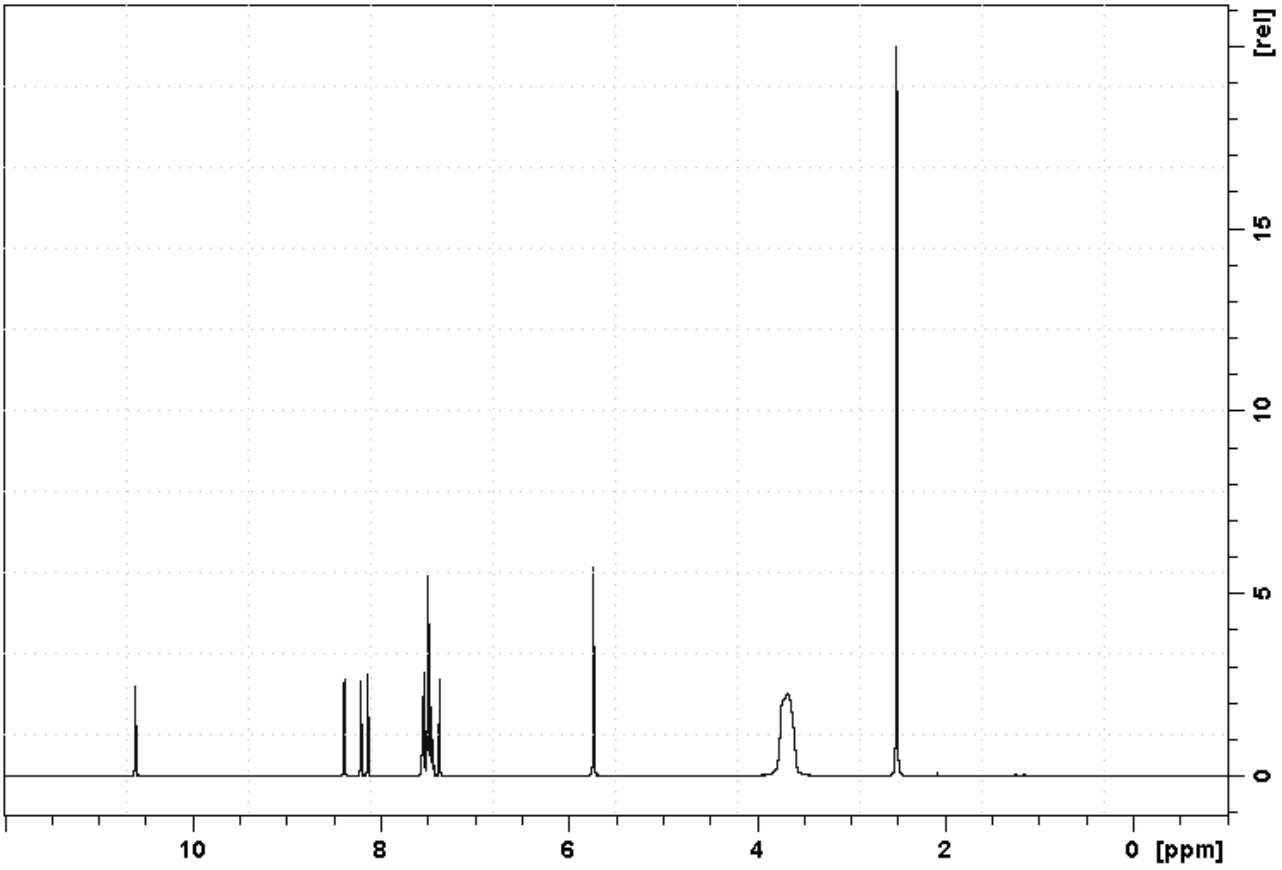

^{1}H-NMR of iso-TTBnHAuCl$_4$ in DMSO-d6, magnification of the compound peaks.

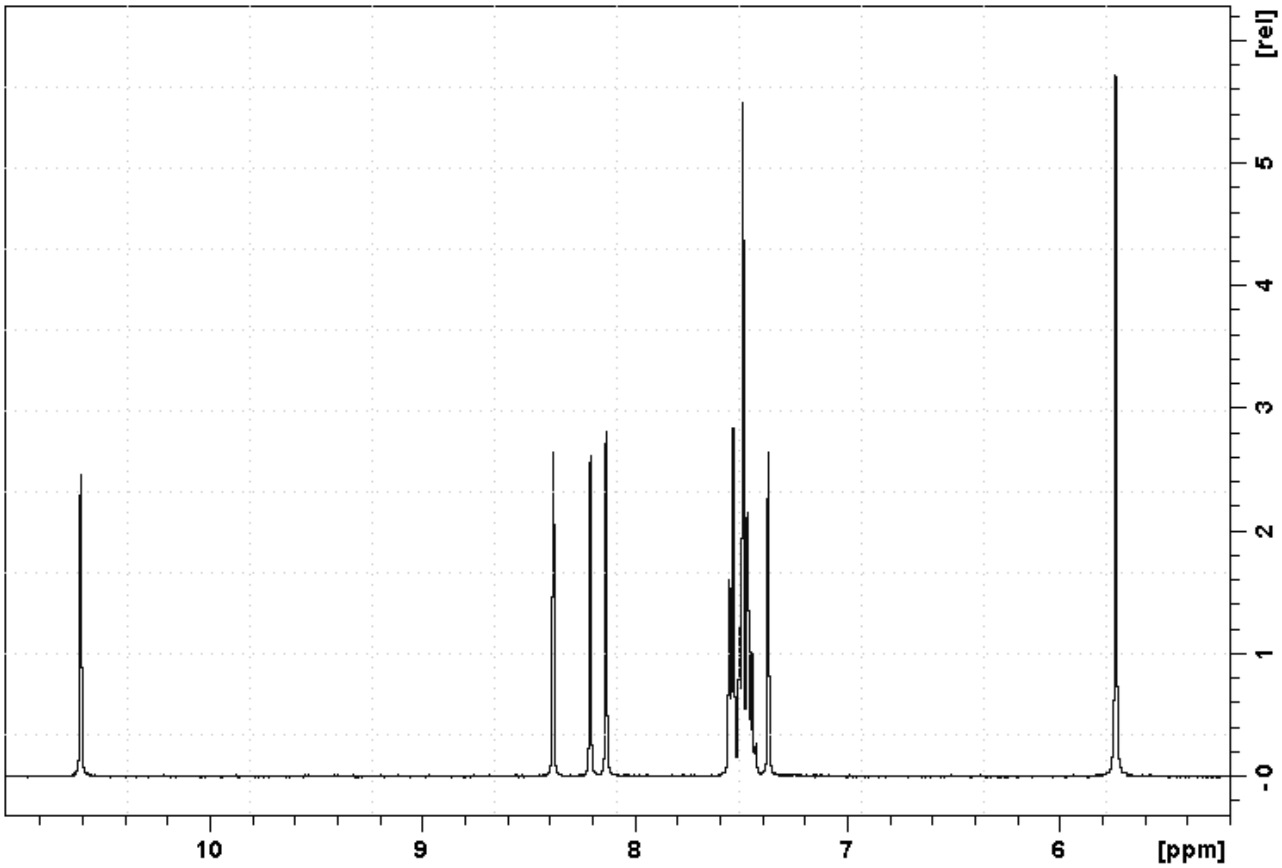

Synthesis of [(THT)AuCl]

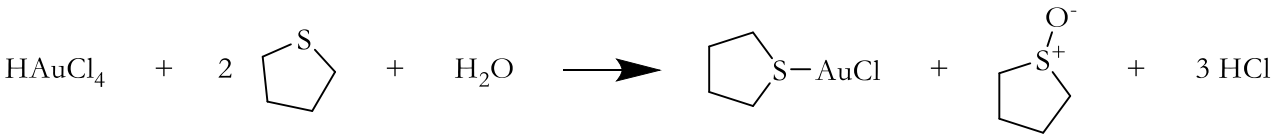

Reagents	V / µL	d / g/mL	m / mg	MM / g/mol	n / mol	Eq
$HAuCl_4$ ·3H_2O	/	/	100.0	393.82	$7.62 \cdot 10^{-4}$	1
THT	141.0	1.00	141.0	88.17	$1.60 \cdot 10^{-3}$	2.1

In a typical reaction, 100 mg of $HAuCl_4$ are dissolved in a mixture of 2.5 mL of ethanol and 0.5 mL of MilliQ water. Once completely dissolved, 141 µL of tetrahydrothiophene are added dropwise under vigorous stirring. The initial precipitation of the orange [(THT)$AuCl_3$] occurs, then the color turns to white because of the reduction and formation of [(THT)AuCl].

After 20 minutes, the precipitate is filtered on Hirsch and dried under vacuum. The product is conserved at a low temperature in the refrigerator.

^{1}H-NMR of [(THT)AuCl] in DMSO-d6

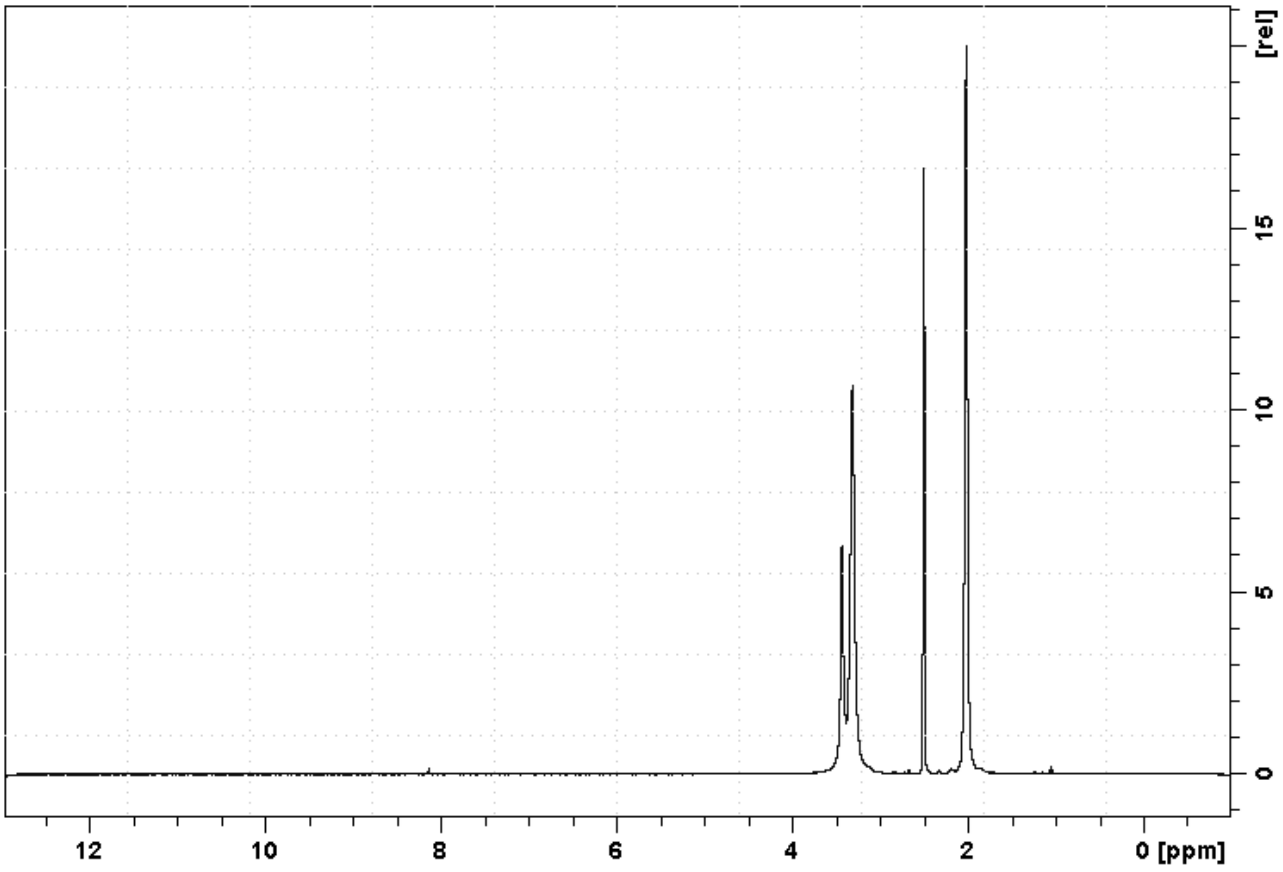

Synthesis of [(iso-TTEt)AuCl]

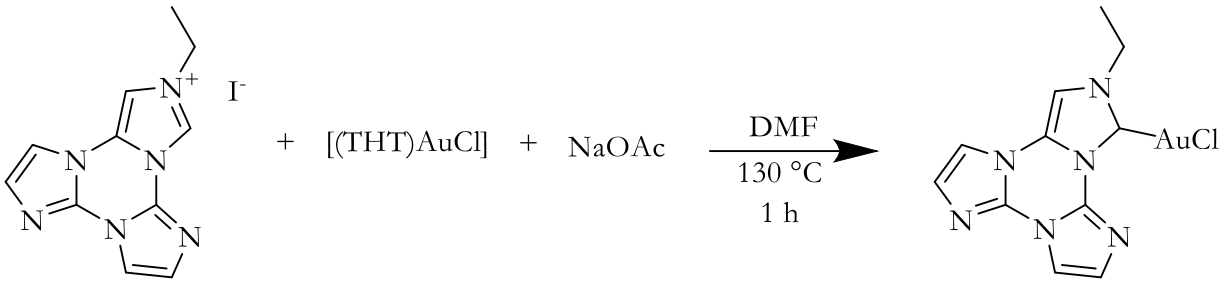

Reagents	m / mg	MM / g/mol	n / mol	Eq
iso-TTEtHI	100.0	354.16	$2.82 \cdot 10^{-4}$	1
[(THT)AuCl]	90.4	320.58	$2.82 \cdot 10^{-4}$	1
NaOAc	92.5	82.03	$1.13 \cdot 10^{-3}$	4

In a typical reaction, 100 mg of iso-TTEtHI are dissolved in 15 mL of DMF in a two-neck round-bottom flask under nitrogen, together with 90.4 mg of [(THT)AuCl]. The mixture is heated to 130 °C, and 92.5 mg of anhydrous sodium acetate are added under nitrogen flow, keeping the temperature steady for 3 hours. After this time, the solution is cooled to room temperature.

The DMF solution is stratified with 80 mL of diethyl ether, leading to the slow precipitation overnight of the desired product.

The product was characterized by NMR spectroscopy

^{1}H-NMR: 8.29 ppm (s, 1H), 8.05 ppm (s, 1H), 7.99 ppm (s, 1H), 7.37ppm (s, 1H), 7.31 ppm (s, 1H), 4.78 ppm (q, 2H), 1.65 ppm (t, 3H).

^{1}H-NMR of the compound in DMSO-d6.

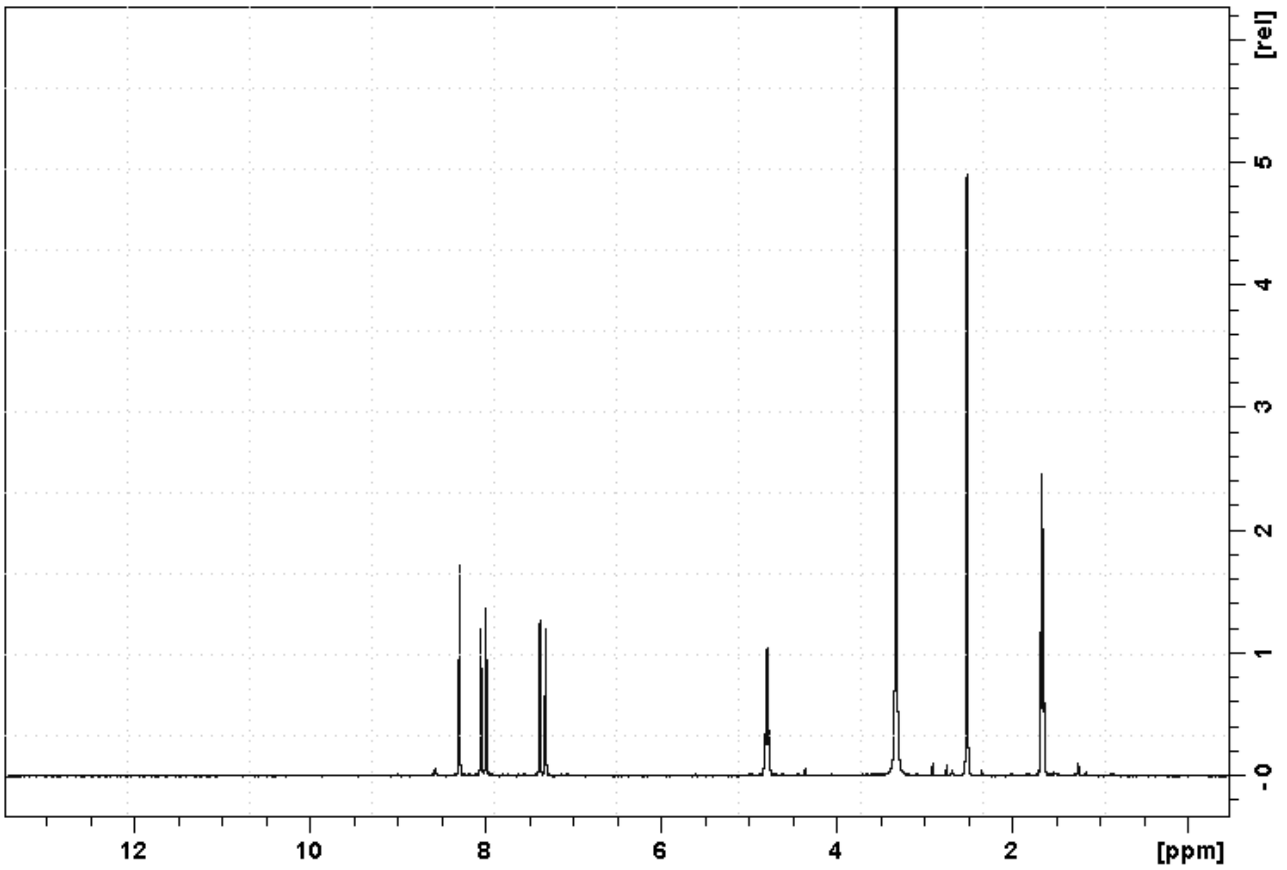

^{1}H-NMR of the compound in DMSO-d6. Magnification of the aromatic peaks.

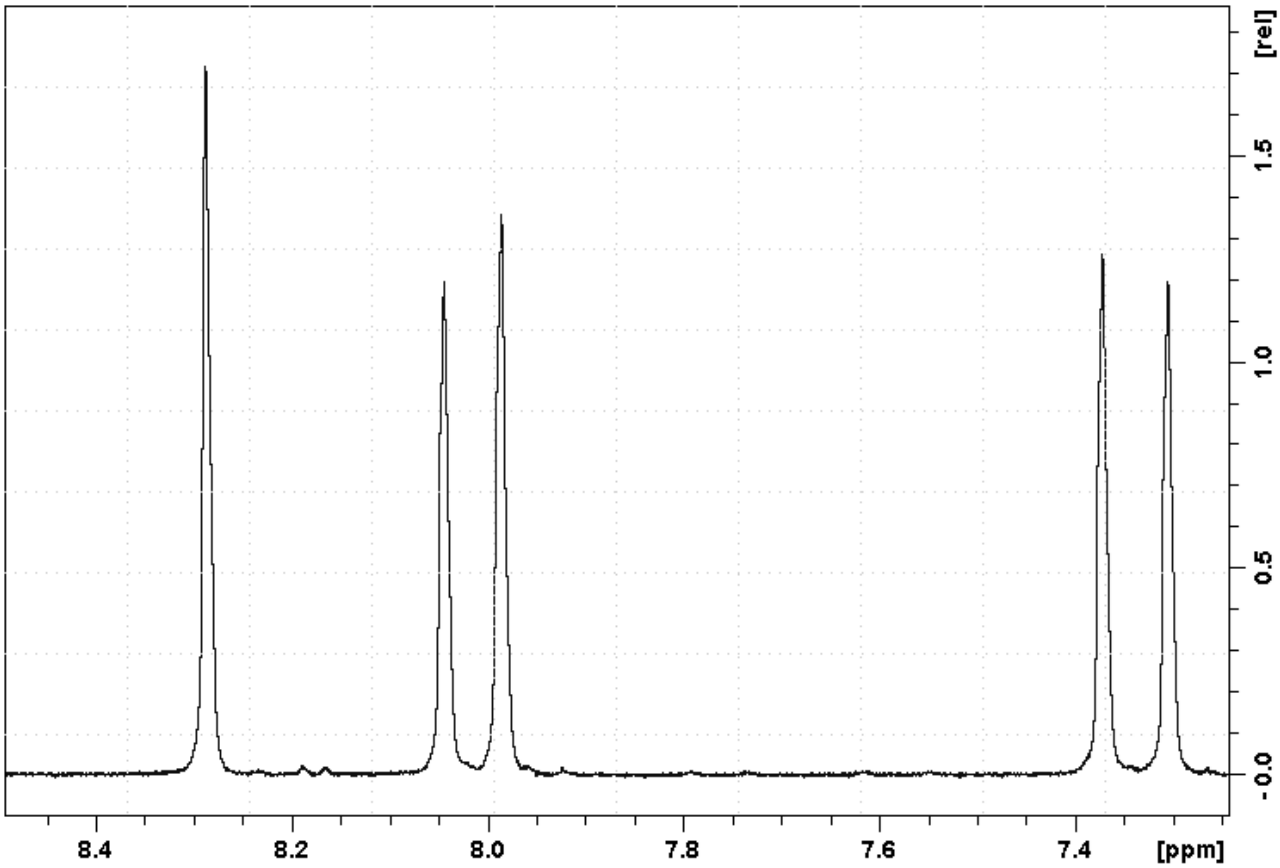

^{1}H-NMR of the compound in DMSO-d6. Magnification of the aliphatic peaks.

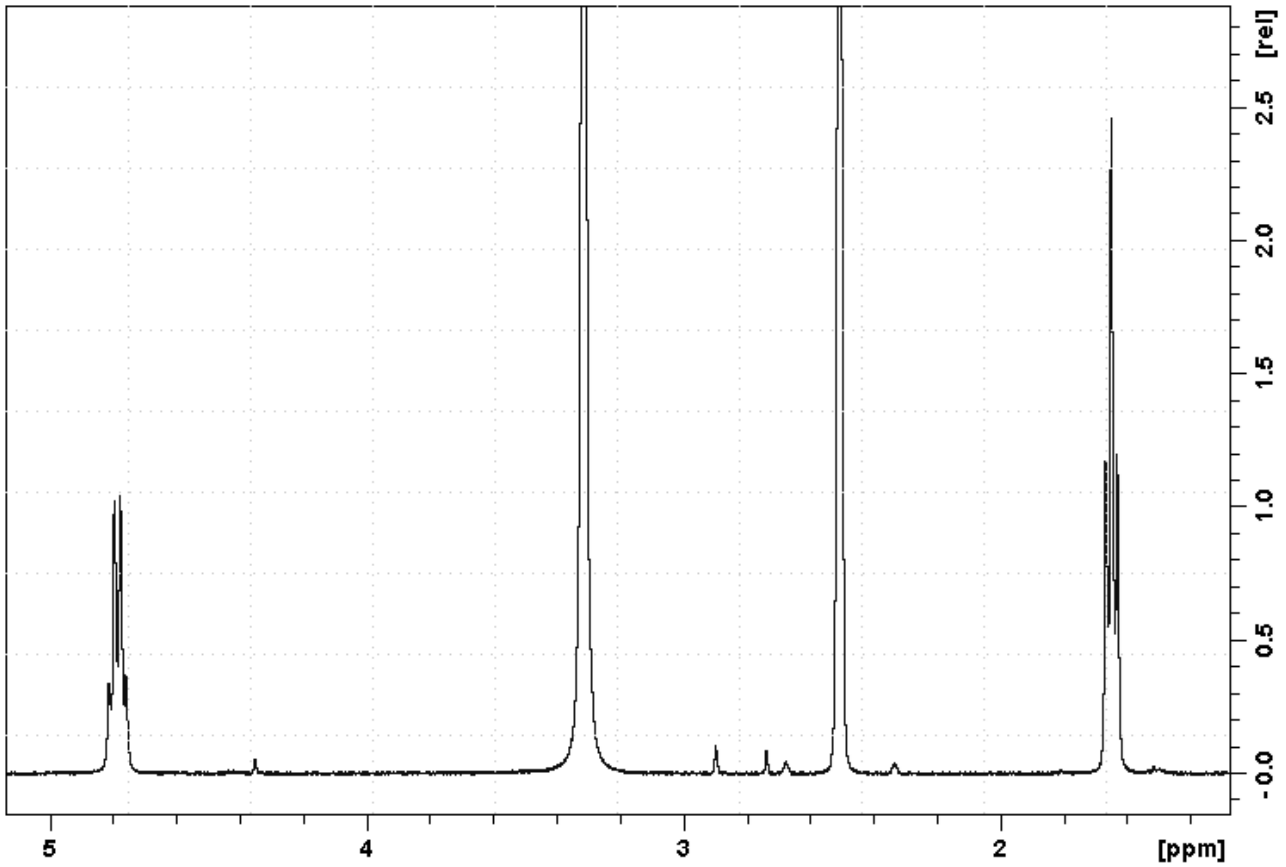

Synthesis of NHC-capped gold nanoparticles

Nanoparticles from iso-TTEtHPF$_6$

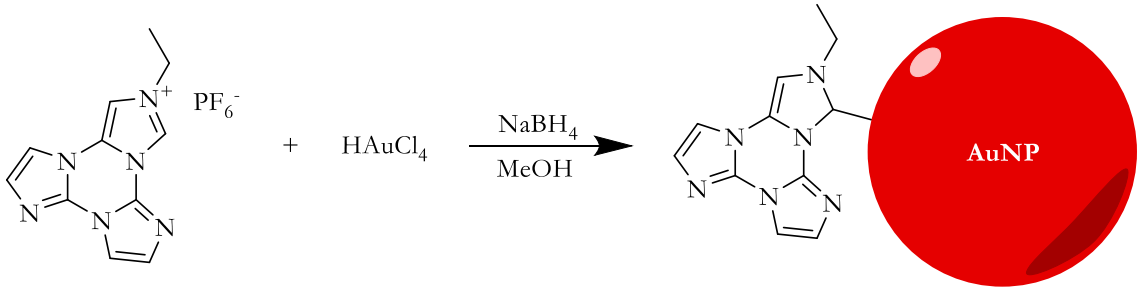

Reagents	V / µL	C / mol/L	m / mg	MM / g/mol	n / mol	Eq
iso-TTEtHPF$_6$	/	/	10.0	372.22	$2.69 \cdot 10^{-5}$	1
HAuCl$_4$	528.9	$5.08 \cdot 10^{-2}$	9.13	339.77	$2.69 \cdot 10^{-5}$	1
NaBH$_4$	/	/	10.2	37.8.	$2.69 \cdot 10^{-4}$	10

In a typical reaction, 10 mg of iso-TTEtHPF$_6$ are dissolved in 25 mL of methanol, and an equimolar amount of tetrachloroauric acid solution is added. When the solution is homogeneous, sodium borohydride is dissolved in 2 mL of methanol and added to the solution.

The prompt formation of gold nanoparticles occurs.

Samples for TEM analysis are prepared from the as-synthesized suspension.

Nanoparticles suspension can be washed to use or to analyze unsupported nanoparticles, or can be used for the preparation of catalytic materials comprised of supported gold nanoparticles.

The same procedure was followed for the synthesis of gold nanoparticles from iso-TTBnHPF$_6$.

Nanoparticles from iso-TTBnHAuCl$_4$

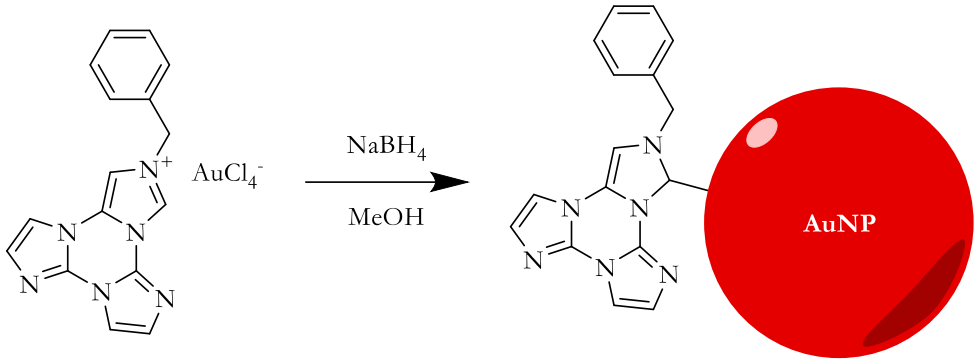

Reagents	m / mg	MM / g/mol	n / mol	Eq
iso-TTBnHAuCl$_4$	15.0	372.22	$2.39 \cdot 10^{-5}$	1
NaBH$_4$	9.0	37.8.	$2.39 \cdot 10^{-4}$	10

In a typical reaction, 15 mg of iso-TTEtHAuCl$_4$ are dissolved in 25 mL of methanol. When completely dissolved, sodium borohydride is dissolved in 2 mL of methanol and added to the solution.

The prompt formation of gold nanoparticles occurs.

Samples for TEM analysis are prepared from the as-synthesized suspension.

Nanoparticles suspension can be washed to use or to analyze unsupported nanoparticles, or can be used for the preparation of catalytic materials comprised of supported gold nanoparticles.

The same procedure was followed for the synthesis of gold nanoparticles from iso-TTEtHAuCl$_4$.

Nanoparticles from [(iso-TTEt)AuCl]

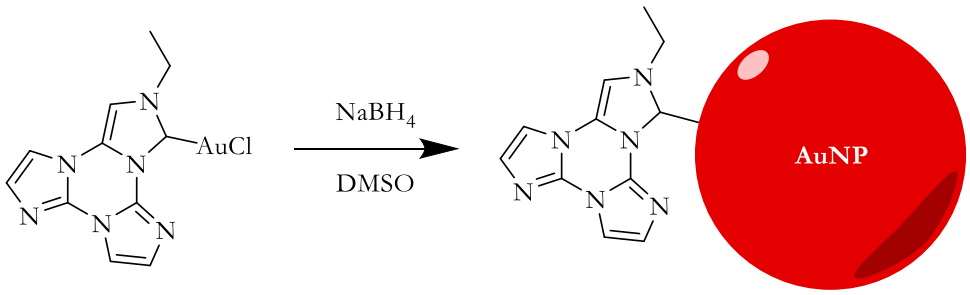

Reagents	m / mg	MM / g/mol	n / mol	Eq
iso-TTEtAuCl	3.0	372.22	$6.53 \cdot 10^{-6}$	1
$NaBH_4$	1.24	37.8.	$6.53 \cdot 10^{-5}$	10

In a typical reaction, 3 mg of iso-TTEtAuCl are dissolved in 3 mL of THF. Once dissolved, $NaBH_4$ is added dissolved in 0.5 mL of MilliQ water.

The prompt formation of gold nanoparticles occurs.

A sample for TEM analysis is prepared from the as-synthesized suspension.

Synthesis of non-functionalized gold nanoparticles

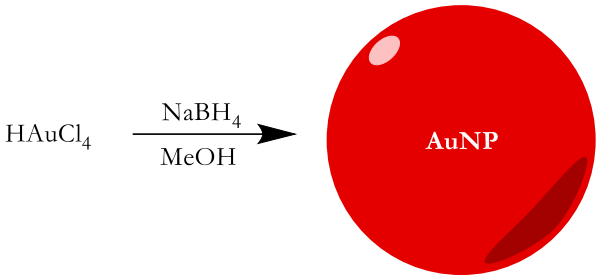

Reagents	V / µL	C / mol/L	m / mg	MM/ g/mol	n / mol	Eq
$HAuCl_4$	528.9	$5.08 \cdot 10^{-2}$	9.13	339.77	$2.69 \cdot 10^{-5}$	1
$NaBH_4$	/	/	5.1	37.8.	$1.35 \cdot 10^{-4}$	5

In a typical reaction, $HAuCl_4$ (50.8 mM solution, 528.9 µL) is diluted in 25 mL of methanol. Sodium borohydride is then dissolved in 2 mL of methanol and added to the solution.

The prompt formation of gold nanoparticles occurs.

Synthesis of catalytic materials

For the preparation of catalytic materials comprised of supported nanoparticles, the proper amount of washed and dried support, calculated to obtain a final loading of gold equal to 1% w/w, is added to the suspension of as-synthesized gold nanoparticles.

As an example, 15 mg of iso-TTBnHAuCl$_4$ ($2.39 \cdot 10^{-5}$ mol) contains 4.53 mg of gold. The amount of support to be added to the suspension is about 453 mg.

DFT Simulations

IR spectra simulations were performed with ORCA 6.0 software. All the calculations were performed at the r^2SCAN-3c level of theory.

For molecular models (iso-TT, iso-TTEtHI, and iso-TTBnHBr), a conformer search was performed on the molecule or the ionic couple. For nanoparticle models, the nanoparticles were simulated as a pyramidal Au20 cluster with an organic molecule bound to the top face. From the results, the three lowest-energy stable conformers were selected, and geometry optimization and vibrational spectrum simulation were performed.

Structures converging to the same conformer were eliminated, and the presence of imaginary frequencies was accurately controlled to avoid saddle points.

Boltzmann-averaged IR spectra were calculated with UCSF ChimeraX 1.9, equipped with the SEQCROW plugin. Spectra were calculated at 298 K, with a FWHM of 8 cm^{-1} and a linear frequency scaling factor of $1.5 \cdot 10^{-2}$.

As an example, here is reported the input file for iso-TT geometrical optimization and IR spectrum simulation.

```
!r2SCAN-3C OPT NUMFREQ TIGHTOPT

* xyz 0 1

  N      -6.65404       0.25467       0.00000

  C      -5.81091       1.32260      -0.00000

  N      -4.48359       1.13263      -0.00000

  C      -3.97599      -0.12950       0.00000

  N      -4.80787      -1.18613      -0.00000

  C      -6.15503      -0.99405       0.00000

  C      -6.07421       2.67076       0.00000

  N      -4.88308       3.32333      -0.00000

  C      -3.92929       2.35567       0.00000

  N      -2.67686      -0.47746      -0.00000

  C      -2.71304      -1.83522      -0.00000
```

C	-4.03285	-2.27856	0.00000
N	-7.10611	-1.94504	-0.00000
C	-8.26385	-1.23485	0.00000
C	-7.98791	0.12973	-0.00000
H	-7.04419	3.14955	-0.00000
H	-2.86440	2.54859	-0.00000
H	-1.83381	-2.46519	0.00000
H	-4.38536	-3.30176	-0.00000
H	-9.24903	-1.68131	-0.00000
H	-8.69803	0.94634	0.00000

*

Optimized geometries and frequencies

Here are reported the results of geometry optimization and vibrational frequencies calculation of the models. For simplicity, only one conformer per model is reported.

iso-TT

CARTESIAN COORDINATES (ANGSTROEM)

N	-6.679467	0.233260	-0.000000
C	-5.869272	1.360035	-0.000000
N	-4.496143	1.149910	-0.000000
C	-3.938288	-0.118485	-0.000000
N	-4.801275	-1.193765	-0.000000
C	-6.177936	-1.049781	-0.000000
C	-6.055543	2.716566	-0.000000
N	-4.828718	3.342658	0.000000
C	-3.915365	2.403044	-0.000000
N	-2.681819	-0.466760	-0.000000
C	-2.716752	-1.851113	0.000000
C	-3.998689	-2.327643	-0.000000
N	-7.104099	-1.970307	-0.000000
C	-8.286747	-1.255441	0.000000
C	-8.061507	0.094563	-0.000000
H	-6.984162	3.268456	-0.000000
H	-2.841485	2.525607	-0.000000
H	-1.802975	-2.428166	0.000000
H	-4.427639	-3.316681	-0.000000
H	-9.242320	-1.760337	0.000000
H	-8.719249	0.949181	-0.000000

Unscaled IR spectrum

Mode	Frequency / cm^{-1}	Epsilon / L/mol·cm	Intensity / km/mol	T^2 / a.u.
6	101.51	0.000011	0.06	0.000034
7	113.10	0.000207	1.05	0.000572
8	113.75	0.000156	0.79	0.000429
9	250.26	0.001217	6.15	0.001517
10	275.20	0.000132	0.66	0.000149
11	285.25	0.000814	4.11	0.000890
12	342.61	0.000011	0.05	0.000010
13	347.77	0.000102	0.51	0.000091
14	482.02	0.001144	5.78	0.000741
15	492.07	0.000653	3.30	0.000414
16	523.63	0.000012	0.06	0.000007
17	615.20	0.000000	0.00	0.000000
18	625.40	0.000774	3.91	0.000386
19	638.22	0.000021	0.11	0.000010
20	654.98	0.000338	1.71	0.000161
21	660.52	0.003121	15.77	0.001474
22	669.41	0.008446	42.68	0.003937
23	680.31	0.005129	25.92	0.002353
24	705.71	0.001060	5.36	0.000469
25	729.24	0.006655	33.63	0.002848
26	774.21	0.007885	39.85	0.003178
27	784.43	0.001435	7.25	0.000571

Mode	Frequency / cm^{-1}	Epsilon / L/mol·cm	Intensity / km/mol	T^2 / a.u.
28	847.47	0.001405	7.10	0.000517
29	854.19	0.000961	4.85	0.000351
30	914.20	0.005298	26.77	0.001808
31	921.19	0.000637	3.22	0.000216
32	923.52	0.000372	1.88	0.000126
33	953.04	0.001352	6.83	0.000443
34	1062.54	0.000558	2.82	0.000164
35	1085.63	0.001120	5.66	0.000322
36	1118.16	0.001344	6.79	0.000375
37	1124.27	0.001986	10.03	0.000551
38	1129.18	0.006012	30.38	0.001662
39	1155.44	0.007943	40.14	0.002145
40	1160.08	0.003207	16.20	0.000863
41	1225.61	0.001093	5.52	0.000278
42	1239.74	0.001844	9.32	0.000464
43	1275.89	0.000010	0.05	0.000002
44	1299.52	0.000754	3.81	0.000181
45	1320.45	0.000715	3.61	0.000169
46	1337.74	0.004006	20.25	0.000935
47	1348.05	0.004723	23.87	0.001093
48	1423.87	0.000290	1.46	0.000063
49	1456.20	0.003930	19.86	0.000842
50	1457.72	0.002407	12.16	0.000515

Mode	Frequency / cm^{-1}	Epsilon / L/mol·cm	Intensity / km/mol	T^2 / a.u.
51	1485.89	0.009074	45.86	0.001906
52	1509.82	0.003177	16.05	0.000657
53	1519.66	0.000183	0.93	0.000038
54	1606.33	0.004949	25.01	0.000961
55	1623.01	0.056576	285.91	0.010878
56	1626.62	0.037998	192.03	0.007290
57	3242.79	0.000377	1.91	0.000036
58	3243.67	0.000544	2.75	0.000052
59	3247.96	0.000398	2.01	0.000038
60	3257.81	0.001511	7.63	0.000145
61	3274.80	0.000342	1.73	0.000033
62	3284.17	0.001263	6.38	

iso-TTEtHI

CARTESIAN COORDINATES (ANGSTROEM)

N	-2.918809	2.416090	-0.032556
C	-3.445226	1.139458	0.000368
C	-1.560651	2.664125	-0.014976
N	-0.712634	1.556810	-0.051613
C	-1.187650	0.258013	-0.039257
N	-2.554171	0.082135	0.004561
C	-0.787614	3.777032	0.040804
N	0.534079	3.339869	0.051397
C	0.567798	1.992121	0.169490
N	-0.521068	-0.857272	-0.087033
C	-1.502649	-1.833495	-0.060695
C	-2.757807	-1.292085	-0.010330
N	-4.747794	1.121046	0.007572
C	-4.013742	3.274836	-0.037808
C	-5.107860	2.456777	-0.013654
H	-1.060237	4.817045	0.086849
H	1.432394	1.369930	0.001538
H	-1.240918	-2.881715	-0.077126
H	-3.750815	-1.710594	0.019638
H	-3.898849	4.346994	-0.051046
H	-6.147186	2.752770	-0.009908
C	1.710118	4.183447	0.305327
C	1.463495	5.209529	1.401645

H	2.006822	4.662848	-0.636222
H	2.505897	3.498316	0.614561
H	0.734685	5.967752	1.099178
H	2.403588	5.724691	1.618468
H	1.121192	4.707546	2.311425
I	0.903182	1.588633	2.943753

Unscaled IR spectrum

Mode	Frequency / cm^{-1}	Epsilon / L/mol·cm	Intensity / km/mol	T^2 / a.u.
6	29.32	0.000474	2.39	0.005039
7	36.66	0.000732	3.70	0.006235
8	47.26	0.000878	4.44	0.005801
9	88.26	0.003164	15.99	0.011189
10	89.74	0.001780	8.99	0.006189
11	109.61	0.000037	0.19	0.000106
12	138.21	0.002520	12.73	0.005689
13	157.01	0.001832	9.26	0.003641
14	183.63	0.000617	3.12	0.001049
15	251.67	0.007253	36.65	0.008993
16	273.00	0.001078	5.45	0.001233
17	279.85	0.002467	12.47	0.002751
18	307.60	0.001010	5.11	0.001025
19	337.74	0.001141	5.77	0.001054
20	378.82	0.000556	2.81	0.000458

Mode	Frequency / cm^{-1}	Epsilon / L/mol·cm	Intensity / km/mol	T^2 / a.u.
21	407.27	0.001304	6.59	0.000999
22	472.91	0.007486	37.83	0.004940
23	493.64	0.002249	11.37	0.001422
24	509.66	0.000255	1.29	0.000156
25	569.07	0.037915	191.61	0.020792
26	605.69	0.000537	2.71	0.000277
27	611.32	0.000040	0.20	0.000020
28	624.67	0.000130	0.65	0.000065
29	658.28	0.004654	23.52	0.002206
30	664.71	0.002121	10.72	0.000996
31	675.88	0.000532	2.69	0.000246
32	687.42	0.013852	70.00	0.006288
33	700.76	0.002605	13.16	0.001160
34	715.91	0.000781	3.94	0.000340
35	732.09	0.006792	34.32	0.002895
36	776.36	0.011661	58.93	0.004687
37	797.30	0.001412	7.14	0.000553
38	854.07	0.001650	8.34	0.000603
39	858.83	0.001012	5.12	0.000368
40	913.48	0.000294	1.49	0.000101
41	919.18	0.000342	1.73	0.000116
42	940.55	0.000029	0.15	0.000010
43	966.76	0.000404	2.04	0.000130

Mode	Frequency / cm^{-1}	Epsilon / L/mol·cm	Intensity / km/mol	T^2 / a.u.
44	1038.01	0.001313	6.64	0.000395
45	1056.47	0.000651	3.29	0.000192
46	1082.87	0.004394	22.21	0.001266
47	1100.64	0.001440	7.28	0.000408
48	1113.16	0.002275	11.50	0.000638
49	1122.16	0.011689	59.07	0.003250
50	1137.56	0.008544	43.18	0.002344
51	1138.85	0.000096	0.48	0.000026
52	1163.38	0.002396	12.11	0.000643
53	1186.53	0.003867	19.54	0.001017
54	1219.49	0.002117	10.70	0.000542
55	1260.41	0.007119	35.98	0.001763
56	1273.03	0.000619	3.13	0.000152
57	1301.12	0.000413	2.09	0.000099
58	1317.45	0.003815	19.28	0.000904
59	1326.19	0.005819	29.41	0.001369
60	1346.93	0.008818	44.56	0.002043
61	1359.99	0.011813	59.70	0.002711
62	1399.92	0.004212	21.29	0.000939
63	1421.93	0.001394	7.05	0.000306
64	1441.25	0.001135	5.73	0.000246
65	1458.79	0.012005	60.67	0.002568
66	1467.84	0.012730	64.33	0.002706

Mode	Frequency / cm^{-1}	Epsilon / L/mol·cm	Intensity / km/mol	T^2 / a.u.
67	1477.11	0.003460	17.48	0.000731
68	1487.17	0.001155	5.84	0.000242
69	1494.06	0.002611	13.20	0.000545
70	1503.74	0.004690	23.70	0.000973
71	1519.19	0.007896	39.90	0.001622
72	1526.20	0.002344	11.85	0.000479
73	1612.47	0.030873	156.02	0.005975
74	1622.63	0.053048	268.08	0.010202
75	1691.95	0.042477	214.66	0.007834
76	3020.56	0.004566	23.07	0.000472
77	3023.33	0.003410	17.23	0.000352
78	3087.11	0.001114	5.63	0.000113
79	3112.77	0.001848	9.34	0.000185
80	3123.54	0.000707	3.57	0.000071
81	3248.05	0.000976	4.93	0.000094
82	3249.77	0.001344	6.79	0.000129
83	3276.33	0.000150	0.76	0.000014
84	3280.38	0.001917	9.69	0.000182
85	3283.09	0.003631	18.35	0.000345
86	3292.60	0.003662	18.51	0.000347

iso-TTEtAu$_{20}$

CARTESIAN COORDINATES (ANGSTROEM)

Au	5.080570	0.291909	3.904155
Au	7.684837	0.699831	4.563897
Au	6.203713	-0.550129	6.491251
Au	5.949393	2.342199	5.845575
Au	4.123481	3.815512	7.121953
Au	2.481828	-0.008833	3.356770
Au	3.217307	1.943886	5.236906
Au	4.429354	1.111082	7.909560
Au	4.600215	-1.668121	8.312709
Au	3.458606	-1.006099	5.836286
Au	0.453702	1.494267	4.936332
Au	2.508069	2.581746	9.273947
Au	1.699381	-1.911661	7.738149
Au	1.245540	3.207660	6.778944
Au	2.156934	5.160298	8.432690
Au	-0.187307	-0.294123	2.982356
Au	0.731933	-1.295827	5.356892
Au	2.833100	-2.672660	10.120977
Au	2.620304	0.004167	9.723898
Au	0.178433	0.636903	7.561776
N	-1.687373	-1.127742	12.418801
C	-1.473319	-2.470575	12.204786
C	-1.474090	-0.178196	11.440230

N	-1.016479	-0.598012	10.187163
C	-0.857483	-1.953459	9.912017
N	-1.060060	-2.847707	10.941267
C	-1.595847	1.169561	11.391962
N	-1.196108	1.541227	10.117874
C	-0.812251	0.490932	9.360333
N	-0.549939	-2.548792	8.790622
C	-0.540120	-3.900154	9.098020
C	-0.853281	-4.113672	10.408558
N	-1.719294	-3.208694	13.249657
C	-2.115502	-2.302024	14.216212
C	-2.107238	-1.019874	13.741478
H	-1.909756	1.879668	12.139270
H	-2.385056	-2.630669	15.209790
H	-2.340773	-0.068524	14.192319
H	-0.298262	-4.633165	8.341979
H	-0.961042	-4.998354	11.015501
C	-1.204433	2.937229	9.650744
C	-2.293230	3.190209	8.620862
H	-0.212513	3.149831	9.231385
H	-1.334062	3.565473	10.537767
H	-2.254374	4.238545	8.309822
H	-3.287121	2.980812	9.029339
H	-2.129917	2.568649	7.735288

Unscaled IR spectrum

Mode	Frequency / cm^{-1}	Epsilon / L/mol·cm	Intensity / km/mol	T^2 / a.u.
6	7.36	0.000064	0.33	0.002734
7	10.92	0.000139	0.70	0.003975
8	21.83	0.000014	0.07	0.000200
9	24.09	0.000011	0.05	0.000141
10	26.69	0.000016	0.08	0.000193
11	27.51	0.000054	0.27	0.000610
12	28.80	0.000005	0.02	0.000050
13	30.52	0.000016	0.08	0.000159
14	32.84	0.000031	0.16	0.000299
15	34.11	0.000139	0.70	0.001272
16	36.81	0.000017	0.09	0.000146
17	38.71	0.000213	1.08	0.001715
18	41.68	0.000011	0.06	0.000084
19	43.31	0.000005	0.02	0.000035
20	45.16	0.000017	0.09	0.000118
21	47.31	0.000005	0.02	0.000030
22	48.15	0.000002	0.01	0.000011
23	48.86	0.000023	0.11	0.000144
24	49.92	0.000034	0.17	0.000210
25	51.25	0.000039	0.19	0.000235
26	53.60	0.000185	0.94	0.001079
27	54.52	0.000017	0.09	0.000099

Mode	Frequency / cm^{-1}	Epsilon / L/mol·cm	Intensity / km/mol	T^2 / a.u.
28	54.75	0.000015	0.08	0.000087
29	55.32	0.000009	0.05	0.000051
30	56.85	0.000026	0.13	0.000142
31	58.45	0.000014	0.07	0.000077
32	60.87	0.000108	0.55	0.000554
33	61.18	0.000023	0.11	0.000116
34	63.61	0.000022	0.11	0.000110
35	64.53	0.000046	0.23	0.000224
36	65.08	0.000014	0.07	0.000066
37	67.45	0.000019	0.09	0.000086
38	68.82	0.000034	0.17	0.000156
39	74.48	0.000003	0.01	0.000012
40	75.64	0.000020	0.10	0.000082
41	76.63	0.000038	0.19	0.000155
42	77.84	0.000008	0.04	0.000031
43	79.79	0.000025	0.13	0.000098
44	81.61	0.000016	0.08	0.000062
45	89.49	0.000015	0.08	0.000053
46	91.81	0.000002	0.01	0.000007
47	92.28	0.000078	0.39	0.000264
48	95.53	0.000028	0.14	0.000093
49	99.26	0.000004	0.02	0.000014
50	102.34	0.000008	0.04	0.000026

Mode	Frequency / cm^{-1}	Epsilon / L/mol·cm	Intensity / km/mol	T^2 / a.u.
51	106.52	0.000012	0.06	0.000037
52	117.35	0.000074	0.37	0.000197
53	118.07	0.000849	4.29	0.002245
54	120.59	0.000043	0.22	0.000112
55	121.45	0.000036	0.18	0.000093
56	124.13	0.000034	0.17	0.000086
57	126.28	0.000033	0.17	0.000082
58	131.46	0.001757	8.88	0.004170
59	137.65	0.000481	2.43	0.001090
60	140.74	0.000856	4.33	0.001898
61	142.95	0.000594	3.00	0.001297
62	148.98	0.001136	5.74	0.002380
63	154.90	0.000845	4.27	0.001702
64	172.20	0.000047	0.24	0.000085
65	173.34	0.000003	0.01	0.000005
66	177.80	0.000486	2.46	0.000854
67	178.94	0.000204	1.03	0.000355
68	180.54	0.000163	0.82	0.000282
69	182.99	0.000130	0.66	0.000221
70	191.95	0.000026	0.13	0.000043
71	202.33	0.000450	2.27	0.000694
72	259.58	0.000760	3.84	0.000914
73	266.19	0.000073	0.37	0.000086

Mode	Frequency / cm^{-1}	Epsilon / L/mol·cm	Intensity / km/mol	T^2 / a.u.
74	287.87	0.000315	1.59	0.000341
75	322.46	0.000394	1.99	0.000381
76	350.46	0.000063	0.32	0.000056
77	390.90	0.000243	1.23	0.000194
78	438.79	0.000466	2.36	0.000332
79	483.72	0.000732	3.70	0.000472
80	509.39	0.000326	1.64	0.000199
81	510.75	0.001682	8.50	0.001028
82	609.80	0.000330	1.67	0.000169
83	620.69	0.001398	7.07	0.000703
84	627.86	0.000662	3.34	0.000329
85	647.13	0.000102	0.51	0.000049
86	664.10	0.008616	43.54	0.004049
87	668.39	0.000157	0.80	0.000074
88	684.40	0.000356	1.80	0.000162
89	701.92	0.000029	0.15	0.000013
90	708.57	0.008003	40.44	0.003525
91	728.87	0.001269	6.41	0.000543
92	738.81	0.007422	37.51	0.003135
93	795.66	0.000767	3.88	0.000301
94	857.30	0.001473	7.44	0.000536
95	863.26	0.001229	6.21	0.000444
96	919.68	0.000476	2.41	0.000162

Mode	Frequency / cm^{-1}	Epsilon / L/mol·cm	Intensity / km/mol	T^2 / a.u.
97	922.72	0.000421	2.13	0.000142
98	941.71	0.000171	0.87	0.000057
99	968.00	0.000360	1.82	0.000116
100	1051.40	0.001070	5.41	0.000318
101	1067.14	0.001671	8.45	0.000489
102	1089.65	0.001596	8.07	0.000457
103	1108.94	0.000437	2.21	0.000123
104	1118.07	0.001332	6.73	0.000372
105	1123.89	0.006595	33.33	0.001831
106	1127.34	0.002709	13.69	0.000750
107	1149.80	0.002273	11.49	0.000617
108	1164.14	0.004822	24.37	0.001293
109	1187.35	0.001207	6.10	0.000317
110	1254.54	0.001004	5.07	0.000250
111	1256.88	0.000471	2.38	0.000117
112	1274.81	0.000135	0.68	0.000033
113	1289.56	0.004680	23.65	0.001133
114	1323.82	0.001781	9.00	0.000420
115	1342.49	0.011409	57.66	0.002652
116	1361.89	0.004170	21.07	0.000955
117	1396.04	0.001385	7.00	0.000310
118	1400.98	0.003726	18.83	0.000830
119	1414.66	0.001265	6.39	0.000279

Mode	Frequency / cm^{-1}	Epsilon / L/mol·cm	Intensity / km/mol	T^2 / a.u.
120	1431.11	0.000222	1.12	0.000049
121	1447.95	0.017165	86.74	0.003699
122	1464.71	0.009091	45.94	0.001937
123	1477.25	0.001130	5.71	0.000239
124	1482.92	0.002575	13.01	0.000542
125	1495.44	0.001413	7.14	0.000295
126	1514.99	0.000142	0.72	0.000029
127	1528.26	0.002053	10.37	0.000419
128	1590.46	0.013804	69.76	0.002708
129	1619.00	0.070823	357.91	0.013651
130	1690.48	0.033417	168.88	0.006169
131	3004.20	0.002325	11.75	0.000241
132	3017.54	0.002159	10.91	0.000223
133	3080.81	0.000462	2.34	0.000047
134	3109.80	0.002162	10.93	0.000217
135	3112.92	0.001723	8.71	0.000173
136	3247.80	0.000384	1.94	0.000037
137	3252.48	0.001256	6.35	0.000121
138	3277.58	0.000119	0.60	0.000011
139	3282.14	0.002344	11.84	0.000223
140	3285.53	0.002734	13.82	0.000260

iso-TTBnHBr

CARTESIAN COORDINATES (ANGSTROEM)

N	-5.362858	1.023062	0.610417
C	-4.862368	-0.208537	0.237531
C	-4.661911	2.199558	0.430477
N	-3.437609	2.112938	-0.235571
C	-2.897998	0.906433	-0.644464
N	-3.625205	-0.234584	-0.379524
C	-4.871204	3.501007	0.742078
N	-3.771680	4.207433	0.251462
C	-2.822759	3.333634	-0.162352
N	-1.788509	0.678116	-1.282598
C	-1.771385	-0.697676	-1.440870
C	-2.883253	-1.285810	-0.904401
N	-5.665663	-1.195732	0.517097
C	-6.755949	-0.588958	1.114836
C	-6.602678	0.766941	1.187515
H	-5.687442	3.985090	1.251566
H	-1.955809	3.592893	-0.749596
H	-0.945527	-1.186820	-1.937092
H	-3.227836	-2.304647	-0.831209
H	-7.596556	-1.172920	1.461590
H	-7.221548	1.555740	1.584631
C	-3.423011	5.570543	0.683238
C	-2.547245	6.262133	-0.327596

H	-2.902097	5.471620	1.646461
H	-4.365145	6.111283	0.821105
C	-3.111784	6.885258	-1.442336
C	-2.299680	7.502561	-2.386339
C	-0.916312	7.498970	-2.222136
C	-0.349614	6.877464	-1.113895
C	-1.161089	6.260337	-0.165926
H	-4.192310	6.887908	-1.569520
H	-2.744722	7.990077	-3.248779
H	-0.281363	7.981974	-2.959263
H	0.728508	6.869814	-0.984307
H	-0.726516	5.751875	0.692110
Br	-1.340584	3.073625	1.952602

Unscaled IR spectrum

Mode	Frequency / cm^{-1}	Epsilon / L/mol·cm	Intensity / km/mol	T^2 / a.u.
6	24.23	0.000053	0.27	0.000688
7	30.02	0.000038	0.19	0.000395
8	36.46	0.000345	1.74	0.002955
9	50.23	0.000875	4.42	0.005437
10	52.07	0.000254	1.29	0.001524
11	100.68	0.002056	10.39	0.006372
12	109.86	0.000155	0.79	0.000442
13	111.67	0.002659	13.44	0.007432
14	141.88	0.002747	13.88	0.006042
15	159.56	0.002119	10.71	0.004145
16	209.08	0.001873	9.47	0.002796
17	226.08	0.000154	0.78	0.000212
18	259.45	0.008878	44.87	0.010679
19	286.50	0.001026	5.18	0.001117
20	335.01	0.000752	3.80	0.000700
21	345.61	0.000807	4.08	0.000729
22	364.53	0.000882	4.46	0.000755
23	381.94	0.000588	2.97	0.000481
24	409.99	0.000026	0.13	0.000020
25	444.78	0.000678	3.43	0.000476
26	491.21	0.000464	2.35	0.000295
27	501.27	0.002515	12.71	0.001565

Mode	Frequency / cm^{-1}	Epsilon / L/mol·cm	Intensity / km/mol	T^2 / a.u.
28	526.16	0.003233	16.34	0.001917
29	560.28	0.027894	140.96	0.015536
30	605.78	0.002237	11.30	0.001152
31	611.27	0.000129	0.65	0.000066
32	613.98	0.000985	4.98	0.000501
33	624.46	0.000063	0.32	0.000032
34	638.23	0.000091	0.46	0.000044
35	658.52	0.004119	20.82	0.001952
36	669.33	0.000112	0.56	0.000052
37	678.41	0.005377	27.17	0.002473
38	684.41	0.009591	48.47	0.004373
39	701.86	0.001288	6.51	0.000573
40	711.05	0.008156	41.22	0.003579
41	726.23	0.008605	43.49	0.003698
42	730.98	0.006781	34.27	0.002895
43	799.91	0.001484	7.50	0.000579
44	824.01	0.009817	49.61	0.003718
45	845.45	0.000921	4.66	0.000340
46	850.87	0.001650	8.34	0.000605
47	856.76	0.000833	4.21	0.000303
48	860.51	0.000237	1.20	0.000086
49	915.80	0.000120	0.61	0.000041
50	920.91	0.000322	1.63	0.000109

Mode	Frequency / cm^{-1}	Epsilon / L/mol·cm	Intensity / km/mol	T^2 / a.u.
51	938.40	0.002170	10.97	0.000722
52	942.22	0.000042	0.21	0.000014
53	960.37	0.000928	4.69	0.000302
54	984.22	0.000346	1.75	0.000110
55	1003.95	0.000421	2.13	0.000131
56	1026.18	0.000155	0.78	0.000047
57	1031.89	0.001109	5.61	0.000336
58	1053.35	0.001738	8.78	0.000515
59	1060.84	0.002358	11.92	0.000694
60	1081.71	0.003698	18.69	0.001067
61	1110.11	0.001942	9.82	0.000546
62	1114.32	0.003901	19.71	0.001092
63	1122.66	0.008668	43.80	0.002409
64	1133.49	0.012056	60.92	0.003319
65	1160.29	0.002192	11.08	0.000590
66	1180.13	0.005524	27.91	0.001461
67	1187.94	0.000040	0.20	0.000011
68	1207.56	0.001019	5.15	0.000263
69	1209.86	0.002051	10.37	0.000529
70	1228.84	0.002387	12.06	0.000606
71	1235.32	0.001350	6.82	0.000341
72	1261.87	0.003075	15.54	0.000761
73	1275.69	0.001076	5.44	0.000263

Mode	Frequency / cm^{-1}	Epsilon / L/mol·cm	Intensity / km/mol	T^2 / a.u.
74	1311.07	0.000940	4.75	0.000224
75	1324.95	0.007970	40.27	0.001877
76	1331.46	0.003271	16.53	0.000767
77	1351.30	0.006662	33.67	0.001538
78	1361.29	0.000255	1.29	0.000058
79	1364.87	0.001049	5.30	0.000240
80	1397.25	0.009433	47.67	0.002107
81	1439.26	0.001336	6.75	0.000290
82	1454.92	0.005930	29.97	0.001272
83	1464.15	0.002605	13.16	0.000555
84	1473.93	0.021023	106.24	0.004451
85	1488.36	0.001221	6.17	0.000256
86	1500.69	0.004901	24.77	0.001019
87	1517.02	0.004837	24.45	0.000995
88	1524.54	0.000382	1.93	0.000078
89	1527.55	0.004873	24.62	0.000995
90	1614.32	0.028827	145.68	0.005572
91	1623.93	0.000160	0.81	0.000031
92	1626.42	0.053125	268.47	0.010193
93	1641.65	0.000362	1.83	0.000069
94	1690.84	0.043628	220.48	0.008052
95	3007.18	0.003289	16.62	0.000341
96	3084.81	0.001100	5.56	0.000111

Mode	Frequency / cm^{-1}	Epsilon / L/mol·cm	Intensity / km/mol	T^2 / a.u.
97	3151.46	0.000976	4.93	0.000097
98	3158.31	0.000721	3.65	0.000071
99	3168.09	0.000453	2.29	0.000045
100	3180.21	0.002137	10.80	0.000210
101	3189.30	0.002956	14.94	0.000289
102	3243.68	0.000473	2.39	0.000045
103	3247.98	0.000522	2.64	0.000050
104	3275.20	0.000244	1.23	0.000023
105	3281.39	0.003420	17.28	0.000325
106	3285.36	0.001867	9.44	0.000177
107	3289.60	0.003513	17.75	0.000333

iso-TTBnAu_{20}

CARTESIAN COORDINATES (ANGSTROEM)

Au	-1.634133	-1.465539	2.540994
Au	-1.059778	-0.393347	0.093729
Au	0.989149	-0.313647	1.877272
Au	-1.369239	1.459545	2.049086
Au	-1.602809	3.160699	4.095642
Au	-2.089074	-2.375538	5.014316
Au	-2.062196	0.405541	4.595483
Au	0.692039	1.546412	3.980277
Au	2.921446	-0.146066	3.715616
Au	0.488447	-1.418266	4.446488
Au	-2.396935	-0.454752	7.229512
Au	0.348598	3.039817	6.322712
Au	2.428427	-1.211996	6.434891
Au	-2.334801	2.121634	6.760474
Au	-1.761320	4.752577	6.297243
Au	-2.456741	-3.142386	7.603309
Au	0.016443	-2.082600	7.069456
Au	4.753452	0.033824	5.699136
Au	2.551396	1.598041	6.093646
Au	0.699673	0.684743	7.940406
N	-2.334587	-1.034610	12.158154
C	-2.044818	-2.375263	12.038955
C	-1.722470	-0.071377	11.382058

N	-0.766139	-0.477874	10.446723
C	-0.394921	-1.814738	10.347436
N	-1.069881	-2.729573	11.125813
C	-1.824443	1.275503	11.298407
N	-0.930892	1.658051	10.309188
C	-0.291736	0.611523	9.740203
N	0.525794	-2.371478	9.606334
C	0.447311	-3.722799	9.905720
C	-0.519936	-3.971811	10.835716
N	-2.738637	-3.129576	12.842990
C	-3.540008	-2.237665	13.533281
C	-3.318167	-0.947611	13.138822
H	-2.420396	1.983792	11.850633
H	-4.238654	-2.582605	14.282092
H	-3.746977	-0.003929	13.436321
H	1.099224	-4.432257	9.416727
H	-0.871791	-4.865659	11.325527
C	-0.804756	3.050800	9.856040
C	-0.812948	4.017115	11.007515
H	-1.624871	3.260324	9.154030
H	0.128159	3.104622	9.281104
C	0.176217	3.949086	11.992130
C	0.171974	4.847724	13.050979
C	-0.816852	5.826898	13.132839
C	-1.800796	5.902168	12.153458

C	-1.800926	4.996372	11.095260
H	-2.568868	5.052951	10.326980
H	-0.816021	6.532435	13.958364
H	-2.571016	6.665498	12.210826
H	0.951851	3.189558	11.922463
H	0.946058	4.792361	13.810640

Unscaled IR spectrum

Mode	Frequency / cm^{-1}	Epsilon / L/mol·cm	Intensity / km/mol	T^2 / a.u.
6	8.07	0.000040	0.20	0.001541
7	10.80	0.000115	0.58	0.003328
8	15.87	0.000022	0.11	0.000428
9	20.33	0.000022	0.11	0.000341
10	23.68	0.000009	0.05	0.000119
11	24.38	0.000113	0.57	0.001445
12	26.54	0.000007	0.04	0.000087
13	28.34	0.000006	0.03	0.000063
14	28.94	0.000034	0.17	0.000365
15	30.44	0.000094	0.47	0.000963
16	31.62	0.000012	0.06	0.000121
17	32.59	0.000032	0.16	0.000302
18	35.91	0.000026	0.13	0.000227
19	38.27	0.000032	0.16	0.000263
20	40.61	0.000134	0.68	0.001030

21	41.86	0.000018	0.09	0.000133
22	43.72	0.000002	0.01	0.000017
23	45.01	0.000023	0.12	0.000159
24	47.23	0.000007	0.03	0.000046
25	48.16	0.000001	0.00	0.000005
26	49.89	0.000021	0.11	0.000130
27	50.11	0.000014	0.07	0.000089
28	50.96	0.000066	0.33	0.000404
29	53.62	0.000041	0.21	0.000241
30	54.68	0.000063	0.32	0.000360
31	56.06	0.000004	0.02	0.000023
32	56.69	0.000025	0.12	0.000135
33	58.81	0.000052	0.26	0.000275
34	61.22	0.000109	0.55	0.000556
35	61.38	0.000026	0.13	0.000131
36	63.98	0.000024	0.12	0.000119
37	64.36	0.000028	0.14	0.000134
38	65.18	0.000003	0.02	0.000015
39	66.39	0.000036	0.18	0.000168
40	69.81	0.000044	0.22	0.000195
41	74.66	0.000010	0.05	0.000041
42	74.70	0.000033	0.17	0.000137
43	76.46	0.000007	0.04	0.000029
44	77.75	0.000014	0.07	0.000058
45	81.81	0.000023	0.12	0.000089

46	84.23	0.000066	0.33	0.000243
47	89.49	0.000015	0.08	0.000052
48	91.61	0.000090	0.45	0.000305
49	94.27	0.000057	0.29	0.000190
50	97.37	0.000019	0.09	0.000060
51	98.89	0.000065	0.33	0.000207
52	100.36	0.000007	0.03	0.000021
53	103.79	0.000002	0.01	0.000007
54	117.20	0.000167	0.85	0.000446
55	117.82	0.000767	3.88	0.002032
56	120.67	0.000076	0.38	0.000196
57	121.79	0.000014	0.07	0.000035
58	124.26	0.000037	0.19	0.000093
59	125.87	0.000060	0.30	0.000150
60	129.17	0.000980	4.95	0.002367
61	136.19	0.000247	1.25	0.000566
62	138.82	0.000630	3.19	0.001417
63	140.82	0.000807	4.08	0.001789
64	142.95	0.000643	3.25	0.001404
65	156.22	0.002576	13.02	0.005145
66	171.79	0.000017	0.09	0.000031
67	173.71	0.000024	0.12	0.000044
68	178.72	0.000019	0.09	0.000032
69	179.65	0.000020	0.10	0.000035
70	181.47	0.000044	0.22	0.000076

71	188.83	0.000191	0.96	0.000315
72	193.51	0.000087	0.44	0.000140
73	200.01	0.001084	5.48	0.001692
74	229.32	0.000248	1.26	0.000338
75	278.36	0.000455	2.30	0.000510
76	289.10	0.000518	2.62	0.000559
77	331.22	0.000400	2.02	0.000377
78	349.65	0.000179	0.91	0.000160
79	369.68	0.000469	2.37	0.000396
80	407.78	0.000112	0.57	0.000086
81	417.49	0.000083	0.42	0.000062
82	452.32	0.000238	1.20	0.000164
83	498.71	0.001891	9.56	0.001183
84	508.53	0.001168	5.90	0.000717
85	526.00	0.000823	4.16	0.000488
86	601.45	0.000372	1.88	0.000193
87	609.75	0.000188	0.95	0.000096
88	621.65	0.000958	4.84	0.000481
89	632.28	0.002512	12.70	0.001240
90	636.47	0.000189	0.95	0.000093
91	640.56	0.000121	0.61	0.000059
92	664.10	0.008420	42.55	0.003957
93	667.83	0.001251	6.32	0.000585
94	694.24	0.002649	13.39	0.001191
95	703.57	0.000659	3.33	0.000292

96	710.70	0.005427	27.43	0.002383
97	723.26	0.006527	32.99	0.002816
98	736.51	0.007082	35.79	0.003000
99	738.78	0.005709	28.85	0.002411
100	799.66	0.001598	8.08	0.000624
101	846.53	0.001881	9.51	0.000694
102	856.67	0.001421	7.18	0.000518
103	858.38	0.000091	0.46	0.000033
104	862.39	0.001313	6.64	0.000475
105	919.49	0.000183	0.92	0.000062
106	922.06	0.000536	2.71	0.000181
107	924.29	0.000258	1.30	0.000087
108	942.97	0.000243	1.23	0.000080
109	972.12	0.000975	4.93	0.000313
110	980.91	0.000066	0.33	0.000021
111	1000.98	0.000002	0.01	0.000000
112	1026.76	0.000242	1.22	0.000073
113	1046.32	0.001743	8.81	0.000520
114	1054.43	0.001846	9.33	0.000546
115	1066.41	0.001330	6.72	0.000389
116	1092.23	0.000980	4.95	0.000280
117	1111.34	0.001720	8.69	0.000483
118	1119.85	0.001652	8.35	0.000460
119	1126.36	0.001465	7.40	0.000406
120	1138.18	0.010585	53.49	0.002902

121	1162.53	0.005079	25.67	0.001363
122	1175.66	0.002055	10.39	0.000545
123	1190.82	0.000048	0.24	0.000013
124	1207.64	0.000640	3.23	0.000165
125	1223.24	0.001597	8.07	0.000407
126	1231.51	0.002127	10.75	0.000539
127	1255.16	0.001875	9.47	0.000466
128	1258.80	0.001060	5.36	0.000263
129	1284.31	0.003163	15.98	0.000768
130	1318.62	0.004875	24.64	0.001154
131	1323.93	0.001235	6.24	0.000291
132	1342.39	0.010221	51.65	0.002376
133	1362.06	0.000469	2.37	0.000107
134	1365.78	0.001536	7.76	0.000351
135	1394.20	0.004391	22.19	0.000983
136	1412.11	0.007643	38.63	0.001689
137	1433.48	0.001491	7.53	0.000324
138	1448.08	0.015352	77.58	0.003308
139	1462.79	0.008689	43.91	0.001854
140	1474.36	0.009388	47.44	0.001987
141	1487.09	0.001747	8.83	0.000367
142	1514.45	0.000214	1.08	0.000044
143	1527.65	0.002069	10.46	0.000423
144	1527.99	0.001724	8.71	0.000352
145	1590.42	0.015112	76.37	0.002965

146	1619.05	0.066129	334.19	0.012746
147	1626.55	0.000793	4.01	0.000152
148	1644.01	0.000998	5.04	0.000189
149	1691.63	0.036779	185.87	0.006785
150	2984.84	0.000201	1.02	0.000021
151	3049.48	0.000586	2.96	0.000060
152	3155.95	0.001092	5.52	0.000108
153	3156.73	0.000740	3.74	0.000073
154	3171.49	0.000285	1.44	0.000028
155	3181.45	0.001525	7.71	0.000150
156	3190.99	0.002601	13.15	0.000254
157	3247.05	0.000382	1.93	0.000037
158	3252.05	0.001137	5.75	0.000109
159	3277.49	0.000074	0.37	0.000007
160	3281.81	0.003482	17.60	0.000331
161	3285.32	0.002685	13.57	0.000255

Catalytic tests

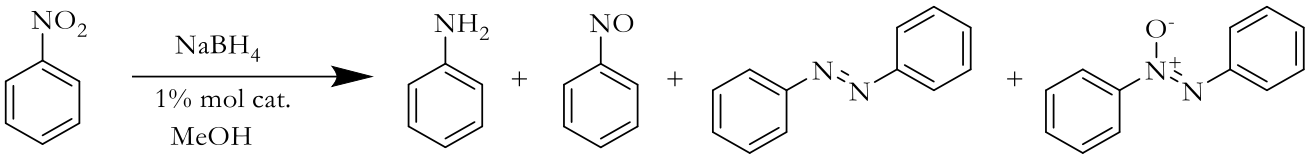

Reagent	V / µL	d / g/mL	m / mg	MM / g/mol	n / mol	Eq.
Nitrobenzene	20.0	1.20	24.0	123.11	$1.95 \cdot 10^{-4}$	1
$NaBH_4$	/	/	73.7	37.8	$1.95 \cdot 10^{-3}$	10

In a typical reaction, 20 µL of nitrobenzene are dissolved in 6 mL of methanol. The proper amount of catalyst (384 µg of unsupported gold nanoparticles or 38.4 mg of supported gold nanoparticles in 1% w/w) are added to the solution, which represents the proper amount to have 1% mol of gold with respect to nitrobenzene (38.4 mg of catalyst contains 0.384 mg of gold, equal to $1.95 \cdot 10^{-6}$ mol).

73.7 mg of $NaBH_4$ are then added to the mixture to start the reduction reaction.

After one hour, bromobenzene is added to the mixture as internal reference, and the catalyst is removed *via* centrifugation. The solution is then analyzed with HPLC for product identification and quantification.

For reuse tests, the catalysts are washed three times with fresh methanol and centrifuged prior to reuse.

Chapter IV Experimental Procedures

Synthesis of the Au/rutile and Au/Al_2O_3 Catalysts

The synthesis of the catalysts was performed with the urea deposition-precipitation technique.

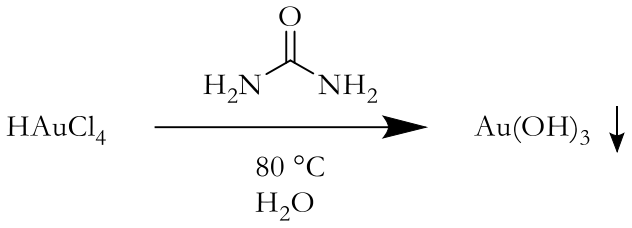

Reagents	m / mg	MM / g/mol	n / mol	Eq
$HAuCl_4 \cdot 3H_2O$	350.0	393.82	$8.89 \cdot 10^{-4}$	1
urea	1600.0	60.06.	$2.67 \cdot 10^{-2}$	30

For a 3.5% Au/rutile catalyst, 350.0 mg of $HAuCl_4 \cdot 3H_2O$ are dissolved in 85 mL of MilliQ with 1.600 g of urea. The solution is heated at 80 °C, and then 5 g of rutile are added. The suspension is stirred for 4 hours, then is cooled down and transferred into a centrifuge tube. After centrifugation, the supernatant is removed, and the catalyst is further washed several times with MilliQ water.

After ten washes, a test with silver nitrate is performed to detect the presence of chlorides with the precipitation of AgCl. If chlorides are still present, the washing process is continued until the silver nitrate test shows no presence of chlorides. Once succeeded, the catalyst is reduced in a furnace under 5% H_2 in Ar flow at 275 °C for 4 hours to reduce the nanoparticles to the metallic state.

The 5% Au/Al_2O_3 is synthesized analogously.

TEM images of 3.5% Au/rutile

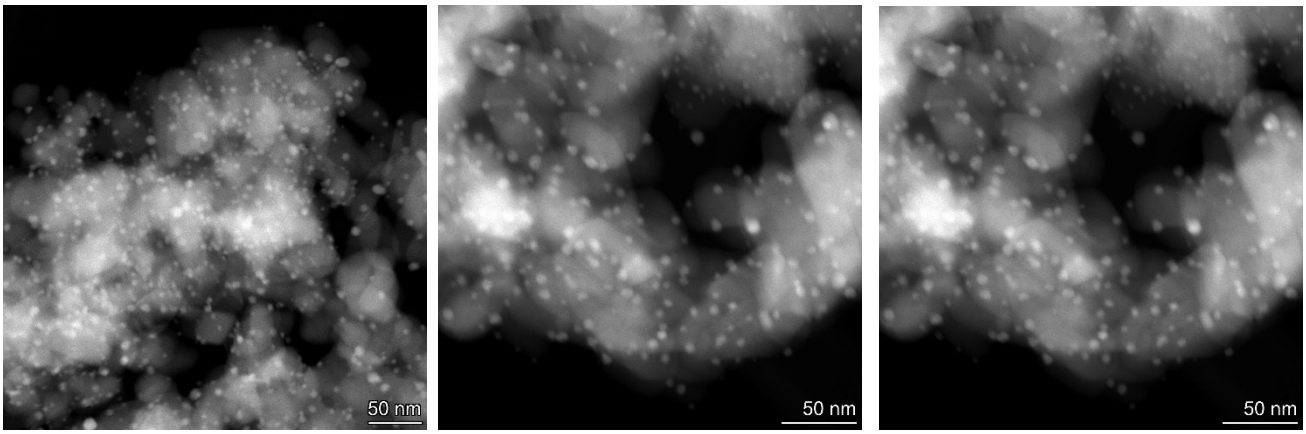

TEM images of iso-TTBn@Au/rutile

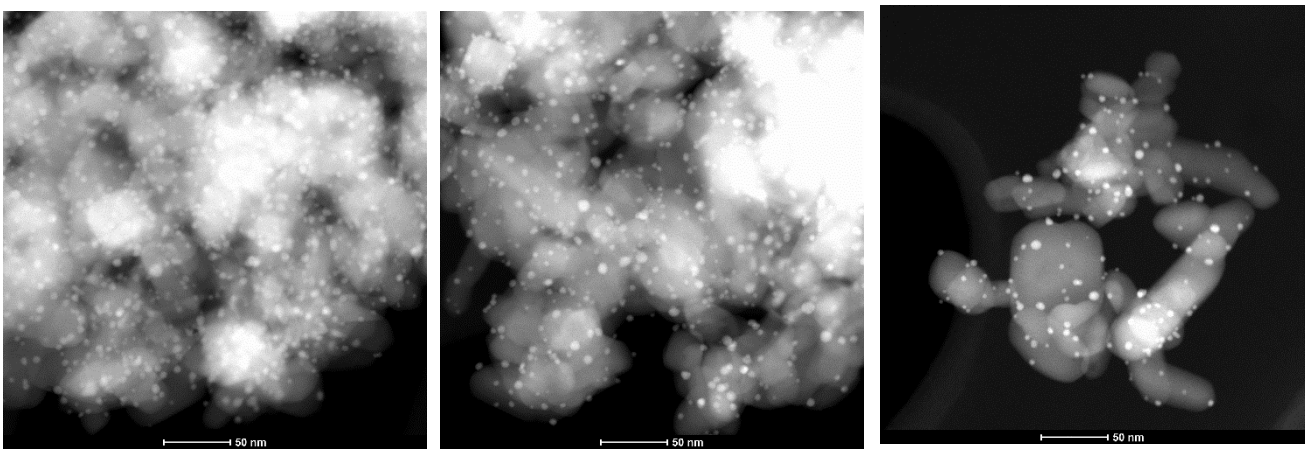

TEM images of 5% Au/Al_2O_3

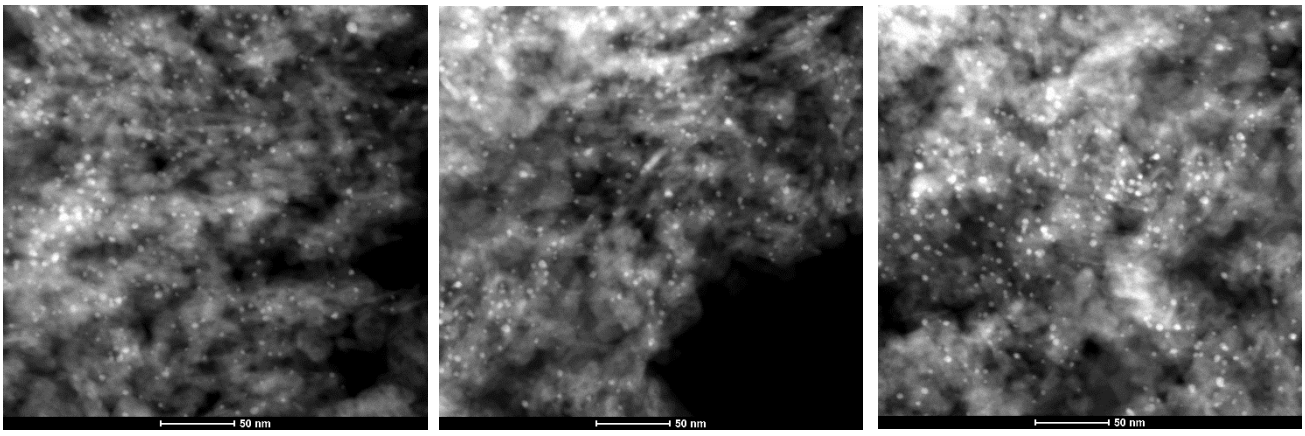

3.5% Au/rutile TEM analysis results

Dimension analysis

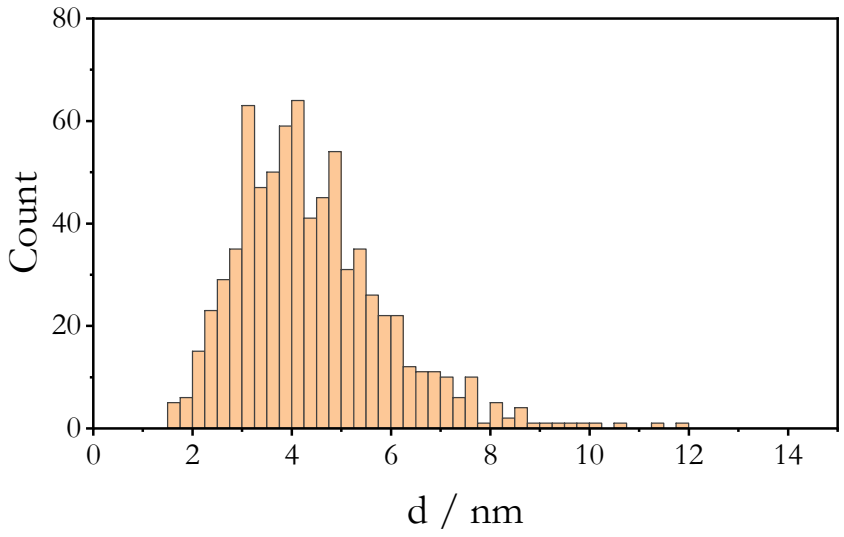

Perimetral atom fraction calculation

diameter / nm (bin average)	diameter / m (bin average)	bin count	perimeter atom fraction (PF)	PF bin total
0.375	3.75E-10	0	2.4635	0
0.625	6.25E-10	0	0.8868	0
0.875	8.75E-10	0	0.4525	0
1.125	1.125E-09	0	0.2737	0
1.375	1.375E-09	0	0.1832	0
1.625	1.625E-09	5	0.1312	0.65595
1.875	1.875E-09	6	0.0985	0.59123
2.125	2.125E-09	14	0.0767	1.07404
2.375	2.375E-09	23	0.0614	1.41257
2.625	2.625E-09	29	0.0503	1.45797
2.875	2.875E-09	35	0.0419	1.4669
3.125	3.125E-09	63	0.0355	2.23485
3.375	3.375E-09	45	0.0304	1.36859
3.625	3.625E-09	50	0.0264	1.31814
3.875	3.875E-09	59	0.0231	1.36119
4.125	4.125E-09	62	0.0204	1.26227

diameter / nm (bin average)	diameter / m (bin average)	bin count	perimeter atom fraction (PF)	PF bin total
4.375	4.375E-09	41	0.0181	0.74206
4.625	4.625E-09	44	0.0162	0.71259
4.875	4.875E-09	54	0.0146	0.78714
5.125	5.125E-09	31	0.0132	0.40887
5.375	5.375E-09	35	0.0120	0.41968
5.625	5.625E-09	26	0.0109	0.28467
5.875	5.875E-09	22	0.0100	0.22081
6.125	6.125E-09	22	0.0092	0.20315
6.375	6.375E-09	12	0.0085	0.10229
6.625	6.625E-09	9	0.0079	0.07104
6.875	6.875E-09	11	0.0073	0.08062
7.125	7.125E-09	10	0.0068	0.06824
7.375	7.375E-09	6	0.0064	0.03822
7.625	7.625E-09	10	0.0060	0.05958
7.875	7.875E-09	1	0.0056	0.00559
8.125	8.125E-09	5	0.0052	0.02624
8.375	8.375E-09	2	0.0049	0.00988
8.625	8.625E-09	4	0.0047	0.01863
8.875	8.875E-09	1	0.0044	0.00440
9.125	9.125E-09	1	0.0042	0.00416
9.375	9.375E-09	1	0.0039	0.00394
9.625	9.625E-09	1	0.0037	0.00374
9.875	9.875E-09	1	0.0036	0.00355
10.125	1.0125E-08	1	0.0034	0.00338
10.375	1.0375E-08	0	0.0032	0
10.625	1.0625E-08	1	0.0031	0.00307
10.875	1.0875E-08	0	0.0029	0
11.125	1.1125E-08	0	0.0028	0
11.375	1.1375E-08	1	0.0027	0.00268

diameter / nm (bin average)	diameter / m (bin average)	bin count	perimeter atom fraction (PF)	PF bin total
11.625	1.1625E-08	0	0.0026	0
11.875	1.1875E-08	1	0.0025	0.00246
12.125	1.2125E-08	0	0.0024	0
12.375	1.2375E-08	0	0.0023	0
12.625	1.2625E-08	0	0.0022	0
12.875	1.2875E-08	0	0.0021	0
13.125	1.3125E-08	0	0.0020	0
13.375	1.3375E-08	0	0.0019	0
13.625	1.3625E-08	0	0.0019	0
13.875	1.3875E-08	0	0.0018	0
14.125	1.4125E-08	0	0.0017	0
14.375	1.4375E-08	0	0.0017	0
14.625	1.4625E-08	0	0.0016	0
14.875	1.4875E-08	0	0.0016	0

total PF average	total PF / %	mol Au_{per}/g catalyst (3.5%)
0.025390663	2.53907	4.51172E-06

Au_{per}/mol Au	µmol Au_{per}/g catalyst (3.5%)
1.52903E+22	4.511718575

mol Au/g catalyst (3.5%)
0.000177692

Au_{per}/g catalyst (3.5%)
2.71696E+18

Surface atom fraction calculation

diameter / nm (bin average)	diameter / m (bin average)	bin count	Surface atom fraction (SF)	SF bin total
0.375	3.75E-10	0	4.1913	0
0.625	6.25E-10	0	2.5148	0
0.875	8.75E-10	0	1.7963	0
1.125	1.125E-09	0	1.3971	0
1.375	1.375E-09	0	1.1431	0
1.625	1.625E-09	5	0.9672	4.8361
1.875	1.875E-09	6	0.8383	5.0296
2.125	2.125E-09	14	0.7396	10.3550
2.375	2.375E-09	23	0.6618	15.2211
2.625	2.625E-09	29	0.5988	17.3641
2.875	2.875E-09	35	0.5467	19.1343
3.125	3.125E-09	63	0.5030	31.6864
3.375	3.375E-09	45	0.4657	20.9566
3.625	3.625E-09	50	0.4336	21.6793
3.875	3.875E-09	59	0.4056	23.9311
4.125	4.125E-09	62	0.3810	23.6238
4.375	4.375E-09	41	0.3593	14.7295
4.625	4.625E-09	44	0.3398	14.9528
4.875	4.875E-09	54	0.3224	17.4101
5.125	5.125E-09	31	0.3067	9.5072
5.375	5.375E-09	35	0.2924	10.2346
5.625	5.625E-09	26	0.2794	7.2650
5.875	5.875E-09	22	0.2675	5.8857
6.125	6.125E-09	22	0.2566	5.6455
6.375	6.375E-09	12	0.2465	2.9586
6.625	6.625E-09	9	0.2372	2.1352
6.875	6.875E-09	11	0.2286	2.5148
7.125	7.125E-09	10	0.2206	2.2060
7.375	7.375E-09	6	0.2131	1.2787

diameter / nm (bin average)	diameter / m (bin average)	bin count	Surface atom fraction (SF)	SF bin total
7.625	7.625E-09	10	0.2061	2.0613
7.875	7.875E-09	1	0.1996	0.1996
8.125	8.125E-09	5	0.1934	0.9672
8.375	8.375E-09	2	0.1877	0.3753
8.625	8.625E-09	4	0.1822	0.7289
8.875	8.875E-09	1	0.1771	0.1771
9.125	9.125E-09	1	0.1722	0.1722
9.375	9.375E-09	1	0.1677	0.1677
9.625	9.625E-09	1	0.1633	0.1633
9.875	9.875E-09	1	0.1592	0.1592
10.125	1.0125E-08	1	0.1552	0.1552
10.375	1.0375E-08	0	0.1515	0
10.625	1.0625E-08	1	0.1479	0.1479
10.875	1.0875E-08	0	0.1445	0
11.125	1.1125E-08	0	0.1413	0
11.375	1.1375E-08	1	0.1382	0.1382
11.625	1.1625E-08	0	0.1352	0
11.875	1.1875E-08	1	0.1324	0.1324
12.125	1.2125E-08	0	0.1296	0
12.375	1.2375E-08	0	0.1270	0
12.625	1.2625E-08	0	0.1245	0
12.875	1.2875E-08	0	0.1221	0
13.125	1.3125E-08	0	0.1198	0
13.375	1.3375E-08	0	0.1175	0
13.625	1.3625E-08	0	0.1154	0
13.875	1.3875E-08	0	0.1133	0
14.125	1.4125E-08	0	0.1113	0
14.375	1.4375E-08	0	0.1093	0
14.625	1.4625E-08	0	0.1075	0
14.875	1.4875E-08	0	0.1057	0

Total SF average	Total SF %	mol Au_{surf}/g cat
3.93E-01	3.93E+01	6.99E-05

Au_{surf}/mol Au		µmol Au_{surf}/g cat
2.37E+23		69.91741

molAu/g cat (3.5%)
0.000178

Au_{surf}/g cat
4.21E+19

5% Au/Al_2O_3 TEM analysis results

Dimension analysis

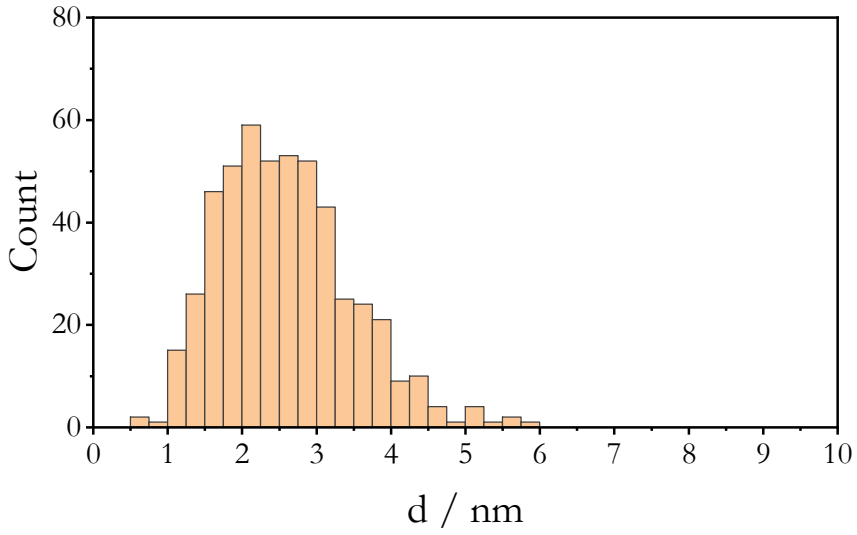

Perimetral atom fraction calculation

diameter / nm (bin average)	diameter / m (bin average)	bin count	perimeter atom fraction (PF)	PF bin total
0.625	6.25E-10	2	0.8868	1.77369
0.875	8.75E-10	1	0.4525	0.45247
1.125	1.125E-09	15	0.2737	4.10577
1.375	1.375E-09	26	0.1832	4.76405
1.625	1.625E-09	46	0.1312	6.03476
1.875	1.875E-09	50	0.0985	4.92693
2.125	2.125E-09	59	0.0767	4.52629
2.375	2.375E-09	52	0.0614	3.19363
2.625	2.625E-09	53	0.0503	2.66456
2.875	2.875E-09	52	0.0419	2.1794
3.125	3.125E-09	43	0.0355	1.52538
3.375	3.375E-09	25	0.0304	0.76033
3.625	3.625E-09	24	0.0264	0.63271
3.875	3.875E-09	21	0.0231	0.48449
4.125	4.125E-09	9	0.0204	0.18323

diameter / nm (bin average)	diameter / m (bin average)	bin count	perimeter atom fraction (PF)	PF bin total
4.375	4.375E-09	10	0.0181	0.18099
4.625	4.625E-09	4	0.0162	0.06478
4.875	4.875E-09	1	0.0146	0.01458
5.125	5.125E-09	4	0.0132	0.05276
5.375	5.375E-09	1	0.012	0.01199
5.625	5.625E-09	2	0.0109	0.0219
5.875	5.875E-09	1	0.01	0.01004
6.125	6.125E-09	0	0.0092	0
6.375	6.375E-09	0	0.0085	0
6.625	6.625E-09	0	0.0079	0
6.875	6.875E-09	0	0.0073	0
7.125	7.125E-09	0	0.0068	0

total PF average	total PF / %	mol Au_{per}/g catalyst (5%)
0.076822151	7.68222	1.9501E-05

Au_{per}/mol Au	μmol Au_{per}/g catalyst (5%)
4.62623E+22	19.50097763

mol Au/g catalyst (5%)
0.000253846

Au_{per}/g catalyst (5%)
1.17435E+19

Synthesis of the carbene-functionalized Au/rutile and Au/Al_2O_3 catalysts

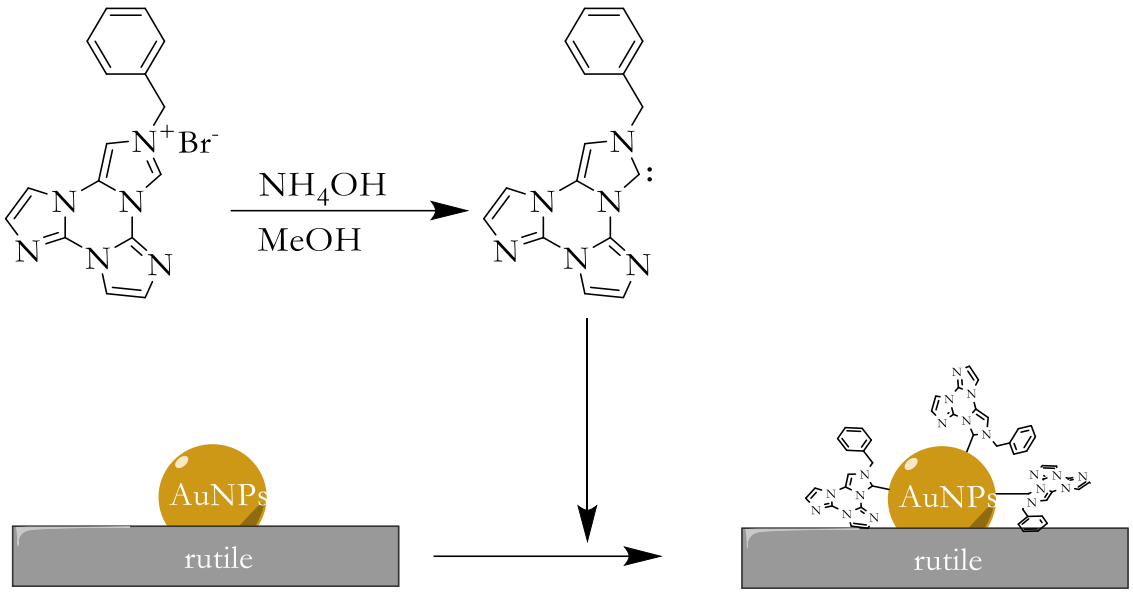

In a typical synthesis for the carbene-functionalization of Au/rutile catalyst, the selected amount of isoTTBnHBr from a stock solution is added to a 100 mL round-bottom flask filled with methanol. The system is bubbled with nitrogen to remove the dissolved oxygen, then a large excess of ammonia is added (e.g., 500 µL 14.8 M solution, $7.5 \cdot 10^{-3}$ mol). At this time, a small amount of solution is sampled as a reference for the initial absorbance. The unfunctionalized catalyst (e.g., 500 mg of 3.5% Au/rutile) is then added, and the suspension is kept under stirring. Samples are taken to monitor the adsorption from the solution. Typically, after 1.5 hours, the adsorption ends.

The catalyst is then centrifuged and washed multiple times with MilliQ to remove ammonia, the unbonded carbene precursor, and bromides. The washing continues until the silver nitrate test for the presence of bromides is negative.

The carbene-functionalized Au/Al_2O_3 catalyst was synthesized analogously.

The adsorbed carbene amount was calculated *via* the difference between the initial and final UV absorbance of the supernatant.

0.095% carbene loading

Time / min	0	15	30	60	120	180
Absorbance λ 274 nm	0.135	0.094	0.064	0.051	0.048	0.052

0.032% carbene loading

Time / min	0	15	30	60	120
Absorbance λ 274 nm	0.118	0.082	0.083	0.049	0.050

0.015% carbene loading

Time / min	0	15	30	60
Absorbance λ 274 nm	0.042	0.023	0.012	0.005

IR Sample Preparation

Pressing of IR pellets

Pellets are pressed with 18 ± 1 mg of material. To grant gas permeability they are pressed under 1 ton for 24 seconds to avoid excessive compaction of the material. To help the powder stick together without breaking, a stainless-steel gauze is inserted in the press to accommodate the pressed material in the gauze mesh.

Carbonate Removal

Catalysts are capable of adsorbing CO_2 from the air, forming carbonates on their surface. If present in high amounts, carbonates can interfere with the hydrogen spillover process. To remove carbonates from a pellet, this is heated to 300 °C while flowing 40% O_2 for half an hour. The oxygen flow is then stopped, and the sample is cooled down to the selected temperature for the following experiment..

Strong-Adsorbed Oxygen treatment (SAO treatment)

This treatment is required for each IR pellet exposed to oxygen, since oxygen can strongly bind to the titania surface. These are the steps to follow: after pressing the pellet and inserting it into the IR cell, heat it to 120 °C, under argon flow through oxygen and water traps. Once at 120 °C, collect pellet spectra as a background, then flow 40% H2 for 1 hour, monitoring the process with repeated scans every minute. After one hour, check whether the spectra are stabilized; otherwise, wait for another ten minutes.

Once stabilized, stop the hydrogen flow and desorb hydrogen. Once desorption is almost complete, the sample can be cooled to the desired temperature for the following experiment.

Pellet Calibration

To perform quantitative measurements with the FT-IR instrument, each pellet is calibrated using tandem experiments at the chemisorption instrument and the FT-IR.

Hydrogen adsorption experiments are performed on a Micromeritics 3Flex instrument. 200 - 300 mg of previously pretreated catalyst (i.e., the Au precursor was already reduced) are evacuated at 120 °C for one hour and then reduced under flowing H_2 at 120 °C for one hour. The sample is then evacuated and purged with helium for 30 min. Two H_2 adsorption isotherms are measured at 120 °C, and then the other two at 70°C; the sample is evacuated to at least 10 µm Hg for 1 hour at the adsorption temperature between isotherms.

An analogous experiment is performed with the pellet in the FT-IR. The pellet is heated at 120°C, and it undergoes the SAO treatment. After desorption, adsorption isotherms are collected at 120°C and 70°C, measuring the BBA area in the 2600-2700 cm^{-1} region.

At each temperature, a system of equations is used to calibrate the BBA signal with the volumetric chemisorption data. Here, an example is reported using the equations fit to the 120°C isotherms. The BBA data (here in red) and chemisorption data (in green) are first fit to natural logarithm functions:

$$y = 1.8\, ln\,(x) + 13.3 \qquad \textit{Equation VII.1}$$

$$y = 1.7\, ln(x) + 13.3 \qquad \textit{Equation VII.2}$$

Equation VII.1 is then solved with respect to x:

$$x = e^{\frac{y-13.3}{1.8}} \qquad \textit{Equation VII.3}$$

And it is then substituted in *Equation VII.2*

$$y = 1.7\, ln\left(e^{\frac{y-13.3}{1.8}}\right) + 13.3 \qquad \textit{Equation VII.4}$$

An analogous procedure is performed for *Equation VII.2*, to obtain the following two equations.

$$y = 1.8\, ln\left(e^{\frac{y-13.3}{1.7}}\right) + 13.3 \qquad \textit{Equation VII.5}$$

$$y = 1.7\, ln\left(e^{\frac{y-13.3}{1.8}}\right) + 13.3 \qquad \textit{Equation VII.6}$$

The experimental BBA values are used in Equation VII.6 to determine the corresponding amount of hydrogen adsorbed (QA). These are referred to as “calculated QA values." Similarly, experimental QA values are used in Equation VII.5 to determine the corresponding BBA values, which are called "calculated BBA values."

The calculated BBA and calculated QA values are the predicted values based on the trends in the experimental BBA and QA data. The BBA calibration factor is found by plotting the calculated QA values vs. the experimental BBA values and the experimental QA values vs. the calculated BBA values for the two temperatures. The calibration factor is the resulting slope between the datasets. For the other experiments, the integrated BBA area is multiplied by the calibration factor to convert the BBA area directly into adsorbed hydrogen per gram of catalyst ($\mu mol_{H^*}/g_{cat}$).

Herein is reported an example of the overlap of the two calibration isotherms from chemisorption (green) and from FT-IR (purple), and the complete calibration line at two different temperatures.

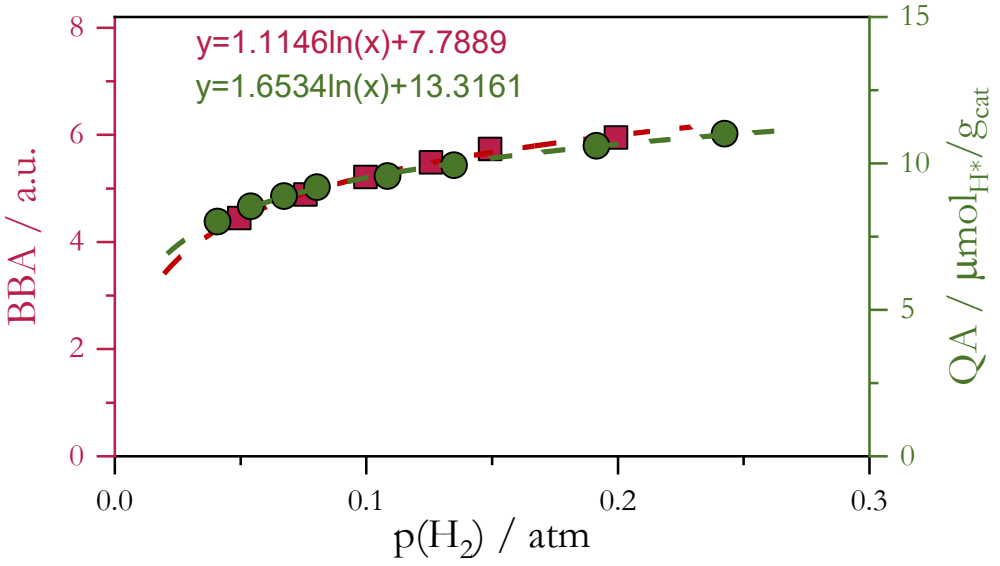

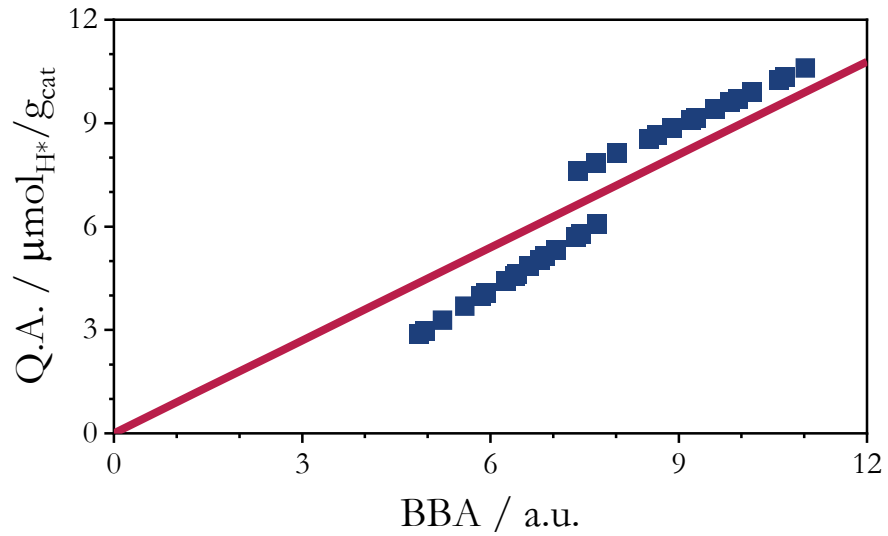

Measurement of Reaction Rate

To measure reaction rates, an MCT detector cooled with liquid nitrogen is used. Twelve scans per spectrum are collected with a scanner velocity of 20 kHz. Spectra are collected with a 6 s time interval.

After sample pretreatment, the pellet is equilibrated at the new temperature under 40 mL/min Ar flow since the water peak is stable. A new background is collected, then H_2 is introduced in the flow while collecting spectra with 6 s intervals. After a few minutes, when the growth of BBA slows down, the hydrogen flow is stopped, and its desorption is monitored. Once fully desorbed, proceed with the following experiment.

The BBA values are then converted into QA values *via* the pellet calibration factor and then normalized based on the amount of Au_{per} (the activation sites). The reaction rate can be determined as the maximum slope of the curve, expressed in $mol_{H^*}/Au_{per}{\cdot}min$.

Arrhenius Analysis

To perform an Arrhenius analysis, the reaction rate is measured at four temperatures (e.g., 45 °C, 60 °C, 75 °C, 90 °C) under the same hydrogen pressure (0.2 atm). After each experiment, the pellet is monitored to confirm complete desorption of adsorbed hydrogen and equilibration of water at the new temperature. From the reaction rate, the kinetic constant referred to the H* species is calculated as $k = r/p_{H_2}^{0.5}$.

The apparent activation energy is obtained as the slope of the ln(k) vs 1000/T plot.

In the following pages, it is reported an example of kinetic constants calculation at different temperatures to perform Arrhenius analysis.

0.095% carbene loading sample: 30 °C. Highlighted data indicates the linear region.

Time / s	BBA / A.U.	mol_H/mol_{Au_per}	Rate / mol_{H*}/Au_{per}·min	K / $1/(min \cdot atm^{0.5})$
0	0	0.00	0.124	0.278
6	0.012260794	0.00		
12	0.01224599	0.00		
18	0.101957477	0.02		
24	0.138859115	0.03		
30	0.206894867	0.05		
36	0.185442291	0.04		
42	0.298406802	0.07		
48	0.328871511	0.08		
54	0.401837073	0.10		
60	0.427832804	0.10		
66	0.460831724	0.11		
72	0.560388766	0.14		
78	0.602498136	0.15		
84	0.606510959	0.15		
90	0.596860133	0.14		
96	0.659858666	0.16		
102	0.665741644	0.16		
108	0.716033302	0.17		
114	0.751307748	0.18		
120	0.766379736	0.19		

0.095% carbene loading sample: 45 °C. Highlighted data indicates the linear region.

Time / s	BBA / A.U.	mol_H/mol_{Au_per}	Rate / mol_{H*}/Au_{per}·min	K / $1/(min \cdot atm^{0.5})$
0	0	0.00	0.175	0.390
6	-0.03076851	-0.01		
12	-0.0295468	-0.01		
18	0.009827547	0.00		
24	0.076078847	0.02		
30	0.154503211	0.04		
36	0.220515057	0.05		
42	0.332841292	0.08		
48	0.365622535	0.09		
54	0.443682328	0.11		
60	0.501028612	0.12		
66	0.593701258	0.14		
72	0.633152023	0.15		
78	0.647270098	0.16		
84	0.76474531	0.18		
90	0.783975855	0.19		
96	0.831280842	0.20		
102	0.915818051	0.22		
108	0.92690368	0.22		
114	0.996164516	0.24		
120	1.049712017	0.25		

0.095% carbene loading sample: 60 °C. Highlighted data indicates the linear region.

Time / s	BBA / A.U.	mol_H/mol_{Au_per}	Rate / mol_{H*}/Au_{per}·min	K / $1/(min \cdot atm^{0.5})$
0	0	0.00	0.247	0.553
6	0.050526604	0.01		
12	0.000628777	0.00		
18	-0.00550778	0.00		
24	0.064045206	0.02		
30	0.103736774	0.03		
36	0.165865511	0.04		
42	0.254480422	0.06		
48	0.364235282	0.09		
54	0.451578528	0.11		
60	0.583324582	0.14		
66	0.695785732	0.17		
72	0.769370884	0.19		
78	0.880271882	0.21		
84	0.991029829	0.24		
90	1.079743594	0.26		
102	1.27843687	0.31		
108	1.405265898	0.34		
114	1.507472486	0.36		
120	1.585253448	0.38		
126	1.680034966	0.41		
132	1.782957286			

0.095% carbene loading sample: 75 °C. Highlighted data indicates the linear region.

Time / s	BBA / A.U.	mol_H/mol_{Au_per}	Rate / mol_{H*}/Au_{per}·min	K / $1/(min \cdot atm^{0.5})$
0	0	0.00	0.478	1.069
6	0.110432502	0.03		
12	0.133317497	0.03		
18	0.22701807	0.05		
24	0.415339988	0.10		
30	0.598768335	0.14		
36	0.712071639	0.17		
42	0.822511774	0.20		
48	0.993614417	0.24		
54	1.188185197	0.29		
60	1.35448597	0.33		
66	1.56933723	0.38		
72	1.698089581	0.41		
78	1.985012751	0.48		
84	2.139075022	0.52		
90	2.331189614	0.56		
96	2.512505275	0.61		
102	2.732263308	0.66		
108	2.927498322	0.71		
114	3.154174786	0.76		
120	3.270261508	0.79		
126	3.494677287	0.84		
132	3.639224272			

Reaction Order Determination

To measure the reaction order, pellets are equilibrated at 75°C. Reaction rates are measured at five different hydrogen pressures (0.10 atm, 0.20 atm, 0.25 atm, 0.30 atm, 0.35 atm).

Since the kinetic constant for H* formation is defined as $k = r/p_{H_2}^{R.O.}$ the reaction order is calculated as the slope of log(r) vs log(p_{H2}) plot.

	p H_2 / atm						
Catalyst	**0.10**	**0.20**	**0.25**	**0.30**	**0.40**	**R.O.**	**Average**
Pristine	1.020	1.354	1.506	1.622	1.810	0.42	0.48 ± 0.08
	0.836	1.256	1.413	1.588	1.661	0.56	
	1.108	1.501	1.613	1.818	1.615	0.45	
NH_3 treat.	0.286	0.421	0.411	0.469	0.482	0.42	0.46 ± 0.07
	0.233	0.367	0.397	0.429	0.452	0.54	
	0.384	0.544	0.562	0.612	0.631	0.42	
0.095% carbene loading	0.292	0.459	0.519	0.595	0.660	0.56	0.71 ± 0.13
	0.229	0.410	0.508	0.486	0.660	0.86	
	0.336	0.625	0.690	0.730	0.787	0.62	

In the following pages, it is reported an example of reaction rate calculation at different temperatures to perform reaction order determination.

Pristine catalyst, 75 °C, 10% H_2. Highlighted data indicates the linear region.

Time / s	BBA / A.U.	mol_H/mol_{Au_per}	Rate / mol_{H*}/Au_{per}·min
0	0	0.00	1.020
6	0.050327299	0.02	
12	0.024467972	0.01	
18	0.040981578	0.01	
24	0.124308391	0.04	
30	0.221807046	0.07	
36	0.390607072	0.13	
42	0.576015247	0.19	
48	0.866663588	0.29	
54	1.164997591	0.39	
60	1.470668925	0.50	
66	1.782390727	0.60	
72	2.103205694	0.71	
78	2.404076589	0.81	
84	2.655065788	0.90	
90	2.875463499	0.97	
96	3.081871284	1.04	
102	3.226405395	1.09	
108	3.398268713	1.15	
114	3.561146511	1.20	
120	3.680286659	1.24	

Pristine catalyst, 75 °C, 20% H_2. Highlighted data indicates the linear region.

Time / s	BBA / A.U.	mol_H/mol_{Au_per}	Rate / mol_{H*}/Au_{per}·min
0	0	0	1.354
6	-0.030864136	-0.01	
12	-0.028789436	-0.01	
18	-0.0263368	-0.01	
24	-0.035987567	-0.01	
30	-0.027250586	-0.01	
36	-0.022044	-0.01	
42	-0.019414044	-0.01	
48	-0.024626866	-0.01	
54	-0.024103567	-0.01	
60	-0.404472511	-0.14	
66	-0.065816134	-0.02	
72	-0.08337738	-0.03	
78	-0.035835942	-0.01	
84	0.013284095	0.00	
90	0.149087627	0.05	
96	0.388325293	0.13	
102	0.71449374	0.24	
108	1.120759834	0.38	
114	1.536398042	0.52	
120	1.966950167	0.66	
126	2.391942371	0.81	
132	2.80240928	0.95	
138	3.1002432	1.05	
144	3.348204721	1.13	
150	3.550644744	1.20	

Pristine catalyst, 75 °C, 25% H_2. Highlighted data indicates the linear region.

Time / s	BBA / A.U.	mol_H/mol_{Au_per}	Rate / mol_{H*}/Au_{per}·min
0	-0.011927444	0.00	1.506
6	-0.011446689	0.00	
12	-0.011962991	0.00	
18	-0.011423964	0.00	
24	-0.014805577	-0.01	
30	-0.01832634	-0.01	
36	-0.020718994	-0.01	
42	-0.023392934	-0.01	
48	-0.02512431	-0.01	
54	-0.010863136	0.00	
60	-0.005259959	0.00	
66	0.010624428	0.00	
72	0.044843279	0.02	
78	0.167293966	0.06	
84	0.423345834	0.14	
90	0.783117235	0.26	
96	1.223326087	0.41	
102	1.695017815	0.57	
108	2.144777298	0.72	
114	2.614307642	0.88	
120	2.979083061	1.01	
126	3.284704447	1.11	
132	3.530079126	1.19	
138	3.733365774	1.26	
144	3.878940582	1.31	
150	4.022082329	1.36	

Pristine catalyst, 75 °C, 30% H_2. Highlighted data indicates the linear region.

Time / s	BBA / A.U.	mol_H/mol_{Au_per}	Rate / mol_{H*}/Au_{per}·min
0	0.018836	0.00636245	1.622
6	-0.00713	0.00	
12	0.011826	0.00	
18	0.003593	0.00	
24	0.011817	0.00	
30	-0.00827	0.00	
36	-0.00291	0.00	
42	0.007207	0.00	
48	0.004202	0.00	
54	0.023253	0.01	
60	-0.00271	0.00	
66	0.052619	0.02	
72	0.078216	0.03	
78	0.230634	0.08	
84	0.51727	0.17	
90	0.925084	0.31	
96	1.397236	0.47	
102	1.90888	0.64	
108	2.425067	0.82	
114	2.876191	0.97	
120	3.279487	1.11	
126	3.586699	1.21	
132	3.809443	1.29	
138	3.990103	1.35	
144	4.116072	1.39	
150	4.246814	1.43	

Pristine catalyst, 75 °C, 40% H_2. Highlighted data indicates the linear region.

Time / s	BBA / A.U.	mol_H/mol_{Au_per}	Rate / mol_{H*}/Au_{per}·min
0	0.001263689	0.00	1.810
6	0.010600252	0.00	
12	0.01134814	0.00	
18	0.061810568	0.02	
24	0.220020592	0.07	
30	0.51873219	0.18	
36	0.99039501	0.33	
42	1.55612886	0.53	
48	2.12766552	0.72	
54	2.673260689	0.90	
60	3.146776915	1.06	
66	3.525159597	1.19	
72	3.790169478	1.28	
78	4.006396294	1.35	
84	4.165929318	1.41	
90	4.310436726	1.46	
96	4.407020569	1.49	
102	4.496407032	1.52	
108	4.56786108	1.54	

CO Adsorption

To perform CO adsorption analysis, a pellet of the catalyst is equilibrated under Ar flow at 30 °C. Since the IR system is not suitable for low-pressure measurements, to achieve low CO pressure in the cell, 40 mL/min of argon is flown, while CO is introduced *via* a leak of the mass flow.

After spectrum acquisition, a scaled subtraction of a gas-phase CO spectrum is performed to reduce its contribution and obtain spectra with the lowest possible interferences.

In the following plot, from top to bottom: raw data; CO spectrum; result of the scaled subtraction.

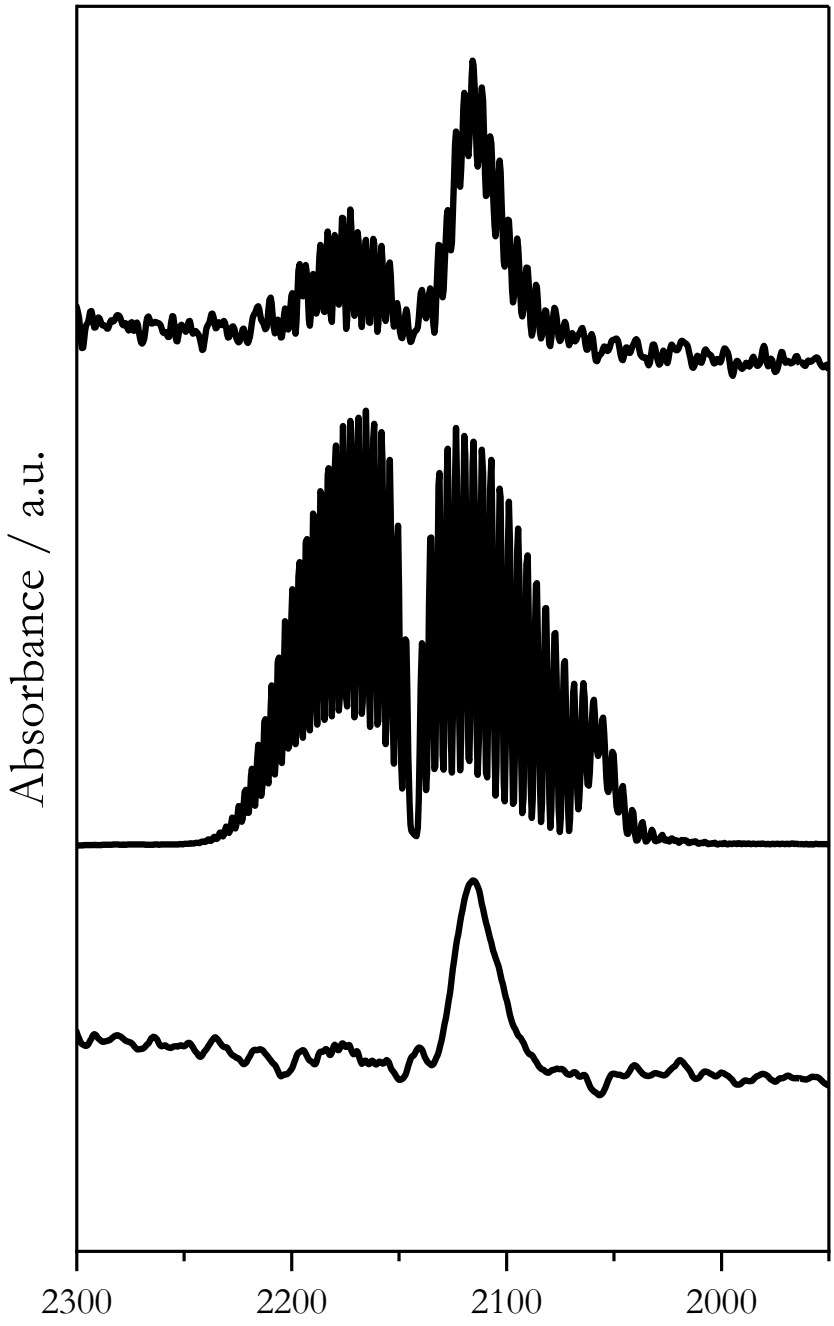

Primary Kinetic Isotopic Effect

Primary kinetic isotopic effect measurements are performed at 75°C. After SAO treatment, the pellet is equilibrated, and 0.20 atm H_2 kinetic data are collected. The pellet is left desorbing under Ar in the IR cell until completion. Once re-equilibrated, 0.20 atm D_2 kinetic data are collected.

The ratio between the kinetic constants gives the primary KIE value:

$$KIE = \frac{r_{H_2-OH}}{r_{D_2-OH}}$$

Sample	r (H_2) / a.u./s	r (D_2) / a.u./s	1° KIE
Pristine	2.183	0.878	2.5
0.095% carbene	1.269	0.482	2.6
Au/P25	16.141	4.679	3.5
Au/P25 oxidized	16.935	4.231	4.0
Au/P25 KDH/APA	/	/	4.1

Secondary Kinetic Isotopic Effect

Secondary kinetic isotopic effect measurements are performed at 75°C. After SAO treatment, the pellet is equilibrated and 0.20 atm D_2 kinetic data are collected. The pellet is then left under Ar in the IR cell until desorption, then argon flow is diverted through a D_2O saturator. D_2O saturated Ar flow is maintained while monitoring the H-D exchange with IR (loss of the Ti-OH_2 scissoring, growth and then loss of the Ti-OHD scissoring, and growth of the Ti-OD_2 scissoring).

Once newly equilibrated, 0.20 atm D_2 kinetic data are collected.

Since on other samples inverse secondary KIE was found, the inverse secondary KIE value is given by the ratio between the kinetic constants:

$$KIE = \frac{r_{D_2-OD}}{r_{D_2-OH}}$$

Sample	r (OH) / a.u./s	r (OD) / a.u./s	2° KIE
Pristine	1.635	1.455	0.89
0.095% carbene	0.563	0.591	1.05
Au/P25	4.679	4.572	0.98
Au/P25 oxidized	3.133	4.186	1.34
Au/P25 KDH/APA	/	/	1.19

Reduction of p-nitrophenol

To monitor p-nitrophenol reduction in the FT-IR instrument, small amounts of catalysts are impregnated with p-nitrophenol. To obtain this, 100 mg of catalyst are dispersed in 4 mL of methanol, and a solution of p-nitrophenol is added to achieve a final concentration of the compound equal to one molecule per nm^2 of catalyst. The suspension is then left drying in the air overnight while gently stirring.

A pellet of material is then pressed and equilibrated in the FT-IR at the desired temperature. The temperature range varies from 60 to 90 °C. Once equilibrated, 40% H_2 is flown, with data collected with 10 s intervals.

To calibrate the p-nitrophenol peaks, the hydrogen flow is maintained until the spectra are equilibrated. All the spectra are then reprocessed using an air background. The last spectrum is then subtracted from the other to eliminate the pellet contribution from the $-NO_2$ asymmetric stretching adsorption band. In this way, the $-NO_2$ signal is calibrated based on the difference between the initial and final area between 1600 and 1565 cm^{-1}.